Diagnosis and Prognosis of Degradation in Lithium-Ion Batteries

Christoph Birkl

Department of Engineering Science
University of Oxford

This dissertation is submitted for the degree of
Doctor of Philosophy

Pembroke College

Michaelmas 2016/2017

Für meine Eltern, Doris und Robert.

Acknowledgements

Firstly, I want to express my sincere appreciation to my supervisor Professor David Howey, who's dedication to his students and to his research have been truly inspirational. Having a genuinely supportive and responsive supervisor like Dave can make all the difference and should not be taken for granted. His advice and guidance have been invaluable and it has been a true pleasure being part of his research group.

I would like to thank the members of the Peter Bruce Group for a very fruitful and inspiring collaboration. My gratitude goes in particular to Dr. Euan McTurk and Dr. Matthew Roberts for their contributions to the development of experimental techniques used in this work and for their general advice and guidance. I would like to acknowledge Stefanie Zekoll, Dr. Felix Richter and Dr. Andy Naylor for their work and advice on SEM and EDX characterisations and Dr. Ola Hekselman and Dr. Liyu Jin for NMR analyses.

For much valued insights and advice on the topic of Bayesian inference I would like to thank Professor Michael Osborne and Dr. Robert Richardson.

I would like to express my appreciation to the EPSRC and Jaguar Land Rover for financial support and to the team at JLR for many engaging meetings and stimulating exchanges of ideas.

A special thank you goes to Nicole Miranda, who shared this journey with me right from the start and has always been there for me.

This DPhil degree has been quite a ride and it would not have been half the fun without all my colleagues and good friends at the EPG, especially Adrien, Rob, Damien, Pietro, Jorn, Pete, Nathan and Johannes. It has been an absolute privilege being part of such a friendly, enthusiastic and brilliant group. I am also grateful to the two admin masterminds Joel and Sukarni for making things happen.

The true reason I have made it this far are my family, especially my parents to whom I dedicate this thesis. Thank you all for supporting me in every way imaginable.

I also want to thank Julian and Miriam Savulescu and the Hutt family who have helped me make a home away from home.

Last but not least, a big thank you to all my friends in Austria for your many visits and all the fun we have had. No matter for how long I am gone, every time we reunite you make me feel as if I had never even left.

Abstract

Lithium-ion (Li-ion) batteries are the most popular energy storage technology in consumer electronics and electric vehicles and are increasingly applied in stationary storage systems. Yet, concerns about safety and reliability remain major obstacles, which must be addressed in order to improve the acceptance of this technology. The gradual degradation of Li-ion cells over time lies at the heart of this problem. Time, usage and environmental conditions lead to performance deterioration and cell failures, which, in rare cases, can be catastrophic due to fires or explosions. The physical and chemical mechanisms responsible for degradation are numerous, complex and interdependent. Our understanding of degradation and failure of Li-ion cells is still very limited and more limited yet are reliable and practical methods for the detection and prediction of these phenomena.

This thesis presents a comprehensive approach for the diagnosis and prognosis of degradation in Li-ion cells. The key to this approach is the extraction of information on electrode-specific degradation through open circuit voltage (OCV) measurements. This is achieved in three stages. Firstly, a parametric OCV model is created, which computes the OCV of each electrode. Secondly, a diagnostic algorithm is devised, through which the OCV model is fitted to OCV measurements recorded on Li-ion cells at various stages throughout their cycle life. The algorithm identifies the nature and quantifies the extent of degradation experienced by the cells. Lastly, the outputs of the algorithm are used to identify the likely failure modes of the cells and predict their end-of-life.

The presented methods improve safe operation and predictions of remaining useful cycle life for commercial Li-ion cells. Greater certainty about the reliability, safety, required maintenance and depreciation of Li-ion battery systems can significantly enhance the competitiveness of battery electric storage in both automotive and stationary applications. The findings presented in this work are therefore not only of technological but also of commercial interest.

Publications

The following publications cover part of the work presented in this thesis.

[1] C. R. Birkl, E. McTurk, M. R. Roberts, P. G. Bruce, D. A. Howey. A Parametric Open Circuit Voltage Model for Lithium Ion Batteries. *Journal of the Electrochemical Society*, 162(12):A2271-A2280, 2015. Publisher copy

[2] E. McTurk, C. R. Birkl, M. R. Roberts, D. A. Howey, P. G. Bruce. Minimally Invasive Insertion of Reference Electrodes into Commercial Lithium-Ion Pouch Cells. *ECS Electrochemistry Letters*, 4(12):A145-A147, 2015. Publisher copy

[3] C. R. Birkl, M. R. Roberts, E. McTurk, P. G. Bruce, D. A. Howey. Degradation Diagnostics for Lithium Ion Cells. *Journal of Power Sources*, 341:373-386, 2017. Publisher copy

[1] presents the parametric OCV model which forms the basis of Chapter 2 in this work. Contributions of other researchers are limited to the manufacture of coin cells and general advice and guidance. The work in [1] was presented at the 227$^{\text{th}}$ Meeting of the Electrochemical Society in May 2015, in Chicago, USA.

[2] Describes the method for the manufacture of 3-electrode cells, which were used in Chapters 2 and 4. My contributions to [2] include participation in the design process for the 3-electrode modification techniques and Figure 1 in [2]. The 3-electrode cells used for the work presented in this thesis were partly made by Euan McTurk and partly by myself.

[3] introduces the diagnostic algorithm presented in Chapter 3. Contributions of other researchers are limited to advice and guidance on the manufacturing of coin cells and general feedback on the work. The work was also presented at the Battery Power Conference in April 2016 in Münster, Germany.

Table of contents

List of figures

List of tables

Nomenclature

Abbreviations

BMS	Battery management system
CC	Constant current
CV	Constant voltage
DMC	Dimethyl carbonate
DoD	Depth of discharge
ECM	Equivalent circuit model
EDX	Energy dispersive X-ray spectroscopy
EIS	Electrochemical impedance spectroscopy
EKF	Extended Kalman filter
EoC	End of charge
EoD	End of discharge
EV	Electric vehicle
GITT	Galvanostatic intermittent titration technique
HEV	Hybrid electric vehicle
ICA	Incremental capacity analsys
LAM	Loss of active material
LAM_{NE}	Loss of active material of the negative electrode
LAM_{PE}	Loss of active material of the positive electrode
LCO	Lithium cobalt oxide
LFP	$LiFePO_4$
Li-ion	Lithium-ion
LLI	Loss of lithium inventory
NCO	Nickel cobalt oxide
NE	Negative electrode
NMP	N-Methyl-2-pyrrolidone
OCV	Open circuit voltage

P	Phase transition of electrode material
PE	Positive electrode
RE	Reference electrode
RMSE	Root-mean-square error
SEI	Solid electrolyte interphase
SEM	Scanning electron microscopy
SNR	Signal-to-noise ratio
SoC	State of charge
SoH	State of health
SPM	Single particle model

Roman symbols

a	Chemical activity [-]
E_0	Standard redox potential [V]
E^{OC}	Open circuit voltage [V]
e	Elementary charge [C]
I	Current [mA]
k	Boltzmann constant [J·K^{-1}]
m	Mean of a probability distribution
p	Probability
Q	Capacity [mAh]
Q_{nom}	Nominal cell capacity [mAh]
s	Standard deviation of a probability distribution
T	Temperature [K]
t	Time [h]
U	Interaction energy [J]
V	Voltage [V]
x	Normalised cell capacity [-]
Δx	Fraction of occupied lattice sites [-]
$\mathbf{Y}$	Data set
y	Data point
z	Number of neighbouring lattice sites

Greek symbols

γ	Activity coefficient [-]
η	Maximum log likelihood
θ	Model parameters
μ	Mean (of a Gaussian distribution)
σ	Standard deviation
ζ	Fitting parameter for OCV model [-]

Subscripts

Cell	Cell
de	Delithiated
EoC	End of charge
EoD	End of discharge
high	Referring to upper limit
li	Lithiated
low	Referring to lower limit
max	Maximum
meas	Measured
min	Minimum
nom	Nominal
NE	Negative electrode
PE	Positive electrode
pl	Referring to onset of lithium plating

Chapter 1

Introduction and literature review

1.1 Introduction

Lithium-ion (Li-ion) batteries are the dominant energy storage solution in consumer electronics and are gaining popularity in the automotive industry. Their high energy density and long lifetime make them attractive for applications in electric vehicles (EVs), hybrid electric vehicles (HEVs) and, increasingly, stationary energy storage systems [1, 2]. However, safety issues and concerns about reliability remain major obstacles that hinder the market penetration of Li-ion batteries, particularly in the automotive sector [3, 4]. The presence of both combustible material and oxidizing agent can result in fires or explosions if the battery is not operated within appropriate safety limits [1, 5, 6]. Safe and reliable operation of Li-ion batteries requires the monitoring of internal states, such as the state of charge (SoC), internal temperature, and the state of health (SoH) [7, 8]. These states cannot be directly measured but must be inferred from models and diagnostic methods that use available measurements as inputs, such as cell voltage, current and surface temperature. Internal states of Li-ion cells change over time and as a result of usage and exposure to environmental conditions, which adds to the difficulty of accurate state estimation [9–12].

In addition to monitoring internal states of Li-ion cells, it is essential to anticipate the development of safety hazards and the end of life. Safety hazards can arise from lithium plating and dendritic growth on graphite anodes, which may cause internal short-circuits, potentially resulting in fires and/or explosions [13–16]. Another safety-critical development is the destabilisation of the cathode structure through excessive delithiation, which may trigger a thermal runaway [17]. The prediction of the end-of-life of Li-ion cells is an equally challenging task. Knowledge about the remaining useful life of individual Li-ion cells is crucial to assess the reliability and depreciation of any battery system.

The degradation of Li-ion cells plays a central role in estimating the SoC, fault detection, and end-of-life estimation. SoC estimation is based on the relationship between the cell's capacity and open circuit voltage (OCV) [18], which is the potential difference between the positive and negative electrode when no current flows. The cell's OCV changes as the cell degrades, which leads to increasingly inaccurate SoC estimates [19]. Degradation also results in capacity fade and rising internal resistance, leading to power fade [20]. Capacity and/or power fade are generally used to define the SoH of a battery. Although there is no consensus on the exact definition of the SoH, it is typically defined as either the battery capacity as a percentage of its nominal capacity, the internal resistance as a percentage of its nominal internal resistance, or a combination of both [21]. Continued degradation ultimately leads to the end-of-life of Li-ion cells, which is reached once the cell does no longer meet the required capacity or power demands. In rare cases, abrupt or catastrophic cell failure can occur, which can result from mismanagement (*e.g.* over-charge, over-discharge, exposure to high temperatures [22]) or gradual processes such as lithium plating at low charging temperature or excessive loss of anode material [23].

In summary, knowledge of the type and extent of degradation in Li-ion cells is necessary in order to maintain safe operation, obtain accurate estimates of SoC and SoH, and predict end-of-life.

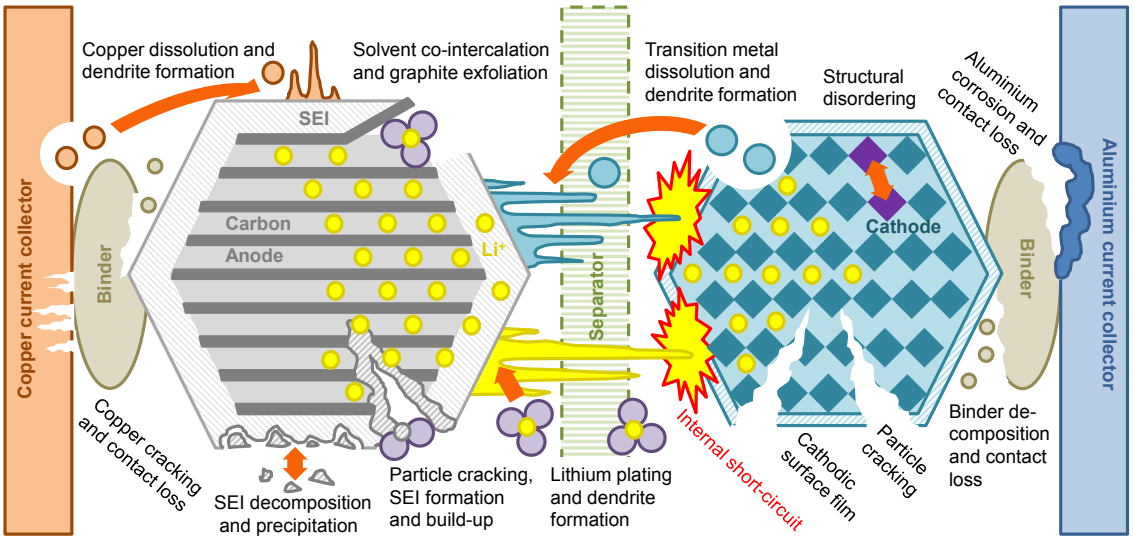

Fig. 1.1 Degradation mechanisms in Li-ion cells

Degradation in Li-ion cells arises from a complex interplay of physical and chemical mechanisms, influenced by environmental conditions, usage patterns, and operational history. Different degradation mechanisms act on the individual cell components: the electrodes, the electrolyte, the separator, and the current collectors [24–29]. Figure 1.1 [30] illustrates some of the most commonly reported degradation mechanisms in Li-ion cells. The large number of degradation mechanisms, as well as their different causes, rates, and inter-dependencies, constitute major challenges for the attempt to model or detect degradation in Li-ion cells. Two general approaches have been taken to tackle the issues of degradation modelling and diagnostics:

1. The empirical, 'top-down' approach: Based on operational data to estimate (and possibly predict) the effects of degradation on cell performance. This approach is not necessarily concerned with the underlying degradation mechanisms.

2. The physics-based, 'bottom-up' approach: Based on cell-specific material properties and operational parameters that model (and possibly predict) a selected number of degradation mechanisms, from which effects on cell performance are derived.

Empirical approaches are reviewed in Section 1.2 and physics-based approaches, in Section 1.3. In the literature, degradation modelling is typically separated from fault detection, although faults are often a direct consequence of certain degradation mechanisms. Contributions on fault detection are discussed in Section 1.4. Section 1.5 assesses the presented literature for gaps in order to identify the most promising avenues of research. The chapter closes with an outline of the thesis.

1.2 Empirical methods

The two general types of empirical methods used to identify and quantify degradation in Li-ion cells are data-driven methods and on-line state estimators.

1.2.1 Data-driven methods

Data-driven methods typically rely on large sets of experimental data obtained by exposing Li-ion cells to detrimental conditions. The data collected during such experiments can thus be used to infer correlations between environmental and operational factors and the symptoms of degradation, such as capacity and power fade.

Bloom *et al.* [12] modelled power fade by fitting data gathered at various temperatures with the equation

$$Q = A \cdot \exp\left(\frac{-E_{\mathrm{a}}}{RT}\right) t^{z} \tag{1.1}$$

where Q is power loss in percent, A the pre-exponential factor, E_{a} the activation energy, R the gas constant, T the absolute temperature, t the time and z an empirically determined exponent. Wang *et al.* [31] adapted this approach to include current rate by substituting time in Equation 1.1 with Ah-throughput, which represents the amount of charge inserted/extracted during cycling. Although

the authors obtained good results for a selection of stress factors such as ambient temperature and current rates, the effects of other factors, such as average cell voltage and charge rate, or combinations of stress factors, are not considered.

Li *et al.* [32] devised a cycle life model which considers stress coupling between multiple degradation factors, such as temperature, cycling rates, end-of-charge and end-of-discharge voltages, and showed that coupling effects have a non-negligible impact on degradation above certain stress levels. This methodology requires extensive test regimes for every new cell type, which are highly resource intensive.

Safari *et al.* [33, 34] applied principles of mechanical fatigue prognostic theory to predict capacity fade. The model was validated against simulated ageing data, generated by a physics-based battery model, which assumes SEI growth as the only source of degradation. Although validation against a higher fidelity model saves time and resources compared to validation against experimental data, it constitutes a compromise in quality, since imperfections and inaccuracies in the higher fidelity model are transferred to the model being validated. In other words, if the outputs of an existing model are used to validate another model, the maximal accuracy of the new model is limited by the accuracy of the original model. This approach may be useful in cases where the system in question is well understood and described with an existing, high fidelity model and new models may be required to reduce complexity or increase speed of computation. Due to the complexity of degradation in Li-ion cells, care must be taken when interpreting the results of a new model validated against an existing model. If a physical model of a particular mechanism is used to validate a new model, the new model can only be evaluated for modelling that particular mechanism and not degradation in general. The methodology for predicting capacity fade presented by Safari *et al.* [33, 34] was validated against a physical model for SEI formation on the anode and can therefore only claim to model SEI formation and not capacity fade in general, which could also be caused by other mechanisms.

He *et al.* [35] proposed an empirical model for capacity fade

$$Q = a \exp(b\, k) + c \exp(d\, k) \tag{1.2}$$

where Q is the cell capacity, k is the cycle number, a and b are empirical parameters related to the impedance and c and d are empirical parameters representing the ageing rate. The model is fitted to the measured cell capacity as a function of cycle number. Extrapolating Equation 1.2 allows for end-of-life prediction. Using the experimental data set to initiate the parameters in Equation 1.2, new data are added as they become available in order to improve the accuracy of predictions. Similar data-driven methods based on empirical degradation models are reported by Chen and Pecht [36], Klass *et al.* [37], Guo *et al.* [38], Liu *et al.* [39], and Liao *et al.* [40].

The advantage of the above methods is that modelling and predicting the effects of degradation on cell performance directly does not necessarily require knowledge of the underlying physical and chemical mechanisms and cell-specific material parameters. Disadvantages are that large sets of experimental data are required to obtain accurate predictions. The recording of such data sets is time consuming and costly, and the data are highly specific to a certain type/make of Li-ion cells and do not necessarily reflect real-life usage if recorded in laboratory conditions. Moreover, there is a presumption that the measured macroscopic data contain all the information relevant to cell failure. Data-driven models trained on large data sets may be well suited to predict gradual changes in capacity or power capability representative of the recorded data. However, such models are unlikely to accurately predict the end-of-life of individual cells whose ageing behaviour deviates significantly from that of the average cell [41]. The identification of individual outliers and potential safety hazards requires knowledge of the underlying degradation mechanisms.

Another type of data-driven method are diagnostic techniques, which aim to extract additional information from cell measurements in order to provide a mecha-

nistic understanding of the driving forces behind the observed degradation. Bloom *et al.* [42] proposed the analysis of differential voltage measurements (dV/dQ), plotted against capacity, as a means to identify different modes of degradation, such as the loss of active electrode material and the shift in alignment of the electrodes due to side reactions. The differentiation of low-rate voltage curves emphasises the features of the voltage curves, which facilitates the interpretation of effects of degradation. For the differential analysis, dV/dQ curves obtained for half-cells were compared to dV/dQ curves of full cells in order to identify the origin of degradation. Such data depends strongly on ambient temperature, which was maintained at 25 °C for the low-rate voltage measurements.

In a similar approach, Dubarry *et al.* [43, 20, 44–49] used incremental capacity analysis (ICA) to identify different degradation modes in Li-ion cells and track capacity and power fade over time. ICA curves are obtained by forming the derivative of measured cell capacity with respect to cell voltage (dQ/dV) recorded at low rates, plotted against terminal voltage. Thereby, voltage plateaus (corresponding to phase transformations and solid solution formations in cathodes and staging in negative graphite electrodes) in voltage-capacity curves are transformed into peaks in ICA curves, which are easier to identify and provide information on prevalent degradation modes.

Smith *et al.* [50] used high-precision ($\pm 10\,\mu V$) battery testers for low-rate voltage measurements in order to compute dQ/dV and differences in dQ/dV on subsequent cycles ($\Delta dQ/dV$), which provide information on the rate of degradation for potential use in quality control.

Wu and Merla *et al.* [51, 52] combined the concept of incremental voltage analysis with temperature measurements in order to infer thermodynamic information. The differential of temperature with respect to voltage (dT/dV), plotted against cell voltage, was used to analyse cell degradation. The authors were primarily interested in identifying combined dominating phase transitions of the two electrodes, which

appear as peaks when plotting the differential measurements dT/dV. Advantages over incremental voltage and capacity techniques include the application of higher current rates (on the order of 2 C) and the extraction of additional thermodynamic information.

In [49], Dubarry *et al.* summarised effects of degradation mechanisms on the OCV (or low-rate voltage curves) of the electrodes and the cell with three so-called degradation modes, namely loss of lithium inventory (LLI), loss of active material of the positive electrode ($\mathrm{LAM_{PE}}$) and loss of active material of the negative electrode ($\mathrm{LAM_{NE}}$). These so-called degradation modes are hereafter referred to as degradation signatures to avoid confusion with physical modes of degradation. Effects of the degradation signatures on the cell's OCV were demonstrated by simulation, using low-rate voltage measurements recorded on half-cells.

Advantages of diagnostic techniques based on the OCV of electrodes include the ability to monitor electrode potentials in order to ensure safe operation. Possible safety hazards, such as excessive PE potentials or the onset of lithium plating on the NE, could be detected. Moreover, identifying electrode-specific degradation enables the tracking of the current rates experienced by individual electrodes and may help improve end-of-life predictions.

General drawbacks of the diagnostic methods presented above are their dependency on OCV measurements of the electrodes as inputs, the temperature dependency of the OCV [53] and measurement noise. For differential techniques, in particular, measurement noise is an issue since such noise is enhanced by taking derivatives. This can be particularly problematic for practical applications, where noisy measurements are likely. Another shortcoming in most diagnostic techniques that aim to identify LLI and LAM is the lack of conclusive, experimental evidence of the effects of these degradation signatures on the cell's OCV.

1.2.2 On-line state estimators

On-line state estimators typically comprise simple dynamic models, such as equivalent circuit models (ECMs), combined with a look-up table for the cell's OCV and adaptive filters or observers to estimate both the fast changing battery states (*e.g.* SoC) and the slower changing, time-varying model parameters, such as internal resistance and cell capacity, which constitute the SoH [54].

Plett [18, 55, 56] implemented a dual estimation approach using a simple ECM in combination with an extended Kalman filter (EKF) to simultaneously estimate SoC and SoH, where SoH is defined as the change in capacity and resistance from the nominal cell values. Measured terminal voltage and current are used as inputs. In a similar approach Verbrugge *et al.* [57] implemented a simple ECM combined with a weighted recursive least squares algorithm to estimate SoC and SoH using voltage and current measurements. The SoH was defined as the values of the ECM parameters relative to their initial values. Neither Plett [56] nor Verbrugge *et al.* [57] demonstrate how their algorithms perform at different operating temperatures.

Kim *et al.* [58] reported yet another approach, consisting of a dual-sliding-mode-observer in combination with a simple ECM for SoC and SoH estimation, where the SoH was defined as capacity fade and resistance increase. The parallel architecture of SoC and SoH observers accounts for effects of degradation on SoC estimates, while keeping computational efforts low (the authors claimed their method to be five times faster than equivalent Kalman filter techniques). The variability of ECM parameters with temperature was considered as model uncertainty and a large operating temperature range ($-30\,^{\circ}\mathrm{C}$ to $55\,^{\circ}\mathrm{C}$) was covered. SoC estimation errors still reached 10%, which would have to be improved for reliable applications.

Saha and Goebel [59] devised a method for simultaneous end-of-discharge and end-of-life prediction based on a particle filtering framework, where the system states are represented as probability density functions, approximated by a set of particles

(points). Effects of temperature were not considered and their approach was not validated for dynamic battery usage.

Remmlinger *et al.* [60] designed a method for on-line estimation of a degradation index which depends on internal resistance, based on an ECM and a regressive linear least-squares algorithm. The identification process was performed on a recurrent battery excitation specific to HEVs, recorded during the start of the combustion engine. Although the separation of SoC and SoH estimations is advantageous in that it reduces computational complexity, this approach is limited to internal resistance as the only measure of SoH.

On-line state estimators are a popular choice for battery management systems (BMS) in industry due to their relatively simple implementation and low computational complexity [8, 61]. A general shortcoming of on-line state estimators is their failure to incorporate effects of degradation and operating temperature on the cell's OCV [53], which is used at the core of most state estimators. SoC estimation is ultimately based on the relationship between OCV and cell capacity. Changes in the cell's OCV resulting from ambient temperature and degradation must be considered to maintain high accuracies in SoC estimation [62]. On-line state estimators are not typically concerned with underlying degradation mechanisms. This makes it difficult to anticipate the safety hazards linked to certain degradation mechanisms.

1.3 Physics-based models

Due to the large number and complex interdependencies of degradation mechanisms, physics-based models usually focus on one or two of the most widely reported degradation mechanisms, such as SEI formation and growth or particle cracking. Modelling of physical and chemical degradation mechanisms requires a dynamic model in order to calculate the forces driving degradation at the electrode level, such as current densities, temperatures and electrode potentials. The single particle model

(SPM) [63, 64] is a popular simplification of a dynamic electrochemical battery model and often provides a basis for physics-based degradation models.

The formation and growth of the SEI layer at the anode is considered the predominant mechanism for capacity fade by many researchers and often forms the central hypothesis in their degradation models [65–71]. Safari and Delacourt [72] employed a SPM to analyse degradation in a LFP cell and identified, in addition to SEI growth, the loss of graphite active material as another source of capacity loss during cycling. Zhang and White [73], also using a SPM, postulated SEI formation and loss of active cathode material as major capacity fade mechanisms for a $LiNiCoO_2$ cell.

Laresgoiti *et al.* [70] use the SPM as the basis to model the break and repair of the SEI as the primary cause for capacity fade in Li-ion cells. Other examples of SPM-based degradation models, are reported by Pinson and Bazant [69], Christensen and Newman [74], Prada *et al.* [75, 76], and Prasad and Rahn [77].

A general drawback of using the SPM as a basis for degradation models is that the SPM does not account for non-uniformities in electrolyte composition within the electrode pores or separator, or ohmic losses resulting from electronic conduction in the solid part of the electrode. The neglect of liquid diffusion and solid-phase conductivity limits validity fo the SPM to currents below 1C [78].

Deshpande *et al.* [79] presented a combined chemical degradation and mechanical fatigue model. In addition to SEI formation and growth, the model also accounts for mechanical degradation in the form of particle cracking, followed by renewed SEI formation and growth. The growth of pre-existing cracks on electrode particles upon cyclic stress was modelled using Paris' law for crack growth [80]. Newly exposed electrode surface was subject to further SEI formation and the growth of SEI thickness was assumed to follow a time to the 1/2 power relationship. Particle cracking is particularly relevant at high C-rates, which lead to high amplitudes of stress on the anode structure [81]. However, the experimental validation of the model was limited

to low, constant current rates of C/2. Batteries used in EV and HEV applications are subjected to dynamic current profiles, resulting from high power requirements during acceleration and regenerative breaking. Since Deshpande *et al.* [79] postulated the stress on the particle surface to be proportional to the cell current, current spikes resulting from a dynamic current profile are expected to have a significant impact on the modelled cycle life of the cell and should be considered for model validation.

Although physics-based models provide valuable mechanistic insights, simplifying degradation by assuming that it results solely from one or two processes risks omitting mechanisms with significant contributions to performance deterioration of Li-ion cells.

Another drawback of physics-based degradation models is their reliance on a large number of material-specific parameters, such as exact material compositions, particle sizes, conductivities, etc. In the interest of IP protection, such parameters are not usually disclosed by the cell manufacturers and must be determined experimentally, which is a cost and resource intensive process. Moreover, identifiability and parameter estimation pose significant challenges in physics-based models [82–86].

Finally, one important factor in Li-ion cell degradation is generally neglected in physical degradation models: inhomogeneities. Most physical models capture degradation mechanisms at the micro scale, *i.e.* on an electrode particle or even molecular level and assume uniform material properties [68, 79]. However, evidence suggests that meso and macro scale features, such as inhomogeneities in the structure of the electrodes, have a significant effect on cell degradation as a whole [87, 88]. Structural non-uniformity can lead to inhomogeneous distributions of current densities and different degrees of lithiation inside the electrode material which, in turn, cause inhomogeneous degradation of the electrode. External influences, such as non-uniform cooling, can lead to similar inhomogeneities in impedance and current flow inside Li-ion cells and affect cell ageing [89].

It is likely that degradation in Li-ion cells is too complex to be modelled in its entirety by physical models in a bottom-up approach and must, at least in part, be supplemented by data-driven or diagnostic techniques.

1.4 Fault diagnosis and prognosis

Faults in Li-ion cells can be broadly categorised as critical faults or performance faults. Critical faults pose safety hazards and may lead to fires or explosions. Performance faults refer to a cell reaching its end-of-life criteria, which could be certain levels of capacity or power fade.

Critical faults typically culminate in exothermic reactions and cell combustion. For this reason, temperature is used as the obvious indicator of a pending critical fault and much effort has been directed toward the monitoring of internal cell temperatures [90–96]. In the case of internal short-circuits, which are among the most common sources of critical faults, cell voltage is another indicator that could allow for early fault diagnosis. However, in large capacity cells typically used for EV and HEV applications, temperature and voltage changes due to critical faults might be insufficient to be reliably measured [97]. Increases in temperature due to an internal short-circuit are, at first, confined to the close vicinity of the fault. In large format cells the increase in average cell temperature may be too slow to be a reliable indicator of imminent cell combustion. Similarly, the voltage drop resulting from an internal short-circuit would be much smaller than that in a small capacity cell. This is due to (i) the smaller impedance of the large cell and (ii) the slower change in OCV resulting from the relatively larger amount of charge stored in the cell. Uncertainties in measurements due to inherent differences among the cells within a battery module further complicate the matter. Thus, there is presently no practical method to directly detect a critical fault in an on-board system directly in

time to prevent catastrophic failure. Fault diagnosis and prognosis must therefore be achieved by a combination of measurements and analytic/predictive computations.

Much of the literature on fault detection in Li-ion cells focuses on performance faults, rather than critical faults, with data-driven, statistical [98–100] and control-based methods [101–104] used as preferred techniques. Electrochemical impedance spectroscopy (EIS) has been applied as a diagnostic tool for performance fault detection [105] and even to facilitate the model-based simulation of internal short-circuits, which are among the most common sources of critical fault [106].

In addition to detecting immediate critical faults, which may be achieved through temperature, voltage, or impedance monitoring, it is crucial to identify scenarios that may develop into critical faults in the future. Examples are excessive delithiation of cathode material and lithium plating on anodes, which can lead to internal short-circuits [15].

1.5 Gap analysis

Based on the above review, the following gaps have been identified in the literature on degradation modelling:

- Empirical and physics-based models relying on the cell's OCV do not generally account for effects of degradation on the OCV.
- Physics-based degradation models do not generally incorporate non-uniform degradation, either due to inhomogeneities in electrode materials or caused by external factors.
- Data-driven, diagnostic techniques rely heavily on almost noise-free measurements and often on electrode-level voltage data, both of which pose challenges in practical applications.

- Diagnostic techniques attempting to identify loss of lithium inventory and loss of active electrode material from OCV measurements lack conclusive, experimental evidence of the effects of these degradation signatures on the cell's OCV

In order to tackle the challenge of identifying and quantifying degradation in Li-ion cells and to fill the gaps in the literature, a comprehensive approach is required, which combines information gained from measurements with physical insights into degradation mechanisms. Ideally, estimates of degradation (such as capacity fade and increased resistance) should be combined with end-of-life prediction and the identification of potential safety hazards. From the viewpoint of practical applications, any proposed approach should meet the following requirements:

- Models must be easily and definitively parameterised using available measurements.
- Measurement noise must be tolerated.
- Cell-to-cell variabilities must be accounted for.
- Non-uniform degradation[1] within cells must be accounted for.

The above requirements point to a diagnostic approach based on frequent cell characterisations, which utilizes available measurements that contain information about the current states of the cell, such as the remaining useful capacity of the individual electrodes. One such measurement is the cell's OCV. The OCV provides characteristic thermodynamic information about the positive [107–109] and the negative [110] electrode. Changes in these characteristics can offer valuable information on path-dependent degradation of both the individual electrodes and the cell as a whole [48, 19, 111]. Although not all degradation mechanisms leave a unique

[1]Non-uniform degradation can be the result of inhomogeneities within the cell materials or of non-uniform environmental conditions across the cell, such as ambient temperature or pressure.

fingerprint on the OCV of the cell and the electrodes, degradation mechanisms with the same physical effects can be clustered into degradation signatures, as suggested by Bloom et. al [42] and Dubarry *et al.* [48]. The three most commonly reported degradation signatures are:

1 **Loss of lithium inventory.** Lithium ions are consumed by parasitic reactions, such as surface film formation (*e.g.* SEI growth), decomposition reactions, lithium plating etc. and are no longer available for cycling between the positive and negative electrode, leading to capacity fade. LLI can also occur as a consequence of electrical isolation of electrode material, if the isolated material was lithiated. In such cases, the lithium remains trapped in the electrode material and is no longer available for cycling.

2 **Loss of active material of the negative electrode.** Active mass of the negative electrode is no longer available for the insertion or extraction of lithium due to particle cracking and loss of electrical contact or blocking of active sites by resistive surface layers. These processes can lead to both capacity and power fade.

3 **Loss of active material of the positive electrode.** Active mass of the positive electrode is no longer available for the insertion or extraction of lithium due to structural disordering, particle cracking or loss of electrical contact. These processes can lead to both capacity and power fade.

Many physical and chemical degradation mechanisms which have an effect on the performance and lifetime of Li-ion cells can be mapped to one of these three degradation signatures. Figure 1.2 provides an overview of the causes and effects of some of the most widely reported degradation mechanisms and their relationship to the three degradation signatures.

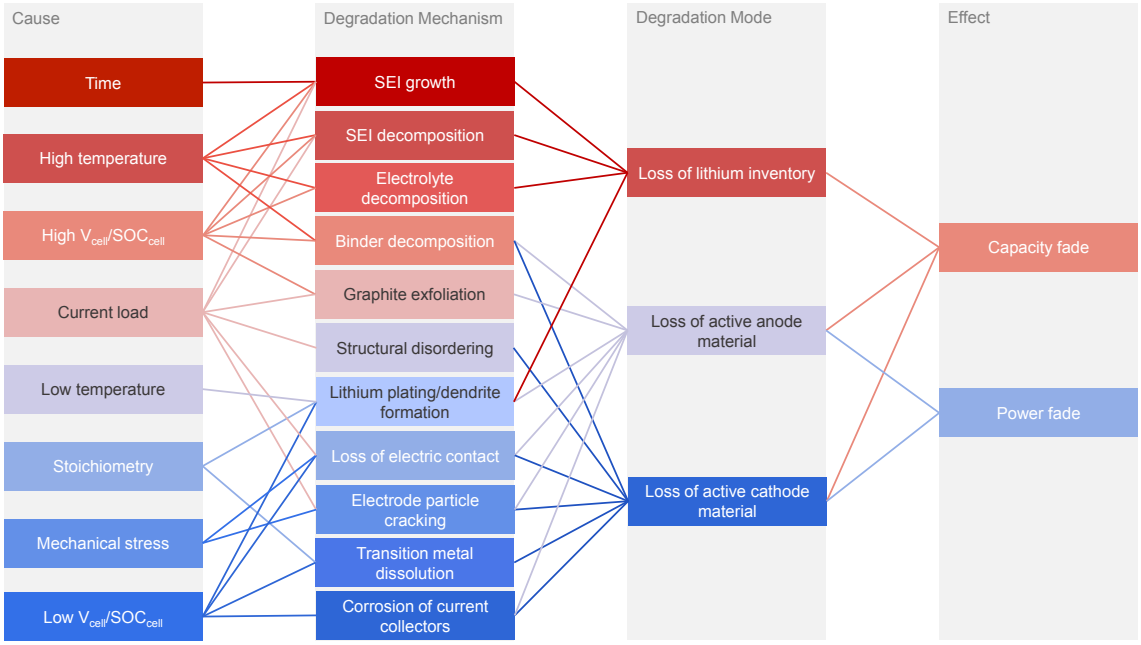

Fig. 1.2 Degradation mechanisms: Causes, effects and degradation signatures.

In order to reliably infer the above degradation signatures from the OCV of Li-ion cells, a principled method must be developed, supported by experiments, which incorporates the effects of the different degradation signatures on the OCV. Moreover, there is a need for an electrode-level OCV model, which allows to reduce the reliance of diagnostic techniques on measurements of electrode OCVs and incorporate the effects of temperature on the OCV. Existing battery models (both empirical and physical) typically use either look-tables of measured OCV as a function of capacity or SoC [8, 54, 56, 112] or empirical, functional expressions [78, 113, 114], which do not consider effects of degradation or ambient temperature. The combination of an electrode-level OCV model with a diagnostic method, updated by frequent cell characterisations, may enable the identification of the nature and the quantification of the extent of degradation in Li-ion cells. Outputs of such a diagnostic method may also be used to identify potential safety hazards and to inform prognostic methods to predict the cells' end-of-life. In order for the above approach to be relevant for practical applications, it should not be chemistry-specific (the term chemistry relating

to the positive electrode material) and model parameters should be obtainable from measurements recorded on commercially available cells and materials.

1.6 Outline

This thesis is divided into six chapters. The above literature review and gap analysis constitute Chapter 1. Chapters 2 to 5 include the main body of the work and each chapter is structured into an introduction and sections describing experiments, methodology, results and discussion, and conclusions.

Chapter 2 presents an electrode-level OCV model, which can be parameterised using measurements obtainable from commercial Li-ion cells. The OCV model is validated using a novel, minimally invasive method for the insertion of a reference electrode into commercial cells.

Chapter 3 introduces a diagnostic algorithm that can identify the nature and quantify the extent of degradation signatures acting on commercial Li-ion cells. The core of the algorithm is formed by the OCV model introduced in Chapter 2, which enables tracking electrode-specific degradation. Experiments are devised with the objective to validate both the diagnostic algorithm and the effects the degradation signatures LLI, $\mathrm{LAM_{PE}}$ and $\mathrm{LAM_{NE}}$ on the OCV.

Chapter 4 applies the diagnostic algorithm to commercial Li-ion cells exposed to extreme cycling conditions, which are expected to trigger the onset of lithium plating. The performance of the diagnostic algorithm is assessed using customised 3-electrode cells (as introduced in Chapter 1) and post mortem materials analysis by means of scanning electrode microscopy (SEM) and energy-dispersive X-ray spectroscopy (EDX).

Chapter 5 demonstrates the application of the diagnostic algorithm to commercial Li-ion cells exposed to long-term tests emulating EV driving conditions. Outputs of

the algorithm are used to assess the performance of a batch of identical cells and to inform end-of-life predictions for faded cells.

Overall conclusions and proposed future work are presented in Chapter 6.

Chapter 2

Parametric OCV model

2.1 Introduction

The OCV of Li-ion cells plays a central role in battery models and diagnostic techniques, as it contains information about the cell's SoC and the available useful capacity of the electrodes [8, 114]. The OCV of a battery cell is the potential difference between the positive electrode and the negative electrode when no current flows and the electrode potentials are at equilibrium. A battery undergoing charge or discharge does not exhibit this potential since it is affected by kinetic effects such as mass transport. However, the OCV of a battery over the full range of states of charge can be obtained by charging or discharging the battery utilizing a galvanostatic intermittent titration technique (GITT) [115] and measuring the potential at the end of each relaxation period (assuming the period is long enough to reach equilibrium).

Battery models and diagnostic techniques typically incorporate the OCV as a function of cell capacity or SoC by storing measured OCV values in look-up tables [56, 8, 112, 54] or by fitting empirical functions to OCV data [78, 113, 114]. These techniques are popular due to their ease of implementation and good initial performance. However, since capacity fade affects the relationship between OCV and cell capacity as the cell degrades, dynamic cell models become increasingly inaccurate

if their underlying OCV expression does not account for capacity fade. Failure to account for the effects of temperature on the OCV can also lead to inaccurate estimates of SoC and capacity fade.

The definitions of SoC and capacity should be clarified here. In electrical engineering terms, the SoC is typically defined as the amount of charge in a cell relative to its fully charged state in percent. The upper and lower limits of the SoC are defined by corresponding voltage limits. In the same manner, the amount of capacity which can be extracted from a cell, in Ah, is measured between the upper and lower voltage limits. A more accurate definition of SoC would be based on the actual lithium concentrations in the electrode materials relative to their maximal concentrations. Equivalently, the useful cell capacity should be defined with reference to the maximal and minimal lithium concentrations. However, since lithium concentrations in electrode materials cannot be measured in working cells, we use the former definition of SoC and cell capacity in this work.

To the best of our knowledge, there exists no electrode-level OCV model which can account for both effects of temperature and degradation. In order to be viable for practical applications using commercial Li-ion cells, an OCV model should fulfil the following requirements:

1. No prior knowledge of material properties (model parameter estimation based on measurements, which can be obtained from commercial cells).

2. An accurate representation of the cells' OCV, derived from the OCV of the electrodes.

3. The ability to account for different operating temperatures.

4. The possibility to accommodate electrode-specific degradation and use the OCV model for degradation diagnostics.

This chapter presents a novel parametric OCV model, which is based on additive terms that represent the phase transitions of the positive and negative electrode materials. The model parameters are identified by fitting the model to OCV data of electrode half-cells and full cells. No prior knowledge of physical parameters relating to the cell's material properties is required, making this model particularly suitable for commercial cells, for which such parameters are not usually accessible. Moreover, the model provides a means to separate the OCV measured on a full cell into its constituent electrode potentials. Tracking the OCV of the positive and negative electrodes independently facilitates the identification of degradation signatures in each electrode. The presented model is temperature dependent. This means that the OCV model parameters only have to be estimated at one operating temperature and the model provides the correct OCV of the electrodes and the cell at any arbitrary operating temperature within their operational limits.

For model validation a modification technique was developed, wherein a reference electrode (RE) is inserted into a commercial Kokam 740 mAh pouch cell. The RE enables the independent measurement of positive and negative electrode potentials. Comparing the measured and computed electrode potentials allows assessment of the accuracy of the OCV model. The 3-electrode cell is also used to assess the model's performance at different operating temperatures.

The OCV model developed in this chapter forms the basis for a diagnostic algorithm (presented in Chapter 3), which can identify the nature and quantify the extent of electrode-specific degradation in commercial Li-ion cells.

A large part of the work presented in this chapter was published in [116] and was presented at the 227$^{\text{th}}$ Meeting of the Electrochemical Society in May 2015, in Chicago, USA. The modification technique for the manufacture of 3-electrode cells was developed in collaboration with Dr Euan McTurk, Dr Matthew Roberts and Professor Peter Bruce from the Department of Materials Science of Oxford University and published in [117]. Contributions of other researchers to the work presented

below are limited to the manufacturing of anode and cathode half-cells and the 3-electrode cell.

2.2 Experimental

The following experiments were conducted:

- Measurement of the OCV of PE and NE half-cells to estimate the electrode-level parameters of the OCV model.
- Measurement of the OCV of a full cell to estimate the cell-level parameters of the OCV model.
- Measurement of the OCV of the positive and negative electrodes in a 3-electrode cell at different ambient temperatures (0 °C, 20 °C and 40 °C) to validate the OCV model.

All OCV data presented in this work were collected using commercially available pouch cells or their harvested electrode materials. The cells were supplied by Kokam, model SLPB 533459H, 740 mAh nominal capacity. The negative electrode material of the Kokam pouch cells was graphite and the positive electrode material was a blend of lithium cobalt oxide (LCO) and lithium nickel cobalt oxide (NCO). Measurements of the specific capacity of the electrode materials gave 180.5 mAh/g for the PE and 270.5 mAh/g for the NE. OCV measurements were conducted at three different temperatures, covering the usage range recommended by the manufacturer: 0 °C, 20 °C and 40 °C. The PE and NE half-cells were fabricated in coin cell format from electrode material harvested from fresh (uncycled) Kokam pouch cells.

2.2.1 Electrode half-cells

The term half-cells used in this work describes electrochemical cells consisting of active electrode materials (graphite in case of the NE and LCO/NCO in case of the PE) as working electrodes and lithium foil as counter electrodes, fabricated in coin cell format. The positive and negative electrode sheets (LCO/NCO on aluminium and graphite on copper, respectively) used for the coin cells were extracted from a Kokam pouch cell under an Argon atmosphere inside a glove box. The pouch cell was cut open with a ceramic scalpel and the PE and NE sheets were removed from the stack. The extracted electrode sheets were rinsed with dimethyl carbonate (DMC) and subsequently dried under vacuum in the antechamber of the glove box.

The current collectors of the Kokam pouch cell were coated on both sides with active electrode material. To improve the electronic conductivity between the electrode sample and the coin cell base, and to prevent a disparity in ionic transport between the side of active material that faces the separator and the side that would face away from it and be pressed up against the coin cell base, the active material was removed from one side of the current collector. This was achieved using small pieces of melamine foam soaked in N-Methyl-2-pyrrolidone (NMP) to clean the active material off one side of the electrode sheets. The other side of the electrode sheets was pressed against a glass surface during the procedure. Active material was only removed from the central sections of the electrode sheets to prevent any NMP from wetting the active material on the other side of the sheets. DMC was used to clean the exposed area of the current collector. Disks of 15 mm diameter were cut from the cleaned area of the electrode sheets using a hole punch, so that each electrode disk had one side of active material and one side of exposed current collector.

The active mass of the electrodes was calculated by subtracting the mass of the current collectors from the total mass of the electrode disks. The mass of the current collectors was determined by cutting disks of 15 mm diameter from electrode sheets

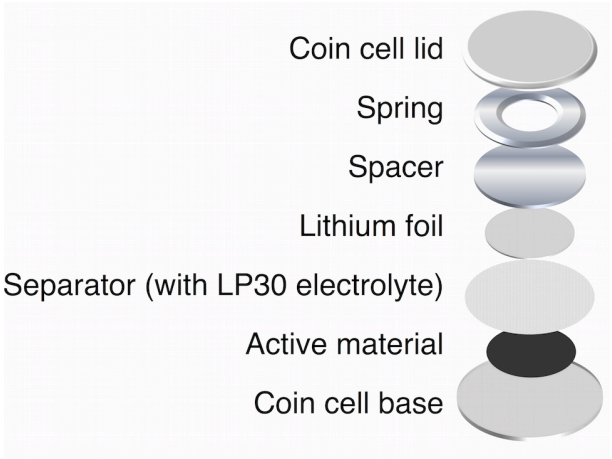

Fig. 2.1 Coin cell assembly of the electrode half-cells.

of the PE and NE and removing the active mass from both sides using NMP, leaving only the current collectors, which were then weighed. The active mass of the PE was measured to be 12.9 mg and that of the NE was 10.7 mg. The half-cell electrodes were placed in a coin cell base, followed by a glass microfibre separator wetted with LP30 ($LiPF_6$ solution in ethylene carbonate (EC) and DMC; 1.0 M $LiPF_6$ in EC/DMC = 50/50 (wt/wt)) electrolyte, lithium foil as the counter electrode, a spacer, a spring for improved contact and the coin cell lid (see Figure 2.1).

2.2.2 Reference electrode insertion

In order to validate the OCV model and algorithm for degradation diagnostics, a novel cell modification method was developed, which consists of the insertion of a RE into commercial pouch cells. The RE enables voltage measurements on both the positive and negative electrode, which are important for the validation of the OCV model. A number of modification techniques were investigated, as described in [117]. The most successful technique was a key hole insertion of the RE through a small incision on the side of the pouch cells.

The REs were fabricated from copper wire (0.8 mm diameter), which was flattened at one end over a length of 20 mm using a metallic press. A 2-electrode electrochemical

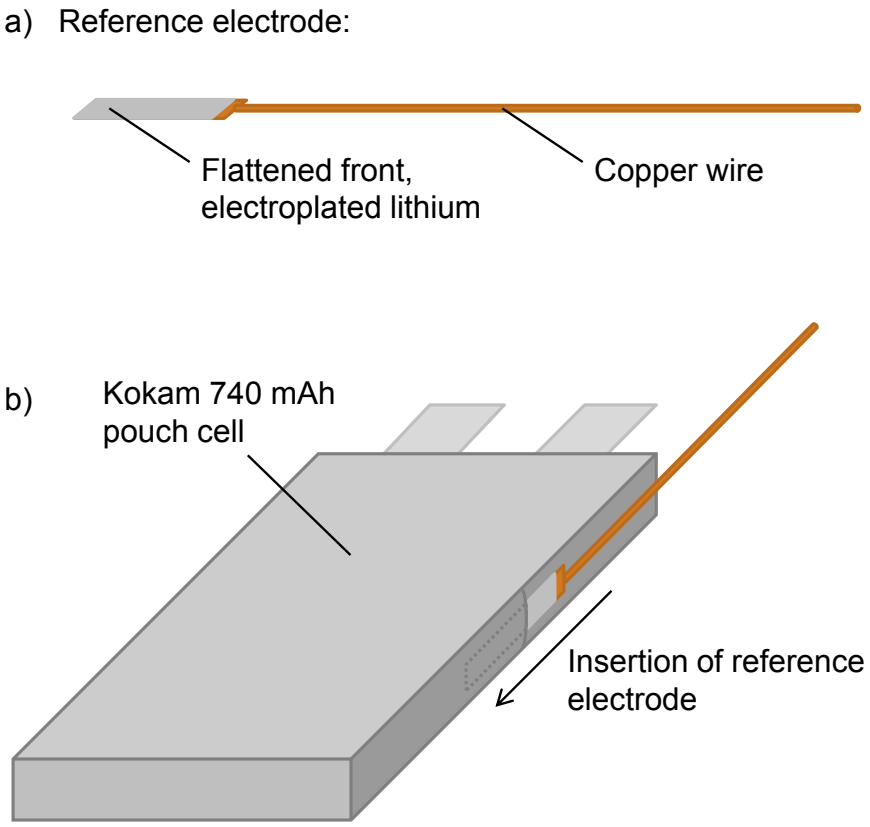

Fig. 2.2 a) RE, b) insertion of the RE into a Kokam pouch cell.

cell was used to electroplate the copper wires with lithium. Lithium foil and the flattened portion of the copper wire were inserted into commercial LP30 electrolyte. The copper wire was plated with lithium galvanostatically with a current density of 10 mA/cm^2 for 30 min. The plated wire was subsequently rinsed with DMC and vacuum dried for 20 min at ambient temperature.

Inside an argon filled glove box, a ceramic scalpel was used to create a small ($\sim$ 5 mm) incision on the side of the pouch cells. The lithium plated end of the REs were inserted into the cells through the incisions. The openings were subsequently sealed with fast setting epoxy resin (Araldite) and left to dry in the glove box overnight. A diagram of the RE and the modification procedure is presented in Figure 2.2.

Electrochemical tests conducted on both modified 3-electrode cells and unmodified cells showed that the modification did not alter the performance of the 3-electrode cells. The results are reported in [117].

2.2.3 OCV measurments

In this work, the term OCV is applied to the full cell and the individual electrodes alike. We define the OCV of an electrode as its equilibrium potential, whereby the electrons of both phases of the redox couple, in this case Li/Li+, are in equilibrium [118]. The OCV of the 3-electrode cell was measured at 0 °C, 20 °C and 40 °C and the OCV of the PE and the NE half-cells was measured at 20 °C. All experiments were carried out using BioLogic SP-150 potentiostats inside a Vötsch thermal chamber to control the environmental temperature. The true OCV measurements over the entire capacity range were obtained using the GITT technique [115], through which the SoC of the 3-electrode cell and the half-cells was changed incrementally, in steps of 1/50 of the nominal capacity ($\Delta Q = Q_{nom}/50$), by applying small currents (C/10) and subsequently allowing the cell voltage to relax for one hour. The nominal electrode half-cell capacities, Q_{nom}, were calculated based on their active masses and their known specific capacities (PE: 180.5 mAh/g, NE: 270.5 mAh/g). The OCV measurements were recorded at the end of each relaxation period. Figure 2.3 illustrates a GITT measurement on a commercial Kokam cell recorded during incremental discharge. The recording of each GITT data set was preceded by a thermal equilibration period of > 3 h at the respective test temperature and a subsequent constant current constant voltage (CCCV) charge. The exact experimental procedures for the GITT tests and preceding charge steps on the 3-electrode cell and the half-cells are given in Table 2.1.

In order to ensure that the OCV measurements of the electrode half-cells were not affected by rapid capacity fade, PE and NE half-cell capacities were recorded on

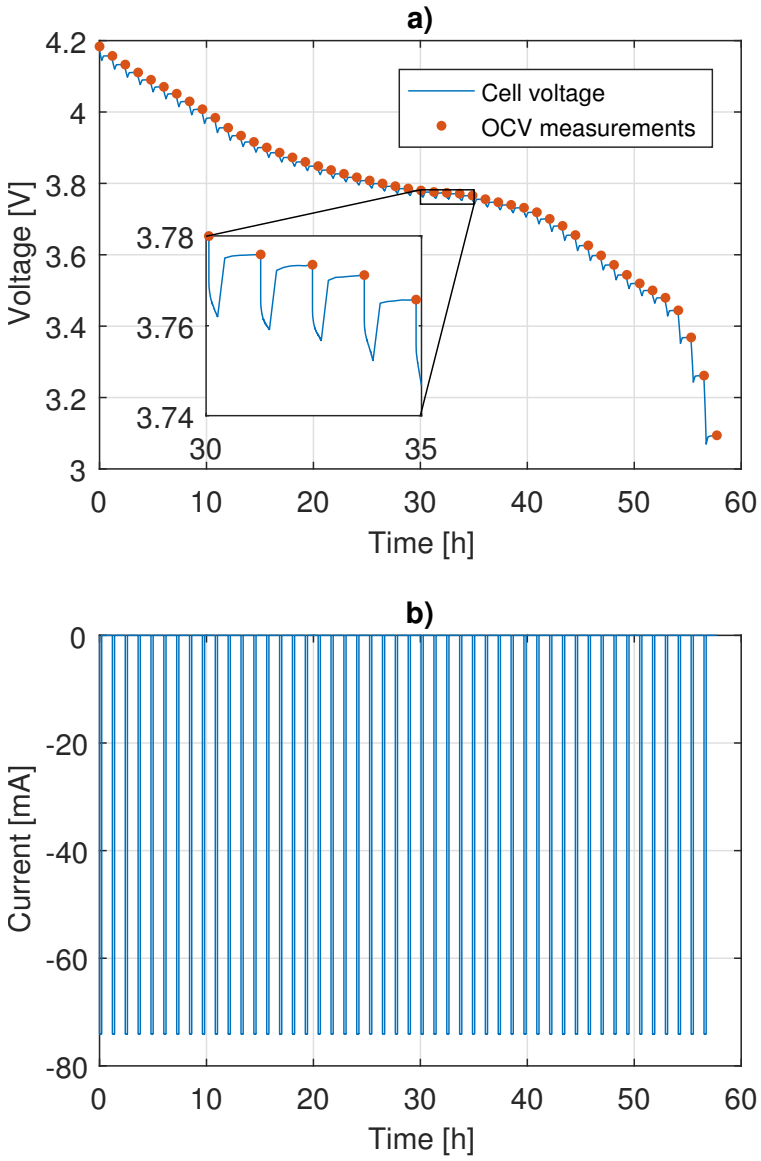

Fig. 2.3 GITT; a) OCV measurements, b) discharge current.

Table 2.1 Experimental procedure for GITT tests

Cell type	Step no	Experimental step	Current rate	Stop-criterion
Full cell	1	Thermal equilibration	-	t > 3 h
	2	Constant current charge	C/10	V > 4.2 V
	3	Constant voltage charge	variable	I < 40 mA
	4	Voltage relaxation	-	t > 3 h
	5	Constant current discharge	C/10	Δ Q > Q_{nom}/50
	6	Voltage relaxation	-	t > 1 h
	7	Repeat steps 5 and 6	-	V < 2.7 V
	8	Constant current charge	C/10	Δ Q > Q_{nom}/50
	9	Voltage relaxation	-	t > 1 h
	10	Repeat steps 8 and 9	-	V > 4.2 V
PE half-cell	1	Thermal equilibration	-	t > 3 h
	2	Constant current charge	C/10	V > 4.5 V
	3	Constant voltage charge	variable	I < 0.01 mA
	4	Voltage relaxation	-	t > 3 h
	5	Constant current charge	C/10	Δ Q > Q_{nom}/50
	6	Voltage relaxation	-	t > 1 h
	7	Repeat steps 5 and 6	-	V < 3.5 V
	8	Constant current charge	C/10	Δ Q > Q_{nom}/50
	9	Voltage relaxation	-	t > 1 h
	10	Repeat steps 8 and 9	-	V > 4.5 V
NE half-cell	1	Thermal equilibration	-	t > 3 h
	2	Constant current charge	C/10	V > 1.25 V
	3	Constant voltage charge	variable	I < 0.01 mA
	4	Voltage relaxation	-	t > 3 h
	5	Constant current discharge	C/10	Δ Q > Q_{nom}/50
	6	Voltage relaxation	-	t > 1 h
	7	Repeat steps 5 and 6	-	V < 0.001 V
	8	Constant current charge	C/10	Δ Q > Q_{nom}/50
	9	Voltage relaxation	-	t > 1 h
	10	Repeat steps 8 and 9	-	V > 1.25 V

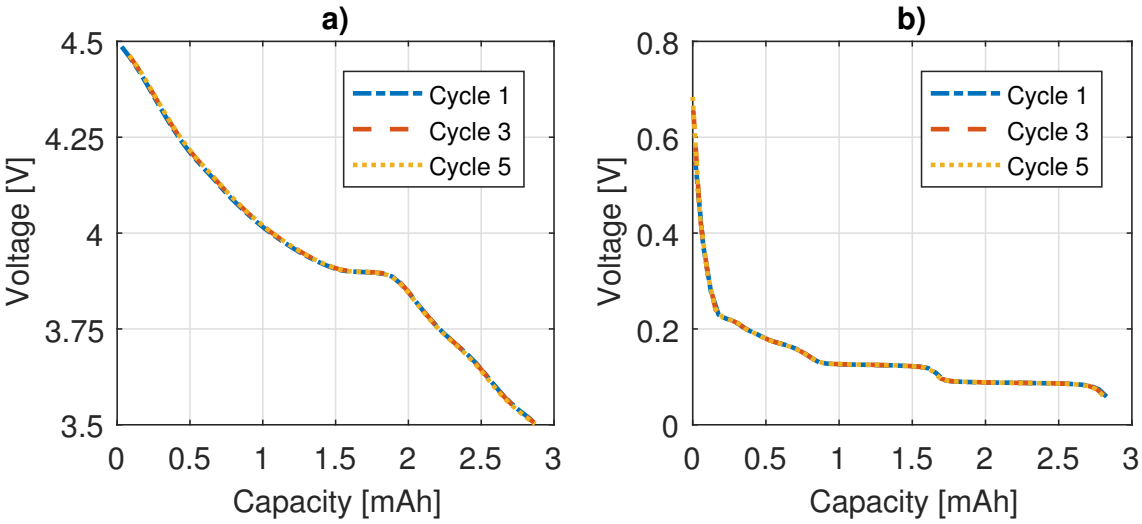

Fig. 2.4 OCV of a) PE and b) NE during cycle 1, 3 and 5.

two additional half-cells during five cycles (GITT during incremental discharge and charge) at 40 °C (see Figure 2.4). The capacity fade of both PE and NE half-cells was $< 0.1\%$ of their initial capacity after the first cycle and $< 1\%$ after five cycles.

2.3 Model development

2.3.1 Electrode sub-models

The first step is the formulation of the open circuit voltage, E^{OC}, according to the Nernst equation [118]

$$E^{\mathrm{OC}} = E_0 - \frac{kT}{e} \ln\left(\frac{x}{1-x}\right) \tag{2.1}$$

where E_0 is the standard redox potential, k is the Boltzmann constant, T is the temperature, e is the elementary charge and x is the ratio of intercalated sites to available sites in the host structure. In intercalation reactions, E_0 reflects the standard[1] potential for a given redox couple intercalated at a certain lattice site [108]. Lattice sites in insertion compounds differ in terms of their site energy and the number of available lattice sites to host ions [119]. Equation 2.1 therefore needs

[1] 'standard' in this case means half the sites in the host structure are occupied.

to be extended to account for N different types of lattice sites and their associated standard redox potentials $E_{0,i}$, (where $i = \{1, 2, ..., N\}$) and the respective fraction of occupied sites x. McKinnon and Haering [107] reformulated Equation 2.1 to give x in terms of E^{OC}

$$x = \frac{1}{1 + \exp[(E^{\mathrm{OC}} - E_0)e/kT]} \tag{2.2}$$

which is also referred to as the Fermi-Dirac distribution [120]. Equation 2.2 can be used to calculate the fraction of occupied sites in a system of N types of lattice sites as a function of the open circuit voltage E according to

$$x(E^{\mathrm{OC}}) = \sum_{i=1}^{N} \frac{\Delta x_i}{1 + \exp[(E^{\mathrm{OC}} - E_{0,i})e/kT]} \tag{2.3}$$

where Δx_i is the fraction of occupied sites of redox potential $E_{0,i}$. Equations 2.1 to 2.3 have been applied by McKinnon and Haering [107] in their discussion of lattice gas models for intercalation systems. However, their approach is limited to single-phase behaviour, whereas real intercalation materials typically exhibit regions of coexisting phases [121]. Ohzuku and Ueda [108] extended Equation 2.1 to account for short-range interactions between z neighbouring ions in a host lattice by

$$E^{\mathrm{OC}}(x) = E_0 - \frac{zU}{e}(1 - 2x) - \frac{kT}{e} \ln\left(\frac{x}{1 - x}\right) \tag{2.4}$$

where U is in joules and e in coulombs. Two-phase regions in intercalation materials can be modelled with large values of U in Equation 2.4 [108]. However, Equation 2.4 can not be solved for x in order to account for multiple types of lattice sites, as encountered in typical intercalation materials. For simplification, we introduce a dimensionless parameter ζ_i to extend the Nernst equation 2.1 for i types of lattice sites to

$$E^{\mathrm{OC}}(x_i) = E_{0,i} - \frac{kT}{\zeta_i e} \ln\left(\frac{x_i}{1 - x_i}\right) \tag{2.5}$$

which offers the flexibility to account for deviations from ideal single-phase behaviour. A similar parameter has been introduced by Verbrugge and Koch [122]. For ideal single-phase behaviour $\zeta = 1$, making Equations 2.1 and 2.5 identical. Large values of ζ minimize the contribution of the logarithmic term in Equation 2.5, reflected by a plateau in the OCV curve, which indicates two-phase behaviour [108]. Based on Verbrugge *et al.* [123], the physical meaning of parameter ζ can be interpreted in terms of the activity coefficients γ_i of the site fractions x_i. By introducing activities a and activity coefficients γ, Equation 2.5 can be written as

$$\begin{aligned} E^{\mathrm{OC}}(x_i) &= E_{0,i} - \frac{kT}{\zeta_i e} \ln\left(\frac{x_i}{1-x_i}\right) \\ &= E_{0,i} - \frac{kT}{e} \ln\left(\frac{x_i}{1-x_i}\right)^{\frac{1}{\zeta_i}} \\ &= E_{0,i} - \frac{kT}{e} \ln\left[\frac{\gamma_i x_i}{\gamma_{H,i}(1-x_i)}\right] \\ &= E_{0,i} - \frac{kT}{e} \ln\left(\frac{a_i}{a_{H,i}}\right) \end{aligned} \tag{2.6}$$

where the subscript H_i denotes host sites. The activities of the different types of lattice sites can thus be calculated using parameter ζ_i by

$$a_i = (x_i)^{\frac{1}{\zeta_i}} \tag{2.7}$$

and

$$a_{H,i} = (1-x_i)^{\frac{1}{\zeta_i}}. \tag{2.8}$$

Unlike Equation 2.4, Equation 2.5 does not account for site interactions. However, it offers a pragmatic approach to model the behaviour of real intercalation systems and a means to approximate excess free energy through the identification of activity coefficients [123]. Including parameter ζ_i in Equation 2.3 yields

$$x(E^{\mathrm{OC}}) = \sum_{i=1}^{N} \frac{\Delta x_i}{1 + \exp[(E^{\mathrm{OC}} - E_{0,i})\zeta_i e/kT]}. \tag{2.9}$$

Equation 2.9 can be solved numerically to compute E^{OC} as a function of x for an intercalation material with N different types of lattice sites. The effects of the term $\frac{zU}{e}(1-2x)$ on E^{OC} were compared to the effects of parameter ζ by comparing the results of Equations 2.9 to those of Equation 2.4 for a range of interaction energies: $-0.4\,\mathrm{V} < f < 0.07\,\mathrm{V}$ where $f = \frac{zU}{e}$. Optimal values for parameter ζ were obtained by fitting Equation 2.9 to the results of Equation 2.4, computed for a range of interaction energies by minimizing the root-mean-squared error (RMSE) on $E^{\mathrm{OC}}(x)$ using nonlinear least squares fitting in Matlab. Figure 2.5, a) shows the comparison of $E^{\mathrm{OC}}(x) - E_0$ calculated with Equations 2.4 and 2.9, respectively, for different interaction energies. The RMSE on $E^{\mathrm{OC}}(x)$ is plotted against a range of f in Figure 2.5, b), alongside the relationship between ζ and f. The approximation of f by parameter ζ is obviously best close to $f = 0$, where $\zeta = 1$ and equations 2.4 and 2.9 are identical. The discrepancy between $E^{\mathrm{OC}}(f, x)$ and $E^{\mathrm{OC}}(\zeta, x)$ increases for increasingly smaller or larger values of f. Figure 2.5, a) shows that for large positive values of f, the voltage can rise with x_{Li} according to Equation 2.4, which is considered unphysical [107]. This behaviour cannot be modelled with Equation 2.9, which is limited by a constant voltage profile for large values of parameter ζ (see Figure 2.5, a): $E^{\mathrm{OC}}(\zeta_{\mathrm{max}}, x)$).

The comparison of $E^{\mathrm{OC}}(f, x)$ and $E^{\mathrm{OC}}(\zeta, x)$ shows that Equation 2.9 gives a good approximation of the results achieved by Equation 2.4 for a wide range of interaction energies. More importantly, Equation 2.9 enables the calculation of the OCV for multiple site energies, as are encountered in real intercalation electrode materials. Equation 2.9 was therefore selected as the basis for the electrode sub-models for the PE and the NE.

It should be emphasized at this stage that the objective was not to derive a model for intercalation electrodes from first principles but to build upon established principles (outlined in Equations 2.1 to 2.4) in order to create an OCV model for

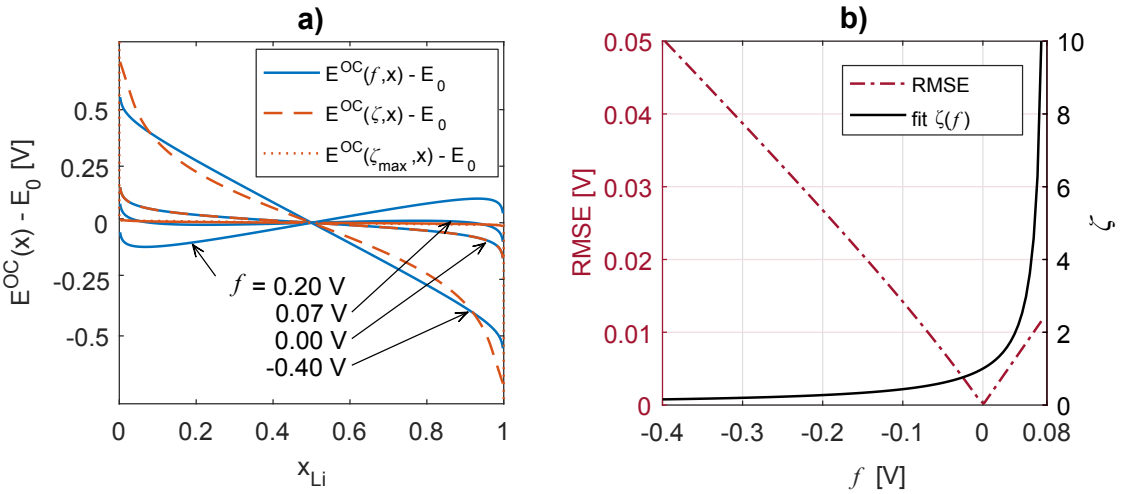

Fig. 2.5 a) Comparison of $E^{\mathrm{OC}}(x) - E_0$ computed by Equation 2.4 (solid line) and Equation 2.9 (broken lines) for various values of f. b) RMSE on $E^{\mathrm{OC}}(x)$ from fitting Equation 2.9 to Equation 2.4 (left axis) and correlation between parameter ζ and f (right axis).

commercial Li-ion cells, which can be identified without prior knowledge of physical parameters of the active electrode materials.

The first step in the model identification process is to estimate the number of different types of lattice sites of the electrode materials. In OCV curves of intercalation materials the different types of lattice sites can be identified by voltage plateaus, which correspond to phase transitions that the material undergoes during intercalation and de-intercalation [121]. In the present case, the intercalation materials were a blend of LCO and NCO (the positive electrode) and graphite (the negative electrode). Since it can be difficult to identify voltage plateaus in curves of voltage versus capacity, we first differentiated half-cell capacity Q with respect to OCV (dQ/dV) in order to obtain more clearly visible peaks [43]. This is illustrated in Figure 2.6, where the voltages of the PE and NE half-cells are shown in the top row (Figure 2.6, a) and b)) and the respective dQ/dV curves are in the bottom row (Figure 2.6, c) and d)).

This analysis indicates that there are four identifiable phase transitions ($N = 4$) in both the positive and the negative electrode material, which leads to the PE and

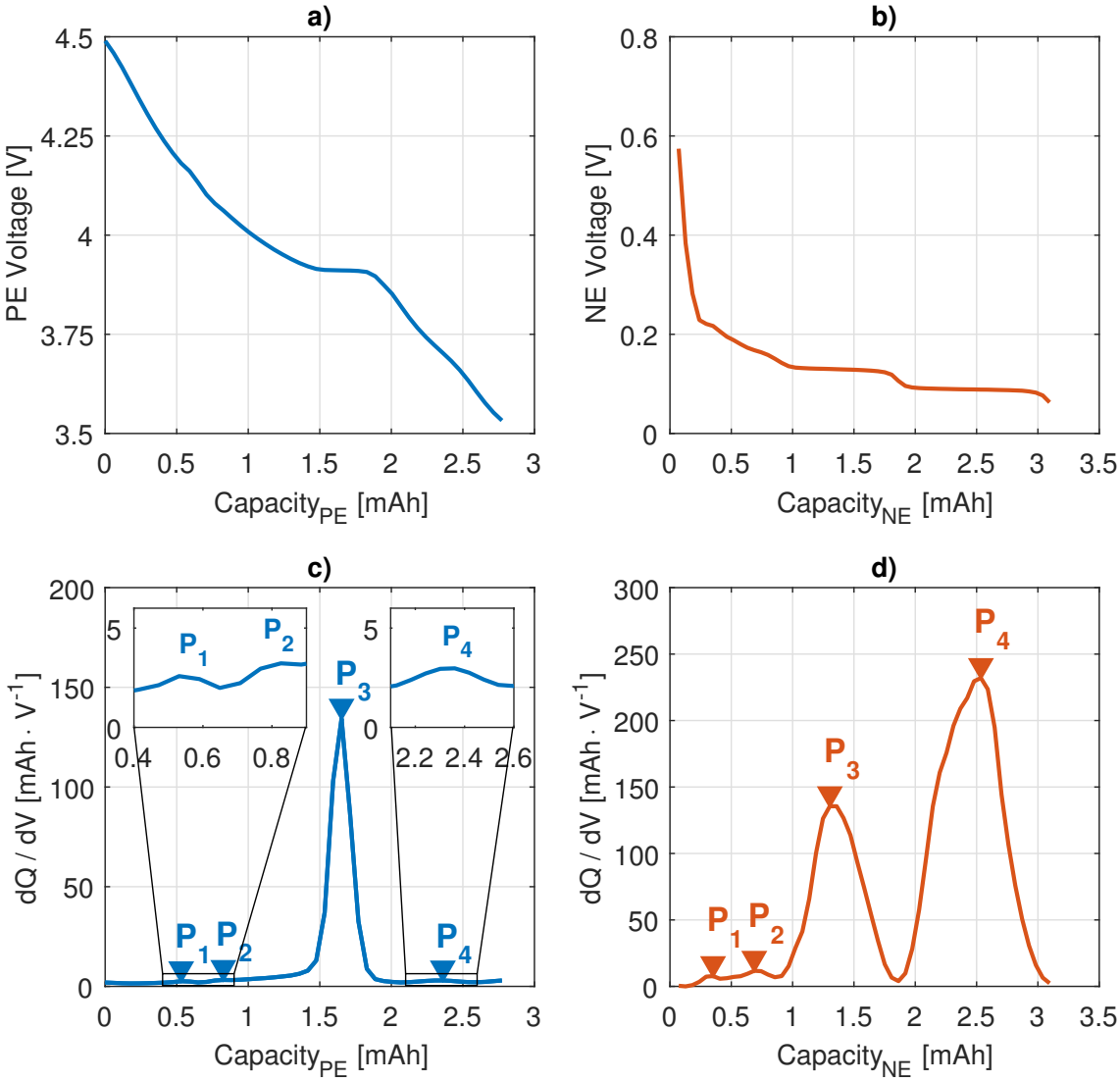

Fig. 2.6 a) PE half-cell voltage, b) NE half-cell voltage, c) dQ/dV of PE, d) dQ/dV of NE. Phase transitions P_i are numbered from the highest to the lowest potential $E_{0,i}$

NE OCV model equations

$$x_{\mathrm{PE}}(E_{\mathrm{PE}}^{\mathrm{OC}}) = \sum_{i=1}^{4} \frac{\Delta x_{\mathrm{PE},i}}{1 + \exp[(E_{\mathrm{PE}}^{\mathrm{OC}} - E_{0,\mathrm{PE},i})\zeta_{\mathrm{PE},i} e/kT]} \tag{2.10}$$

and

$$x_{\mathrm{NE}}(E_{\mathrm{NE}}^{\mathrm{OC}}) = \sum_{i=1}^{4} \frac{\Delta x_{\mathrm{NE},i}}{1 + \exp[(E_{\mathrm{NE}}^{\mathrm{OC}} - E_{0,\mathrm{NE},i})\zeta_{\mathrm{NE},i} e/kT]}. \tag{2.11}$$

Given the voltage ranges $\mathbf{E}_{\mathrm{PE},0}^{\mathrm{OC}}$ and $\mathbf{E}_{\mathrm{NE},0}^{\mathrm{OC}}$ (which are vectors of equally spaced elements ranging from the minimum to the maximum OCV of the electrodes), Equations 2.10 and 2.11 were used to determine the ratio of occupied to available sites ($x_{\mathrm{PE}}(\mathbf{E}_{\mathrm{PE},0}^{\mathrm{OC}})$ and $x_{\mathrm{NE}}(\mathbf{E}_{\mathrm{NE},0}^{\mathrm{OC}})$) in the electrode materials for all identified phase transitions $i = \{1, 2...4\}$. Equations 2.10 and 2.11 require three parameters $\Delta x_i, E_{0,i}$ and ζ_i to be be estimated for each phase transition, which gives 12 parameters for each electrode. The parameters were estimated by fitting the measured OCV of the PE and NE half-cells, as described in Section 2.3.3.

To calculate electrode potentials as functions of their lithium content, Equations 2.10 and 2.11 must be solved numerically. This was achieved by interpolating $\mathbf{E}_{\mathrm{PE},0}^{\mathrm{OC}}$ and $\mathbf{E}_{\mathrm{NE},0}^{\mathrm{OC}}$ at the points given by the vectors $\mathbf{x}_{\mathrm{PE}}$ and $\mathbf{x}_{\mathrm{NE}}$, which consist of equally spaced elements ranging from 0 to 1. In reality, the electrode materials are not fully intercalated at $\mathbf{x} = 1$ or fully de-intercalated at $\mathbf{x} = 0$. However, from a practical viewpoint, the upper and lower voltage limits of the electrodes dictate the maximal amount of useful electrode capacity, which can support the reversible insertion and extraction of lithium without being damaged. $\mathbf{x}_{\mathrm{PE}}$ and $\mathbf{x}_{\mathrm{NE}}$ can thus be interpreted as the normalised, usable capacity of the electrodes.

The interpolation of $\mathbf{E}_{\mathrm{PE},0}^{\mathrm{OC}}$ and $\mathbf{E}_{\mathrm{NE},0}^{\mathrm{OC}}$ at $\mathbf{x}_{\mathrm{PE}}$ and $\mathbf{x}_{\mathrm{NE}}$ yields the vectors $\hat{\mathbf{E}}_{\mathrm{PE}}^{\mathrm{OC}}$ and $\hat{\mathbf{E}}_{\mathrm{NE}}^{\mathrm{OC}}$—the estimated OCV of the PE and NE, respectively—which provide the basis for calculating the cell voltage.

It should be noted that Equations 2.10 and 2.11 are intended to capture the phase transitions in the active electrode materials that are observable with the available methods, which may not be equivalent to the theoretical number of phase transitions that the materials undergo.

2.3.2 The cell model

The OCV of the cell is calculated as the difference between the OCV of the PE and the NE according to

$$E_{\mathrm{Cell}}^{\mathrm{OC}} = E_{\mathrm{PE}}^{\mathrm{OC}}(x_{\mathrm{PE,Cell}}) - E_{\mathrm{NE}}^{\mathrm{OC}}(x_{\mathrm{NE,Cell}}) \tag{2.12}$$

where $x_{\mathrm{PE,Cell}}$ and $x_{\mathrm{NE,Cell}}$ are the capacity ranges of the PE and NE, respectively, which are utilized within the full cell. $x_{\mathrm{PE,Cell}}$ and $x_{\mathrm{NE,Cell}}$ can be described by vectors $\hat{\mathbf{x}}_{\mathrm{PE,Cell}}$ and $\hat{\mathbf{x}}_{\mathrm{NE,Cell}}$, which are subsets of $\mathbf{x}_{\mathrm{PE}}$ and $\mathbf{x}_{\mathrm{NE}}$:

$$\begin{aligned} \mathbf{x}_{\mathrm{PE}} &= \{0...1\} \\ \hat{\mathbf{x}}_{\mathrm{PE,Cell}} &= \{x_{\mathrm{PE},1}...x_{\mathrm{PE},n}\} \\ \hat{\mathbf{x}}_{\mathrm{PE}} &\subset \mathbf{x}_{\mathrm{PE}} \end{aligned} \tag{2.13}$$

$$\begin{aligned} \mathbf{x}_{\mathrm{NE}} &= \{0...1\} \\ \hat{\mathbf{x}}_{\mathrm{NE,Cell}} &= \{x_{\mathrm{NE},1}...x_{\mathrm{NE},n}\} \\ \hat{\mathbf{x}}_{\mathrm{NE}} &\subset \mathbf{x}_{\mathrm{NE}}. \end{aligned} \tag{2.14}$$

$x_{\mathrm{PE/NE},1}$ and $x_{\mathrm{PE/NE},n}$ are the lower and upper limits of $\hat{\mathbf{x}}_{\mathrm{PE,Cell}}$ and $\hat{\mathbf{x}}_{\mathrm{NE,Cell}}$, which were estimated by fitting the measured OCV of the cell, as described in Section 2.3.3. The ranges of $\hat{\mathbf{x}}_{\mathrm{PE,Cell}}$ and $\hat{\mathbf{x}}_{\mathrm{NE,Cell}}$ are smaller than $\mathbf{x}_{\mathrm{PE}}$ and $\mathbf{x}_{\mathrm{NE}}$ because not all of the available electrode capacity is utilized within the full cell. The estimated OCV

of the cell as a function of $\hat{\mathbf{x}}_{\mathrm{PE,Cell}}$ and $\hat{\mathbf{x}}_{\mathrm{NE,Cell}}$ is given by

$$\hat{\mathbf{E}}^{\mathrm{OC}}_{\mathrm{Cell}} = \hat{\mathbf{E}}^{\mathrm{OC}}_{\mathrm{PE}}(\hat{\mathbf{x}}_{\mathrm{PE,Cell}}) - \hat{\mathbf{E}}^{\mathrm{OC}}_{\mathrm{NE}}(\hat{\mathbf{x}}_{\mathrm{NE,Cell}}). \tag{2.15}$$

2.3.3 Parameter estimation

For the given electrode materials (LCO/NCO cathode and graphite anode), the proposed OCV model is defined by a total of 28 parameters:

a. 12 parameters for the PE ($\Delta x_{\mathrm{PE},i}, E_{0,\mathrm{PE},i}$ and $\zeta_{\mathrm{PE},i}$, where $i = \{1, 2...4\}$)

b. 12 parameters for the NE ($\Delta x_{\mathrm{NE},i}, E_{0,\mathrm{NE},i}$ and $\zeta_{\mathrm{NE},i}$, where $i = \{1, 2...4\}$)

c. The limits of the PE and NE capacity ranges utilized within the full cell ($x_{\mathrm{PE},1}$, $x_{\mathrm{PE},n}$, $x_{\mathrm{NE},1}$ and $x_{\mathrm{NE},n}$)

Parameter estimations in steps a) and b) are based on fitting the computed OCV of the PE, $\hat{\mathbf{E}}^{\mathrm{OC}}_{\mathrm{PE}}$, and the NE, $\hat{\mathbf{E}}^{\mathrm{OC}}_{\mathrm{NE}}$, to the OCV measured on the PE, $\mathbf{E}^{\mathrm{OC}}_{\mathrm{PE}}$, and NE, $\mathbf{E}^{\mathrm{OC}}_{\mathrm{NE}}$, half-cells, respectively. The parameter estimation of step c) is carried out by fitting the computed OCV of the cell, $\hat{\mathbf{E}}^{\mathrm{OC}}_{\mathrm{Cell}}$, to the measured OCV, $\mathbf{E}^{\mathrm{OC}}_{\mathrm{Cell}}$. The measured OCV of the full cell, $\mathbf{E}^{\mathrm{OC}}_{\mathrm{Cell}}$, the PE half-cell, $\mathbf{E}^{\mathrm{OC}}_{\mathrm{PE}}$, and the NE half-cell, $\mathbf{E}^{\mathrm{OC}}_{\mathrm{NE}}$, are vectors of voltage measurements recorded within the respective voltage limits, as defined by the relations

$$\begin{aligned} \mathbf{E}^{\mathrm{OC}}_{\mathrm{Cell}} &= \{E^{\mathrm{OC}}_{\mathrm{Cell,min}} ... E^{\mathrm{OC}}_{\mathrm{Cell,max}}\} \\ \mathbf{E}^{\mathrm{OC}}_{\mathrm{PE}} &= \{E^{\mathrm{OC}}_{\mathrm{PE,min}} ... E^{\mathrm{OC}}_{\mathrm{PE,max}}\} \\ \mathbf{E}^{\mathrm{OC}}_{\mathrm{NE}} &= \{E^{\mathrm{OC}}_{\mathrm{NE,min}} ... E^{\mathrm{OC}}_{\mathrm{NE,max}}\}. \end{aligned} \tag{2.16}$$

$\mathbf{x}_{\mathrm{Cell}}, \mathbf{x}_{\mathrm{PE}}$ and $\mathbf{x}_{\mathrm{NE}}$ are the corresponding vectors of normalised capacity of the full cell, the PE half-cell and the NE half-cell, respectively. The vectors $\mathbf{x}$ range from 0 (fully delithiated) to 1 (fully lithiated). The PE half-cell is considered fully lithiated ($\mathbf{x}_{\mathrm{PE}} = 1$) at a voltage of $E^{\mathrm{OC}}_{\mathrm{PE,min}} = 3.5\,\mathrm{V}$ and fully delithiated ($\mathbf{x}_{\mathrm{PE}} = 0$)

at $E^{\mathrm{OC}}_{\mathrm{PE,max}} = 4.5\,\mathrm{V}$. The NE half-cell is considered fully lithiated ($\mathbf{x}_{\mathrm{NE}} = 1$) at a voltage of $E^{\mathrm{OC}}_{\mathrm{NE,min}} = 0.001\,\mathrm{V}$ and fully delithiated ($\mathbf{x}_{\mathrm{NE}} = 0$) at $E^{\mathrm{OC}}_{\mathrm{NE,max}} = 1.25\,\mathrm{V}$. These voltage limits were imposed in order to avoid damage to the PE and NE materials during tests. In the case of the full cell, the fully charged state is associated with a lithiated NE and a delithiated PE and $\mathbf{x}_{\mathrm{Cell}}$ is defined as 0, whereas the fully discharged state is associated with a delithiated NE and a lithiated PE and $\mathbf{x}_{\mathrm{Cell}}$ is defined as 1. The corresponding maximum and minimum voltage limits are $E^{\mathrm{OC}}_{\mathrm{Cell,max}} = 4.2\,\mathrm{V}$ and $E^{\mathrm{OC}}_{\mathrm{Cell,min}} = 2.7\,\mathrm{V}$. All fitting was conducted using Matlab's constrained optimization function fmincon.

PE parameter estimation

The PE parameters $E_{0,\mathrm{PE},i}, \Delta x_{\mathrm{PE},i}$ and $\zeta_{\mathrm{PE},i}$ for phase transitions $i = \{1, 2...4\}$ are summarized in a 4 by 3 matrix by

$$\theta_{\mathrm{PE}} = \begin{bmatrix} E_{0,\mathrm{PE},1} & \Delta x_{\mathrm{PE},1} & \zeta_{\mathrm{PE},1} \\ E_{0,\mathrm{PE},2} & \Delta x_{\mathrm{PE},2} & \zeta_{\mathrm{PE},2} \\ \vdots & \vdots & \vdots \\ E_{0,\mathrm{PE},4} & \Delta x_{\mathrm{PE},4} & \zeta_{\mathrm{PE},4} \end{bmatrix}. \tag{2.17}$$

The PE parameters are estimated by minimizing the RMSE between the computed and the measured OCV of the PE half-cell, $\hat{\mathbf{E}}^{\mathrm{OC}}_{\mathrm{PE}}(\theta_{\mathrm{PE}})$ and $\mathbf{E}^{\mathrm{OC}}_{\mathrm{PE}}$, respectively. $\hat{\mathbf{E}}^{\mathrm{OC}}_{\mathrm{PE}}(\theta_{\mathrm{PE}})$ is computed for the capacity range $\mathbf{x}_{\mathrm{PE}} = \{0...1\}$. The $\mathrm{RMSE}(\theta_{\mathrm{PE}})$ is calculated by

$$\mathrm{RMSE}(\theta_{\mathrm{PE}}) = \sqrt{\frac{\sum_{i=1}^{n}(\hat{\mathbf{E}}^{\mathrm{OC}}_{\mathrm{PE},i}(\theta_{\mathrm{PE}}) - \mathbf{E}^{\mathrm{OC}}_{\mathrm{PE},i})^2}{n}}. \tag{2.18}$$

The objective function solved to estimate the PE parameters $\hat{\theta}_{\mathrm{PE}}$ is

$$\hat{\theta}_{\mathrm{PE}} = \arg\min_{\theta_{\mathrm{PE}}} \mathrm{RMSE}(\theta_{\mathrm{PE}}) \tag{2.19}$$

NE parameter estimation

The NE parameters $E_{0,\mathrm{NE},i}, \Delta x_{\mathrm{NE},i}$ and $\zeta_{\mathrm{NE},i}$ for phase transitions $i = \{1, 2...4\}$ are summarized in a 4 by 3 matrix by

$$\theta_{\mathrm{NE}} = \begin{bmatrix} E_{0,\mathrm{NE},1} & \Delta x_{\mathrm{NE},1} & \zeta_{\mathrm{NE},1} \\ E_{0,\mathrm{NE},2} & \Delta x_{\mathrm{NE},2} & \zeta_{\mathrm{NE},2} \\ \vdots & \vdots & \vdots \\ E_{0,\mathrm{NE},4} & \Delta x_{\mathrm{NE},4} & \zeta_{\mathrm{NE},4} \end{bmatrix}. \tag{2.20}$$

The NE parameters are estimated by minimizing the RMSE between the computed and the measured OCV of the NE half-cell, $\hat{\mathbf{E}}^{\mathrm{OC}}_{\mathrm{NE}}(\theta_{\mathrm{NE}})$ and $\mathbf{E}^{\mathrm{OC}}_{\mathrm{NE}}$, respectively. $\hat{\mathbf{E}}^{\mathrm{OC}}_{\mathrm{NE}}(\theta_{\mathrm{NE}})$ is computed for the capacity range $\mathbf{x}_{\mathrm{NE}} = \{0...1\}$. The RMSE$(\theta_{\mathrm{NE}})$ is calculated by

$$\mathrm{RMSE}(\theta_{\mathrm{NE}}) = \sqrt{\frac{\sum_{i=1}^{n}(\hat{\mathbf{E}}^{\mathrm{OC}}_{\mathrm{NE},i}(\theta_{\mathrm{NE}}) - \mathbf{E}^{\mathrm{OC}}_{\mathrm{NE},i})^2}{n}}. \tag{2.21}$$

The objective function solved to estimate the NE parameters $\hat{\theta}_{\mathrm{NE}}$ is

$$\hat{\theta}_{\mathrm{NE}} = \underset{\theta_{\mathrm{NE}}}{\arg\min}\ \mathrm{RMSE}(\theta_{\mathrm{NE}}). \tag{2.22}$$

Estimation of PE and NE capacity ranges

Using the estimated OCV of the PE, $\hat{\mathbf{E}}^{\mathrm{OC}}_{\mathrm{PE}}$, and the NE, $\hat{\mathbf{E}}^{\mathrm{OC}}_{\mathrm{NE}}$, the portions of the normalized capacity of the PE, $\hat{\mathbf{x}}_{\mathrm{PE,Cell}}$, and the NE, $\hat{\mathbf{x}}_{\mathrm{NE,Cell}}$, utilized within the full cell, can be estimated by fitting the OCV computed for the full cell (Equation 2.15) to the measured cell voltage $\mathbf{E}^{\mathrm{OC}}_{\mathrm{Cell}}$. The vectors $\hat{\mathbf{x}}_{\mathrm{PE,Cell}}$ and $\hat{\mathbf{x}}_{\mathrm{NE,Cell}}$ are defined by $x_{\mathrm{PE},1}$, $x_{\mathrm{PE},n}$, $x_{\mathrm{NE},1}$ and $x_{\mathrm{NE},n}$ (Equations 2.13 and 2.14), which comprise the matrix

$$\theta_x = \begin{bmatrix} x_{\mathrm{PE},1} & x_{\mathrm{PE},n} \\ x_{\mathrm{NE},1} & x_{\mathrm{NE},n} \end{bmatrix}. \tag{2.23}$$

The parameters in θ_x are estimated by minimizing the RMSE between $\mathbf{E}^{\mathrm{OC}}_{\mathrm{Cell}}$ and $\hat{\mathbf{E}}^{\mathrm{OC}}_{\mathrm{Cell}}$ for n OCV measurements. The RMSE(θ_x) is calculated by

$$\mathrm{RMSE}(\theta_x) = \sqrt{\frac{\sum_{i=1}^{n}(\hat{\mathbf{E}}^{\mathrm{OC}}_{\mathrm{Cell},i}(\theta_x) - \mathbf{E}^{\mathrm{OC}}_{\mathrm{Cell},i})^2}{n}} \tag{2.24}$$

The objective function solved to estimate $\hat{\theta}_x$ is

$$\hat{\theta}_x = \arg\min_{\theta_x} \mathrm{RMSE}(\theta_{\mathrm{x}}). \tag{2.25}$$

2.4 Results and discussion

The OCV fitting results obtained for the electrode half-cells are presented in Section 2.4.1 and the results for the full-cell in Section 2.4.2. Section 2.4.3 shows the validation of the OCV model by means of a comparison of the electrode and cell OCVs computed by the model and measured on the 3-electrode cell at different temperatures.

2.4.1 Half-cell fitting results

The OCV data recorded on the PE and the NE half-cells (at 20 °C) was fitted using the methodology described in Section 2.3.3. The results are depicted in Figure 2.7, a) for the PE and b) for the NE. Markers indicate measured data points and lines the model results. Good fits were achieved with a RMSE of 6 mV for the PE and 3 mV for the NE. The high fit qualities indicate a good representation of the electrode OCVs by the model. The OCV model parameters estimated for the PE and NE are listed in Table 2.2 for each phase transition Pi. The parameters Δx_i are fractions of the total normalised electrode capacity utilized within the cell and parameters ζ_i are dimensionless.

Table 2.2 OCV model parameters.

	PE			NE		
P_i	$E_{0,\mathrm{PE},i}$	$\Delta x_{\mathrm{PE},i}$	$\zeta_{\mathrm{PE},i}$	$E_{0,\mathrm{NE},i}$	$\Delta x_{\mathrm{NE},i}$	$\zeta_{\mathrm{NE},i}$
1	4.377 V	0.106	0.567	0.379 V	0.048	0.305
2	4.056 V	0.397	0.282	0.180 V	0.270	1.143
3	3.918 V	0.207	3.053	0.129 V	0.286	8.000
4	3.661 V	0.365	0.249	0.088 V	0.399	7.988

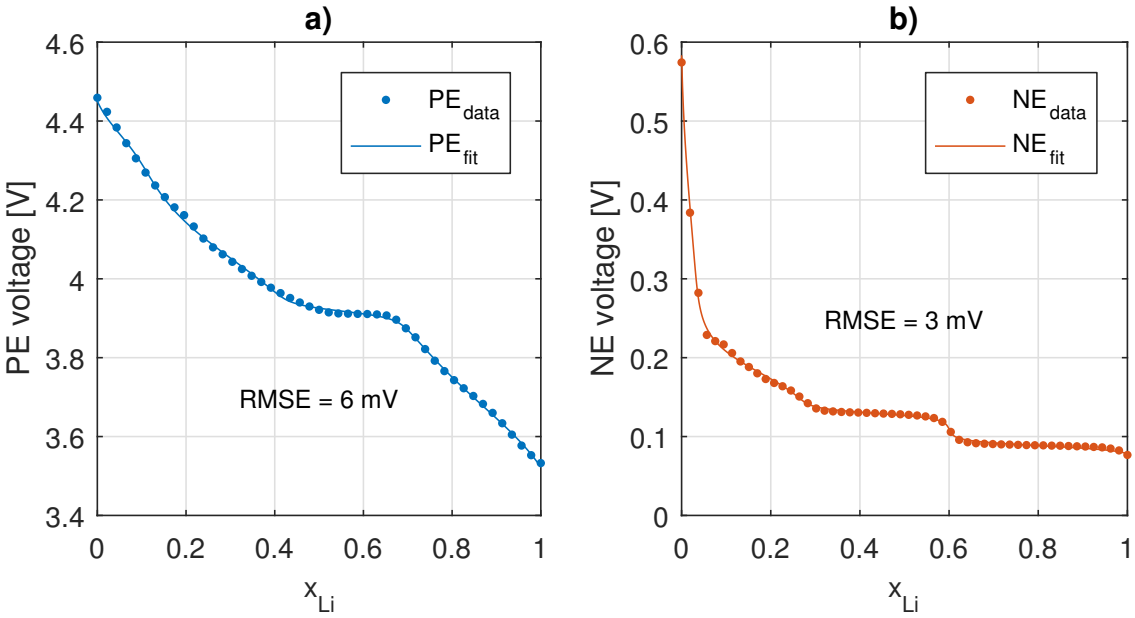

Fig. 2.7 OCV fitting results of a) the PE half-cell and b) the NE half-cell.

2.4.2 Cell fitting results

Using the results obtained from the PE and NE model fits, the cell voltage of the 3-electrode cell was fitted by estimating the capacity ranges of the PE and NE utilized within the full cell, as described in Section 2.3.3. The fit results are illustrated in Figure 2.8. The cell and PE voltages are plotted on the left vertical axis and the NE voltage on the right vertical axis, against depth of discharge (DoD). The grey markers show the measured OCV of the cell and the grey line, the fitted cell voltage. A high quality of fit was achieved with a RMSE of 6.6 mV. The blue and red markers indicate the OCV of the PE and the NE, respectively, measured by means of the inserted RE. The blue and red lines depict the modelled OCV of the PE and the NE, as inferred from the cell voltage fit. From the RMSE values (6.2 mV for the PE and 4.7 mV for the NE) it is evident that the OCVs of the electrodes were modelled to a high degree of accuracy. It should be emphasized that the parameters of the electrode sub-model were estimated by fitting the OCV of half-cells, not the OCV of the PE and the NE recorded on the 3-electrode cell. The OCVs of the electrodes measured on the 3-electrode cell only served for the validation of the model.

This analysis demonstrates that the presented OCV model and parameter estimation technique meet the first and second objective of the OCV model; all parameters were successfully estimated using only OCV measurements recorded on a PE half-cell, an NE half-cell and a full cell, and an accurate representation of the OCV of the cell as well as the electrodes was achieved.

2.4.3 Model validation at different temperatures

In addition to the measurements recorded on the 3-electrode cell at 20 °C, the OCV was also recorded at 0 °C and 40 °C to evaluate the performance of the model at different operating temperatures. RMSE values for the full cell and the electrodes were calculated for all temperatures. To assess the benefit of the temperature dependency

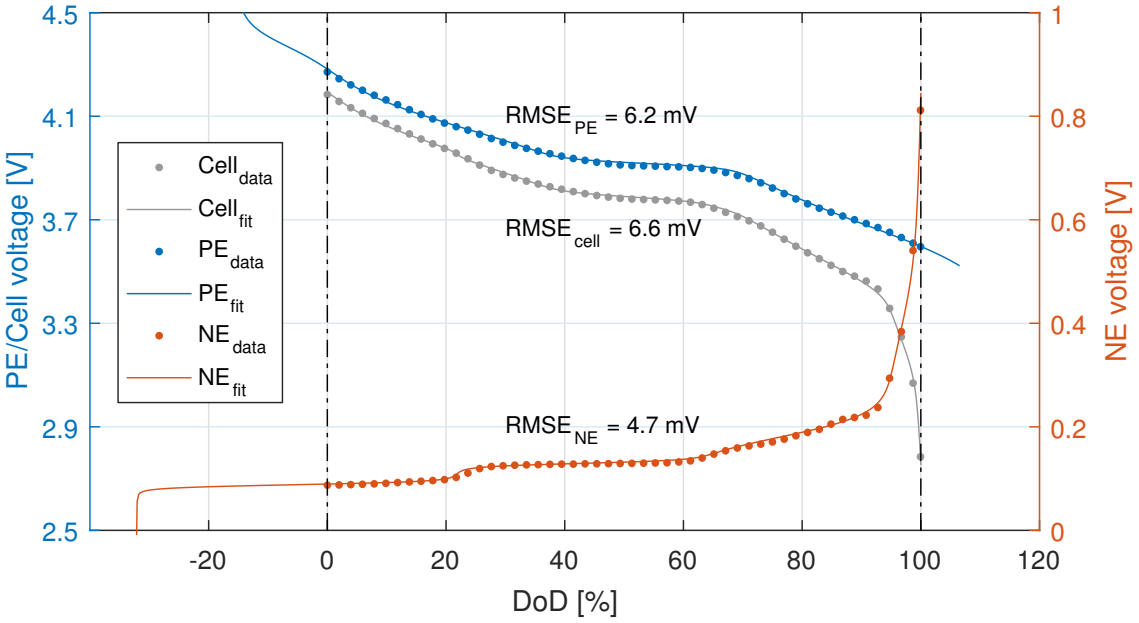

Fig. 2.8 OCV fitting results of the 3-electrode cell.

of the OCV model, RMSE values were also calculated for all temperatures using the OCV of the cell and electrodes estimated at 20 °C. It should be emphasized here that the model parameters $E_{0,i}, \Delta x_i$ and ζ_i are not assumed to be temperature dependent and were only estimated using the cell OCV recorded at 20 °C. The temperature dependency of the OCV is accounted for by the temperature term in the OCV model.

Figure 2.9 illustrates the results generated by the model for a temperature of a) 0 °C, b) 20 °C (also shown in Figure 2.8) and c) 40 °C. Although the qualities of the fits at 0 °C and 40 °C are inferior compared to the fit at 20 °C (where the model was parameterised), the errors are smaller compared to the case where no temperature variation was taken into account. The RMSE values for the OCVs of the cell, the PE and the NE for both cases are listed in Table 2.3. The RMSE values for the OCV of the cell and the NE are reduced by around 10 mV when the different operating temperatures are taken into account. The results demonstrate that it is beneficial for an OCV model to allow for different operating temperatures, which also satisfies the third objective laid out for the OCV model.

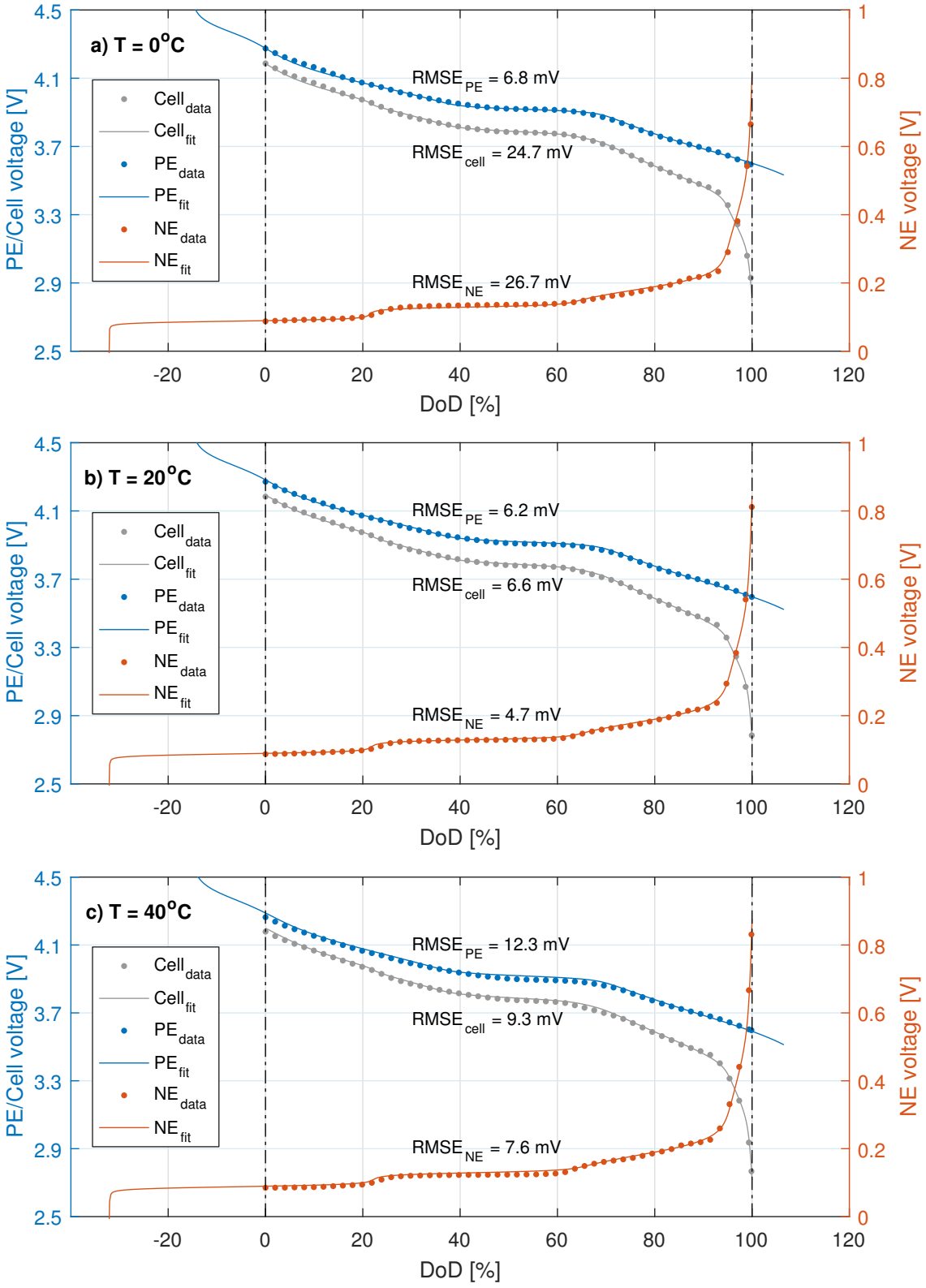

Fig. 2.9 OCV fitting results of the 3-electrode cell a) at 0 °C, b) at 20 °C and c) at 40 °C

Table 2.3 RMSE of fitting with and without temperature adjustment.

	T. adjustment			No T. adjustment		
	Cell	PE	NE	Cell	PE	NE
T = 0°C	24.7	6.8	26.7	38.2	5.2	38.6
T = 20°C	6.6	6.2	4.7	6.6	6.2	4.7
T = 40°C	9.3	12.3	7.6	18.3	11.0	17.9

2.5 Conclusions

The presented OCV model was motivated by four essential requirements:

1. No prior knowledge of material properties (model parameter estimation based on measurements, which can be obtained from commercial cells).

2. An accurate representation of the cells' OCV, derived from the OCV of the electrodes.

3. The ability to account for different operating temperatures.

4. The possibility to accommodate electrode-specific degradation and use the OCV model for degradation diagnostics.

Section 2.3 addressed the first objective by describing how the OCV model parameters can be easily estimated from OCV measurements of the full-cell and electrode half-cells. No cell-specific material properties are required.

The second objective was assessed by evaluating the fitting quality of the OCV of the cell and the electrode half-cells, as discussed in Sections 2.4.1 and 2.4.2. High fitting qualities were achieved for both half-cell and cell data, indicating good representation of the OCV by the model. The OCV model was further validated by comparing the computed OCV of the PE and the NE with respective OCV measurements recorded on the 3-electrode cell. This analysis demonstrated close agreement between the estimated OCV of the electrodes and the measurements recorded on a 3-electrode cell.

The third objective was evaluated by computing the OCV of a cell and its PE and NE at three different operating temperatures: 0 °C, 20 °C and 40 °C using the OCV model and comparing the results to the OCV measured at the same temperatures using a 3-electrode cell. The results, presented in Section 2.4.3, demonstrate that OCV computations are improved by considering the operating temperature.

The fourth and final objective is the subject of Chapters 3, 4 and 5. The key to detecting electrode-specific degradation lies in the presented OCV model structure and the parameter estimation technique. Devising an OCV model based on the OCV of the PE and the NE was the first step to accommodating electrode-specific degradation. The parameter estimation technique separates the parameterisation of the electrode models from the cell model. Assuming that there are no fundamental changes in the material properties of the electrodes over the lifetime of cell, the electrode OCV sub-models only have to be parameterised once, using measurements recorded on pristine half-cells. By re-fitting the OCV of the full cell at different stages in the cells' cycle life, changes in the capacity ranges of the electrodes utilized within the full cell can be captured and quantified. These changes provide information on electrode-specific degradation signatures, as discussed in depth in Chapters 3, 4 and 5.

Chapter 3

Degradation diagnostics

3.1 Introduction

The identification of the root causes of degradation in Li-ion cells using non-destructive methods remains one of the greatest challenges for Li-ion battery management systems. Efforts to identify the nature and quantify the extent of degradation in Li-ion cells are motivated by the following objectives:

1. Safety: Identification of potentially dangerous scenarios such as lithium plating (internal short-circuits) and excessive cathode potentials.

2. Identification and quantification of electrode-specific modes of degradation and cell failure (particularly useful for improvements in cell design).

3. Assessment and comparison of cell quality and quality spread within a cell batch.

4. Prediction of cell failure.

An important aspect in developing diagnostic techniques for Li-ion cells are possible inhomogeneities in the electrode material, which are not generally accounted for in physics-based degradation models [87, 88]. Evidence of such inhomogeneities

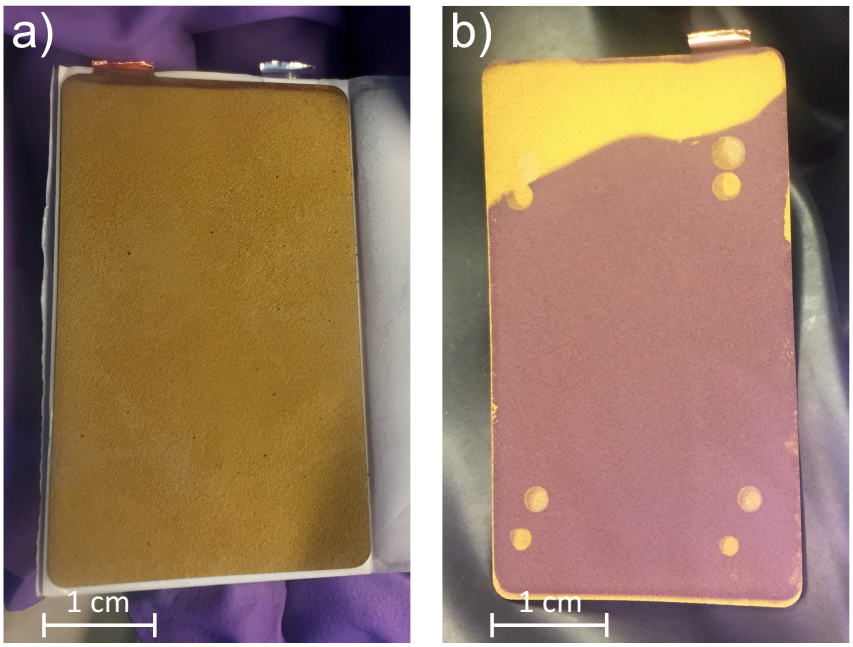

Fig. 3.1 Graphite anode sheets extracted from a fully charged Kokam pouch cell; a) uniformly lithiated, b) non-uniformly lithiated.

has also been observed in the course of a post-mortem analysis of commercial Kokam pouch cells, which are the subject of this work. After low rate (C/25) capacity tests, five cells were opened in an argon filled glove box and their electrode sheets visually inspected. Each cell consists of 20 sheets of positive and negative electrodes. Some of the investigated cells were fully charged, *i.e.* their negative graphite electrodes fully lithiated. Lithiated graphite has a golden colour as opposed to the black colour of delithiated graphite [124]. Figure 3.1 illustrates the difference in lithiation of graphite electrode sheets extracted from the same, fully charged cell. Whereas most negative electrode sheets appeared to be uniformly lithiated (Figure 3.1, a)), one negative electrode sheet was clearly non-uniformly lithiated, as shown in Figure 3.1, b). The standard deviation between the capacities of the five investigated pouch cells was less than 0.2% and the cell with one non-uniformly lithiated graphite sheet actually exhibited the highest capacity. This illustrates that meso and macro scale inhomogeneities can not easily be identified in commercial Li-ion cells but they may have long term effects on degradation.

Diagnostic techniques reported in the literature link the OCV of Li-ion cells to specific degradation signatures [19, 48, 125, 126]. To facilitate the analysis of changes in the OCV indicative of degradation, differential methods such as incremental capacity analysis (ICA) [43] and differential voltage analysis (DVA) [42] are applied, which are sensitive to measurement noise. To date, no experimental evidence has been presented to confirm the links between the proposed degradation signatures and the OCV of Li-ion cells. For practical Li-ion battery systems it is crucial to use available measurements recorded on commercial cells to identify and quantify degradation signatures with methods that tolerate a certain amount of measurement noise. These open questions have prompted the following objectives for this chapter:

1. Experimental verification of the manifestations of LLI, $\mathrm{LAM_{NE}}$ and $\mathrm{LAM_{PE}}$ on the OCV of Li-ion cells.

2. The identification of the nature and the quantification of the extent of electrode-specific degradation signatures in Li-ion cells based exclusively on the cell's OCV without performing derivative operations on the measurements.

The first objective is addressed with a series of experiments on coin cells which were engineered to simulate the three different degradation signatures: LLI, $\mathrm{LAM_{PE}}$ and $\mathrm{LAM_{NE}}$. This was achieved by manufacturing coin cells with different, known amounts of lithium inventory and active electrode material.

To meet the second objective, a diagnostic algorithm is introduced, which identifies and quantifies the nature and extent of each degradation signature by fitting the cells' OCV. At its core, the diagnostic algorithm uses the parametric OCV model presented in Chapter 2. The algorithm is based on the general theory on degradation signatures reported in the literature, which is refined and combined with a parameter estimation technique to allow for a diagnostic, rather than a simulative approach.

Most of the work presented in this chapter has been published in [30] and was presented at the Battery Power Conference in April 2016 in Münster, Germany. The

contributions of other researchers to the work presented in this chapter are limited to advice and guidance on the manufacturing process of coin cells.

3.2 Experimental

3.2.1 Material preparation

Coin cells were constructed with known amounts of lithium inventory and active electrode materials to emulate the different degradation signatures. The coin cells were made in the same way as described in Section 2.2.1 except that full cells were made instead of half-cells. This means that instead of a working electrode and lithium foil as counter electrode, each cell contained a PE sheet and a NE sheet as working and counter electrodes.

Five reference cells were assembled with electrodes extracted from discharged (0% SoC) and fully charged (100% SoC) cells. Both positive and negative electrode disks were cut to a diameter of 15 mm and the separator to 20 mm, as illustrated in Figure 3.2, a). The reference electrodes served as a baseline against which the degradation signatures were compared, and provided a measure for the reproducibility of the coin cell manufacturing process.

Two half-cells, one with positive and one with negative electrode material, with 15 mm electrode disks, were made as described in Section 2.2.1 (see Table 3.1). The half-cells served to parametrize the OCV model, as described in Section 3.4.1. The reference cells and half-cells used in the experiments are listed in Table 3.1 along with the SoC of the electrodes at the time of assembly and the electrode disk diameters. The SoC of the electrodes refers to the degree of lithiation of the respective electrode at the time of assembly. For example, in a fully charged cell, the SoC of the positive electrode is 0% and the SoC of the negative electrode is 100%.

Table 3.1 Baseline cell and half-cell electrodes

Reference cells	Coin cell ID	SoC PE	SoC NE	Diameter PE	Diameter NE
Full cells	Ref 1	100%	0%	15 mm	15 mm
	Ref 2	100%	0%	15 mm	15 mm
	Ref 3	100%	0%	15 mm	15 mm
	Ref 4	0%	100%	15 mm	15 mm
	Ref 5	0%	100%	15 mm	15 mm
Half-cells	HC_{PE}	100%	-	15 mm	-
	HC_{NE}	-	0%	-	15 mm

LLI was emulated by combining the positive electrode of a pouch cell discharged to a higher SoC with the negative electrode of a pouch cell discharged to a lower SoC. For example, combining a positive electrode from a cell discharged to 25% SoC with a negative electrode from a cell discharged to 0% creates a cell with 25% LLI, since the negative electrode is the limiting electrode during discharge and once it has reached its upper voltage limit (the lower voltage limit of the cell), no more lithium can be extracted. In coin cells with emulated LLI, both electrode disks were 15 mm in diameter.

Loss of NE material (LAM_{NE}) was simulated by combining a larger positive electrode disk with a smaller negative electrode disk. Figure 3.2, b) illustrates a cell with 36% LAM_{NE}, where the negative electrode disk is 12 mm in diameter and the positive electrode disk is 15 mm in diameter. Loss of PE material (LAM_{PE}) was simulated by combining a larger negative electrode disk with a smaller positive electrode disk. Figure 3.2, c) shows a cell with 36% LAM_{PE}, where the positive electrode disk is 12 mm in diameter and the negative electrode disk is 15 mm in diameter.

Theoretically, active electrode material can be lost in lithiated, delithiated and partially lithiated states. Loss of lithiated negative electrode material ($LAM_{NE,li}$) was emulated by combining a 12 mm negative electrode disk with a 15 mm positive electrode disk, both harvested from a fully charged pouch cell (SoC = 100%).

Equivalently, loss of delithiated negative electrode material $LAM_{NE,de}$ was emulated by combining a 12 mm negative electrode disk with a 15 mm positive electrode disk, both harvested from a fully discharged pouch cell (SoC = 0%). The same principle was used to create loss of lithiated positive electrode material ($LAM_{PE,li}$). This experimental approach relies on the assumption that lithium transport in the liquid phase is not limiting, so that the active material of the larger electrode disk that extends beyond the overlapping area with the smaller disk gets de/lithiated. This assumption is valid for low currents and widely used in the SPM [64]. Given that the coin cells used in this experiment were flooded with electrolyte and the rate of the characterisation cycles was C/25, the different disk diameters should not pose an issue.

A combination of LLI and $LAM_{PE,li}$ was explored by combining a 14 mm positive electrode disk harvested from a pouch cell previously discharged to 25% SoC with a 15 mm negative electrode disk harvested from a pouch cell previously discharged to 0% SoC.

Table 3.2 provides a list of all the coin cells manufactured to emulate the different degradation signatures, including the SoC of the electrodes and the diameter of the electrode disks.

Table 3.2 Overview of coin cells

Deg. mode	Coin cell ID	SoC PE	SoC NE	Diameter PE	Diameter NE
25% LLI	LLI25	75%	0%	20 mm	20 mm
50% LLI	LLI50	50%	0%	20 mm	20 mm
36% $LAM_{NE,li}$	$LAM_{NE,li}$	0%	100%	15 mm	12 mm
36% $LAM_{NE,de}$	$LAM_{NE,de}$	100%	0%	15 mm	12 mm
36% $LAM_{PE,li}$	$LAM_{PE,li}$	100%	0%	12 mm	15 mm
25% LLI+13% $LAM_{PE,li}$	LLI+LAM_{PE}	75%	0%	14 mm	15 mm

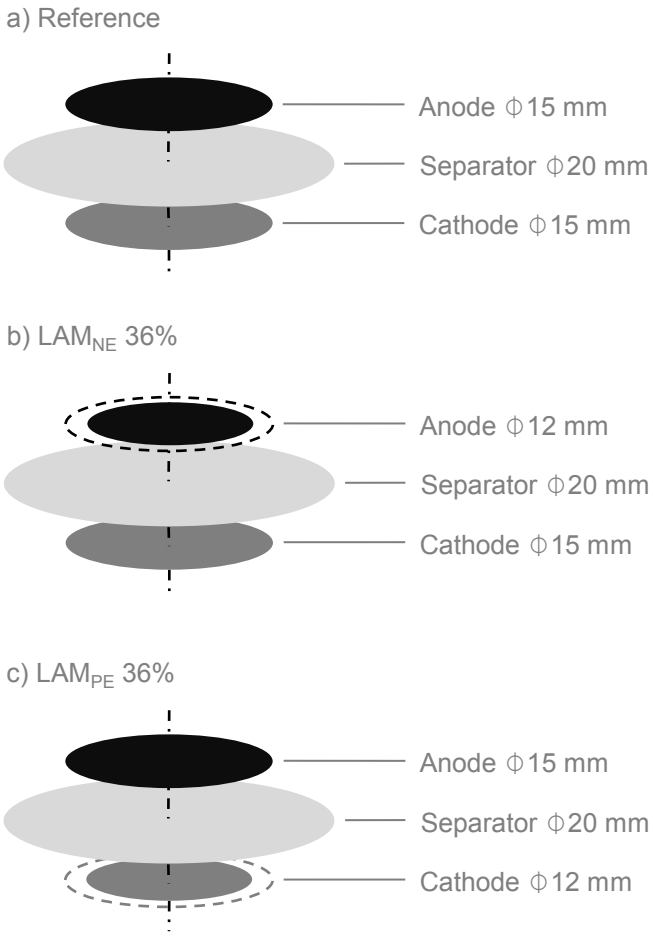

Fig. 3.2 Sizes of electrode disks and separators used in coin cells for a) reference cells and cells with LLI, b) cells with 36% LAM_{NE} and c) cells with 36% LAM_{PE}.

3.2.2 Cell testing

All cell tests were conducted in thermal chambers at 30 °C using BioLogic potentiostats of type MPG-205 and SP-150. Before the start of tests, pouch cells and coin cells were stored in the thermal chambers for 3 h for thermal equilibration. The pouch cells from which the electrodes were extracted for the coin cell manufacturing were prepared according to the test schedule listed in Table 3.3. Firstly, the capacities of the pouch cells (Q_{meas}) were measured during a C/25 (29.6 mA) discharge following a C/25 charge. Secondly, following another C/25 charge, the SoC of the pouch cells was adjusted by a C/25 discharge to the levels required for the respective coin cells, based on the initial capacity measurements.

Table 3.3 Test procedure for pouch cell preparation

SoC at end of test	Test step	Current	Stop-criterion
0%	CC charge	29.6 mA	$V_{Cell} > 4.2$ V
	CC discharge	29.6 mA	$V_{Cell} < 2.7$ V
100%	CC charge	29.6 mA	$V_{Cell} > 4.2$ V
	CC discharge	29.6 mA	$V_{Cell} < 2.7$ V
	CC charge	29.6 mA	$V_{Cell} > 4.2$ V
50%	CC charge	29.6 mA	$V_{Cell} > 4.2$ V
	CC discharge	29.6 mA	$V_{Cell} < 2.7$ V
	CC charge	29.6 mA	$V_{Cell} > 4.2$ V
	Rest	0 mA	time > 10 min
	CC discharge	29.6 mA	$Q_{dch} > 0.5 \times Q_{meas}$
25%	CC charge	29.6 mA	$V_{Cell} > 4.2$ V
	CC discharge	29.6 mA	$V_{Cell} < 2.7$ V
	CC charge	29.6 mA	$V_{Cell} > 4.2$ V
	Rest	0 mA	time > 10 min
	CC discharge	29.6 mA	$Q_{dch} > 0.75 \times Q_{meas}$

The reference coin cells and the coin cells with induced degradation signatures were tested according to the test schedule in Table 3.4, which consisted primarily of one cycle at C/2 and one cycle at C/25. The C/2 cycle served to assess the general performance of the cells, based on which under-performing cells were discarded, and the C/25 cycle served as pseudo-OCV measurement.

Table 3.4 Test procedure for coin cells

Test ID	Test step	Current	Stop-criterion
C/2 cycle	CC charge	1.118 mA	$V_{Cell} > 4.2$ V
	CC discharge	1.118 mA	$V_{Cell} < 2.7$ V
	CC charge	1.118 mA	$Q_{ch} > 1.118$ mAh
C/25 cycle	CC charge	0.089 mA	$V_{Cell} > 4.2$ V
	CC discharge	0.089 mA	$V_{Cell} < 2.7$ V
	CC charge	0.089 mA	$V_{Cell} > 4.2$ V

At a current rate of C/25, the voltage drop in the coin cells was measured to be on the order of 9×10^{-4} mV, which was considered negligible and any voltage measurements recorded at a current rate of C/25 were treated as pseudo-OCV. These pseudo-OCV measurement were used in the degradation model to estimate the degradation signatures. The expected capacities of the coin cells were calculated based on the active surface areas of the electrodes. The electrode sheets of the pouch cells had a surface area of 5 cm x 3 cm = 15 cm^2. The pouch cells had 20 double-sided sheets of each PE and NE, which gives a total active surface area of 600 cm^2. The average pouch cell capacity measured at C/25 was 759 mAh with a standard deviation of $< 0.2\%$. This gives a specific capacity of 1.265 mAh/cm^2, which was assumed to be the same for the coin cells. Given a surface area of 1.767 cm^2 in all coin cells with electrode diameters of 15 mm, the C/25 current was calculated to be 0.089 mA and the C/2 current 1.118 mA. The standard deviation of the capacities of all five reference coin cells measured at a C/2 current rate was 5.39%, which served as the measure of uncertainty for the estimation of degradation signatures. The positive and negative electrode half-cells were cycled at C/25 (0.089 mA).

3.3 Model Development

3.3.1 Theory

The theory underlying the proposed degradation signatures and their effects on the OCV of cells and electrodes is well documented in the literature [48, 127, 126]. This section explains the approach and the extensions of the presented work.

In Li-ion cells, the end of charge (EoC; 100% SoC) and the end of discharge (EoD; 0% SoC) are defined by a corresponding maximum and minimum cell voltage, to ensure safe operation. The lithium cycled within these limits constitutes the cell's useful capacity. During charge, the PE is limiting, since its rising voltage, resulting from de-lithiation, triggers the cell's EoC voltage limit (in this case 4.2 V). Analogously, the NE is limiting during discharge, triggering the EoD voltage limit (in this case 2.7 V).

Figure 3.3, a) shows the base case of a pristine cell. The bars on the left symbolise the anode (NE, in red) and the cathode (PE, blue). The areas of the bars represent the electrode capacities (not to scale). The golden area represents the cyclable lithium, which corresponds to the cell capacity, in this case intercalated in the NE in a fully charged cell. In commercial Li-ion cells, there is generally an excess of NE material, which is illustrated by the larger NE bar. The misalignment of the two bars indicates which electrode is limiting at 100% SoC and 0% SoC, respectively. The plot on the right of Figure 3.3, a) depicts the OCV curves of the PE in blue, the NE in red and the cell in grey, as functions of the cell's normalised capacity, denoted as $\mathrm{SoC_{Cell}}$ in %. The horizontal dash/dot lines highlight the upper and lower voltage limits of the cell at 4.2 V and 2.7 V, respectively, and the vertical dash/dot lines highlight the corresponding maximum and minimum SoC of the whole cell. The points on the OCV of the PE and NE that correspond to the cell's upper and lower voltage limits are indicated by circular markers on the respective OCV curves. As LLI, $\mathrm{LAM_{NE}}$

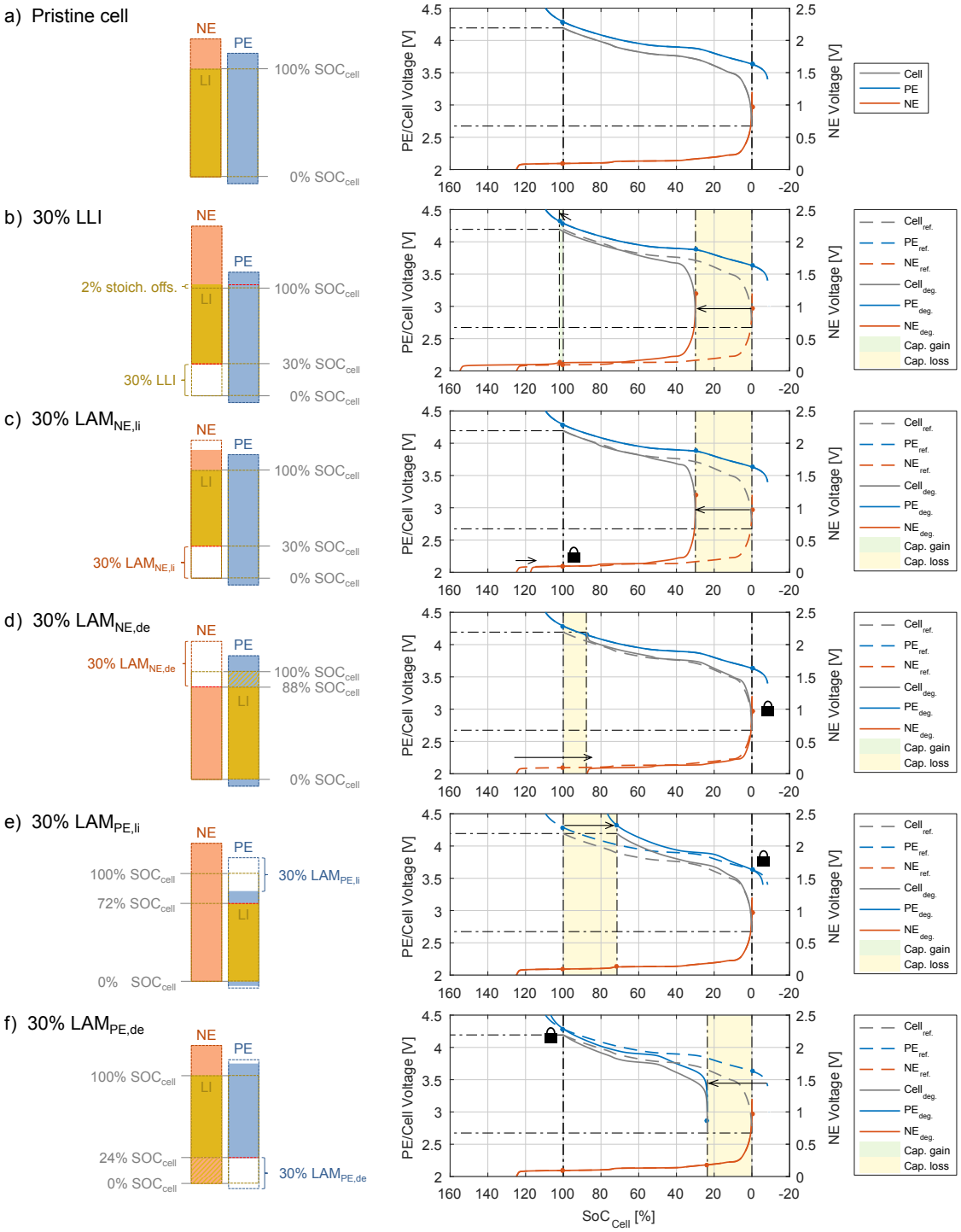

Fig. 3.3 Examples of degradation signatures. Bars in the left column illustrate utilised electrode capacities (not to scale). Plots on the right show the corresponding OCV of the electrodes and the cell. The padlock symbol indicates that the electrode voltage remains unchanged at EoC or EoD.

and LAM_{PE} come into effect, the utilized portions of the electrodes change, which is reflected in their OCVs. This means that the OCVs of the electrodes at EoC and EoD may also change accordingly. The EoC and EoD OCVs of the electrodes are further affected by maintaining constant upper and lower cell voltage limits of 4.2 V and 2.7 V, respectively. Imposing these voltage limits can lead to a stoichiometric offset between the electrodes, the effects of which are discussed individually for each degradation mode.

The loss of cyclable lithium leads to an increased offset between the positive and negative electrode, which reduces the available capacity of the active materials. The example of 30% LLI is illustrated by both the shift of the bars on the left of Figure 3.3, b) and the shift of the negative electrode's OCV curve in the plot on the right. The OCV curves of the base case are depicted for comparison as broken lines. The yellow areas in the plots on the right of Figure 3.3 indicate lost cell capacity. The OCVs of the electrodes at the EoC and EoD are also affected by the stoichiometric offset due to the imposed cell voltage limits. When a cell which has lost 30% of its lithium inventory approaches its EoD (0% SoC), the PE voltage is significantly higher than it would be in a pristine cell at EoD (compare the two circular blue markers on the PE OCV curve at the EoD in Figure 3.3, b)). If the cut-off voltage of the NE remained unchanged, the minimum cell voltage of 2.7 V could not be reached. In reality, as the cell approaches its EoD and the cell voltage is driven towards 2.7 V, more lithium is extracted from the NE and inserted into the positive electrode, leading to a steep rise in the NE voltage, and ultimately reaching the minimum cell voltage of 2.7 V (compare the two circular red markers on the NE OCV curves at the EoD in Figure 3.3, b)). Equivalently, as a cell with 30% LLI approaches its EoC, the NE voltage is higher than in a pristine cell. Therefore, as the cell is driven toward its upper voltage limit of 4.2 V, more lithium is extracted from the PE and inserted into the negative electrode, until the rise in PE voltage triggers the upper cut-off condition of the cell (compare the two circular blue markers

on the PE voltage curve at the EoC in Figure 3.3, b). In the case of 30% LLI, this stoichiometric offset causes a noticeable increase in cell capacity, on the order of 2%, as indicated by the green area in the OCV plot of Figure 3.3, b). Driving the PE to ever higher voltages can destabilize the structure and, in the worst case, trigger an exothermic reaction between the delithiated cathode material and the electrolyte, which can culminate in thermal runaway [17].

The loss of lithiated active material in the NE ($LAM_{NE,li}$) can occur as a result of particle cracking or electronic contact loss between particles of the active electrode material or between the active material and the current collector. The lithium that is trapped inside the isolated graphite particles and can no longer be cycled, leading to a decrease in the cell's capacity. This capacity loss is illustrated by a shortened red/golden NE bar on the left of Figure 3.3, c) and the yellow area in the OCV plot on the right of the figure. Less NE material remains to receive and release lithium, which is manifested in a shrinkage of the OCV curve of the NE, as shown in Figure 3.3, c). Less NE material means that the current density on the remaining material is increased during cycling, which could in turn lead to accelerated ageing of the NE and, in the worst case, to lithium plating on the surface if the charging rates exceed the rates of lithium diffusion into graphite. In the event that only fully lithiated NE material is lost, the EoC voltage of the NE remains the same (as indicated by the padlock symbol in the plot of Figure 3.3, c). The EoD voltage of the PEs and NEs change in the same manner as they would in the case of LLI (indicated by the circular markers).

The loss of delithiated NE material ($LAM_{NE,de}$) initially only has a small effect on the capacity of the cell, since there is an excess of NE material and the OCV of the NE at EoD remains constant (see Figure 3.3, d)). However, the OCV of the NE at the EoC gradually decreases as a result of the loss of active material, which limits the PE to a lower OCV at the EoC thus extracting less lithium. Once the remaining capacity of the NE is smaller than the original cell capacity, the cell loses capacity

at the same rate as it loses active NE material. The capacity loss is equivalent to the portion of lithium inventory that remains trapped in the PE at higher voltages, which is indicated by the blue/gold striped area in the PE bar of Figure 3.3, d). The example of 30% $\mathrm{LAM_{NE,de}}$, illustrated in Figure 3.3, d), effectively leads to a capacity loss of 12%. Moreover, since the cell is still driven to its upper voltage limit of 4.2 V, the NE can be forced to negative voltages, which initiates lithium plating. This is a mechanism that must be prevented in practical applications, since it can lead to dendrite formation and internal short-circuits, which in turn cause catastrophic cell failure [128, 129].

The loss of lithiated PE material ($\mathrm{LAM_{PE,li}}$) is analogous to $\mathrm{LAM_{NE,li}}$; it is a result of electronic contact loss to lithiated PE particles. An example of 30% $\mathrm{LAM_{PE,li}}$ is given in Figure 3.3, e). The OCV curve of the PE shrinks compared to its original extent, since a smaller amount of active material contains less lithium and is discharged faster. At the cell's EoC, this means that less lithium is inserted into the NE, leaving it at a higher OCV, which must be matched by a higher OCV of the PE to reach the cell's upper voltage limit of 4.2 V. A similar scenario arises as discussed for the case of LLI—increasing $\mathrm{LAM_{PE,li}}$ leads to ever higher PE voltages, potentially destabilizing the PE material.

A loss of delithiated PE material ($\mathrm{LAM_{PE,de}}$) can potentially affect the cell capacity at early stages, since there is only a smaller buffer of PE material compared to that in the negative electrode. A scenario of 30% $\mathrm{LAM_{PE,de}}$ is illustrated in Figure 3.3, f). The OCV of both electrodes at the cell's EoC remains constant but the OCV of the PE at the cell's EoD decreases as the OCV curve of the PE shrinks compared to its original extent. In the case of commercial LCO/NCO material, there can be a steep drop in OCV below $\sim 3.4\,\mathrm{V}$. Such a drop leads to an equivalently lower OCV of the NE at the cell's EoD (indicated by the circular markers in the OCV plot of Figure 3.3, f)). The lithium inserted in the NE at higher NE voltages can no longer

be accessed for cycling (illustrated by the red/gold striped pattern in the NE bar of Figure 3.3, f)), which causes the observed capacity loss of 24%.

3.3.2 The degradation model

The parametric OCV model introduced in Chapter 2 is used as the basis for modelling and estimating the degradation signatures. Parameter estimation for the OCV model is carried out as described in Section 2.3.3, with one difference: an additional phase transition was added to the OCV model equations 2.10 and 2.11, bringing the total number of phase transitions for the PE and the NE to $N = 5$. This improved the quality of fit (from RMSE values of 6 mV and 3 mV to 3 mV and 2 mV for the PE and NE, respectively—see Section 3.4.1), which minimizes the effects of OCV fitting errors on the estimation of degradation signatures. The OCV model parameters for the PE and NE were obtained by fitting the pseudo-OCV measurements recorded on the electrode half—cells, HC_{PE} and HC_{NE}, and the reference coin cell.

It is important to emphasize that the OCV model is only parameterised once for the base case. Fitting the OCVs of degraded cells (*i.e.* coin cells with simulated degradation signatures), thus identifying the degradation signatures, is achieved using the degradation model described below. This is based on the assumption that the degradation does not impact the individual phase transitions of the electrode materials in different ways. This assumption is supported by the work of Bloom *et al.* [42] and Dubarry *et al.* [20, 46–48] who showed, by means of differential voltage and capacity analysis, that while peaks associated with electrode specific phase transitions shift and shrink proportionally as a result of degradation, the differences between the peaks of one electrode do not change disproportionally.

The degradation model is designed to estimate three parameters only; the degradation signatures LLI, LAM_{NE}, and LAM_{PE}. The objective of the model is to estimate the extent of the different degradation signatures at any point in a cell's

life by fitting the cell's OCV. Only the full cell's OCV measurement is required for this; the parameters of the OCV model remain unaltered.

The degradation signatures affect the electrodes' capacity ranges in terms of: (i) their offset, increased by LLI, (ii) their scaling, affected by $\mathrm{LAM_{NE}}$ and $\mathrm{LAM_{PE}}$ and (iii) the stoichiometric offset, at EoC (Δx_{EoC}) and EoD (Δx_{EoD}) due to the constant upper and lower cell voltage limits.

Equations 3.1 to 3.4 describe how LLI, $\mathrm{LAM_{PE}}$, $\mathrm{LAM_{NE}}$, Δx_{EoC} and Δx_{EoD} affect the normalised capacity of the positive electrode at the cell's EoC ($x_{\mathrm{PE,EoC}}$) and EoD ($x_{\mathrm{PE,EoD}}$) and the normalised capacity of the negative electrode at the cell's EoC ($x_{\mathrm{NE,EoC}}$) and EoD ($x_{\mathrm{NE,EoD}}$).

$$x_{\mathrm{PE,EoC}} = \frac{\Delta x_{\mathrm{EoC}}}{1 - \mathrm{LAM_{PE}}} \tag{3.1}$$

$$x_{\mathrm{PE,EoD}} = \frac{\Delta x_{\mathrm{EoD}} + 1 - \mathrm{LLI} + \mathrm{LAM_{PE}}}{1 - \mathrm{LAM_{PE}}} \tag{3.2}$$

$$x_{\mathrm{NE,EoC}} = \frac{\Delta x_{\mathrm{EoC}} + \mathrm{LLI} - \mathrm{LAM_{NE}}}{1 - \mathrm{LAM_{NE}}} \tag{3.3}$$

$$x_{\mathrm{NE,EoD}} = \frac{\Delta x_{\mathrm{EoD}}}{1 - \mathrm{LAM_{NE}}} \tag{3.4}$$

LLI, $\mathrm{LAM_{PE}}$ and $\mathrm{LAM_{NE}}$ in Equations 3.1 to 3.4 range from 0 to 1, where 1 is equivalent to the cell's original capacity; *e.g.* LLI = 0.1 means that the loss of lithium inventory is equivalent to 10% of the cell's original capacity. $\mathrm{LAM_{PE}}$ and $\mathrm{LAM_{NE}}$ refer to the loss of active material as a fraction of the active material originally utilised within the capacity range of the full cell. The normalised capacities of the positive and negative electrodes at EoC and EoD are linked through the cell's upper and lower voltage limits, denoted as $E^{\mathrm{OC}}_{\mathrm{Cell,high}}$ and $E^{\mathrm{OC}}_{\mathrm{Cell,low}}$, respectively, according to

$$E^{\mathrm{OC}}_{\mathrm{Cell,high}} - \hat{E}^{\mathrm{OC}}_{\mathrm{PE,EoC}}(x_{\mathrm{PE,EoC}}) + \hat{E}^{\mathrm{OC}}_{\mathrm{NE,EoC}}(x_{\mathrm{NE,EoC}}) = 0 \tag{3.5}$$

and

$$E^{\mathrm{OC}}_{\mathrm{Cell,low}} - \hat{E}^{\mathrm{OC}}_{\mathrm{PE,EoD}}(x_{\mathrm{PE,EoD}}) + \hat{E}^{\mathrm{OC}}_{\mathrm{NE,EoD}}(x_{\mathrm{NE,EoD}}) = 0. \tag{3.6}$$

Equations 3.5 and 3.6 define the OCV of electrodes and cell at 100% SoC and 0% SoC, respectively, when upper and lower cell voltage limits are imposed. The respective points on the OCV curves of cell and electrodes are marked by the vertical, dash/dotted lines in Figure 3.3. $E^{\mathrm{OC}}_{\mathrm{Cell,high}}$ and $E^{\mathrm{OC}}_{\mathrm{Cell,low}}$ have predefined values, in this case 4.2 V and 2.7 V, respectively. $\hat{E}^{\mathrm{OC}}_{\mathrm{PE/NE,EoC}}$ and $\hat{E}^{\mathrm{OC}}_{\mathrm{PE/NE,EoD}}$ are the modelled OCV of the positive and negative electrode at the EoC and EoD, respectively. The OCVs of the electrodes at the cell's EoC and EoD in Equation 3.5 and 3.6 ($\hat{E}^{\mathrm{OC}}_{\mathrm{PE,EoC}}, \hat{E}^{\mathrm{OC}}_{\mathrm{NE,EoC}}, \hat{E}^{\mathrm{OC}}_{\mathrm{PE,EoD}}, \hat{E}^{\mathrm{OC}}_{\mathrm{NE,EoD}}$) are calculated using Equation 2.9 for both the PE and the NE. Δx_{EoC} and Δx_{EoD} can be calculated by substituting Equations 3.1 to 3.4 into Equations 3.5 and 3.6 and solving the linear system of equations. The estimated LLI, $\mathrm{LAM_{PE}}$ and $\mathrm{LAM_{NE}}$ are inserted into Equations 3.1 to 3.4 during the optimisation described below.

The normalised capacity ranges of the electrodes in a degraded cell are defined by vectors of discrete values limited by the normalised capacities at EoC and EoD according to

$$\hat{\mathbf{x}}_{\mathrm{PE}} = \{x_{\mathrm{PE,EoC}}, ...x_{\mathrm{PE,EoD}}\} \tag{3.7}$$

$$\hat{\mathbf{x}}_{\mathrm{NE}} = \{x_{\mathrm{NE,EoC}}, ...x_{\mathrm{NE,EoD}}\}. \tag{3.8}$$

The number of elements in the vectors depends on the number of sampling points obtained for the pseudo-OCV measurements. The OCVs of the electrodes in a degraded cell ($\hat{E}^{\mathrm{OC}}_{\mathrm{PE}}, \hat{E}^{\mathrm{OC}}_{\mathrm{NE}}$) can thus be calculated by numerically solving Equation 2.9 for E^{OC} of the respective electrode, using the normalised electrode capacity ranges $\hat{\mathbf{x}}_{\mathrm{PE}}$ and $\hat{\mathbf{x}}_{\mathrm{NE}}$.

At the cell level, the normalised cell capacity at EoC and EoD is calculated using Equations 3.9 and 3.10.

$$x_{\text{Cell,EoC}} = \Delta x_{\text{EoC}} \tag{3.9}$$

$$x_{\text{Cell,EoD}} = 1 - \text{LLI} + \Delta x_{\text{EoD}} \tag{3.10}$$

In a pristine cell 100% SoC is equivalent to $x_{\text{Cell,EoC}} = 0$ and 0% SoC to $x_{\text{Cell,EoD}} = 1$. The cell's original capacity is normalised, so that

$$x_{\text{Cell,EoD}} - x_{\text{Cell,EoC}} = 1. \tag{3.11}$$

The difference between $x_{\text{Cell,EoD}}$ and $x_{\text{Cell,EoC}}$ (Δx_{Cell}) in a degraded cell corresponds to the cell's normalised capacity as a fraction of its original capacity; *e.g.* $\Delta x_{\text{Cell}} = 0.9$ means that the cell has lost 10% of its original capacity. The normalised capacity range of the cell is defined by a vector of discrete values limited by $x_{\text{Cell,EoC}}$ and $x_{\text{Cell,EoD}}$ according to

$$\hat{\mathbf{x}}_{\text{Cell}} = \{x_{\text{Cell,EoC}}, ...x_{\text{Cell,EoD}}\}. \tag{3.12}$$

Finally, the OCV of the degraded cell, $\hat{E}^{\text{OC}}_{\text{Cell,deg}}$, is calculated for capacity range $\hat{\mathbf{x}}_{\text{Cell}}$, by fitting the measured pseudo-OCV, $E^{\text{OC}}_{\text{Cell,deg}}$. Parameters LLI, LAM_{NE} and LAM_{PE} are estimated by minimising the objective function

$$\hat{\theta}_{\text{deg}} = \arg\min_{\theta_{\text{deg}}} \text{RMSE}(\theta_{\text{deg}}) \tag{3.13}$$

where

$$\text{RMSE}(\theta_{deg}) = \sqrt{\frac{\sum_i^n (\hat{E}^{\text{OC}}_{\text{Cell,deg}}(\theta_{deg}) - E^{\text{OC}}_{\text{Cell,deg}})^2}{n}} \tag{3.14}$$

where n is the number of measurements and θ_{deg} are the parameters

$$\theta_{deg} = [\mathrm{LLI}, \mathrm{LAM_{PE}}, \mathrm{LAM_{NE}}]\,. \tag{3.15}$$

Figure 3.4 provides an overview of the diagnostic algorithm presented in this chapter.

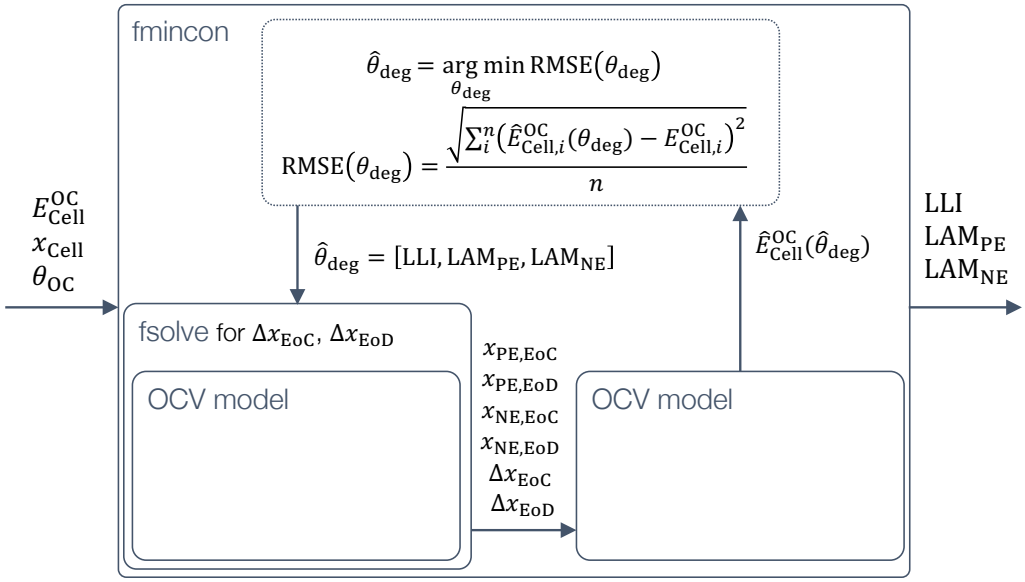

Fig. 3.4 Overview of diagnostic algorithm.

Optimizations were conducted using Matlab's global optimisation function fmincon. Since the cell's OCV drops off rapidly near the EoD, errors calculated at low OCV are generally greater than errors at higher OCV where the OCV curve is flat. In order to avoid a bias of the fit toward the lower end of the OCV curve, the calculation of the RMSE as described in Equation 3.13 was confined to the part of the OCV curve with a gradient of $\frac{\Delta E^{\mathrm{OC}}_{\mathrm{Cell,deg}}}{\Delta \mathrm{SoC}} < 0.1$.

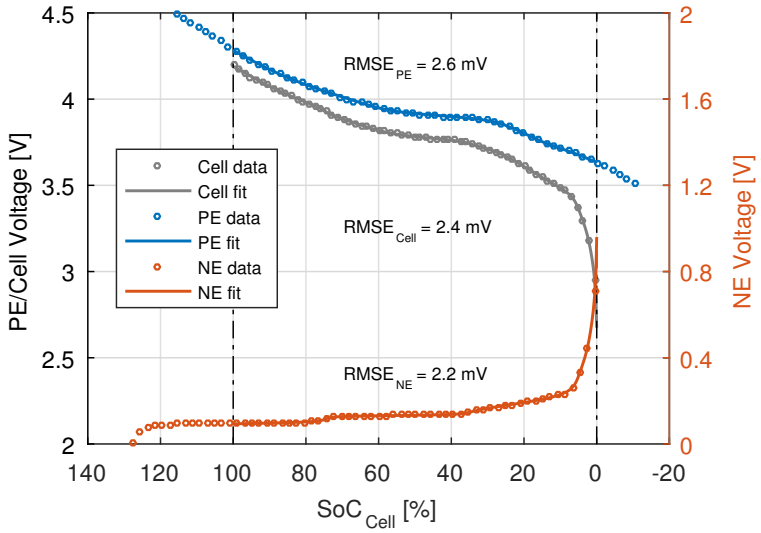

Fig. 3.5 OCV fitting results for reference cell, PE and NE half-cells.

3.4 Results and discussion

3.4.1 OCV model fitting

The OCV model described in Chapter 2 was parameterised by fitting the pseudo-OCV measurements recorded on the electrode half-cells and a reference coin cell, following the parameter estimation procedure described in Section 2.3.3. The fitting results are displayed in Figure 3.5 and the estimated OCV parameters are listed in Table 3.5 for each phase transition Pi. The parameters Δx_{i} are fractions of the total normalised electrode capacity utilized within the cell and parameters ζ_i are dimensionless.

Table 3.5 Estimated OCV model parameters

	PE			NE		
P$_i$	$E_{0,\mathrm{PE},i}$	$\zeta_{\mathrm{PE},i}$	$\Delta x_{\mathrm{PE},i}$	$E_{0,\mathrm{NE},i}$	$\zeta_{\mathrm{NE},i}$	$\Delta x_{\mathrm{NE},i}$
1	5.038 V	1.753	0.021	0.226 V	18.072	0.025
2	4.079 V	0.178	0.523	0.219 V	0.165	0.112
3	3.936 V	0.681	0.124	0.173 V	1.188	0.243
4	3.900 V	3.074	0.136	0.132 V	14.773	0.254
5	3.688 V	0.470	0.178	0.094 V	6.690	0.365

High qualities of fit were achieved for both the OCV of the electrodes and the cell with RMSE < 3 mV (see Figure 3.5). The solid lines in Figure 3.5 show the fitted

OCV results of the cell and the electrodes over the normalised capacity range of the pristine cell. The high fitting accuracy is essential for the degradation model since any deviation from the actual OCV makes it more difficult to identify degradation signatures, which may only have very slight effects on the OCV of a degraded cell.

3.4.2 Test of the diagnostic algorithm using synthesized data

With the OCV model parameterised, the degradation model described in Section 3.3.2 was used in 'forward mode' to create a number of scenarios of cells with known amounts of LLI, LAM_{PE} and LAM_{NE}. The OCVs of the hypothetical degraded cells were subsequently used to test the ability of the diagnostic algorithm to identify and quantify the correct degradation signatures. It is important to point out that the model estimates the total amounts of lost active materials LAM_{PE} and LAM_{NE}, both lithiated and delithiated. Any lithium contained in lost active electrode material is included in the estimate of the total LLI; *i.e.* the total estimated LLI includes both the lithium lost through pure LLI (*e.g.* by SEI build up) and the lithium lost in lithiated active material ($LAM_{PE,li}$ and $LAM_{NE,li}$). For example, 10% of pure LLI and 5% of $LAM_{NE,li}$ gives a total of 15% LLI. The reason for the diagnostic algorithm to be designed in this manner is that a combination of *e.g.* LLI and $LAM_{NE,de}$ creates the same OCV signature as an equal amount of $LAM_{NE,li}$. The same holds true for combinations of LLI and LAM_{PE}. The fractions of lithiated and delithiated LAM can therefore not be uniquely identified if the assumption is that LLI can occur simultaneously, resulting from a different mechanism. An exceptional case would be one where LAM is detected but no LLI. In such a case, the respective LAM could be uniquely identified as loss of delithiated active material.

Three artificial scenarios were created to test the diagnostic algorithm by running the degradation model in 'forward mode'. The scenarios are listed in Table 3.6. The values in Table 3.6 are given as percentage of the cell's original capacity. Values of

LAM refer to the loss of active material as a fraction of the active material originally utilised within the capacity range of the full cell.

Table 3.6 Scenarios for synthetic OCV data

Scenario	LLI (pure)	$LAM_{NE,li}$	$LAM_{NE,de}$	$LAM_{PE,li}$	$LAM_{PE,de}$	LLI (total)
I	12%	0%	23%	6%	0%	18%
II	21%	4%	0%	0%	7%	25%
III	9%	0%	14%	0%	11%	9%

The diagnostic algorithm was used to fit the degradation model to the synthetically generated cell OCVs, thereby identifying the amounts of total LLI, LAM_{PE} and LAM_{NE}. The fitting results are depicted in Figure 3.6, which shows the fitted cell and electrode OCVs on the left (Figure 3.6, a), c) and d)) and the amounts of real and estimated LLI, LAM_{PE} and LAM_{NE} on the right (Figure 3.6, b), d) and f)). The dash/dotted horizontal lines in the OCV plots of Figure 3.6 indicate the cell's upper and lower voltage limits and the vertical lines indicate the corresponding relative capacity. The broken lines show the OCVs of the electrodes and cell of the reference (pristine) cell. Areas filled with yellow indicate capacity loss. Perfect fits were obtained for all three scenarios and all degradation signatures accurately identified, which proves the ability of the diagnostic algorithm to uniquely identify the three different degradation signatures by fitting the OCV of a degraded cell.

As a second test case, white Gaussian noise was added to the above scenarios with known amounts of LLI, LAM_{PE} and LAM_{NE} to test the algorithm's performance with noisy data. Up to a signal-to-noise ratio (SNR) of 40, the degradation signatures in all three scenarios were accurately estimated with $< 1\%$ error. The results are displayed in Figure 3.7, where the grey lines in Figure 3.7, a), c) and e) are the artificial OCV data of the degradation scenarios with added white Gaussian noise and the black lines are the estimated OCV of the cells. Figures 3.7, b), d) and f) show the real and estimated amounts of LLI, LAM_{PE} and LAM_{NE}. Errors of the

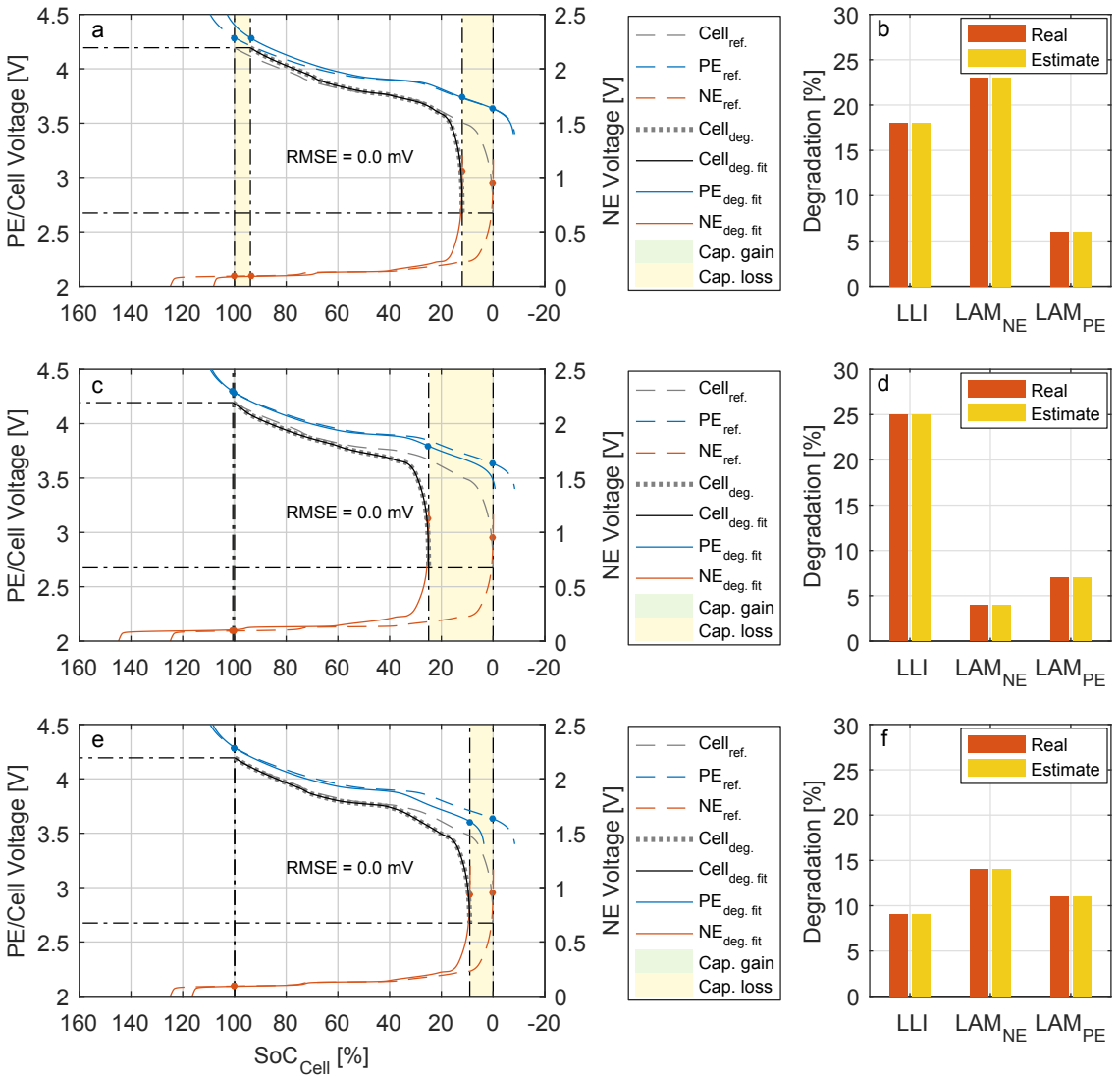

Fig. 3.6 Estimation of degradation signatures using synthetic data: a, b) Scenario I; c, d) Scenario II; e, f) Scenario III.

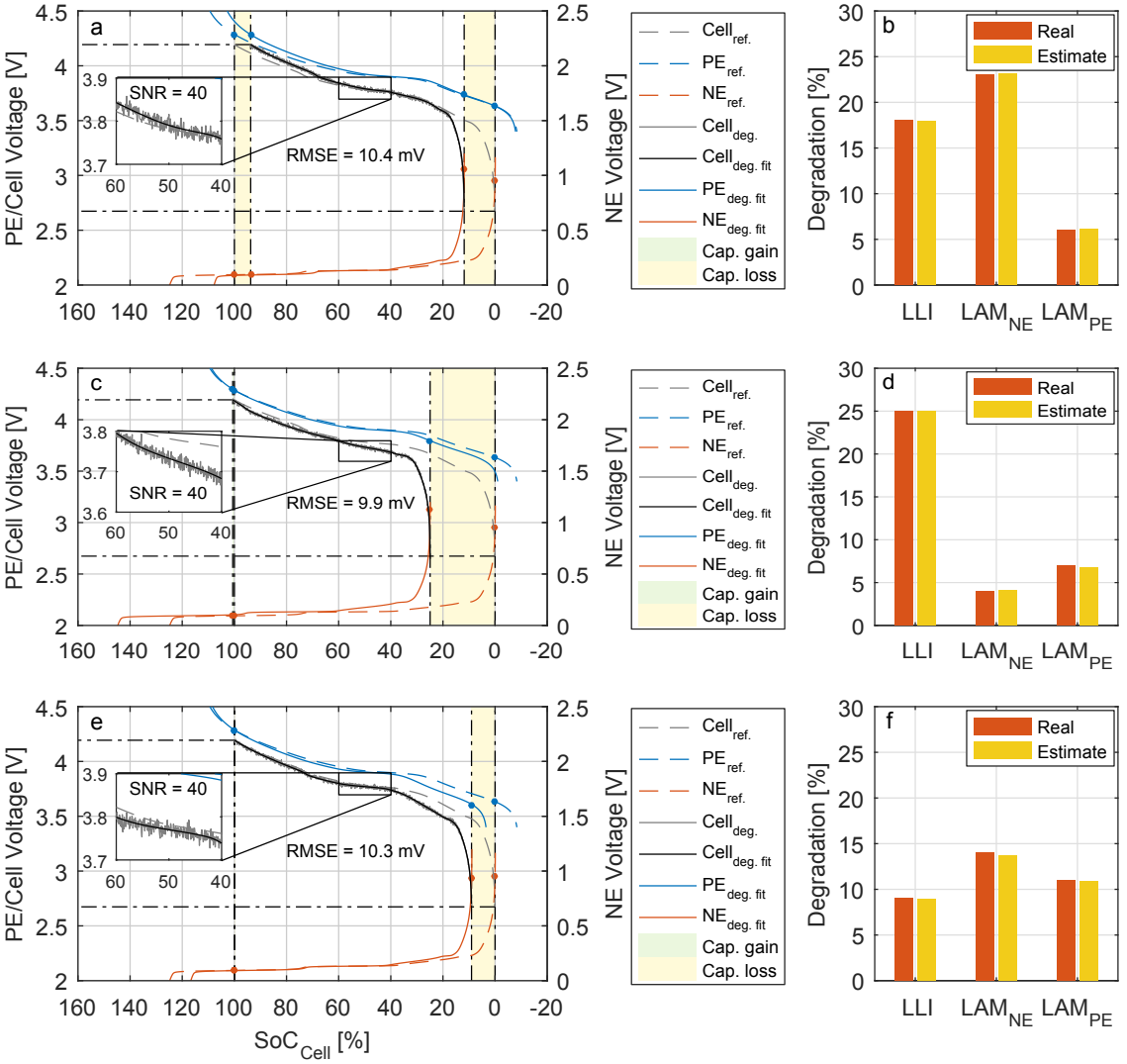

Fig. 3.7 Estimation of degradation signatures using synthetic data with added white Gaussian noise: a, b) Scenario I; c, d) Scenario II; e, f) Scenario III.

estimated degradation signatures in the three scenarios, as well as RMSE values of the estimated OCV are given in Table 3.7.

This analysis demonstrates that the diagnostic algorithm is capable of estimating degradation signatures even at low signal-to-noise ratios in voltage measurements, which is a significant advantage for practical use.

Table 3.7 Estimation errors with synthetic, noisy data.

Scenario	LLI error	LAM_{NE} error	LAM_{PE} error	RMSE
I	0.02 %	0.17 %	0.09 %	10.4 mV
II	0.08 %	0.06 %	0.23 %	9.9 mV
III	0.02 %	0.32 %	0.08 %	10.3 mV

3.4.3 Validation of the diagnostic algorithm using coin cell data

The diagnostic algorithm was used to estimate the degradation signatures engineered by means of the customised coin cells (described in Section 3.2.1). The degradation model was fitted to the pseudo-OCV measurements recorded on the coin cells and the results are displayed in Figure 3.8; OCV fitting results on the left and the extent of real and estimated degradation signatures on the right. The broken lines in the OCV plots on the left of the figure show the cell and electrode OCV of the reference (pristine) cell. The filled areas at EoC and EoD indicate capacity loss (in yellow) or capacity gain (in green) of the respective cell as a result of degradation. Capacity gain refers to the extraction of additional lithium from the positive electrode as a result of the imposed upper cell voltage limit, leading to a stoichiometric offset. This can be detrimental to the cell, since the positive electrode is driven to higher voltages, which may accelerate its degradation. The capacity gain at the EoC is never greater than the accompanying capacity loss at the EoD but it can slightly reduce the overall capacity loss. The RMSE values displayed in the OCV plots were calculated from the measured and the fitted cell voltages for the entire cell voltage window of 2.7 V to 4.2 V. The error bars on the bar charts on the right of Figure 3.8 are based on the standard deviation of the capacities of the reference coin cells (5.39%), as described in Section 3.2.2. The results are discussed individually for each degradation scenario.

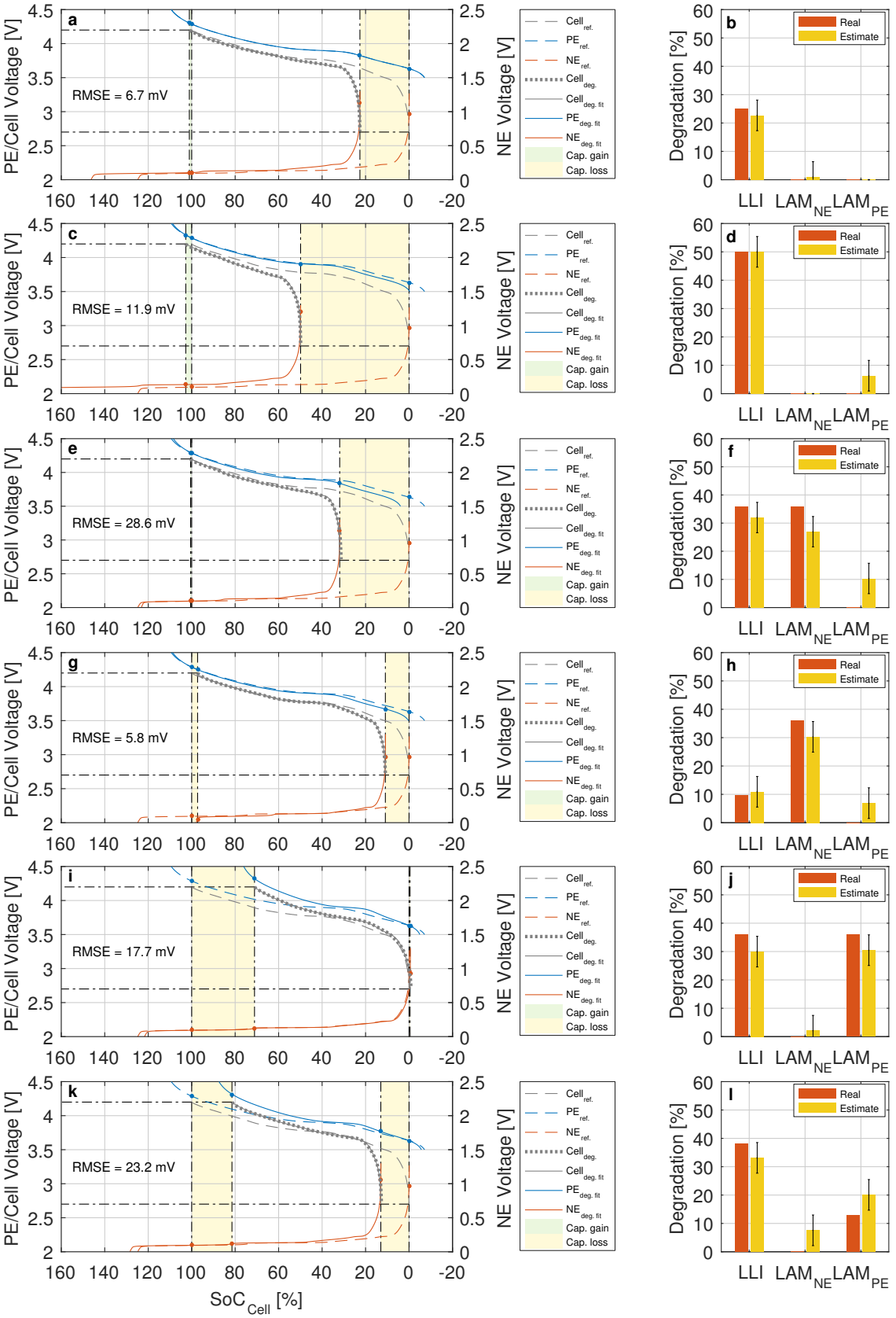

Fig. 3.8 Results of degradation diagnostics; fitted cell OCVs (left column) estimated degradation signatures (right column); a, b) cell LLI25; c, d) cell LLI50; e, f) cell $LAM_{NE,li}$; g, h) cell $LAM_{NE,de}$; i, j) cell $LAM_{PE,li}$; k, l) cell LLI+$LAM_{PE,li}$.

25% LLI

The fitted OCV and estimated degradation signature of cell LLI25 (25% LLI) are shown in Figure 3.8, a) and b), respectively. The diagnostic algorithm accurately estimated the extent of LLI within the margin of error (see Figure 3.8, b)). The coin cell's OCV was fitted with a RMSE of 6.7 mV. The 25% LLI led to the expected increased offset between the PE and NE's OCVs, illustrated by a left-shift of the NE's OCV in Figure 3.8, a), which directly translates into capacity loss of the cell. The offset and imposed upper cell voltage limit forced the positive electrode to a slightly higher OCV, extracting a small amount of additional lithium at the EoC, offsetting $\sim 1\%$ of the overall capacity loss. This is indicated by the dash-dotted vertical lines at the cell's EoC and the circular markers on the PE and NE's OCVs in Figure 3.8, a).

50% LLI

Figure 3.8, c) and d) show the fitted OCV and estimated degradation signature of cell LLI50 (50% LLI). 50% LLI was accurately estimated and other degradation signatures were found to be negligible within the margin of error. The RMSE of the OCV fit was 11.9 mV. The same trends were observed as for cell LLI25, albeit to a greater extent; a large offset between the positive and negative electrode and a noticeably higher positive electrode OCV at EoC, extracting an additional $\sim 2\%$ of lithium from the positive electrode. The results obtained for cells LLI25 and LLI50 confirm the theory of LLI discussed in Section 3.3.1.

36% $\mathbf{LAM_{NE,li}}$

Figure 3.8, e) and f) show the fitted OCV and estimated degradation signature of cell $LAM_{NE,li}$ (36% $LAM_{NE,li}$). LAM_{NE} was successfully identified as a major degradation mode, although to a slightly smaller extent than expected, exceeding the margin of

error by $\sim 4\%$. Against expectations, a small amount of $\mathrm{LAM_{PE}}$ was detected by the diagnostic algorithm, exceeding the margin of error by $\sim 5\%$. This discrepancy could be explained as an artefact of the coin cell manufacturing technique. The hole punch used to cut the 12 mm electrode disks slightly crimped the disks around the edge, creating a small rim which extended beyond the 12 mm electrode disks. The additional active NE material contained in this rim would reduce the expected $\mathrm{LAM_{NE}}$, assuming the active mass on this rim remained electronically connected. The additional lithium contained in the rim of the lithiated NE would reduce the expected LLI. No rims were created for the larger 15 mm disks, in this case the PE. This means that there is now a larger amount of lithium available to lithiate the PE, which would appear as $\mathrm{LAM_{PE}}$. A rim of merely 0.15 mm around a 12 mm disk contains an additional 5% of the electrode's capacity, which could account for the discrepancy between the expected and estimated amounts of $\mathrm{LAM_{NE}}$, $\mathrm{LAM_{PE}}$ and LLI. Overall, the predominant degradation signatures were correctly identified—LLI and $\mathrm{LAM_{NE}}$. In this scenario, all of the lost lithium was contained in the lithiated negative electrode. The diagnostic algorithm correctly identified equal amounts of LLI and $\mathrm{LAM_{NE}}$, suggesting that the prevalent mechanism was most likely $\mathrm{LAM_{NE,li}}$.

36% $\mathbf{LAM_{NE,de}}$

The diagnostic results for cell $\mathrm{LAM_{NE,de}}$ are displayed in Figure 3.8, g) and h)—fitted OCV and estimated degradation signatures, respectively. Since a 36% loss of delithiated negative electrode material exceeds the additional negative electrode capacity buffer, lithium plating on the negative electrode was expected in this scenario during charging. The onset of lithium plating occurs once the negative electrode voltage drops below 0 V. The cells used in this work have a negative electrode capacity buffer of $\sim 25\%$, which can be inferred from the OCV of the reference cell's negative electrode, shown as broken red line in the plots on the left of Figure 3.8. The amount of $\mathrm{LAM_{NE,de}}$ required to consume all of the negative electrode buffer and reach

the onset of lithium plating ($\mathrm{LAM_{NE,pl}}$) can be calculated as follows. Firstly, the normalised capacity of the negative electrode at $E_{\mathrm{NE}}^{\mathrm{OC}} = 0\,\mathrm{V}$, scaled with respect to the normalised cell capacity ($x_{\mathrm{NE,Cell,pl}}$), is calculated. $x_{\mathrm{NE,Cell,pl}}$ is equivalent to the normalised and scaled capacity of the positive electrode, where $E_{\mathrm{PE}}^{\mathrm{OC}} = 4.2\,\mathrm{V}$. $x_{\mathrm{NE,Cell,pl}}$ can be calculated using Equation 2.9 for the positive electrode with 4.2 V plugged in as E^{OC}, multiplying the result by the ratio of cell capacity to positive electrode capacity and adding the offset between the normalised cell capacity and the normalised positive electrode capacity, which is equivalent to x_{PE} at $E_{\mathrm{Cell}}^{\mathrm{OC}} = 4.2\,\mathrm{V}$ (as obtained by the OCV model). Now $\mathrm{LAM_{NE,pl}}$ can be calculated through

$$\mathrm{LAM_{NE,pl}} = 1 - \frac{x_{\mathrm{NE,Cell,pl}}}{x_{\mathrm{NE,Cell,max}}}, \tag{3.16}$$

where $x_{\mathrm{NE,Cell,max}} = 1.25$ is the maximum of the normalised capacity of the negative electrode, scaled with respect to the cell capacity, in the reference cell. Equation 3.16 yields $\mathrm{LAM_{NE,pl}} = 26.4\%$, which means that any loss of delithiated negative electrode material exceeding 26.4% causes the onset of lithium plating on the negative electrode and leads to further capacity loss due to irreversible deposition of metallic lithium. Although some of the lithium plated during charging may be recovered by stripping during discharging [23], the assumption in this work is that the amount of stripped lithium is negligible and any plated lithium reacts to form SEI, causing LLI. The amount of LLI resulting from plating can be approximated by calculating the difference between $\mathrm{LAM_{NE,de}}$ and $\mathrm{LAM_{NE,pl}}$, in this case amounting to 9.6% LLI. The diagnostic algorithm accurately identified both the amount of $\mathrm{LAM_{NE}}$ and LLI within the margin of error, as shown in Figure 3.8, h). The capacity loss attributed to $\mathrm{LAM_{NE,de}}$ is illustrated by the yellow area at the cell's EoC in Figure 3.8, g). Note that capacity lost due to $\mathrm{LAM_{NE,de}}$ is not included in the total amount of LLI. The capacity lost as a result of lithium plating is marked by the yellow area at the

cell's EoD in Figure 3.8, g). The small amount of LAM_{PE}, which was also identified, exceeds the margin of error by only $\sim 1\%$ and is therefore considered negligible.

36% $LAM_{PE,li}$

Figure 3.8, i) and j) display the fitted OCV and estimated degradation signature of cell $LAM_{PE,li}$ (36% of $LAM_{PE,li}$). Figure 3.8, i) illustrates the effect of lost lithiated positive electrode material on the cell's capacity, which is significantly reduced at the EoC. The correct amounts of LAM_{PE} and LLI contained in the lost electrode material were estimated using the diagnostic algorithm.

25% LLI + 13% $LAM_{PE,li}$

Figure 3.8, k) and l) show the fitted OCV and estimated degradation signature of cell LLI+$LAM_{PE,li}$ (25% of LLI and 13% of $LAM_{PE,li}$). In this case, two degradation signatures were combined. The total amount of LLI (38%) includes the pure LLI (25%) and the lithium lost inside the active positive electrode material (13%). The yellow area at the EoC in Figure 3.8, k) represents the capacity loss due to $LAM_{PE,li}$ and the yellow area at the EoD the capacity loss due to pure LLI. As shown in Figure 3.8, l), the total amount of LLI was accurately estimated and the LAM_{PE} was slightly overestimated, exceeding the margin of error by 1.6%. A small amount of LAM_{NE} was detected, exceeding the margin of error by $\sim 1\%$. This could be due to the same effect as described for cell $LAM_{NE,li}$. Overall, the predominant degradation signatures were successfully identified, even in the presence of two independent degradation signatures.

3.5 Conclusions

This work has built on the theory of degradation signatures in Li-ion cells as a manifestation of a host of different physical and chemical mechanisms. The

general theory behind the degradation signatures LLI, LAM_{PE} and LAM_{NE} has been expanded to account for the effects of imposed upper and lower cell voltage limits on the different degradation signatures. This expanded theory was used to create a diagnostic algorithm to identify and quantify LLI, LAM_{PE} and LAM_{NE} using only pseudo-OCV measurements of full cells. The diagnostic algorithm was validated using test cells with known amounts of LLI, LAM_{PE} and LAM_{NE}. The results led to three key findings:

- Experimental evidence of the effects of LLI, LAM_{PE} and LAM_{NE} on the cell's OCV.
- A diagnostic algorithm has been demonstrated to successfully identify and quantify LLI, LAM_{PE} and LAM_{NE}.
- The diagnostic algorithm can identify the onset of potentially dangerous processes such as excessively high voltages on the PE and lithium plating on the NE.

Experimental evidence has been presented to demonstrate that the OCV of Li-ion cells can be used to provide accurate estimates of LLI, LAM_{PE} and LAM_{NE}. The diagnostic algorithm was evaluated for six different scenarios of degradation signatures. Once the OCV model has been parameterised, the diagnostic algorithm requires only pseudo-OCV measurements to estimate the degradation signatures at any point in the cell's life. Since the algorithm uses the pseudo-OCV measurements as a direct input, rather than the derivative of voltage or capacity, it is less sensitive to noise compared to other techniques proposed in the literature. These attributes, combined with the low complexity of the diagnostic algorithm, make it ideal for BMS applications to keep track of the cells' useful capacity and to maintain safe operation.

The algorithm presented in this chapter is used in Chapters 4 and 5, where it is applied to commercial Kokam pouch cells, to test its performance under extreme conditions and for automotive applications.

Chapter 4

Applications of degradation diagnostics: Low temperature cycling

4.1 Introduction

A diagnostic algorithm for the identification and quantification of the degradation signatures LLI, $\mathrm{LAM_{PE}}$ and $\mathrm{LAM_{NE}}$ was presented and validated in Chapter 3, using customized coin cells with known extents of degradation. This chapter explores the application of the diagnostic algorithm to commercial Kokam 740 mAh pouch cells. The test subjects were aged by cycling at $-10\,^{\circ}\mathrm{C}$. A low temperature ageing protocol was chosen because low charging temperatures reportedly have a significant effect on cell degradation and may lead to lithium plating on the negative electrode [23, 130–132] and possibly internal short-circuits [14]. Identifying such potentially dangerous scenarios is of paramount importance in practical applications of Li-ion batteries.

For the purpose of experimental validation of the estimated degradation signatures, both unmodified cells and 3-electrode cells were used in the experiments.

Comparing the electrode potentials measured on the 3-electrode cells with the potentials computed by the diagnostic algorithm allows evaluation of the algorithm's performance. This study also allows one to assess the validity of the OCV model, which was parameterised on a fresh cell, over the cell's life.

For additional validation of the findings produced by the diagnostic algorithm, post-mortem analyses in the form of scanning electron microscopy (SEM) and energy-dispersive X-ray spectroscopy (EDX) were carried out on a selection of the tested cells. The post-mortem analysis was conducted in collaboration with researchers of the Peter Bruce Group in the Department of Materials at Oxford University. Samples were prepared by Euan McTurk and SEM and EDX were carried out by Stefanie Zekoll and Felix Richter.

Overall, the objectives of this chapter can be summarised as

1. Test the suitability of the diagnostic algorithm to estimate the degradation signatures of commercial Kokam 740 mAh pouch cells exposed to extreme cycling conditions.

2. Validate the OCV model by comparing modelled and measured electrode potentials, using 3-electrode cells.

3. Validate the results by post-mortem analysis.

4.2 Experimental

In order to meet the objectives outlined above, the following types of experiments were required:

- Half-cell tests for parameterisation of the OCV model.

- Electrical tests of 3-electrode cells and unmodified pouch cells for the validation of the diagnostic algorithm.

- Post-mortem analysis for further validation of the diagnostic algorithm, consisting of SEM and EDX.

4.2.1 Electrical cell tests

A total of nine Kokam 740 mAh pouch cells were used for the experiments. This includes one pristine cell, which did not undergo any electrical tests but was used for comparative post-mortem analysis with SEM and EDX. Reference electrodes were introduced into four of the cells while the remaining four were unmodified. The 3-electrode cells used for the experiments in this chapter were fabricated following the procedure described in Section 2.2.2. The cells containing reference electrodes are labelled with standard numerals and the unmodified cells are labelled with Roman numerals. All cells were subjected to high-rate, low-temperature cycling at −10 °C and repeated low-rate characterisation at 25 °C. The cell and electrode voltages recorded during the characterisation steps served as pseudo-OCV measurements used for the diagnostic algorithm. The low-temperature cycles consisted of constant current (CC) charging at a rate of 2C (1480 mA) followed by constant voltage (CV) charging, followed by CC discharging at 2C. The characterisation procedures are described in Tables 4.2 and 4.3. The intervals between characterisations and the CV charging period during low-temperature cycling were varied between the different cells. Table 4.1 gives an overview of the test subjects and the corresponding test conditions. SEM and EDX were carried out on a selection of the cells, as specified in Table 4.1.

The test procedures are described in detail in Table 4.2 for cell 1 and I and in Table 4.3 for all other cells. All experiments were carried out in a Vötsch thermal chamber, using Bio-Logic SP-150 and HCP 1005 battery testers.

Table 4.1 Overview of test subjects

Cell ID	Ref electrode	Cycles	CV period	Charact. intervals	Post-mortem
Cell 0	✗	0	-	-	SEM, EDX
Cell 1	✓	120	20 min	variable	EDX
Cell 2	✓	70	25 min	10 cycles	-
Cell 3	✓	80	25 min	20 cycles	-
Cell 4	✓	80	25 min	20 cycles	SEM, EDX
Cell I	✗	120	20 min	variable	EDX
Cell II	✗	80	25 min	20 cycles	SEM, EDX
Cell III	✗	80	25 min	20 cycles	-
Cell IV	✗	80	25 min	20 cycles	-

Table 4.2 Test procedure cell 1 and I

Test	Step	Current	Stop-criterion
Charact. (at T = 25°C)	Rest	0 mA	t > 3 h
	CC charge	740 mA	V_{cell} > 4.2 V
	CV charge	variable	I < 40 mA
	Rest	0 mA	t > 3 h
	C/25 discharge	29.6 mA	V_{cell} < 2.7 V
Cycling (at T = -10°C)	Rest	0 mA	t > 3 h
	CC charge	1480 mA	V_{cell} > 4.2 V
	CV charge	variable	t > 20 min
	CC discharge	1480 mA	V_{cell} < 2.7 V

Table 4.3 Test procedure cells 2, 3, 4, II, III, IV

Test	Step	Current	Stop-criterion
Charact. (at T = 25°C)	Rest	0 mA	t > 3 h
	CC discharge	370 mA	V_{cell} < 2.7 V
	C/25 charge	29.6 mA	V_{cell} > 4.2 V
	C/25 discharge	29.6 mA	V_{cell} < 2.7 V
Cycling (at T = -10°C)	Rest	0 mA	t > 3 h
	CC charge	1480 mA	V_{cell} > 4.2 V
	CV charge	variable	t > 25 min
	CC discharge	1480 mA	V_{cell} < 2.7 V

4.2.2 Half-cell tests

Two half-cells—one anode and one cathode half-cell—were made from electrode sheets harvested from a pristine Kokam 740 mAh pouch cell following the same manufacturing procedure as detailed in Section 2.2.1. The electrode disks used for the half-cells were 12 mm in diameter.

The half-cells were cycled at a rate of C/25—the same rate as used for the characterisation steps of the pouch cells. Given a measured active electrode surface area of 600 cm^2 (see Section 3.2.2) and a nominal capacity of 740 mAh, the nominal current density of the pouch cells is 1.233 mA/cm^2. Assuming the same nominal current density for the coin cells with a diameter of 12 mm (surface area of 1.767 cm^2), a C-rate of C/25 for the coin cells is equivalent to 0.056 mA. The half-cells tests were conducted inside a Vötsch thermal chamber at 25 °C using a Bio-Logic SP150 potentiostat. Voltage measurements were recorded every 1 min or 1 mV change. The second cycle was used for the parameterisation of the OCV model.

4.2.3 SEM and EDX

Samples for SEM images and EDX spectra were extracted from the positive and negative electrodes of the pristine cell 0 and cycled pouch cells 1, 4, I and II. The cells were opened in an argon-filled glove box using a ceramic scalpel. Positive and negative electrode sheets were extracted from the cell stack, rinsed with dimethyl carbonate and dried under vacuum for 20 min. Square sections of roughly 5 x 5 mm were cut from both the positive and negative electrode using a scalpel.

Both SEM images and EDX spectra were recorded on a Merlin-60-62 instrument. The SEM images were recorded using a secondary electron detector at a working distance of 8.9-9.2 mm and an accelerating voltage of 2 kV. EDX spectra were recorded at a working distance of 8.2-8.8 mm and an accelerating voltage of 10 kV.

4.3 Methodology

The diagnostic algorithm presented in Chapter 3 was used to identify and quantify the degradation signatures in Kokam pouch cells exposed to extreme cycling conditions. The OCV model was parameterised at the beginning of the cell tests by fitting pseudo-OCV measurements. As the cell degrades, more pseudo-OCV measurements were recorded at various stages in the cell's life. The diagnostic algorithm identifies and quantifies the degradation signatures by adjusting the utilized capacity ranges of the electrodes to fit these pseudo-OCV curves.

The diagnostic algorithm is based on the assumption that the parameters of the OCV model, identified on a pristine cell, are not affected by degradation. In other words, the cell's OCV is assumed to change only on the basis of decreasing amounts of active electrode material or an increasing offset between the OCV of the two electrodes, not because of fundamental changes within the electrode materials. In order to investigate whether there are noticeable changes in the OCV of the electrodes and to asses the impact of such changes on estimates of degradation signatures, LLI, $\mathrm{LAM_{PE}}$ and $\mathrm{LAM_{NE}}$ were computed in two ways, using

1. A baseline scenario, in which degradation signatures were estimated by fitting the pseudo-OCV of the electrodes, measured on 3-electrode cells. In case of poor fits, OCV parameters were re-estimated.

2. The diagnostic algorithm (as presented in Chapter 3), which estimates the degradation signatures by fitting the pseudo-OCV measurements of the full cell. OCV parameters were not re-estimated.

4.3.1 OCV model parameter estimation

Initially, the OCV model parameters were estimated following the three steps described in Section 2.3.3:

1. PE parameter estimation

2. NE parameter estimation

3. Estimation of PE and NE capacity ranges

The electrode OCVs were calculated as described in Section 2.3.1 by numerically solving Equation 2.9 for E^{OC}, with five phase transitions for each the positive and negative electrode. OCV model parameters for the PE and the NE (θ_{PE} and θ_{NE}) were obtained by fitting the calculated OCVs, $\hat{E}^{\mathrm{OC}}_{\mathrm{PE}}$ and $\hat{E}^{\mathrm{OC}}_{\mathrm{NE}}$, to the pseudo-OCV measured on the electrode half-cells. The capacity ranges of PE and NE were calculated by fitting the cell OCV (Equation 2.12) to the measured pseudo-OCV of the 3-electrode cells.

In an additional step, the electrode parameters, θ_{PE} and θ_{NE} were refined by re-fitting the OCV model to the electrodes' pseudo-OCV measurements directly, recorded on the 3-electrode cells. This was done to minimize any effects of inaccuracies of the initial OCV fit on the fitting results at later stages in the cells' cycle life. The main objective of this work is to validate the performance of diagnostic algorithm, not the quality of initial OCV fits, which was the subject of Chapter 2.

The electrode OCV parameters, θ_{PE} and θ_{NE}, estimated using half-cell pseudo-OCV measurements, were used as initial guess in fitting the electrode's pseudo-OCVs measured on the 3-electrode cells, $E^{\mathrm{OC}}_{\mathrm{PE\,3-el},i}$ and $E^{\mathrm{OC}}_{\mathrm{NE\,3-el},i}$. $\hat{E}^{\mathrm{OC}}_{\mathrm{PE}}$ and $\hat{E}^{\mathrm{OC}}_{\mathrm{NE}}$ were fitted by solving the objective functions for the PE

$$\hat{\theta}_{\mathrm{PE}} = \underset{\theta_{\mathrm{PE}}}{\arg\min}\ \mathrm{RMSE}(\theta_{\mathrm{PE}}) \tag{4.1}$$

and the NE

$$\hat{\theta}_{\mathrm{NE}} = \underset{\theta_{\mathrm{NE}}}{\arg\min}\ \mathrm{RMSE}(\theta_{\mathrm{NE}}) \tag{4.2}$$

where

$$\mathrm{RMSE}(\theta_{\mathrm{PE}}) = \sqrt{\frac{\sum_{i=1}^{n}(\hat{E}^{\mathrm{OC}}_{\mathrm{PE},i}(\theta_{\mathrm{PE}}) - E^{\mathrm{OC}}_{\mathrm{PE\ 3-el},i})^2}{n}} \tag{4.3}$$

and

$$\mathrm{RMSE}(\theta_{\mathrm{NE}}) = \sqrt{\frac{\sum_{i=1}^{n}(\hat{E}^{\mathrm{OC}}_{\mathrm{NE},i}(\theta_{\mathrm{NE}}) - E^{\mathrm{OC}}_{\mathrm{NE\ 3-el},i})^2}{n}}. \tag{4.4}$$

4.3.2 Estimation of degradation signatures

For the diagnostic algorithm, degradation signatures were estimated as described in Section 3.3.2.

For the baseline, instead of Equation 3.13, the objective function used to estimate the degradation signatures, is

$$\hat{\theta}_{\mathrm{deg}} = \underset{\theta_{\mathrm{deg}}}{\arg\min}\ \mathrm{RMSE}(\theta_{\mathrm{deg}}) \tag{4.5}$$

where

$$\begin{aligned}\mathrm{RMSE}(\theta_{\mathrm{deg}}) = \quad & \sqrt{\frac{\sum_{i}^{n}(\hat{E}^{\mathrm{OC}}_{\mathrm{PE},i}(\theta_{\mathrm{deg}}) - E^{\mathrm{OC}}_{\mathrm{PE\ 3-}el,i})^2}{n}} \\ & + \sqrt{\frac{\sum_{i}^{n}(\hat{E}^{\mathrm{OC}}_{\mathrm{NE},i}(\theta_{\mathrm{deg}}) - E^{\mathrm{OC}}_{\mathrm{NE\ 3-}el,i})^2}{n}}\end{aligned} \tag{4.6}$$

where $E^{\mathrm{OC}}_{\mathrm{PE\ 3-}el,i}$ and $E^{\mathrm{OC}}_{\mathrm{NE\ 3-}el,i}$ are the pseudo-OCV of the PE and NE, respectively, measured on the 3-electrode cells.

If significant errors were observed for one or both of the electrodes, their OCV model parameters $E_{0,i}$ and ζ_i were re-estimated for each phase transition i as part of the baseline fitting technique. In this case, the RMSE function used for fitting the pseudo-OCV data is

$$\begin{aligned}\mathrm{RMSE}(\theta_{\mathrm{deg}}, \theta_{\mathrm{PE}}, \theta_{\mathrm{NE}}) = \quad & \sqrt{\frac{\sum_{i}^{n}(\hat{E}^{\mathrm{OC}}_{\mathrm{PE},i}(\theta_{\mathrm{deg}}, \theta_{\mathrm{PE}}) - E^{\mathrm{OC}}_{\mathrm{PE\ 3-}el,i})^2}{n}} \\ & + \sqrt{\frac{\sum_{i}^{n}(\hat{E}^{\mathrm{OC}}_{\mathrm{NE},i}(\theta_{\mathrm{deg}}, \theta_{\mathrm{NE}}) - E^{\mathrm{OC}}_{\mathrm{NE\ 3-}el,i})^2}{n}}\end{aligned} \tag{4.7}$$

where

$$\theta_{\mathrm{PE}} = \begin{bmatrix} E_{0,PE,1} & \zeta_{\mathrm{PE},1} \\ E_{0,PE,2} & \zeta_{\mathrm{PE},2} \\ \vdots & \vdots \\ E_{0,PE,5} & \zeta_{\mathrm{PE},5} \end{bmatrix} \tag{4.8}$$

and

$$\theta_{\mathrm{NE}} = \begin{bmatrix} E_{0,\mathrm{NE},1} & \zeta_{\mathrm{NE},1} \\ E_{0,\mathrm{NE},2} & \zeta_{\mathrm{NE},2} \\ \vdots & \vdots \\ E_{0,\mathrm{NE},5} & \zeta_{\mathrm{NE},5} \end{bmatrix}. \tag{4.9}$$

The parameters $E_{0,i}$ determine the level of the voltage plateaus in the electrode's OCVs and ζ_i the slope of the plateaus. The width of a given plateau is defined by Δx_i, which is not altered as part of the above procedure, since this would interfere with the estimation of the capacity range of the electrodes utilized within the cell. The latter is used to compute the degradation signatures LLI, $\mathrm{LAM_{PE}}$ and $\mathrm{LAM_{NE}}$.

4.3.3 Post-mortem analysis

SEM and EDX analyses were carried out on anode and cathode samples of a pristine cell (cell 0), an unmodified cell after 80 cycles (cell II) and a modified, 3-electrode cell after 80 cycles (cell 4). EDX analyses were also conducted after 120 cycles on anode and cathode samples of the unmodified cell I, and the modified, 3-electrode cell 1.

SEM results provide information about the surface properties of the samples, which could indicate the formation of surface films or large cracks in the active materials of anode and cathode.

EDX reveals the composition of the electrodes near the electrode surface. Changes in composition between the samples of the pristine cell and the cycled cells provide insights about the chemical changes near the electrodes' surfaces, which could arise

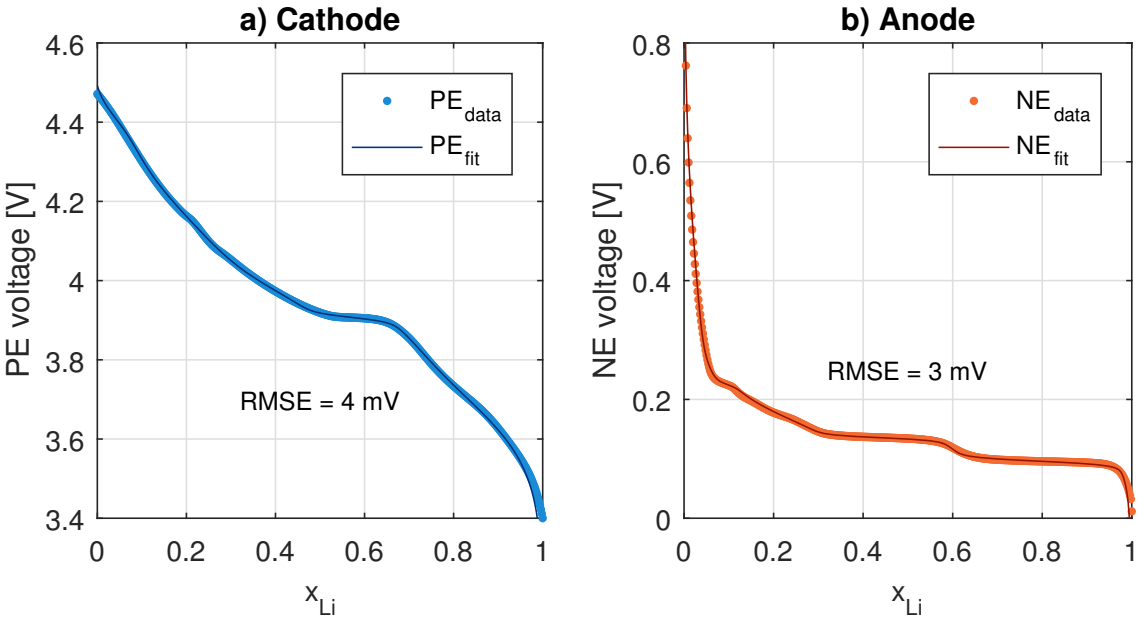

Fig. 4.1 Pseudo-OCV fitting results of a) PE half-cell and b) NE half-cell.

from surface film formation, metallic depositions or decomposition reactions affecting active materials and/or the electrolyte.

Post-mortem experiments were conducted in order to validate, qualitatively, the degradation signatures estimated using the diagnostic algorithm. Moreover, the analyses should reveal whether the cell modification has an effect on cell degradation by comparing the results of modified and unmodified cells.

4.4 Results and discussion

4.4.1 OCV model parameter estimation results

The results of the initial pseudo-OCV fits of the positive and negative electrode half-cells are displayed in Figure 4.1. High quality fits were achieved with a RMSE of 4 mV for the PE and 3 mV for the NE. Estimated OCV model parameters of the positive and negative electrode are listed in Table 4.4. The parameters Δx_i are fractions of the total normalised electrode capacity utilized within the cell and parameters ζ_i are dimensionless.

Table 4.4 OCV model parameters.

	PE			NE		
Phase	$E_{0,PE,i}$	$\Delta x_{\mathrm{PE},i}$	$\zeta_{\mathrm{PE},i}$	$E_{0,\mathrm{NE},i}$	$\Delta x_{\mathrm{NE},i}$	$\zeta_{\mathrm{NE},i}$
P_1	4.418 V	0.064	0.803	0.374 V	0.063	0.187
P_2	4.175 V	0.266	0.298	0.225 V	0.030	8.274
P_3	3.967 V	0.196	0.597	0.164 V	0.327	0.933
P_4	3.907 V	0.151	4.674	0.135 V	0.241	11.838
P_5	3.699 V	0.323	0.295	0.096 V	0.338	8.505

The initial estimates of the OCV parameters for the PE and NE were used as initial guess to fit the pseudo-OCV of the electrodes measured on the 3-electrode cells. The fitting results obtained for cells 1, 2 and 3 are displayed in Figure 4.2. PE and cell voltages are plotted on the left vertical axis and NE voltages on the right vertical axis, against depth of discharge. The RMSE of the fits of electrode and cell OCVs are indicated in the figure. RMSE values do not exceed 1.7 mV for the electrode fits and 2.4 mV for the cell fits of all cells.

4.4.2 Electrical cell test results

Electrical cell tests consisted of low-temperature cycling and frequent low-rate (pseudo-OCV) characterisations. Figure 4.3 shows the electrode and cell voltages recorded on three 3-electrode cells (cell 1, 2 and 3) during a low-temperature cycle. PE and cell voltages are plotted on the left vertical axis and NE voltages on the right vertical axis, against time.

Cell 1 was exposed to a shorter CV charging period than cells 2 and 3. From the voltage data in Figure 4.3 it is evident that the low temperature significantly affects the cells' overpotentials, as reflected by rapid increases in the PE and cell voltages during charge and a pronounced drop of the PE and cell voltages at the beginning of discharge. Moreover, the low temperature and relatively high charging current rate of 2 C caused the NE voltage to drop below 0 V shortly after the start of the

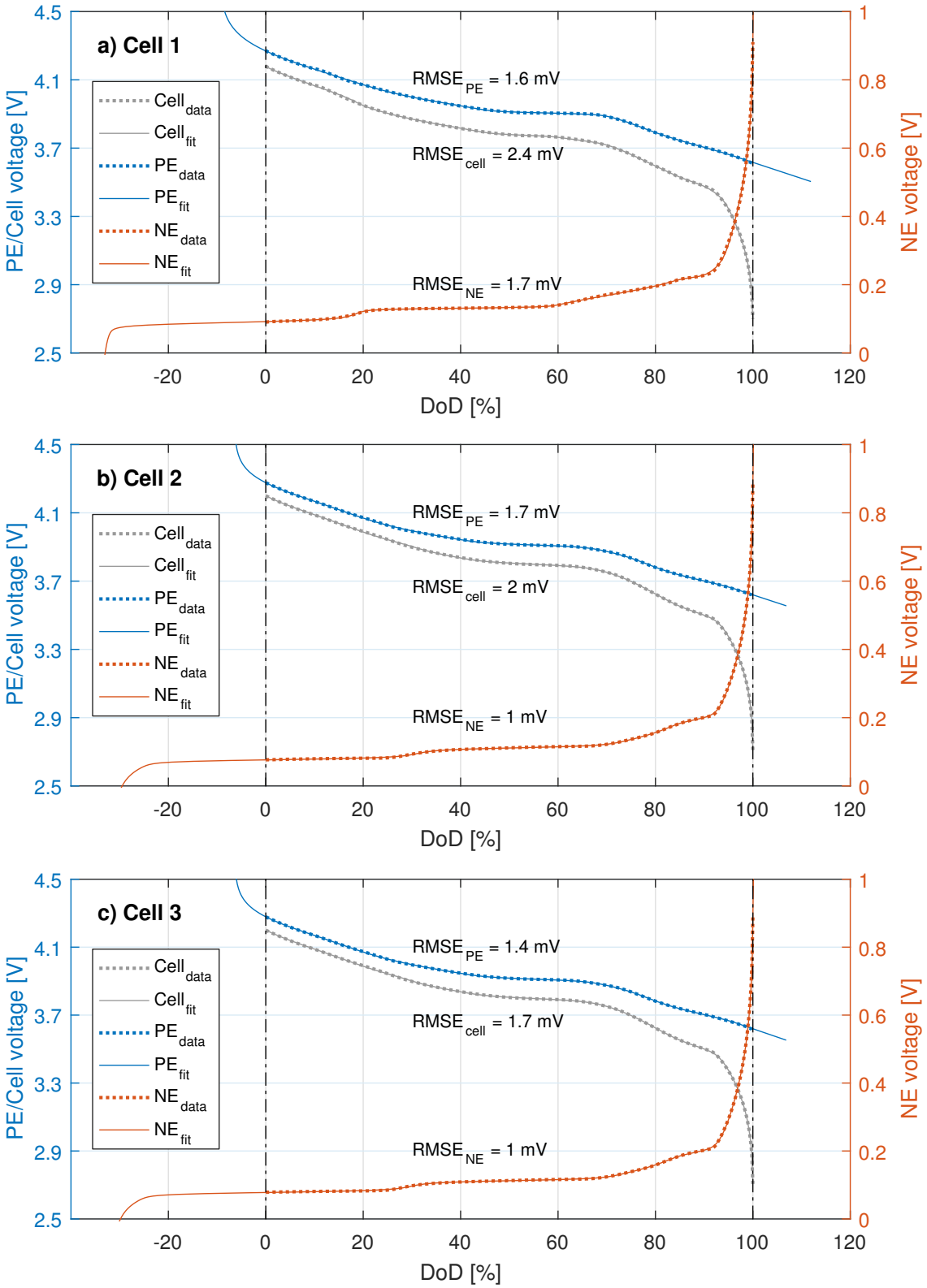

Fig. 4.2 Pseudo-OCV measurements and fit results of 3-electrode cells a) cell 1, b) cell 2 and c) cell 3.

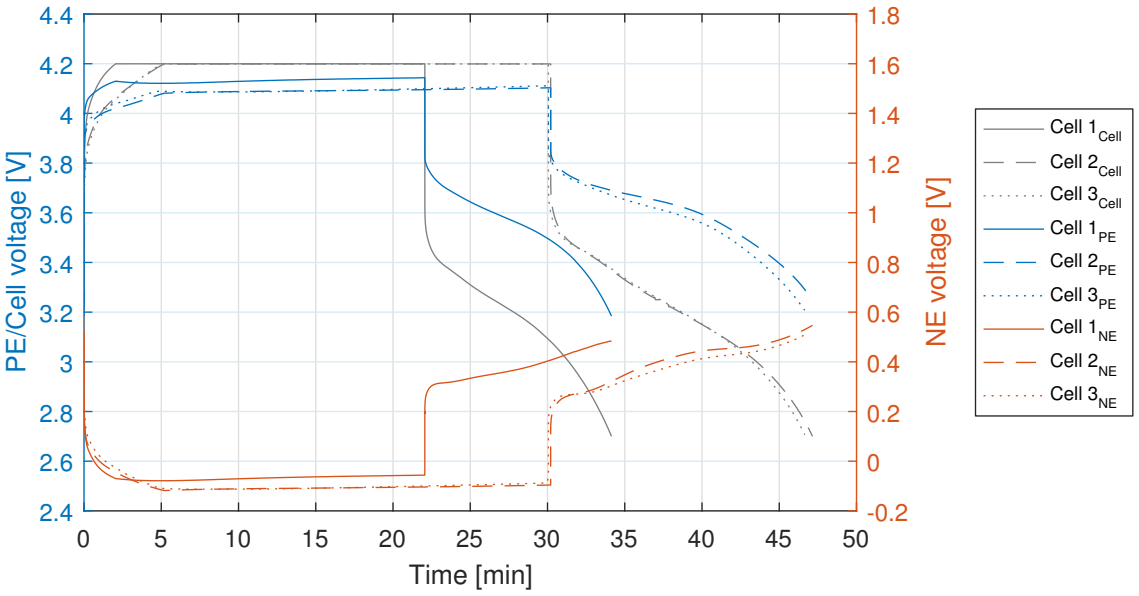

Fig. 4.3 Voltage of 3-electrode cells during 2 C cycle at −10 °C.

charging step, until the start of the discharging step. At negative potentials, metallic lithium can be plated on the anode surface, creating a safety hazard if dendrites are formed which could pierce the separator and lead to internal short-circuits.

No internal short-circuits were observed during the cell tests but all cells exposed to low-temperature cycling faded rapidly, as illustrated in Figure 4.4, which shows the first (a) and last (b) characterisation cycle of all cells. 3-electrode cells are plotted with dashed lines and unmodified cells with continuous lines of matching colours. Figure 4.4, b) illustrates that there is no significant difference in capacity fade between the modified 3-electrode cells and the unmodified cells, which is a first indication that the modification did not affect the cells' cycle lives.

4.4.3 Estimation of degradation signatures

As a first step, the degradation signatures of the tested cells were estimated using the diagnostic algorithm at every characterisation step, by fitting the measured pseudo-OCVs of the electrodes. Examples of the fitting results are provided in Figure 4.5 for the diagnostic algorithm (a-d) and the baseline (e-h). Figure 4.5, a) shows

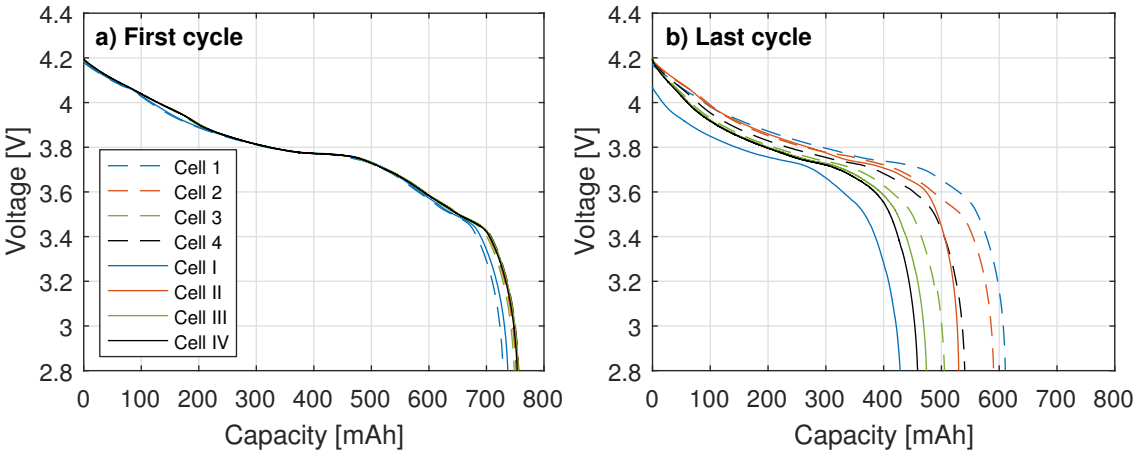

Fig. 4.4 Pseudo-OCV measurements of three-electrode cells and unmodified cells a) at first cycle and b) at last cycle.

the measured and fitted pseudo-OCVs of cell 2 at cycle 0, 50 and 70. PE and cell voltages are plotted on the left vertical axis and NE voltages on the right vertical axis, against depth of discharge. Residuals of cell, PE and NE voltages are displayed in Figure 4.5, b), c) and d), respectively. From Figure 4.5, a)-d) it is evident that good fitting results were achieved for both electrodes using the diagnostic algorithm up to cycle 50. Residuals for the PE and NE do not exceed 25 mV and are less than 10 mV for most of the voltage curves. At cycle 70, fitting errors increase, particularly for the NE, reaching almost 50 mV at the end of discharge. From Figure 4.5, a) it is clear that the NE voltage measured at cycle 70 is markedly different from the voltage measured at cycle 0 and 50; the gradient of the NE voltage between 0% DoD and $\sim$ 60% DoD is visibly steeper than the gradient at cycle 0 and 50.

For the baseline, the measured pseudo-OCVs of the electrodes are fitted at each characterisation cycle. Based on the quality of fits achieved using the diagnostic algorithm, the OCV model parameters $E_{0,\mathrm{NE},i}$ and $\zeta_{\mathrm{NE},i}$ of the NE are re-estimated for each phase transition i as part of the fitting procedure. OCV fitting results of the baseline are displayed in Figure 4.5, e) with residuals of cell, PE and NE voltages in Figure 4.5, f), g) and h). From the plots of the residuals, it is clear that better fits are achieved for PE, NE and cell in case of the baseline, with fitting errors

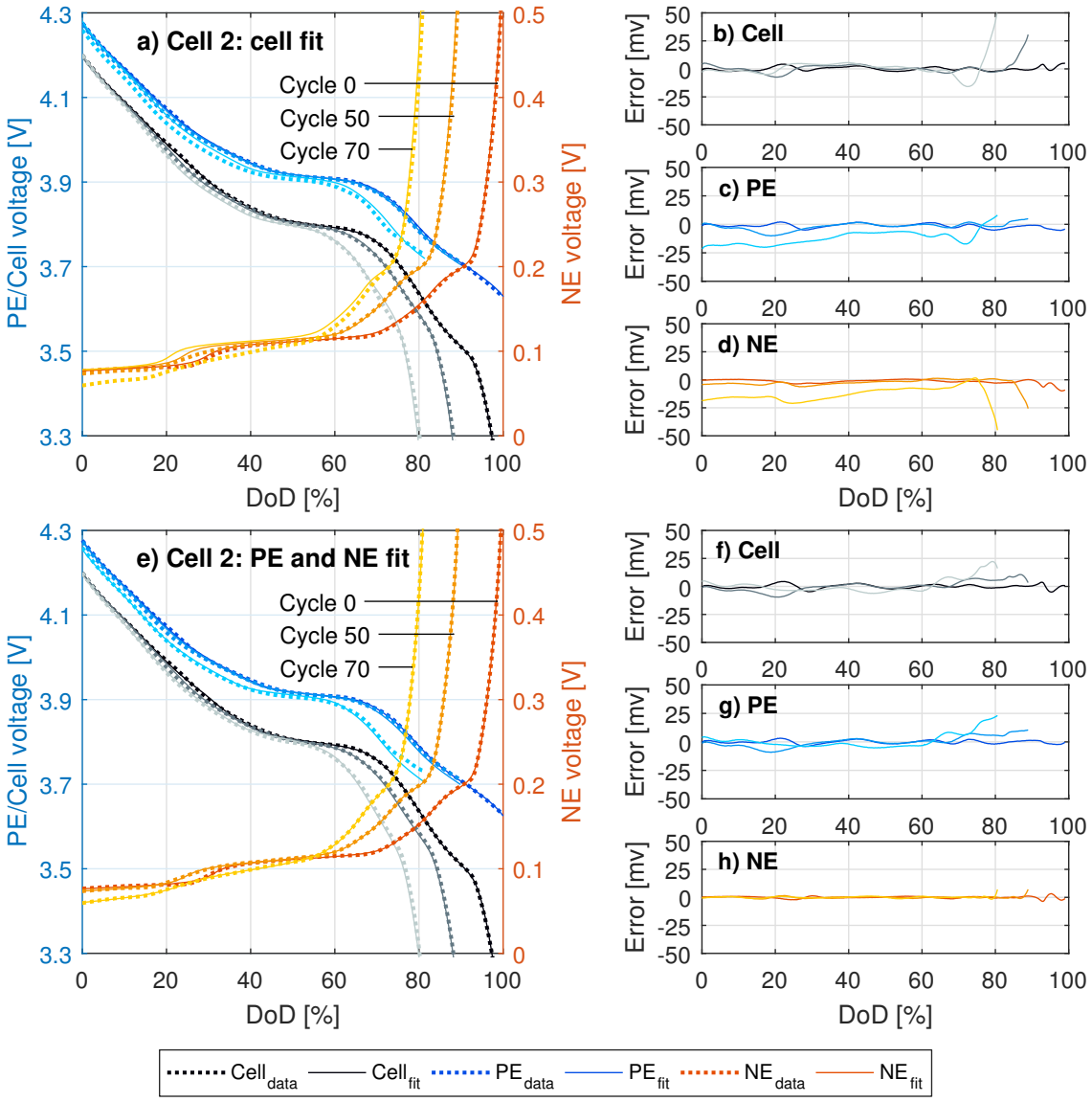

Fig. 4.5 Pseudo-OCV fitting results of cell 2, a) diagnostic algorithm, residuals of cell and electrode fits in b), c) and d); e) baseline, residuals of cell and electrode fits in f) g) and h).

not exceeding 25 mV for any cycle. By minimizing the errors in OCV fits, higher certainties regarding the estimated degradation signatures are expected.

Figure 4.6 depicts the fitting results of cells 1, 2 and 3 for all characterisation cycles. The left column shows the baseline results and the right column the results of the diagnostic algorithm. PE and cell voltages are plotted on the left vertical axes and NE voltages on the right vertical axes, against depth of discharge. Different cell test procedures were applied to the three cells (see Table 4.1). The longer CV charging period experienced by cells 2 and 3 clearly accelerated the rate of degradation. From the measured pseudo-OCV of the NE, it appears that longer CV charging at low temperatures has a significant effect on the NE. The differences in NE degradation between the three cells are also evident from the comparison of the OCV model parameters $E_{0,\mathrm{NE},i}$ and $\zeta_{\mathrm{NE},i}$, which were re-fitted for the baseline at each characterisation cycle. $E_{0,\mathrm{NE},i}$ and $\zeta_{\mathrm{NE},i}$ are displayed in Figure 4.7, where the NE parameters are plotted against cycle number for cell 1 (a and b), cell 2 (c and d) and cell 3 (e and f). Cell 1 clearly shows the smallest changes in $E_{0,\mathrm{NE},i}$ and $\zeta_{\mathrm{NE},i}$ over its cycle life, which indicates that most of the NE degradation was captured by the diagnostic algorithm. The evolution of the parameters $E_{0,\mathrm{NE},i}$ and $\zeta_{\mathrm{NE},i}$ shows similar trends for cells 2 and 3. There is a slight decrease in parameters $E_{0,\mathrm{NE},3-5}$ from cycle 40 onward. The parameters $E_{0,\mathrm{NE},i}$ reflect the voltages at the voltage plateaus of phase transition i of the NE. $E_{0,\mathrm{NE},2}$ remains relatively constant and $E_{0,\mathrm{NE},1}$ increases slightly for both cells 2 and 3. Parameters $\zeta_{\mathrm{NE},1}$ and $\zeta_{\mathrm{NE},3}$ remain constant for both cells 2 and 3, whereas a general decrease in the remaining parameters $\zeta_{\mathrm{NE},2}$ and $\zeta_{\mathrm{NE},4-5}$ can be observed. The parameters $\zeta_{\mathrm{NE},i}$ are a measure of the voltage gradient of the NE voltage; lower values of $\zeta_{\mathrm{NE},i}$ indicate steeper gradients in NE voltage. The evolution of parameters $\zeta_{\mathrm{NE},i}$ agrees with the observations made on Figure 4.5; steeper gradients in the pseudo-OCV of the NE are observed at lower DoD.

The degradation signatures LLI, $\mathrm{LAM_{PE}}$ and $\mathrm{LAM_{NE}}$ calculated for both the baseline and the diagnostic algorithm are displayed in Figure 4.8. Degradation modes

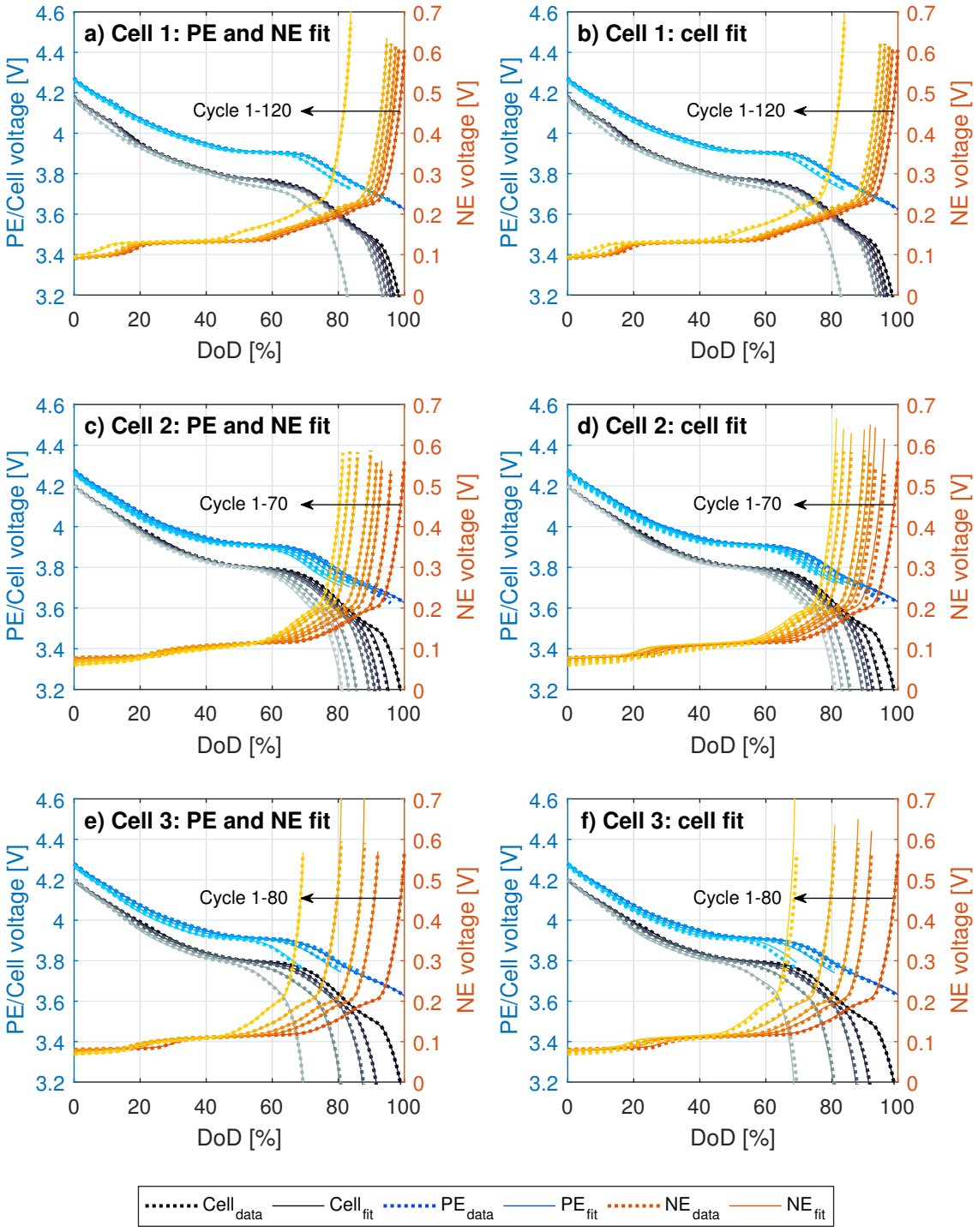

Fig. 4.6 OCV fitting results of cells 1 (a,b), 2 (c,d) and 3 (e,f). Left column: baseline, right column: diagnostic algorithm.

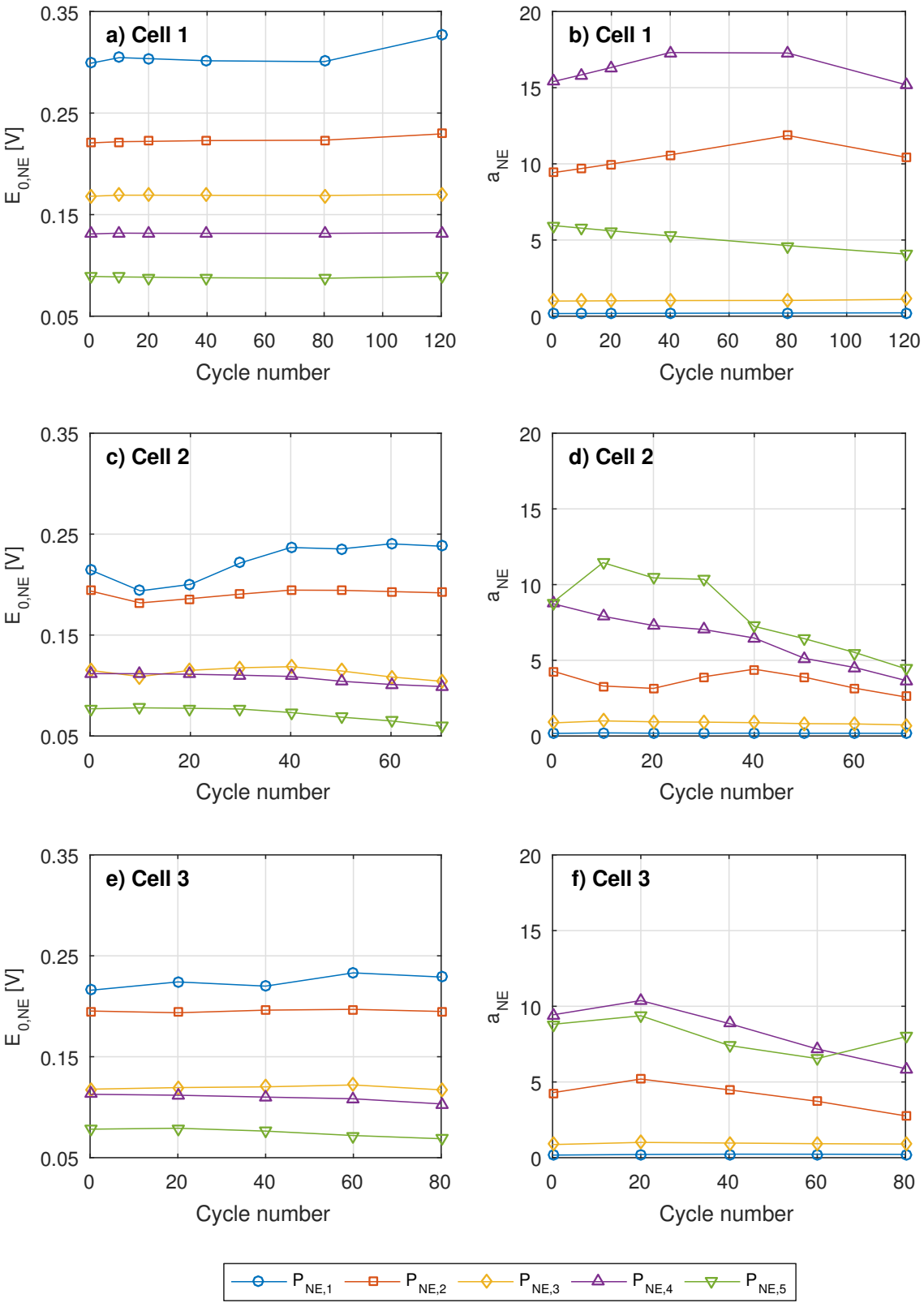

Fig. 4.7 OCV model parameters $E_{0,\mathrm{NE},i}$ and $\zeta_{\mathrm{NE},i}$ from the NE fit of Cell 1 (a, b), Cell 2 (c, d) and Cell 3 (e, f).

are plotted against cycle number for cell 1 (a), cell 2 (b) and cell 3 (c). Baseline results are depicted by broken lines and the results of the diagnostic algorithm by solid lines. Measured capacity loss is also displayed. The accuracies of estimated $\mathrm{LAM_{PE}}$ and $\mathrm{LAM_{NE}}$ depend on the qualities of pseudo-OCV fits of the PE and NE, respectively. LLI depends on the fitting quality of both PE and NE. Since the degradation signatures are calculated as percentages of the original cell capacity, uncertainties are related to errors in the estimated, normalised capacity. Error bars for the estimated $\mathrm{LAM_{PE}}$ and $\mathrm{LAM_{NE}}$ are derived from the RMSE on the estimated, normalised capacity of the PE and NE, respectively. Error bars for the estimated LLI are based on the sum of the RMSE on the estimated, normalised capacity of PE and NE. The RMSE on estimated capacity is calculated by

$$\mathrm{RMSE}_x = \sqrt{\frac{\sum_{i=1}^{n}(x_i(E_i^{\mathrm{OC}}) - \hat{x}_i(\hat{E}_i^{\mathrm{OC}}))^2}{n}} \cdot 100\% \tag{4.10}$$

for each, the PE and the NE capacity. $x_i(E_i^{\mathrm{OC}})$ is the measured, normalised capacity, $\hat{x}_i(\hat{E}_i^{\mathrm{OC}})$ is the fitted, normalised capacity and n is the number of measurements. To provide an example, a RMSE on the estimated, normalised PE capacity of 2% translates directly to an uncertainty of $\pm 2\%$ in $\mathrm{LAM_{PE}}$, represented by the error bars in Figure 4.8.

Figure 4.8 demonstrates close agreement, largely within the margin of error, between LLI, $\mathrm{LAM_{PE}}$ and $\mathrm{LAM_{NE}}$ produced by both the baseline and the diagnostic algorithm. The largest RMSE values for pseudo-OCV fits of the PE and NE using the diagnostic algorithm were obtained for cell 2, reaching 2% for the PE and 4% for the NE by cycle 70. The close agreement between the results obtained with the two different methods indicates that the OCV model, parameterised using a pristine cell, remains valid for the whole cycle life of the tested cells, even under extreme operating conditions.

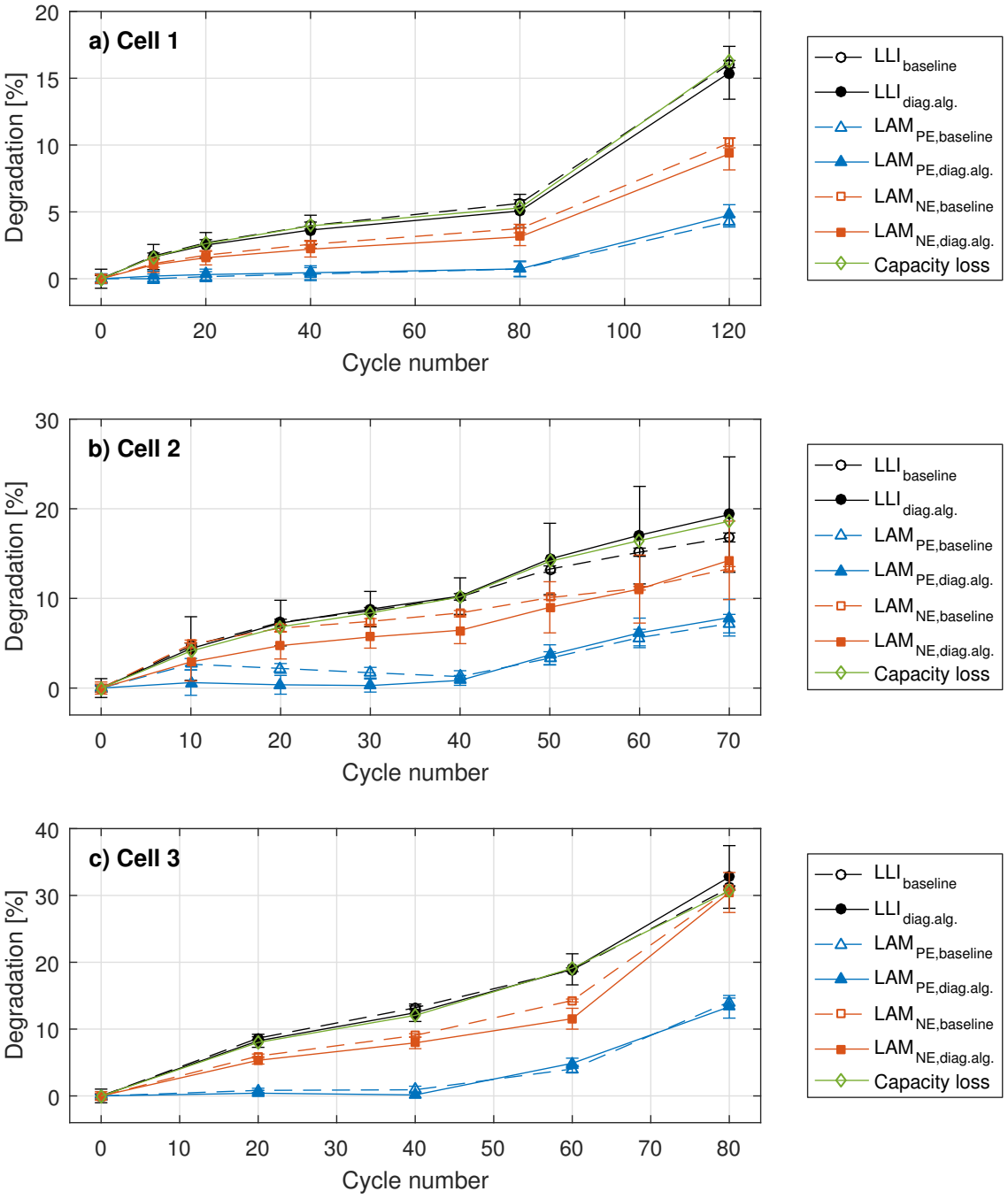

Fig. 4.8 Degradation modes estimated by fitting the cell OCV of a) cell 1, b) cell 2 and c) cell 3 (solid lines) and baseline degradation signatures obtained from fitting electrode OCVs (broken lines).

Aside from the validation of the diagnostic algorithm and OCV model, further observations were made about the effects of the different test regimes on the degradation of the tested cells. The evolution of degradation signatures over the cells' lives shows that cycling at −10 °C primarily affects the anode, as reflected by a rapid rise in $\mathrm{LAM_{NE}}$. The extended CV charging periods at −10 °C, experience by cells 2 and 3, caused greater rates of degradation than exhibited by cell 1. By cycle 80, cell 1 had lost roughly 5% of capacity and 3-4% of active NE material. By comparison, cell 3 had lost 30% of capacity by cycle 80 and the same amount of active NE material. By the end of tests (cycle 120), cell 1 experienced $\sim$ 5% $\mathrm{LAM_{PE}}$ and $\sim$ 10% of $\mathrm{LAM_{NE}}$. Cells 2 and 3 had lost close to 10% of active PE material, as well as $\sim$ 15% and $\sim$ 30% of $\mathrm{LAM_{NE}}$, respectively, by the end of tests (cycle 70). Cells 2 and 3 showed very similar modes of degradation up until cycle 60. The onset of $\mathrm{LAM_{PE}}$ did not occur before cycle 40 for both cells. The higher frequency of characterisation cycles recorded on cell 2 did not cause major differences in degradation compared to cell 3 for most of the cells' cycle life.

4.4.4 SEM and EDX results

The results presented in Section 4.4.3 suggest that the low-temperature cycling procedure heavily affected the anodes of the tested cells. Some loss of active cathode material was also identified. Post-mortem analyses by means of SEM and EDX were conducted in order to provide further experimental validation of the estimated degradation signatures.

SEM images were recorded on anode and cathode samples of the pristine cell 0, which had not been cycled (Figure 4.9, a) and b)), of cell 4 after 80 cycles (Figure 4.9, c) and d)) and of cell II after 80 cycles (Figure 4.9, e) and f). Comparing the images in Figure 4.9 allows for a qualitative comparison of the morphology of the anode surface (left column) and the cathode surface (right column). The most significant

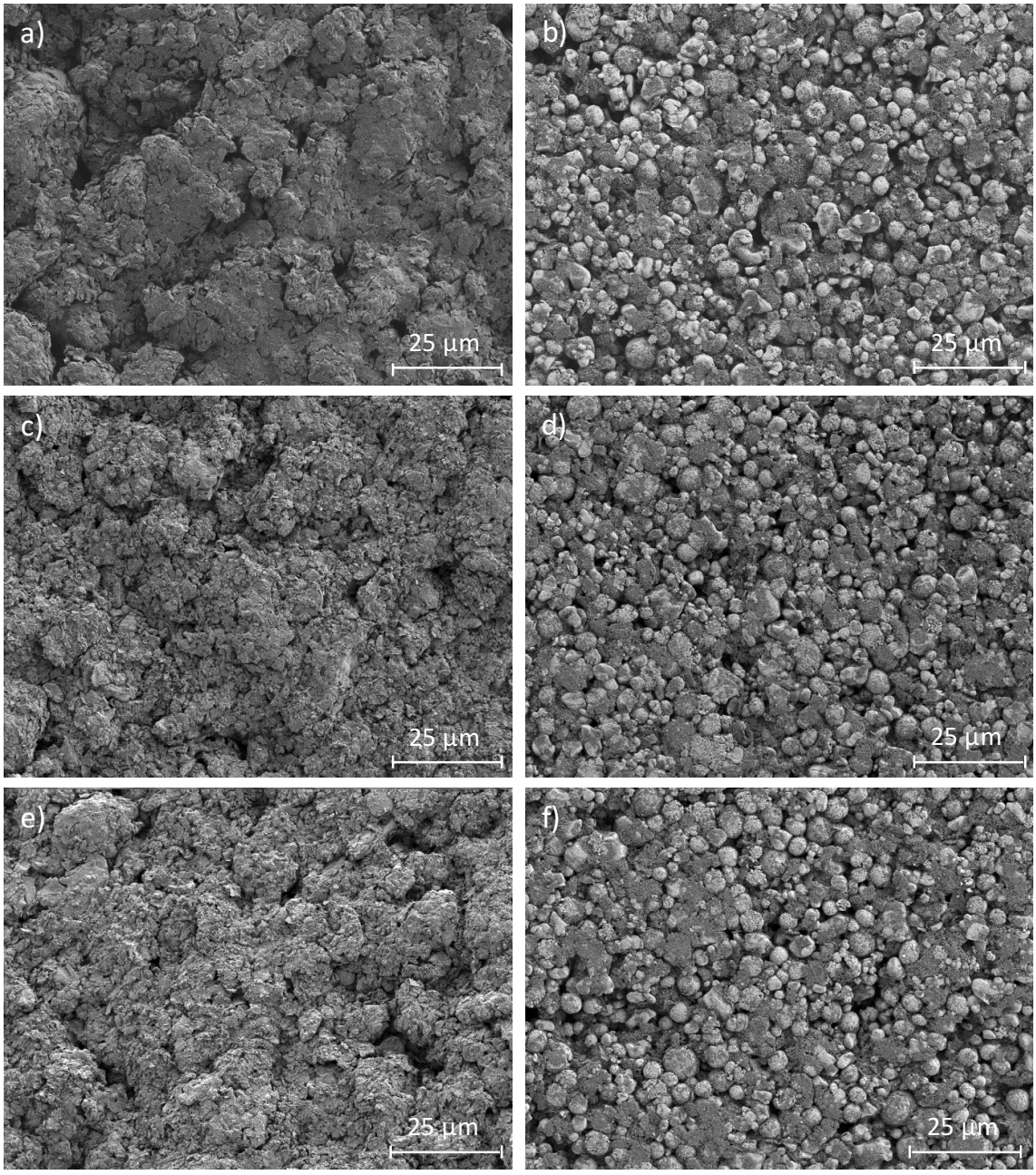

Fig. 4.9 SEM images of anode (left column) and cathode (right column) of cell 0 (a, b), cell 4 after 80 cycles (c, d) and cell II after 80 cycles (e, f).

differences can be observed between the anode surface of the pristine cell and the cycled cells. While the graphite surface of the pristine cell in Figure 4.9, a) appears largely smooth, the surfaces of the cycled cells in Figure 4.9, c) and e) appear to be covered in mossy deposits. EDX analyses were conducted in order to reveal the composition of these deposits. There is no discernible difference between the anode surfaces of the 3-electrode cell 4 and the unmodified cell II.

In contrast to the anode, no significant differences can be observed between the cathode surfaces of the pristine and the cycled cells (Figure 4.9 b), d) and f)). These findings are in line with the estimated degradation signatures; the anodes were expected to be more heavily affected by the low-temperature cycling procedures than the cathodes.

EDX spectra were recorded on anode and cathode samples of the pristine cell 0, the 3-electrode cell 1 and the unmodified cell I after 120 cycles, and on samples of the 3-electrode cell 4 and the unmodified cell II after 80 cycles. The results are illustrated with colour maps for visual indication of the identified elements, and with tables summarizing the weight percentages (wt.%) of the identified elements.

The EDX colour map of a pristine anode sample (cell 0) in Figure 4.10 shows a surface mainly consisting of pure carbon, illustrated in red. It should be pointed out that the pristine cell was purchased as a commercial product, which would have undergone the typical SEI formation procedure, consisting of a number of formation cycles. The SEI is most likely too thin to be detected by EDX. The NE surfaces of cell 4 and cell II in Figures 4.11 and 4.12 appear to be largely covered in oxygen-rich deposits, illustrated in cyan. Some uncoated or moderately coated carbon appears in red in Figures 4.11 and 4.12. A very similar picture was obtained for cells 1 and I, illustrated in Figures A.1 and A.2 of appendix A.1, with carbon illustrated in red and oxygen rich deposits in green.

The weight percentages of the elements detected on the anode samples of the pristine and cycled cells are listed in Table 4.5. The quantitative results for the

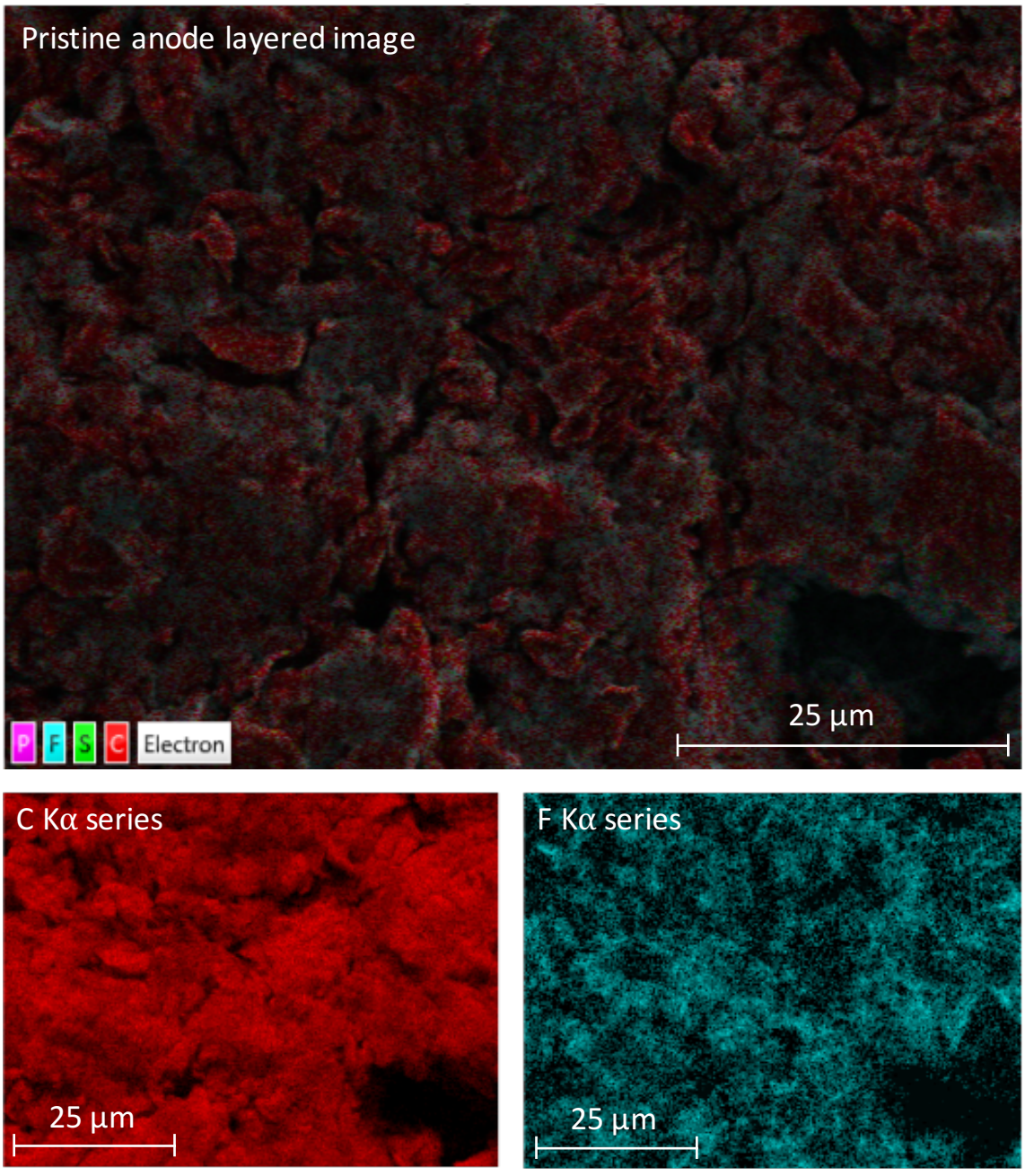

Fig. 4.10 EDX, pristine anode; layered image (top) and Kα series of C and F (bottom).

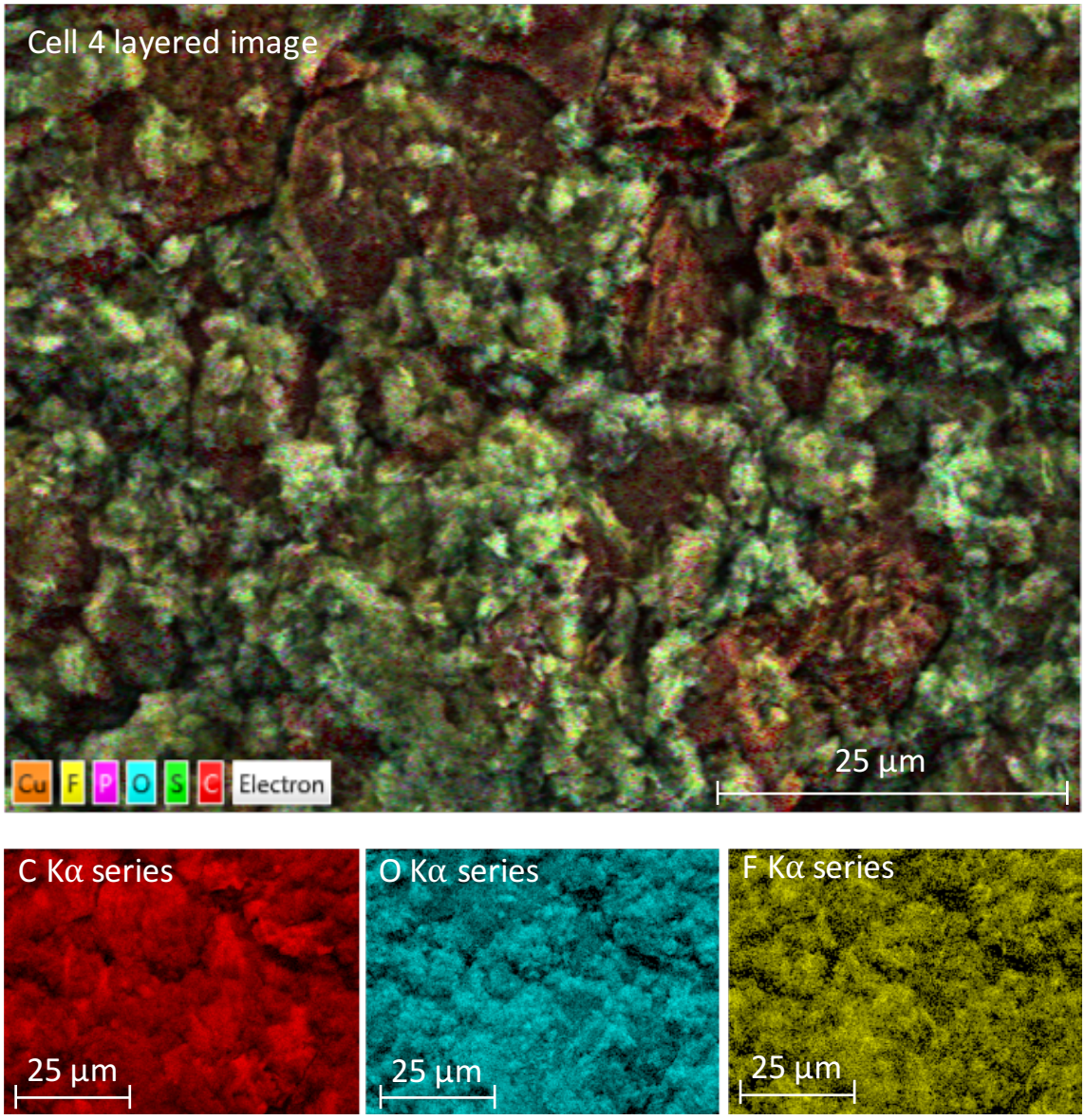

Fig. 4.11 EDX, cell 4 anode; layered image (top) and Kα series of C, O and F (bottom).

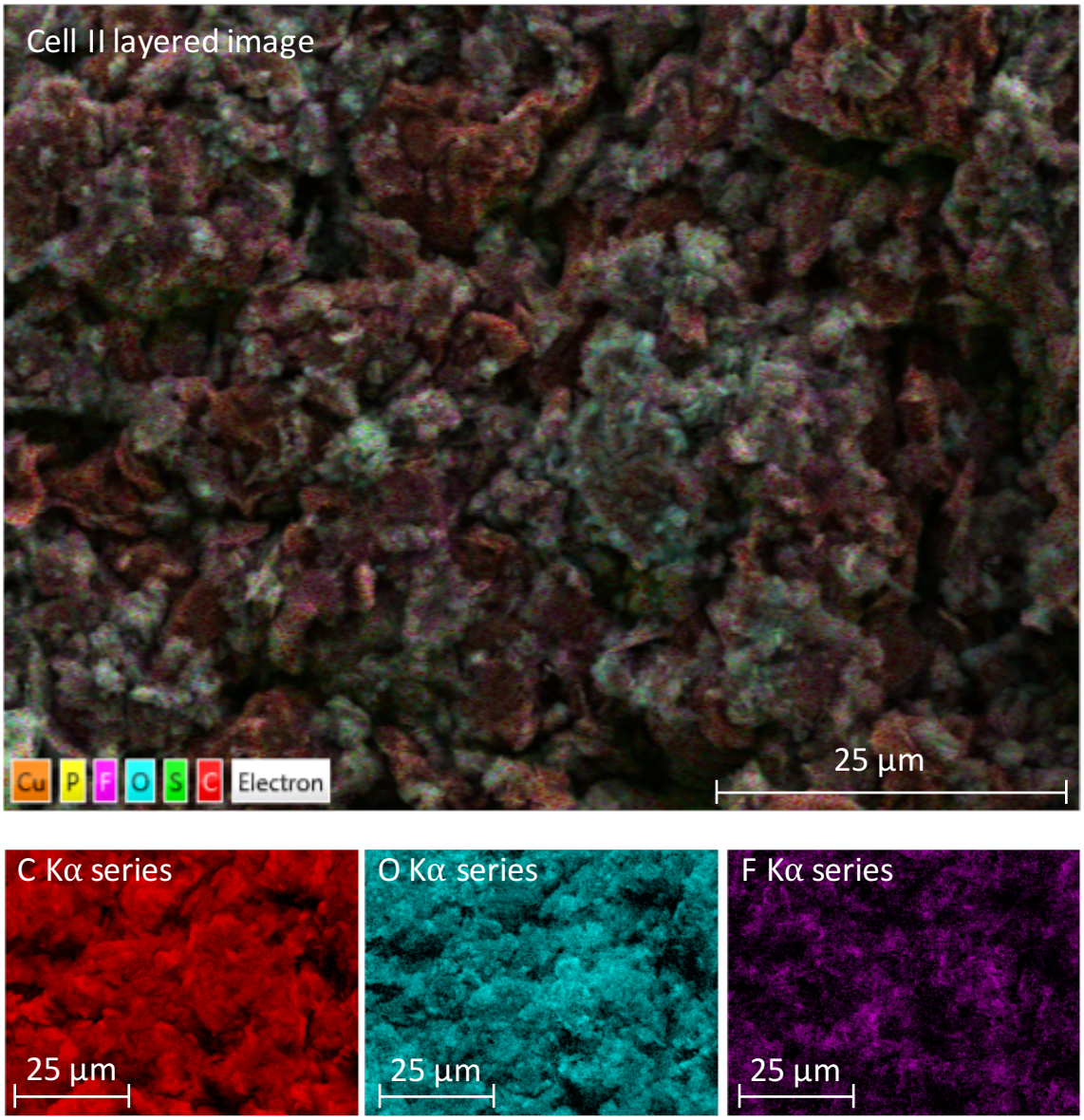

Fig. 4.12 EDX, cell II anode; layered image (top) and Kα series of C, O and F (bottom).

pristine anode reveal that no oxygen was detected. In case of the cycled cells, however, significant amounts of oxygen, on the order of 25 wt.%, were found on all cycled anodes. Moreover, the fraction of fluorine decreased from roughly 11% detected on the pristine anode, to 5-7% on the cycled anodes. Fluorine forms part of the electrolyte in most commercial cells. It is well documented in the literature that electrolyte solvents and additives are reduced at the graphite surface to form carbonates [25, 133]. In this study the NE potential of the test subjects was frequently pushed below zero, which may have accelerated the rate of solvent and/or additive reduction at the NE, leading to increased formation of surface films. Another possible origin of the surface films could be from metallic lithium irreversibly deposited on the anodes during low-temperature charging. Lithium is too light to be detected with standard EDX methods. However, the transfer of the anode samples in air may have led to oxidation of the metallic lithium. Moreover, the rinsing of the electrodes with DMC may have affected any metallic lithium on the electrode surface. The surface deposits observed on the NE of the cycled cells are unlikely to be typical SEI, since a SEI was already present on the pristine cell and could not be detected by EDX. Similar weight percentages of carbon and oxygen found on the anodes of the 3-electrode cells and of the unmodified cells suggest that the NE of both cells experienced the same mode of degradation.

Table 4.5 Weight % of carbon, oxygen, fluorine and sulfur in anodes.

Cell ID	**C**	**O**	**F**	**S**
Cell 0	88.3%	0.0 %	10.9 %	0.5 %
Cell 1	67.5%	25.8 %	5.2 %	1.1 %
Cell I	68.2 %	25.3 %	4.9 %	1.1 %
Cell 4	65.0 %	26.6 %	6.7 %	1.2 %
Cell II	66.8 %	24.9 %	7.0 %	0.8 %

The EDX colour maps of the cathodes are shown in Figure 4.13 for the pristine cell and in Figures 4.14 and 4.15 for the cycled cells. Cobalt is illustrated in cyan in Figure 4.13 and magenta in Figures 4.14 and 4.15. Nickel is in yellow and carbon,

typically used to enhance electrical conductivity in cathode materials, in red. Oxygen contained in both cobalt and nickel oxide appears in green. Unlike in the case of the anodes, there are no obvious differences in the EDX colour maps between the cathodes of the pristine cell and those of the cycled cells. The same is true for the EDX colour maps of the cathodes of cells 1 and I, illustrated in Figures A.3 and A.4 in Appendix A.1.

The quantitative results, listed in terms of wt.% in Table 4.6, do not show any significant differences in cathode composition either. The results obtained from the diagnostic algorithm indicated small amounts of LAM_{PE}. These losses of active material could be due to particle cracking resulting from thermal cycling, which may not be possible to detect with SEM and EDX. Another possible reason for LAM_{PE} could be electrical contact loss between particles of active material, active material and carbon particles or between active material and current collector. If the PE did indeed suffer from mechanical damage, it would have to be due to cracks too small to be detected by the SEM analysis presented above. The formation of surface films, too thin to detect with EDX, could also account for LAM_{PE}. Surface films on LCO and NCO materials can reportedly consist of carbonates as well as polymers and polycarbonates [134] and may block active sites on the cathode material.

Table 4.6 Weight % of cobalt, nickel, carbon, oxygen and fluorine in cathodes.

Cell ID	**Co**	**Ni**	**C**	**O**	**F**
Cell 0	19.4 %	11.4 %	41.0 %	20.4 %	6.9 %
Cell 1	23.1 %	10.6 %	38.3 %	21.1 %	6.2 %
Cell I	21.4 %	15.3 %	37.0 %	21.0 %	4.6 %
Cell 4	23.5 %	16.4 %	33.1 %	21.0 %	5.3 %
Cell II	19.0 %	13.5 %	40.1 %	20.4 %	6.9 %

Overall, the SEM and EDX results revealed a clear change in surface morphology and composition of the anodes of the cycled cells. These findings support the results obtained from the diagnostic algorithm, which identified LAM_{NE} as the primary source of degradation in the low-temperature tests. No physical reason for the loss

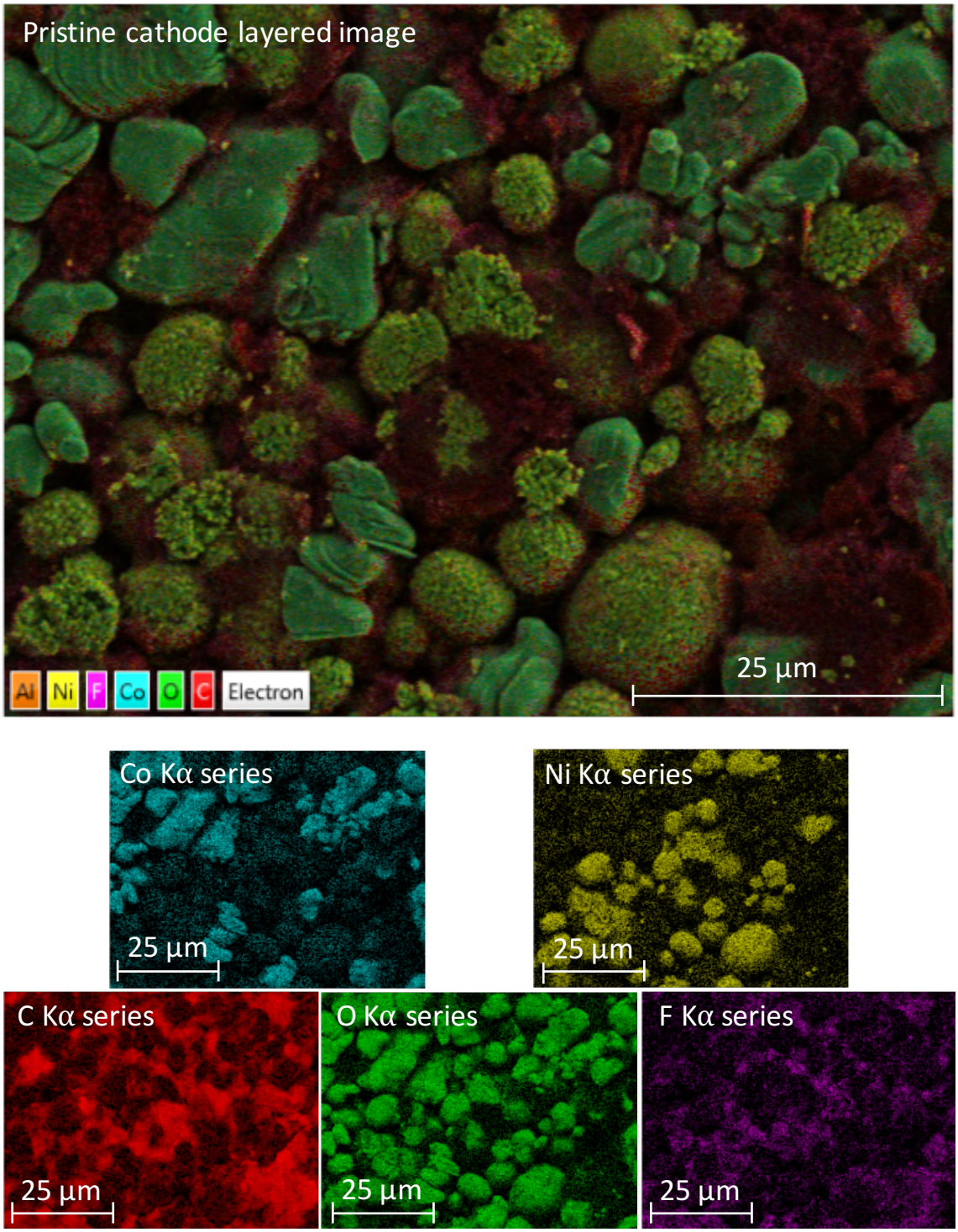

Fig. 4.13 EDX, pristine cathode; layered image (top) and Kα series of Co, Ni, C, O and F (bottom).

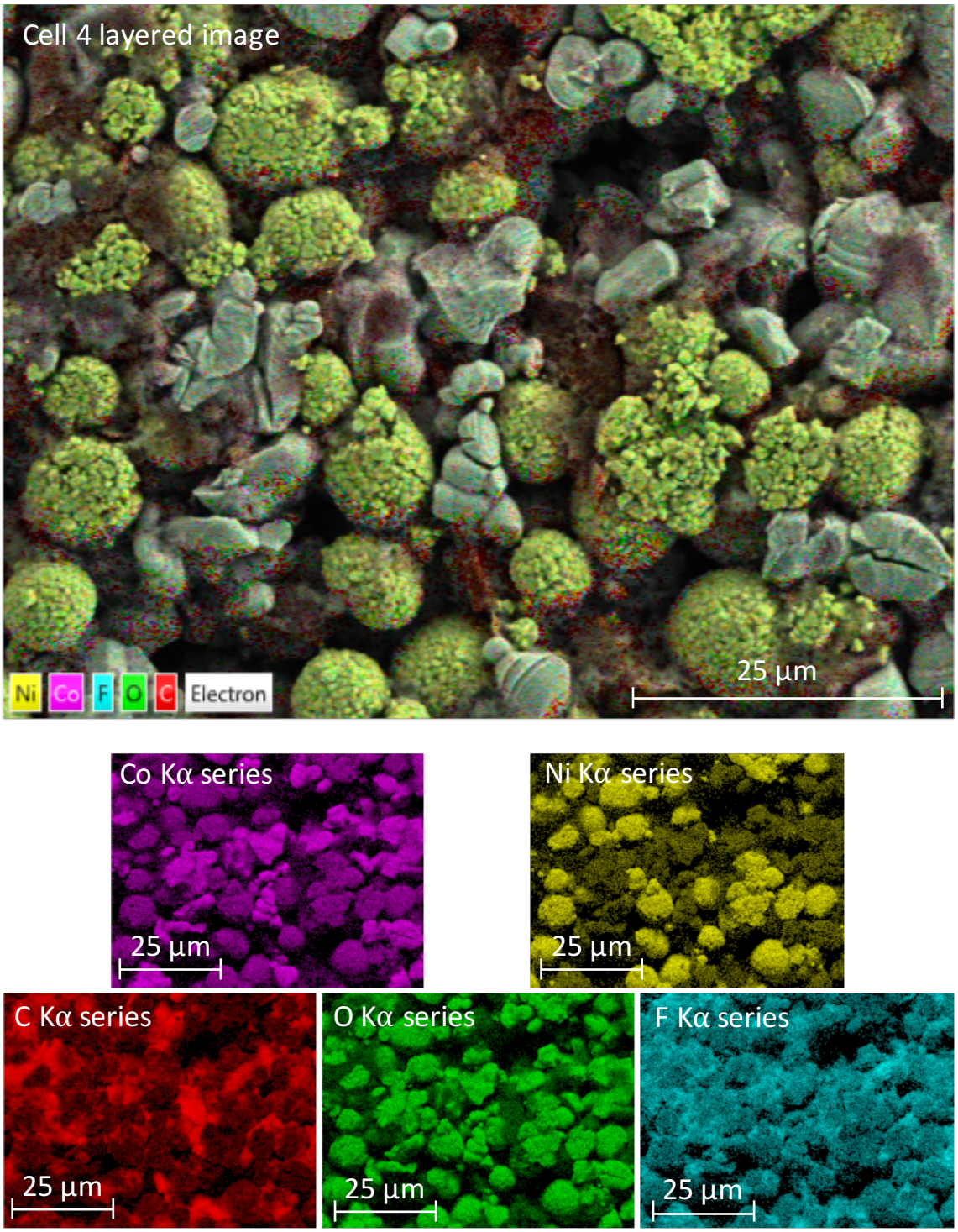

Fig. 4.14 EDX, cell 4 cathode; layered image (top) and Kα series of Co, Ni, C, O and F (bottom).

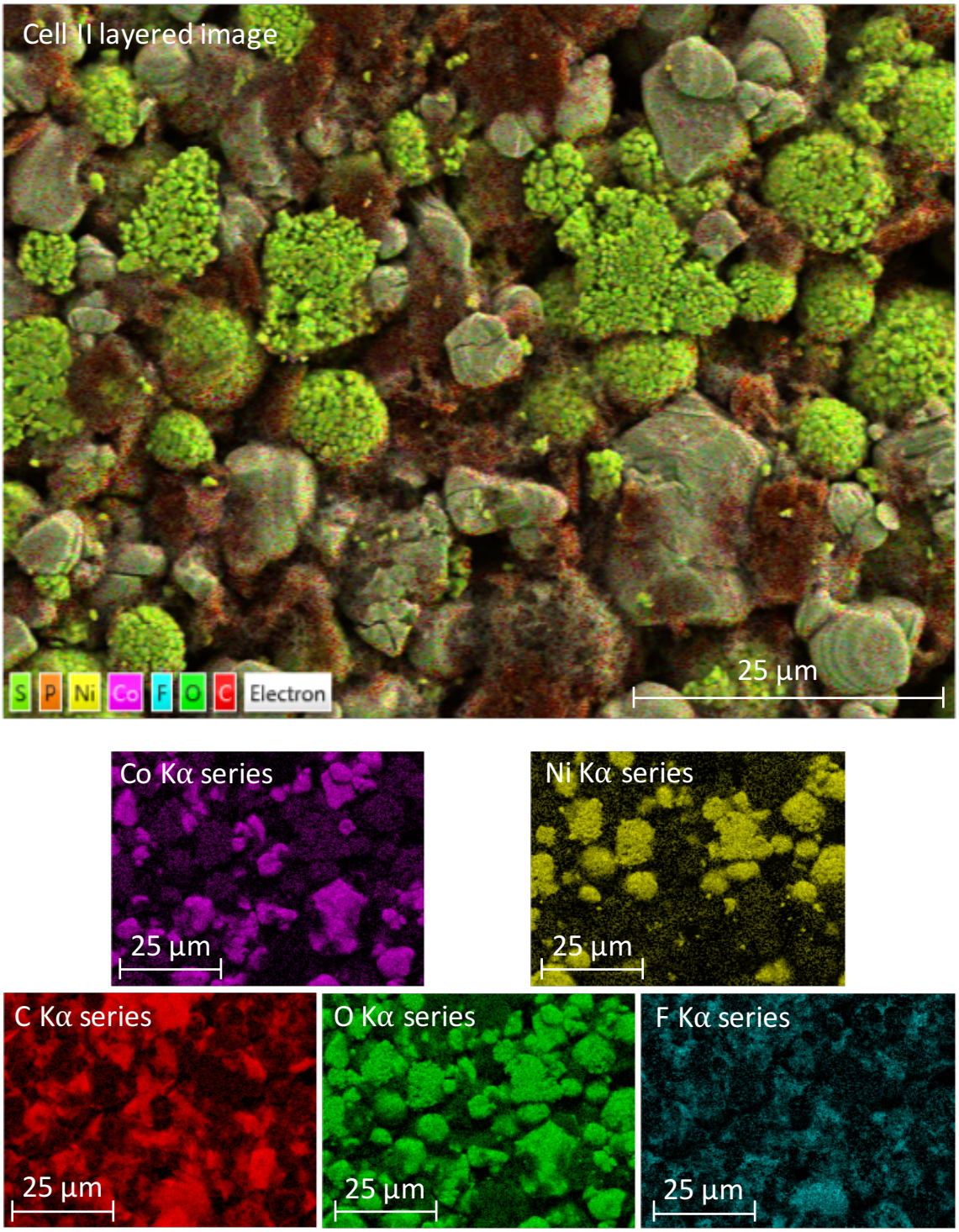

Fig. 4.15 EDX, cell II cathode; layered image (top) and Kα series of Co, Ni, C, O and F (bottom).

of active cathode material was found using SEM and EDX. There was no discernible difference in degradation between the 3-electrode cells and the unmodified cells, suggesting that the modification does not affect the cells' performance and cycle life.

It should be emphasized that the SEM and EDX analyses were merely conducted as complementary, qualitative analyses and are not suitable to draw definite conclusions about the exact degradation mechanisms that acted on the electrodes. Moreover, a recent study demonstrated that pre-analysis washing of graphite electrode surfaces can affect surface films [135], which is another reason for caution when interpreting the presented SEM and EDX results.

4.5 Conclusions

3-electrode cells and unmodified cells were exposed to extreme cycling conditions with charge and discharge rates of 2 C and an ambient temperature of $-10\,^{\circ}\mathrm{C}$. The harsh conditions pushed the NE potential below 0 V for every charging step. This favoured lithium plating on the graphite anodes and rapid rates of anode degradation were expected. The diagnostic algorithm developed in Chapter 3 was applied to estimate the degradation signatures experienced by the tested cells.

The results showed good agreement between the OCVs modelled by the diagnostic algorithm and the pseudo-OCVs measured for the 3-electrode cells. A baseline scenario was introduced where the measured pseudo-OCVs were fitted directly in order to minimize effects of fitting errors on estimates of degradation signatures. The degradation signatures produced by the baseline scenario and by the diagnostic algorithm were in close agreement, suggesting that the OCV model identified on the pristine cells remains valid for the whole cycle life of the cells and that degradation signatures can be estimated simply by fitting the measured pseudo-OCV of the full cell.

As expected, LAM_{NE} was identified by the diagnostic algorithm as the primary degradation signature for all cells. SEM and EDX results supported this finding by revealing oxygen-rich deposits on the anodes of the cycled cells, which were not present on the anode of a pristine cell.

The comparison of electrical test results and post-mortem results of the 3-electrode cells and the unmodified cells demonstrated that the insertion of the reference electrode into the pouch cells did not noticeably alter the degradation of the modified cells.

Although it was not possible, with the applied methods, to uniquely observe lithium plating, it was demonstrated that the diagnostic algorithm can identify early indicators which may lead to lithium plating, such as rapid or excessive LAM_{NE}, which pose a substantial safety hazard.

Chapter 5

Degradation diagnostics for automotive applications

5.1 Introduction

In this chapter, the OCV model developed in Chapter 2 is used in conjunction with the diagnostic algorithm, presented in Chapter 3, to identify and track the degradation signatures of eight 740 mAh Kokam pouch cells throughout their cycle lives. The cells were cycled under the Artemis Drive Cycle [136] until failure or until at least 20% of their original capacity was lost. Unlike the 3-electrode cells used in Chapter 4, the cells used for this study were not modified.

The purpose of the work presented in this chapter is to demonstrate the viability of the diagnostic algorithm for the case of unmodified Li-ion cells used under simulated electric vehicle conditions. Moreover, a method for the prediction of end-of-life is proposed, based on the outputs of the diagnostic algorithm. These objectives are in line with the original motivations for the diagnostic algorithm, presented in Chapter 3:

1. Safety: Identification of potentially dangerous scenarios such as lithium plating (internal short-circuits) and excessive positive electrode potentials.

2. Identification of electrode-specific modes of degradation and cell failure.

3. Assessment and comparison of cell quality and quality spread within a cell batch.

4. Prediction of cell failure.

The first and second objectives have been the subject of chapters 3 and 4 and will be addressed in this chapter in the context of a larger batch of unmodified cells.

The third objective is particularly relevant for multi-cell systems, where the spread in quality and lifetime among identical cells is a critical design parameter. Battery models used in conventional systems typically assume uniform degradation across identical cells exposed to the same operating conditions. The same is true for many advanced bottom-up physics-based degradation models, which assume uniform cell properties among identical cells and use environmental and operating conditions as model inputs to calculate degradation. The validity of these assumptions is tested by an analysis of the different modes of degradation and failure in a collection of eight identical cells presented in this chapter.

The final objective is the prediction of cell failure, which is extremely important for commercial multi-cell systems and poses a formidable challenge for any system designer. To date and to the best of the author's knowledge, there exists no satisfactory and reliable method to predict the end-of-life of Li-ion cells. The final section of this chapter explores the merits of using estimated degradation signatures to predict cell failure.

5.2 Experimental

Two types of cell tests were conducted for this chapter: (i) low rate, constant current (CC) charge and discharge cycles on positive and negative electrode half-cells to parameterise the OCV model and (ii) long-term term cycling tests on eight commercial (unmodified) Kokam 740 mAh pouch cells consisting of drive cycles and frequent characterisation cycles. The test procedures for both half-cells and full cells are described in detail in the following two sections.

5.2.1 Half-cell test procedures

Two half-cells—one negative electrode and one positive electrode half-cell—were made from electrode sheets harvested from a pristine Kokam 740 mAh pouch cell following the same manufacturing procedure as detailed in Section 2.2.1. The electrode disks used for the half-cells were 15 mm in diameter.

The half-cells were cycled at a rate of C/18.5—the same rate as used for the characterisation cycles of the pouch cells. Given a measured active electrode surface area of 600 cm^2 and a nominal capacity of 740 mAh, the nominal current density of the pouch cells is 1.233 mA/cm^2. Assuming the same nominal current density for the coin cells with a diameter of 15 mm (surface area of 1.767 cm^2), a C-rate of C/18.5 for the coin cells is equivalent to 0.118 mA. The half-cells tests were conducted inside a Vötsch thermal chamber at 40 °C using a Bio-Logic SP150 potentiostat.

The cycling procedure for the half-cells consists of two CC cycles at 0.118 mA. Voltage measurements were recorded every 1 min or 1 mV change. The second cycle was used for the parameterisation of the OCV model.

5.2.2 Full-cell test procedures

The objective of the cell tests was to age eight commercial, identical cells under identical and realistic electric vehicle driving conditions, while recording frequent

characterisation cycles. For this purpose, the cells were exposed to a dynamic driving profile—the Artemis urban drive cycle [136]—and characterization cycles, consisting of low rate CC charge and discharge cycles, repeated every 100 cycles. The voltage measurements recorded during the characterisation cycles are used as inputs for the diagnostic algorithm. The drive cycle consists of a time series of current values with 1 s intervals. Based on the speed profile of the Artemis drive cycle [136], the current values were calculated using a simplified vehicle model and scaled to a maximal current of 5 A, as described in Appendix B.1. The drive cycle consists of discharge and charge (emulating regenerative braking) periods and is meant to represent urban driving of an electric vehicle. The cells were located in a Binder thermal chamber, set to a constant temperature of 40 °C during the entire experiment. An elevated test temperature was chosen in order to speed up the ageing process of the cells. An 8-channel Bio-Logic MPG-205 battery tester was used to record all data. The pouch cells were mounted on custom cell holders, which are described in Appendix B.2.

The cycling procedure is comprised of CC charging at a rate of 2 C (1480 mA) and the Artemis drive cycle, with an average discharge current of 1.36 A. Voltage measurements were recorded every 1 s. The cycling portion of the test is repeated 100 times, followed by a characterisation cycle. The characterisation procedure consists of CC charge and discharge cycles at C/18.5 (40 mA), repeated every 100 drive cycles. Voltage measurements were recorded every 1 min. The characterisation cycle is preceded by a C/10 (74 mA) charge, followed by an 8 h rest. The cycling and characterisation procedures are detailed in Table 5.1.

The drive cycles and characterisation cycles are repeated until the lower voltage limit of the cell is reached during discharge, which indicates the cell's end-of-life. The lower voltage limit is set to 2.7 V for continuous discharge (over a period of > 10 s) or 0 V for any measurable period of time. The lower voltage limit is reached in aged cells because of increased internal resistance, which is a result of degradation.

Table 5.1 Cell test procedures.

Test	Step	Current	Stop-criterion
Characterisation	CC charge	74 mA	V > 4.2 V
	Rest	0 mA	t > 8 h
	CC discharge	40 mA	V < 2.7 V
	CC charge	40 mA	V > 4.2 V
Cycling	CC charge	1480 mA	V > 4.2 V
	Artemis discharge	variable	t > 52 min

5.3 Data processing

In Chapters 3 and 4, LLI, $\mathrm{LAM_{PE}}$ and $\mathrm{LAM_{NE}}$ are estimated by minimising the RMSE on the modelled pseudo-OCV, using a global optimisation algorithm. The estimation results are validated against known amounts of LLI, $\mathrm{LAM_{PE}}$ and $\mathrm{LAM_{NE}}$ (Chapter 3) or against measured electrode potentials (Chapter 4). In the work presented in this chapter, the cells are unmodified (no reference electrode) and the extents of lithium and active material loss unknown. It is therefore crucial to calculate the uncertainties associated with the estimated model parameters, which is not possible using constrained global optimisation techniques. In order to overcome this challenge, a Bayesian approach is taken, whereby the parameter estimates are calculated as the mean of a posterior probability distribution. This enables the quantification of the uncertainties associated with the estimated model parameters, accounts for probabilities of parameters beyond the global optimum and gives information about how informative the data are.

In order to facilitate a Bayesian approach, the number of parameters is reduced by directly estimating the OCV of the PE at the end of charge ($\hat{E}^{\mathrm{OC}}_{\mathrm{PE,EoC}}$) and end of discharge ($\hat{E}^{\mathrm{OC}}_{\mathrm{PE,EoD}}$). The degradation signatures LLI_i, $\mathrm{LAM_{PE},}_i$ and $\mathrm{LAM_{NE},}_i$ are estimated at each characterisation cycle i. Figure 5.1 gives an example of the characterisation cycles recorded on cell A8. LLI_i, $\mathrm{LAM_{PE},}_i$ and $\mathrm{LAM_{NE},}_i$ can be

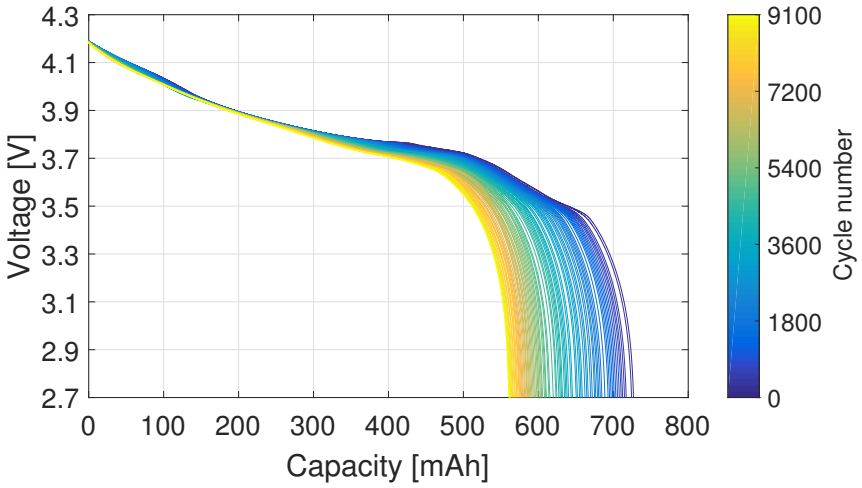

Fig. 5.1 Pseudo-OCV discharge curves of cell A8.

expressed as

$$\mathrm{LLI}_i = 1 - \Delta x_{\mathrm{Cell},i} - \frac{x_{\mathrm{NE,EoD},0} - x_{\mathrm{NE,EoD},i}}{\Delta x_{\mathrm{NE},0}} + \frac{x_{\mathrm{PE,EoC},0} - x_{\mathrm{PE,EoC},i}}{\Delta x_{\mathrm{PE},0}} \tag{5.1}$$

$$\mathrm{LAM}_{\mathrm{PE},i} = \frac{x_{\mathrm{PE,EoD},i} - x_{\mathrm{PE,EoC},0}}{\Delta x_{\mathrm{PE},0}} \tag{5.2}$$

$$\mathrm{LAM}_{\mathrm{NE},i} = \frac{x_{\mathrm{NE,EoC},0} - x_{\mathrm{NE,EoC},i}}{\Delta x_{\mathrm{NE},0}} \tag{5.3}$$

where

$$\Delta x_{\mathrm{Cell},i} = x_{\mathrm{Cell,EoD},i} - x_{\mathrm{Cell,EoC},i} \tag{5.4}$$

$$\Delta x_{\mathrm{PE},0} = x_{\mathrm{PE,EoD},0} - x_{\mathrm{PE,EoC},0} \tag{5.5}$$

$$\Delta x_{\mathrm{NE},0} = x_{\mathrm{NE,EoD},0} - x_{\mathrm{NE,EoC},0}. \tag{5.6}$$

$x_{\mathrm{Cell,EoD}}$ and $x_{\mathrm{Cell,EoC}}$ are the normalised cell capacity at the end of discharge and end of charge, respectively. Index 0 indicates the value was measured during the first characterisation cycle (*i.e.* on a pristine cell) and index i indicates the value was measured during characterisation cycle i. Equivalently, $x_{\mathrm{PE,EoD}}$, $x_{\mathrm{PE,EoC}}$, $x_{\mathrm{NE,EoD}}$ and $x_{\mathrm{NE,EoC}}$ are the normalised capacities of the positive and negative electrode at

EoD and EoC, respectively. In Section 2.3.3, the OCV model was developed based on the equations 2.10 and 2.11. The number of phase transitions $N = 5$ for both the PE and the NE, as described in Chapters 3 and 4. The OCV model parameters were estimated for every cell following the procedure reported in Section 2.3.3. For a more detailed description of the OCV model and parameter estimation procedure, please refer to Chapter 2. The OCV of the cell is limited by the upper and lower cut-off voltages

$$E^{\mathrm{OC}}_{\mathrm{Cell,EoC}} = 4.2\,\mathrm{V} \tag{5.7}$$

$$E^{\mathrm{OC}}_{\mathrm{Cell,EoD}} = 2.7\,\mathrm{V}, \tag{5.8}$$

which are given by the manufacturer's cell specifications (see Figure B.3 in Appendix B.3). The OCV of the cell is calculated from the OCV of the electrodes

$$E^{\mathrm{OC}}_{\mathrm{Cell}} = E^{\mathrm{OC}}_{\mathrm{PE}} - E^{\mathrm{OC}}_{\mathrm{NE}}. \tag{5.9}$$

From Equation 5.7 to 5.9 it follows that

$$E^{\mathrm{OC}}_{\mathrm{NE,EoC}} = E^{\mathrm{OC}}_{\mathrm{PE,EoC}} - 4.2\,\mathrm{V} \tag{5.10}$$

$$E^{\mathrm{OC}}_{\mathrm{NE,EoD}} = E^{\mathrm{OC}}_{\mathrm{PE,EoD}} - 2.7\,\mathrm{V}. \tag{5.11}$$

Using Equations 5.10 and 5.11, the normalised capacity of both the positive and negative electrode can be calculated with Equations 2.10 and 2.11, which in turn enables the calculation of LLI, $\mathrm{LAM_{PE}}$ and $\mathrm{LAM_{NE}}$ through Equations 5.1 to 5.3. The only inputs that are required are $E^{\mathrm{OC}}_{\mathrm{PE,EoC}}$ and $E^{\mathrm{OC}}_{\mathrm{PE,EoD}}$. The estimation of parameters $\hat{E}^{\mathrm{OC}}_{\mathrm{PE,EoC}}$ and $\hat{E}^{\mathrm{OC}}_{\mathrm{PE,EoD}}$ is described as follows.

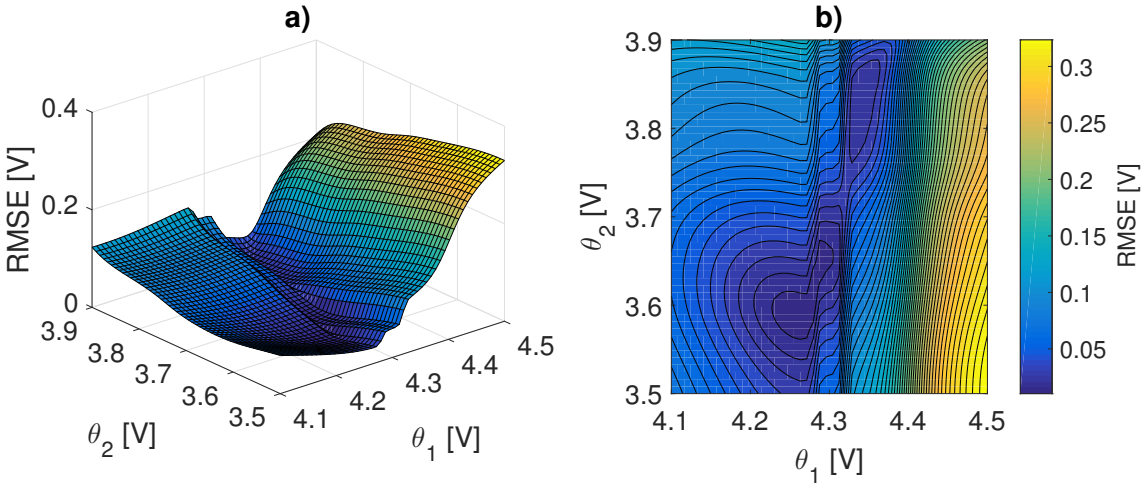

Fig. 5.2 RMSE of modelled cell OCV of cell A1; a) surface plot, b) contour plot.

5.3.1 A Bayesian approach to parameter estimation

In this section, the model parameters $\hat{E}^{\mathrm{OC}}_{\mathrm{PE,EoC}}$ and $\hat{E}^{\mathrm{OC}}_{\mathrm{PE,EoD}}$ are referred to as $\boldsymbol{\theta} = \{\theta_1, \theta_2\}$. In Chapters 3 and 4, the RMSE between the measured and modelled cell voltage was used as the cost function for parameter estimation. Figure 5.2 illustrates the RMSE of cell A1 at the first characterisation cycle, over the parameters θ_1 and θ_2, which features multiple local minima. Standard global optimisation would only account for the single global minimum in RMSE, whereas a Bayesian approach accounts for the entire distribution of the cost function over the parameter space.

The parameters $\boldsymbol{\theta}$ are estimated by finding the mean of the posterior probability distribution of $\boldsymbol{\theta}$, given the data $\mathbf{Y} = \{y_1, ..., y_N\}$. The data is comprised of N pseudo-OCV measurements recorded during a characterisation cycle. The posterior probability distribution is given by Bayes' theorem [137, p. 21-30]

$$p(\boldsymbol{\theta}|\mathbf{Y}) = \frac{p(\mathbf{Y}|\boldsymbol{\theta})\, p(\boldsymbol{\theta})}{p(\mathbf{Y})} \tag{5.12}$$

where $p(\mathbf{Y}|\boldsymbol{\theta})$ is the likelihood function, which expresses how probable the data are given the parameters $\boldsymbol{\theta}$, $p(\boldsymbol{\theta})$ is the prior probability distribution of the model parameters and $p(\mathbf{Y})$ is the normalisation constant or evidence, which can be

expressed in terms of the likelihood function and the prior probability distribution as

$$p(\mathbf{Y}) = \int p(\mathbf{Y}|\boldsymbol{\theta})\, p(\boldsymbol{\theta})\, \mathrm{d}\boldsymbol{\theta}. \tag{5.13}$$

A Gaussian distribution is assumed as the basis for the likelihood function. A Gaussian distribution, where each datum y_i is independent and identically distributed, is defined by

$$\mathcal{N}(y_i|\mu, \sigma^2) = \frac{1}{(2\pi\sigma^2)^{1/2}} \quad \exp\left\{-\frac{(y_i - \mu)^2}{2\sigma^2}\right\} \tag{5.14}$$

where μ is the mean and σ^2 the variance. The Gaussian probability distribution of a data set $\mathbf{Y}$ given mean μ and variance σ^2 of the data can be written as

$$p(\mathbf{Y}|\mu, \sigma^2) = \prod_{i=1}^{N} \mathcal{N}(y_i|\mu, \sigma^2) \tag{5.15}$$

which is also referred to as the likelihood function of the Gaussian. The product of a large number of data points with small probabilities can lead to numerical issues if the result underflows the computer precision. This issue can be avoided by computing the log of the likelihood, where the probabilities of the data set are summed. Based on Equations 5.14 and 5.15, the log likelihood of the dataset $\mathbf{Y}$ can be written as

$$\ln p(\mathbf{Y}|\mu, \sigma^2) = -\frac{1}{2\sigma^2}\sum_{i=1}^{N}(y_i - \mu)^2 - \frac{N}{2}\ln \sigma^2 - \frac{N}{2}\ln (2\pi). \tag{5.16}$$

The log likelihood of a dataset $\mathbf{Y}$, given a model with parameters $\boldsymbol{\theta}$, can be computed by substituting μ for the OCV model output $\hat{y}_i(\boldsymbol{\theta})$

$$\ln p(\mathbf{Y}|\boldsymbol{\theta}) = -\frac{1}{2\sigma^2}\sum_{i=1}^{N}(y_i - \hat{y}_i(\boldsymbol{\theta}))^2 - \frac{N}{2}\ln \sigma^2 - \frac{N}{2}\ln (2\pi). \tag{5.17}$$

The OCV model output, $\hat{y}_i(\boldsymbol{\theta})$, is given by Equation 5.9, where $E_{\mathrm{PE}}^{\mathrm{OC}}$ and $E_{\mathrm{NE}}^{\mathrm{OC}}$ are obtained from the numerical solution of Equations 2.10 and 2.11. Using Equations

5.10 and 5.11 to compute $E^{\mathrm{OC}}_{NE,EoC}$ and $E^{\mathrm{OC}}_{NE,EoD}$, only $\boldsymbol{\theta}$ is required as input to calculate $\hat{y}_i(\boldsymbol{\theta})$.

When converting back from log likelihood to likelihood, large numbers of $\ln p(\mathbf{Y}|\boldsymbol{\theta})$ can cause overflow issues, which are avoided by bounding $\ln p(\mathbf{Y}|\boldsymbol{\theta})$ with 0. This is achieved by finding the maximum of the log likelihood, η, which is subtracted from $\ln p(\mathbf{Y}|\boldsymbol{\theta})$ to give a function

$$f(\boldsymbol{\theta}) = \ln p(\mathbf{Y}|\boldsymbol{\theta}) - \eta \tag{5.18}$$

and

$$p(\mathbf{Y}|\boldsymbol{\theta}) = \exp(f(\boldsymbol{\theta}))\exp(\eta). \tag{5.19}$$

Given the lack of knowledge about the prior distribution of parameters $\boldsymbol{\theta}$, $p(\boldsymbol{\theta})$ is assumed to be uniform over the parameter space, defined by

$$p(\boldsymbol{\theta}) = \begin{cases} \frac{1}{(\boldsymbol{\theta}_h - \boldsymbol{\theta}_l)^2}, & \text{if } \boldsymbol{\theta} \in [\boldsymbol{\theta}_h, \boldsymbol{\theta}_l)] \\ 0, & \text{otherwise} \end{cases} \tag{5.20}$$

where $\boldsymbol{\theta}_h$ and $\boldsymbol{\theta}_l$ are the upper and lower limits of $\boldsymbol{\theta}$, respectively.

Inserting Equation 5.19 into Equation 5.13, the posterior probability distribution $p(\boldsymbol{\theta}|\mathbf{Y})$ can be written as

$$p(\boldsymbol{\theta}|\mathbf{Y}) = \frac{\exp(f(\boldsymbol{\theta}))\, p(\boldsymbol{\theta})}{\int \exp(f(\boldsymbol{\theta}))\, p(\boldsymbol{\theta})\, \mathrm{d}\boldsymbol{\theta}}. \tag{5.21}$$

The model parameters are computed as the mean of the posterior probability distribution by

$$m(\boldsymbol{\theta}) = \frac{\int \boldsymbol{\theta}\, p(\mathbf{Y}|\boldsymbol{\theta})\, p(\boldsymbol{\theta})\, \mathrm{d}\boldsymbol{\theta}}{\int p(\mathbf{Y}|\boldsymbol{\theta})\, p(\boldsymbol{\theta})\, \mathrm{d}\boldsymbol{\theta}}. \tag{5.22}$$

Inserting Equation 5.19 into Equation 5.22 yields

$$m(\boldsymbol{\theta}) = \frac{\int \boldsymbol{\theta} \exp(f(\boldsymbol{\theta}))\, p(\boldsymbol{\theta})\, \mathrm{d}\boldsymbol{\theta}}{\int \exp(f(\boldsymbol{\theta}))\, p(\boldsymbol{\theta})\, \mathrm{d}\boldsymbol{\theta}}. \tag{5.23}$$

The variance of the parameters is calculated as the variance of the posterior probability distribution by

$$s^2(\boldsymbol{\theta}) = \frac{\int (\boldsymbol{\theta} - m(\boldsymbol{\theta}))^2\, p(\mathbf{Y}|\boldsymbol{\theta})\, p(\boldsymbol{\theta})\, \mathrm{d}\boldsymbol{\theta}}{\int p(\mathbf{Y}|\boldsymbol{\theta})\, p(\boldsymbol{\theta})\, \mathrm{d}\boldsymbol{\theta}}. \tag{5.24}$$

Inserting Equation 5.19 into Equation 5.24 gives

$$s^2(\boldsymbol{\theta}) = \frac{\int (\boldsymbol{\theta} - m(\boldsymbol{\theta}))^2 \exp(f(\boldsymbol{\theta}))\, p(\boldsymbol{\theta})\, \mathrm{d}\boldsymbol{\theta}}{\int \exp(f(\boldsymbol{\theta}))\, p(\boldsymbol{\theta})\, \mathrm{d}\boldsymbol{\theta}}. \tag{5.25}$$

5.3.2 Application of Bayesian parameter estimation

This section demonstrates the application of the above described methodology for parameter estimation using the example of cell A1. In this example, the parameter estimation technique is applied to pseudo-OCV data measured during the cell's first characterisation cycle. The same procedure is applied to all recorded characterisation cycles of all eight Kokam cells, as discussed in Section 5.4.

Log likelihood

Given the large data sets of pseudo-OCV measurements ($N \sim 1000$), it is convenient to compute the log likelihood using Equation 5.17 for the parameters $\boldsymbol{\theta} = \{\theta_1, \theta_2\}$ in the intervals

$$\theta_1 \in [\theta_{1,l}, \theta_{1,h}] \tag{5.26}$$

$$\theta_2 \in [\theta_{2,l}, \theta_{2,h}]. \tag{5.27}$$

where

$$\theta_{1,l} = 4.1\,\mathrm{V} \tag{5.28}$$

$$\theta_{1,h} = 4.5\,\mathrm{V} \tag{5.29}$$

$$\theta_{2,l} = 3.5\,\mathrm{V} \tag{5.30}$$

$$\theta_{2,h} = 3.9\,\mathrm{V} \tag{5.31}$$

The upper bound of θ_1 and the lower bound of θ_2 reflect the voltage limits on the positive electrode. From the results presented in Section 3.4.3 it is evident that the voltage of the positive electrode at the end of charge is normally higher than 4.1 V and the voltage at the end of discharge is normally lower than 3.9 V, even after considerable degradation. These values are therefore selected as the lower bound of θ_1 and the upper bound of θ_2, respectively.

The log likelihood $\ln p(\mathbf{Y}|\boldsymbol{\theta})$ of the pseudo-OCV data of cell A1 is calculated using Equation 5.17. The variance, σ^2, of the data was estimated based on the voltage measurements obtained during five subsequent pseudo-OCV curves recorded on one cell under the same test conditions as applied to all test subjects (T = 40 °C, I = 40 mA). For five pseudo-OCV curves of N voltage measurements, the variance was calculated as the mean variance over N measurements in each pseudo-OCV curve according to

$$\sigma^2 = \frac{1}{N}\sum_{i=1}^{N}\frac{1}{4}\sum_{j=1}^{5}(y_{i,j} - \mu_i)^2 \tag{5.32}$$

where

$$\mu_i = \frac{1}{5}\sum_{j=1}^{5} y_{i,j} \tag{5.33}$$

The variance, σ^2, was estimated to be 17 µV, which is used to compute the log likelihood. $\ln p(\mathbf{Y}|\boldsymbol{\theta})$ is illustrated in Figure 5.3.

The maximum log likelihood η is identified using Matlab's non-linear programming solver fmincon with upper and lower bounds on $\boldsymbol{\theta}$ as specified in Equations 5.26 and

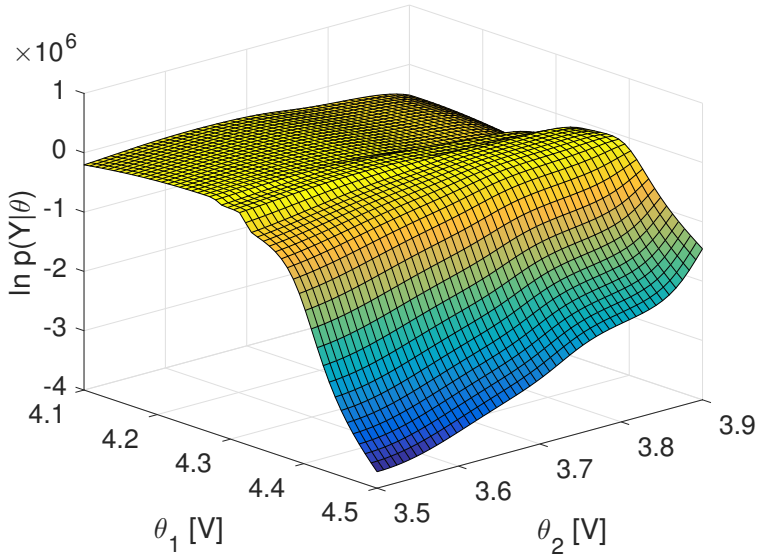

Fig. 5.3 Log likelihood ln $p(\mathbf{Y}|\boldsymbol{\theta})$ of cell A1, first characterisation cycle

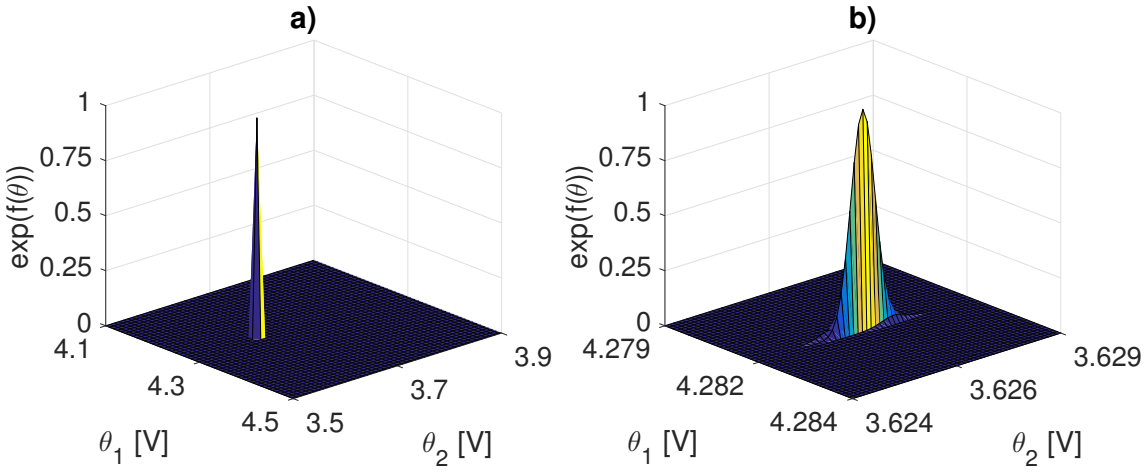

Fig. 5.4 exp($f(\boldsymbol{\theta})$) over a) full range of $\boldsymbol{\theta}$, b) magnified.

5.27. Using η in Equation 5.18 yields the function $f(\boldsymbol{\theta})$, which is upper-bounded by 0 and used to compute the posterior likelihood $p(\boldsymbol{\theta}|\mathbf{Y})$. Figure 5.4 provides plots of exp($f(\boldsymbol{\theta})$) over parameters $\boldsymbol{\theta}$. In Figure 5.4, a), exp($f(\boldsymbol{\theta})$) is plotted over the same parameter range as ln $p(\mathbf{Y}|\boldsymbol{\theta})$ in Figure 5.3, which illustrates the narrow distribution of exp($f(\boldsymbol{\theta})$). In order to better resolve exp($f(\boldsymbol{\theta})$), the distribution is plotted over a narrow window centred on the maximum log likelihood $[\theta_{\eta,1}, \theta_{\eta,2}] \pm 2.5\,\mathrm{mV}$ in Figure 5.4, b).

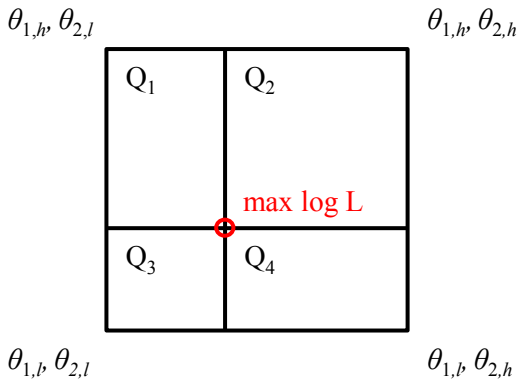

Fig. 5.5 Pattern for double integral over θ_1, θ_2.

Prior probability distribution

The uniform prior probability distribution $p(\boldsymbol{\theta})$ is calculated using Equation 5.20 for

$$\boldsymbol{\theta}_h = [\theta_{1,h}, \theta_{2,h}] \tag{5.34}$$

$$\boldsymbol{\theta}_l = [\theta_{1,l}, \theta_{2,l}] \tag{5.35}$$

Posterior probability distribution

The posterior probability distribution $p(\boldsymbol{\theta}|\mathbf{Y})$ is calculated using Equation 5.21. The integral $\int \exp(f(\boldsymbol{\theta}))\, p(\boldsymbol{\theta})\, \mathrm{d}\boldsymbol{\theta}$ in Equation 5.21 is solved numerically using Matlab's *integral2* solver. The narrow distribution of $\exp(f(\boldsymbol{\theta}))$ can cause numerical issues when computing the integral over θ_1, θ_2. Using the Matlab procedure, these issues can be overcome by splitting up the parameter space into four quadrants, arranged around the location of the maximum log likelihood, η, as illustrated in Figure 5.5. The double integral is solved for each quadrant and the solutions are subsequently summed up. Applying the upper and lower limits of θ_1 and θ_2 to Equation 5.21, the posterior probability distribution can be calculated by

$$p(\boldsymbol{\theta}|\mathbf{Y}) = \frac{\exp(f(\boldsymbol{\theta}))\, p(\boldsymbol{\theta})\, \mathrm{d}\theta_1 \mathrm{d}\theta_2}{\int_{\theta_{1,l}}^{\theta_{1,h}} \int_{\theta_{2,l}}^{\theta_{2,h}} \exp(f(\boldsymbol{\theta}))\, p(\boldsymbol{\theta})\, \mathrm{d}\theta_1 \mathrm{d}\theta_2}. \tag{5.36}$$

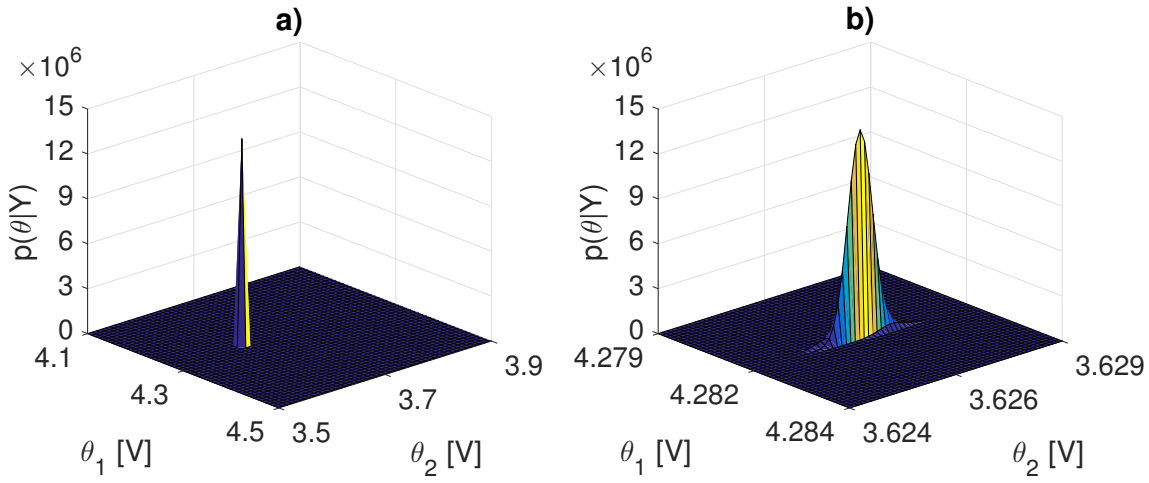

Fig. 5.6 $p(\boldsymbol{\theta}|\mathbf{Y})$ over a) full range of $\boldsymbol{\theta}$, b) magnified.

$p(\boldsymbol{\theta}|\mathbf{Y})$ is plotted in Figure 5.6; a) illustrates the narrow distribution of $p(\boldsymbol{\theta}|\mathbf{Y})$ over the full range of θ_1 and θ_2 and b) shows $p(\boldsymbol{\theta}|\mathbf{Y})$ over a reduced range of θ_1 and θ_2; $[\theta_{\eta,1}, \theta_{\eta,2}] \pm 2.5\,\mathrm{mV}$.

Model parameters and variance

The model parameters are computed as the mean of the posterior probability distribution $m(\boldsymbol{\theta})$ using Equation 5.23. Applying the limits given in Equation 5.28 to 5.31 to Equation 5.23, $m(\theta_1)$ and $m(\theta_2)$ can be computed by

$$m(\theta_1) = \frac{\int_{\theta_{1,l}}^{\theta_{1,h}} \int_{\theta_{2,l}}^{\theta_{2,h}} \theta_1 \exp(f(\boldsymbol{\theta}))\, p(\boldsymbol{\theta})\, \mathrm{d}\theta_1 \mathrm{d}\theta_2}{\int_{\theta_{1,l}}^{\theta_{1,h}} \int_{\theta_{2,l}}^{\theta_{2,h}} \exp(f(\boldsymbol{\theta}))\, p(\boldsymbol{\theta})\, \mathrm{d}\theta_1 \mathrm{d}\theta_2} \tag{5.37}$$

$$m(\theta_2) = \frac{\int_{\theta_{2,l}}^{\theta_{2,h}} \int_{\theta_{1,l}}^{\theta_{1,h}} \theta_2 \exp(f(\boldsymbol{\theta}))\, p(\boldsymbol{\theta})\, \mathrm{d}\theta_2 \mathrm{d}\theta_1}{\int_{\theta_{2,l}}^{\theta_{2,h}} \int_{\theta_{1,l}}^{\theta_{1,h}} \exp(f(\boldsymbol{\theta}))\, p(\boldsymbol{\theta})\, \mathrm{d}\theta_2 \mathrm{d}\theta_1}. \tag{5.38}$$

Equivalently, the variance of the parameters is calculated as $s^2(\boldsymbol{\theta})$ according to Equation 5.24. The same methodology is applied as for calculating $m(\boldsymbol{\theta})$, described above. $s^2(\theta_1)$ and $s^2(\theta_2)$ are computed by

$$s^2(\theta_1) = \frac{\int_{\theta_{1,l}}^{\theta_{1,h}} \int_{\theta_{2,l}}^{\theta_{2,h}} (\theta_1 - m(\theta_1))^2 \exp(f(\boldsymbol{\theta}))\, p(\boldsymbol{\theta})\, \mathrm{d}\theta_1 \mathrm{d}\theta_2}{\int_{\theta_{1,l}}^{\theta_{1,h}} \int_{\theta_{2,l}}^{\theta_{2,h}} \exp(f(\boldsymbol{\theta}))\, p(\boldsymbol{\theta})\, \mathrm{d}\theta_1 \mathrm{d}\theta_2} \tag{5.39}$$

$$s^2(\theta_2) = \frac{\int_{\theta_{2,l}}^{\theta_{2,h}} \int_{\theta_{1,l}}^{\theta_{1,h}} (\theta_2 - m(\theta_2))^2 \exp(f(\boldsymbol{\theta}))\, p(\boldsymbol{\theta})\, \mathrm{d}\theta_2 \mathrm{d}\theta_1}{\int_{\theta_{2,l}}^{\theta_{2,h}} \int_{\theta_{1,l}}^{\theta_{1,h}} \exp(f(\boldsymbol{\theta}))\, p(\boldsymbol{\theta})\, \mathrm{d}\theta_2 \mathrm{d}\theta_1}. \tag{5.40}$$

5.4 Results and discussion

5.4.1 Experimental results

All eight Kokam pouch cells are cycled (under the Artemis drive cycle) until one of the lower voltage limits is reached during discharge ($< 2.7\,\mathrm{V}$ for $> 10\,\mathrm{s}$ or $0\,\mathrm{V}$ for any measurable period of time), which indicates the cell's end-of-life. At the time of writing, cells A2, A4, A5, A6 and A8 had reached their end-of-life. All cells reached the $0\,\mathrm{V}$ limit, indicating a strong increase in internal resistance. Cell A5 was the first cell to reach its end-of-life at cycle 4800. The remaining cells (A1, A3 and A7) had lost more than 20% of their original capacity after 9100 cycles at the time of writing. The cell capacities measured during each pseudo-OCV discharge are displayed in Figure 5.7.

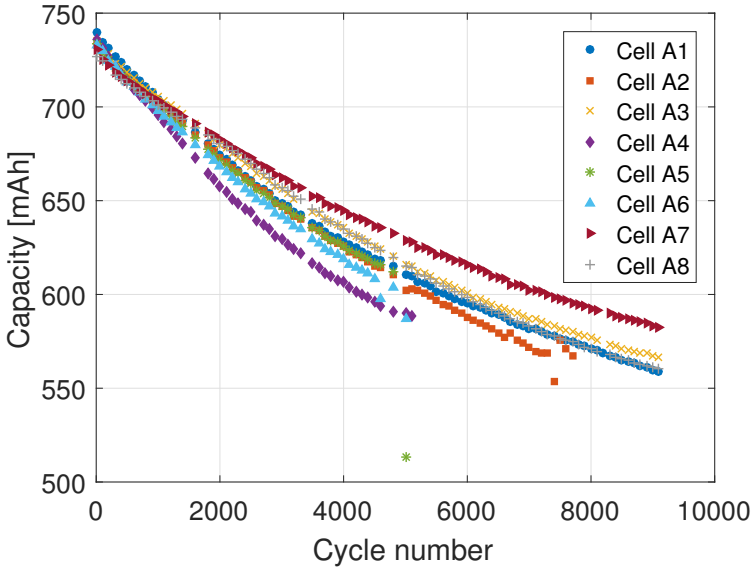

Fig. 5.7 Cell capacities measured during pseudo-OCV discharge.

Pseudo-OCV curves corresponding to the first characterisation cycle and cycle 4800 are plotted in Figure 5.8, a) and b), respectively. It is clear from Figure 5.8,

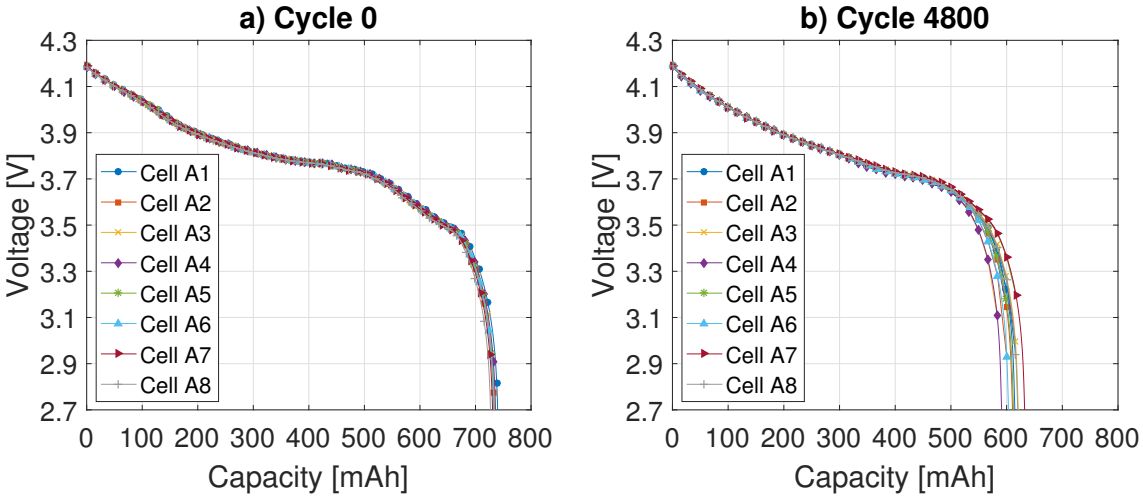

Fig. 5.8 Pseudo-OCV discharge data of all cells recorded at a) cycle 0 and b) cycle 4800.

a) that the pseudo-OCV measurements of all cells were very similar during the first characterisation cycle. The standard deviation of all cell capacities measured during the first characterisation cycle was 3.8 mAh or 0.5% of the mean capacity (733.5 mAh). By cycle 4800, the first cell failed and the standard deviation of cell capacities increased to 12.4 mAh or 2.0% of the mean capacity (613.1 mAh).

5.4.2 OCV Model parameter estimation

The OCV model parameters for the positive and negative electrode were estimated following the procedure described in Section 2.3.3. The results of the pseudo-OCV fits of the positive and negative half cells are displayed in Figure 5.9. High quality fits were achieved with a RMSE of 6 mV for the PE and a RMSE of 2 mV for the NE. Estimated OCV model parameters of the positive and negative electrode are listed in Table 5.2. The parameters Δx_i are fractions of the total normalised electrode capacity utilized within the cell and parameters $\zeta_{PE,i}$ are dimensionless.

The cell OCV is calculated from the electrode OCVs as described in Section 5.3. The parameters necessary to calculate the cell OCV from the half-cell OCVs are the same parameters from which the degradation signatures are derived, namely $\hat{E}^{\mathrm{OC}}_{\mathrm{PE,EoC}}$ and $\hat{E}^{\mathrm{OC}}_{\mathrm{PE,EoD}}$ (referred to as $\mathrm{m}(\theta_1)$ and $\mathrm{m}(\theta_2)$ in Section 5.3). The OCV

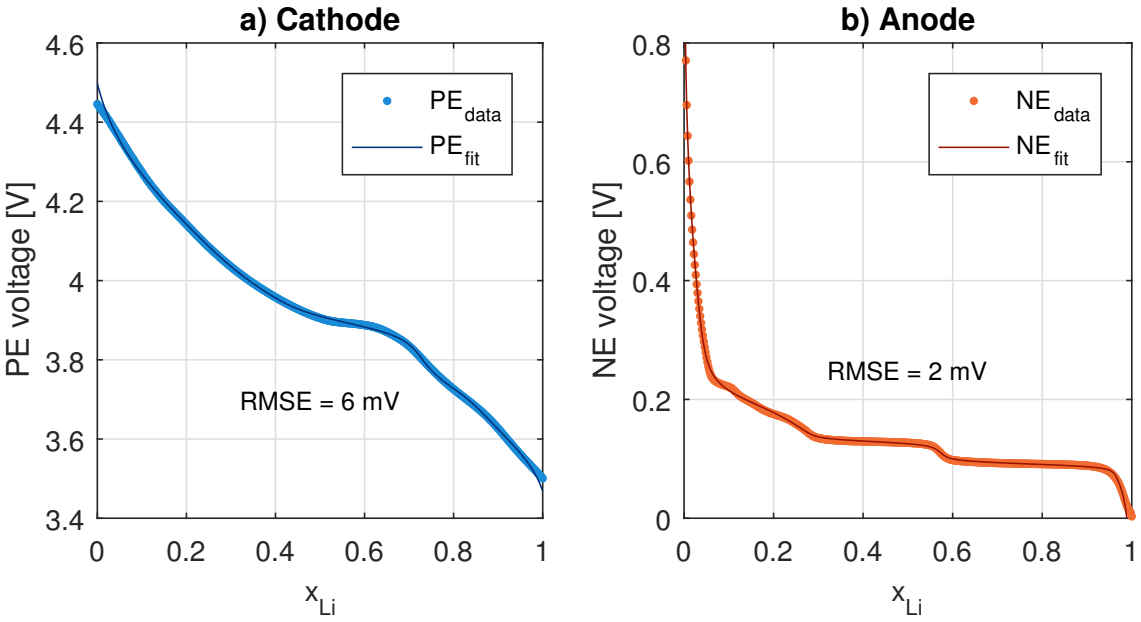

Fig. 5.9 Pseudo-OCV fitting results of a) PE half-cell and b) NE half-cell.

model is only parametrised once to obtain the electrode-specific model parameters. Any changes in the cell OCV resulting from degradation are accounted for by re-fitting the cell's pseudo-OCV measurements to obtain $\hat{E}^{\mathrm{OC}}_{\mathrm{PE,EoC}}$ and $\hat{E}^{\mathrm{OC}}_{\mathrm{PE,EoD}}$ at each characterisation cycle. The estimation results for $\hat{E}^{\mathrm{OC}}_{\mathrm{PE,EoC}}$ and $\hat{E}^{\mathrm{OC}}_{\mathrm{PE,EoD}}$, and the corresponding degradation signatures are presented in the following Section.

Table 5.2 OCV model parameters.

	PE			NE		
Pi	$E_{0,\mathrm{PE},i}$	$\Delta x_{\mathrm{PE},i}$	$\zeta_{\mathrm{PE},i}$	$E_{0,\mathrm{NE},i}$	$\Delta x_{\mathrm{NE},i}$	$\zeta_{\mathrm{NE},i}$
P_1	4.132 V	0.469	0.188	0.325 V	0.072	0.177
P_2	3.960 V	0.100	0.668	0.196 V	0.104	1.795
P_3	3.891 V	0.205	1.532	0.147 V	0.230	0.769
P_4	3.733 V	0.072	1.108	0.129 V	0.241	10.000
P_5	3.602 V	0.175	0.450	0.091 V	0.352	10.000

5.4.3 Estimation of degradation signatures

The model parameters $\mathrm{m}(\theta_1)$ and $\mathrm{m}(\theta_2)$ were estimated for all cells by fitting the cells' pseudo-OCV measurements at each characterisation cycle throughout the lifetime of

all eight Kokam cells. Examples of pseudo-OCV fits at the beginning, middle and end-of-life of all cells are illustrated in Figure 5.10. The cycle numbers corresponding to the fitting results are displayed in the figure. The fitted pseudo-OCV of the cells is plotted against DoD in grey and the corresponding PE and NE voltages in blue and red, respectively. The cell and PE voltages are plotted on the left y-axis and the NE voltage on the right y-axis. Figure 5.10 illustrates the increasing offset between the positive and negative electrode voltages with progressing cycle number, which is an indication of LLI. It is also evident that the PE voltage curves shrink with increasing cycle numbers compared to their original extent at cycle 0, suggesting $\mathrm{LAM_{PE}}$. $\mathrm{LAM_{NE}}$ would appear as shrinking of the NE voltage curve compared to its original extent. $\mathrm{LAM_{NE}}$ is harder to detect visually from Figure 5.10 since the offset due to LLI is illustrated as a shift of the NE voltage curve with respect to the PE voltage curve. All cells were estimated to have similar amounts of excess NE material at cycle 0; on the order of 40% of the original cell capacity.

The cells' OCVs are obtained at each characterisation cycle by estimating the parameters $\mathrm{m}(\theta_1)$ and $\mathrm{m}(\theta_2)$. As an example, $\mathrm{m}(\theta_1)$ and $\mathrm{m}(\theta_2)$ of cell A1 are depicted in Figure 5.11; lines show estimated parameter values plotted against cycle number and the filled areas show the corresponding 2σ credible intervals, which were calculated by

$$2\sigma(\boldsymbol{\theta}) = \sqrt{s(\boldsymbol{\theta})^2}. \tag{5.41}$$

The credible intervals are less than $\pm 1\,\mathrm{mV}$ for both $\mathrm{m}(\theta_1)$ and $\mathrm{m}(\theta_2)$ (best visible in Figure 5.11,b)), which indicates high levels of certainty in the estimation results. The parameters $\mathrm{m}(\theta_1)$ and $\mathrm{m}(\theta_2)$, which correspond to $\hat{E}^{\mathrm{OC}}_{\mathrm{PE,EoC}}$ and $\hat{E}^{\mathrm{OC}}_{\mathrm{PE,EoD}}$, are used to calculate the degradation signatures LLI, $\mathrm{LAM_{PE}}$ and $\mathrm{LAM_{NE}}$ with Equations 5.10, 5.11, 2.10, 2.11 and 5.1 to 5.3. The credible intervals for the degradation signatures LLI, $\mathrm{LAM_{PE}}$ and $\mathrm{LAM_{NE}}$ are obtained by re-calculating the degradation signatures using $m(\boldsymbol{\theta}) \pm 2\sigma(\boldsymbol{\theta})$.

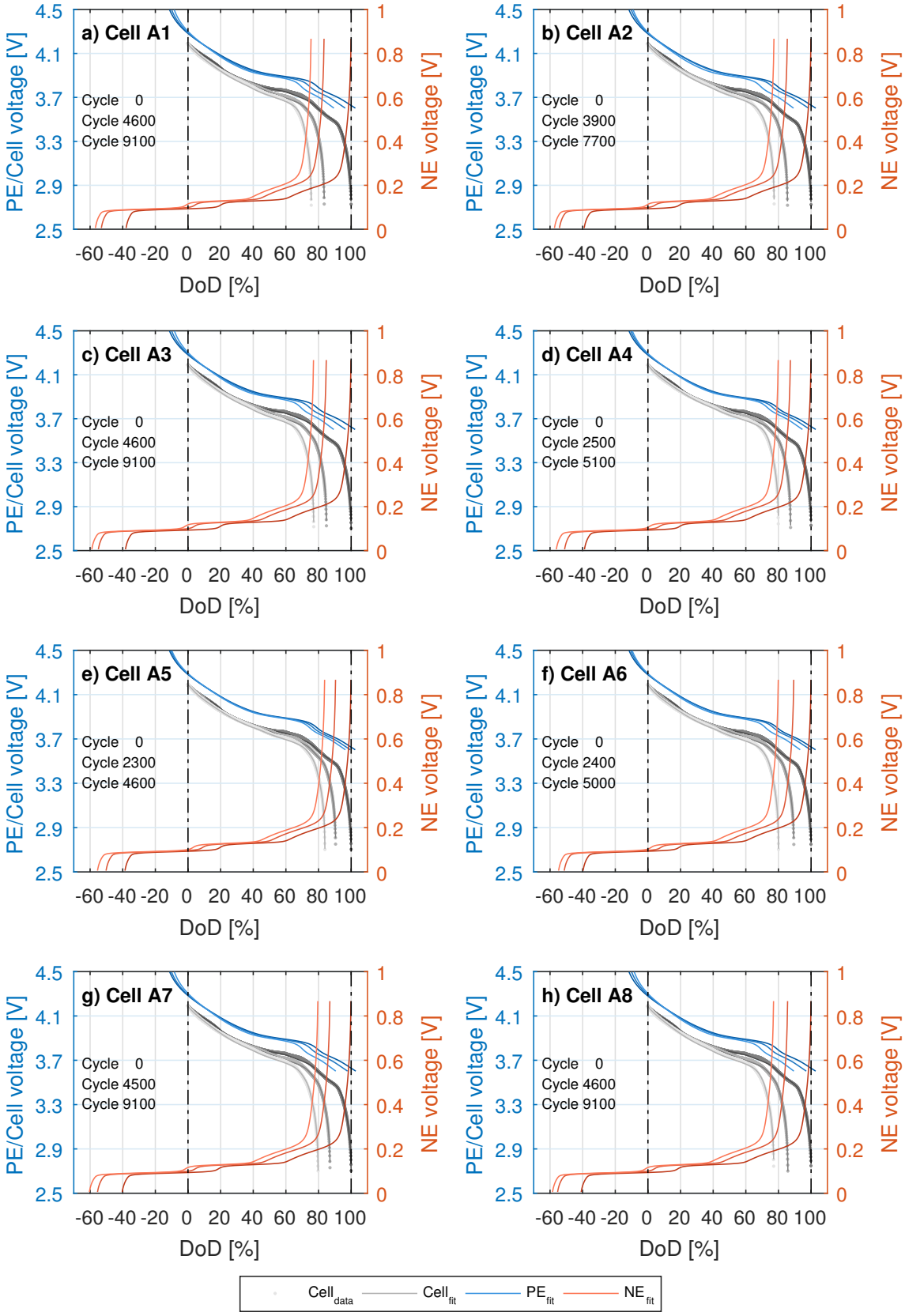

Fig. 5.10 Pseudo-OCV fitting results of all cells at their beginning, middle and end-of-life.

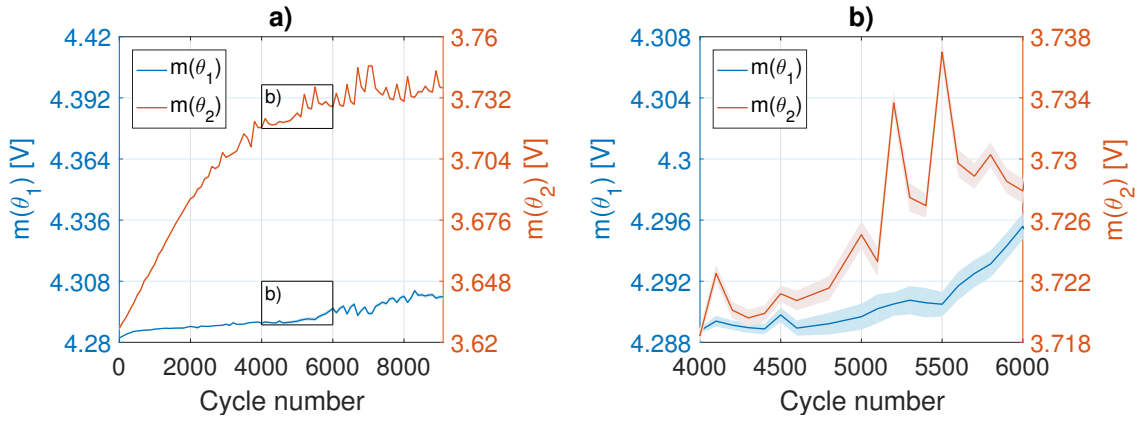

Fig. 5.11 $m(\theta_1)$ (left y-axis) and $m(\theta_2)$ (right y-axis) of cell A1. b) shows the insets marked by the rectangular boxes in a). Filled areas represent 2σ credible intervals.

Figure 5.12 illustrates LLI, LAM_{PE} and LAM_{NE} of all cells, estimated at each characterisation cycle. Values for degradation signatures are given as percentage of original cell capacity, as indicated on the left vertical axes of the plots. Lines indicate estimation results and filled areas of respective colours represent 2σ credible intervals. The measured capacity loss of the cells is also illustrated by the circular markers in Figure 5.12. The RMSE between the measured and modelled cell OCVs are displayed as black, filled markers on the right vertical axes.

Credible intervals are narrow for all degradation signatures and all cells, generally not exceeding $\pm 1\%$ with the exception of a few outliers in LAM_{NE} estimates. Examples of such outliers can be observed on cells A1, A3, A6, A7 and A8 (Figure 5.12, a), c), f), g) and h)) close to cycle 2000. RMSE values are relatively uniform ($\sim 8 - 12\,\text{mV}$) throughout the cells' cycle life, rising only slightly toward end-of-life. This suggests that the model remains valid for the whole cycle lives of the cells.

The estimation results of LAM_{NE} show that the spikes in LAM_{NE} values are either accounted for by higher uncertainty in the estimation results or by poorer fitting quality reflected by outliers in RMSE values. A general observation for all cells is that noisier capacity measurements coincide with noisier estimates of degradation signatures; capacity measurements tend to be smoother near the beginning of the

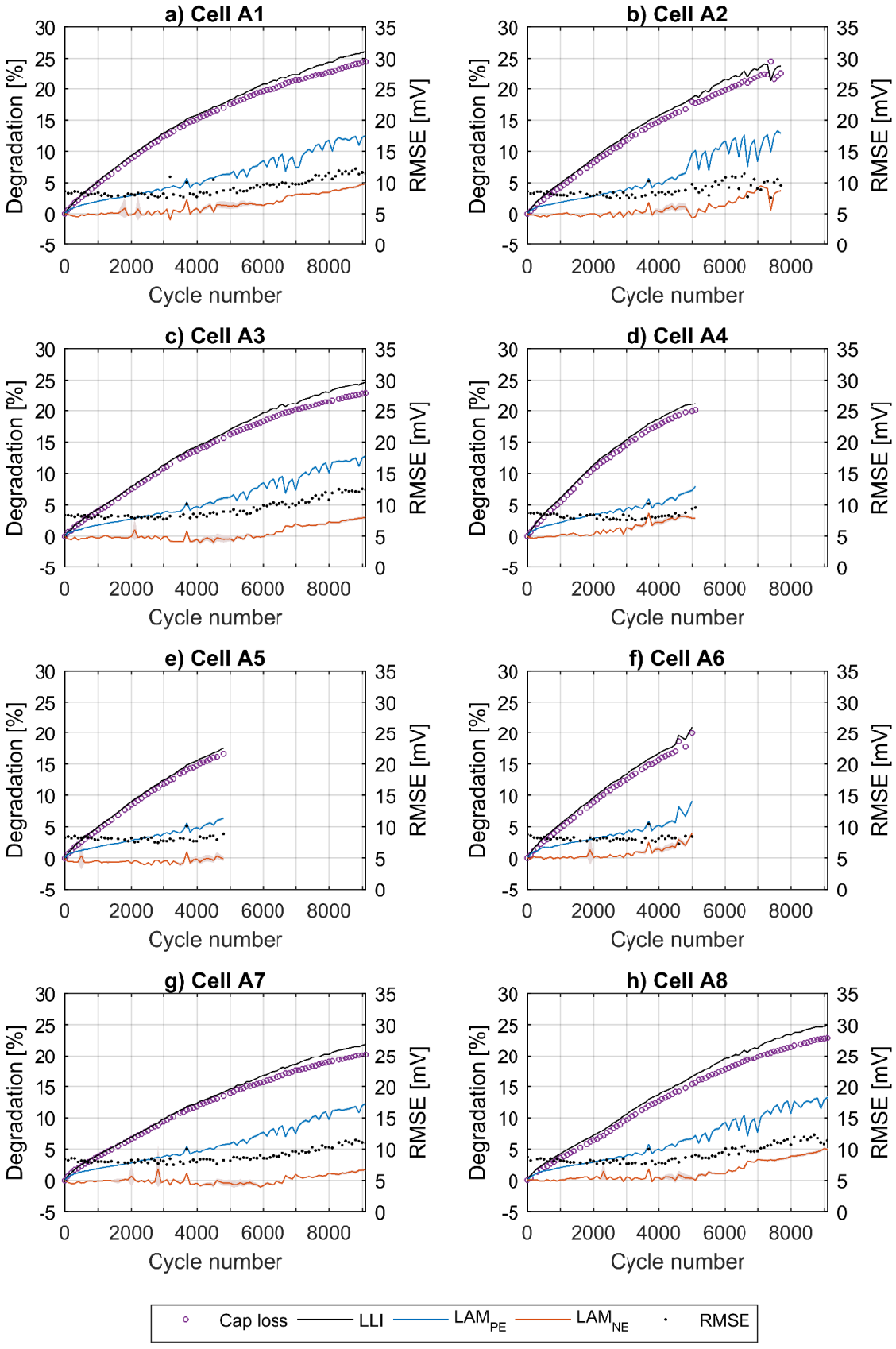

Fig. 5.12 Measured capacity loss and estimated LLI, $\mathrm{LAM_{PE}}$ and $\mathrm{LAM_{NE}}$, filled areas represent credible interval (left vertical axes); RMSE of pseudo-OCV fits (right vertical axes).

cells' cycle lives and noisier towards the end. This effect is particularly pronounced for cell A2—measured capacity loss becomes much noisier from cycle 5000 onwards, which corresponds to noisier estimates of $\mathrm{LAM_{PE}}$.

Given the constant environmental conditions inside the thermal chamber, it is unlikely that the noise in later capacity measurements is due to external influences. This indicates that the noisy capacity measurements and corresponding estimates of degradation signatures originate from physical processes inside the cells, such as partial electronic contact loss or partially reversible build-up of surface layers. One possible cause of partial electronic contact loss is gassing inside the cells, which was indicated by slightly bloated cell pouches. Evidence to support the hypothesis of reversible build-up of surface films is more difficult to obtain and would require a post mortem analysis of electrode materials.

5.4.4 Analysis of degradation signatures and cell failure

Based on the estimated degradation signatures (as depicted in Figure 5.12), similar trends in the evolution of degradation signatures over the cells' cycle lives can be summarised as:

1. $\mathrm{LAM_{PE}}$ is significantly greater than $\mathrm{LAM_{NE}}$.
2. $\mathrm{LAM_{PE}}$ occurs from the very beginning of the cells' lives.
3. $\mathrm{LAM_{NE}}$ does not occur until the mid to late stages of the cells' lives.
4. LLI is slightly greater than the measured capacity loss, particularly toward end-of-life.

The most notable dissimilarities between the cells were the rates at which the identified degradation signatures progressed, the extents to which the degradation signatures developed, and the onset of $\mathrm{LAM_{NE}}$. For better comparison of measured

capacity loss and degradation signatures between all eight cells, the measured capacity loss, estimated LLI, LAM_{PE}, and LAM_{NE} are displayed in the same plots for all cells in Figure 5.13.

The capacity loss measured for every cells (Figure 5.13, a)) appears to follow a relatively smooth, almost parabolic trajectory with no signs of changes in trajectory before end-of-life. The estimated LLI of all cells generally follows the same trend as the measured capacity loss, which was expected, since the loss of capacity is ultimately due to the loss of lithium. The estimated LLI is consistently greater than the measured capacity loss for each cell, which is also apparent in Figure 5.12. This is due to the stoichiometric offset between the electrodes, caused by maintaining the cells' upper and lower voltage limits over their cycle lives, as discussed in Section 3.3.1. The differences between capacity loss (Figure 5.13, a)) and LLI (Figure 5.13, b)) are greatest for the cells A2, A4, A6 and cell A8, which have relatively higher rates of LLI than capacity loss by comparison with the remaining cells (see also Figure 5.12). Cells A2, A4, A6 and cell A8 have failed at the time of writing.

The relative differences in LAM_{PE} between the cells (Figure 5.13, c)) are comparable to the differences in capacity loss during the first 4000 cycles. After roughly 4000 cycles the rate of LAM_{PE} increased for cells A4 and A6, which failed at cycle 5100 and 5000, respectively. LAM_{PE} of cell A2 was distinctly higher than that of all other cells from cycle 5000 onwards. Cell A2 was the fourth cell to fail after cycle 7700. The next cell to fail, cell A8, showed a notably larger extent of LAM_{PE} than cells A1, A3, and A7 (all of which were still functioning at the time of writing) after about 6000 cycles. Both cell A2 and A8 failed with 13% LAM_{PE}.

The earliest onset of LAM_{NE} was found for cells A4 and A6 between cycle 2000 and 3000. Cells A4 and A6 were the first cells to fail around cycle 5000, as did cell A5. Interestingly, no LAM_{NE} was detected for cell A5. Both cell A4 and A6 failed with 3-4% LAM_{NE}. The onset of LAM_{NE} for cells A1, A2 and A8 occurred around cycle 5000 and progressed at similar rates, until the rate of LAM_{NE} increased for

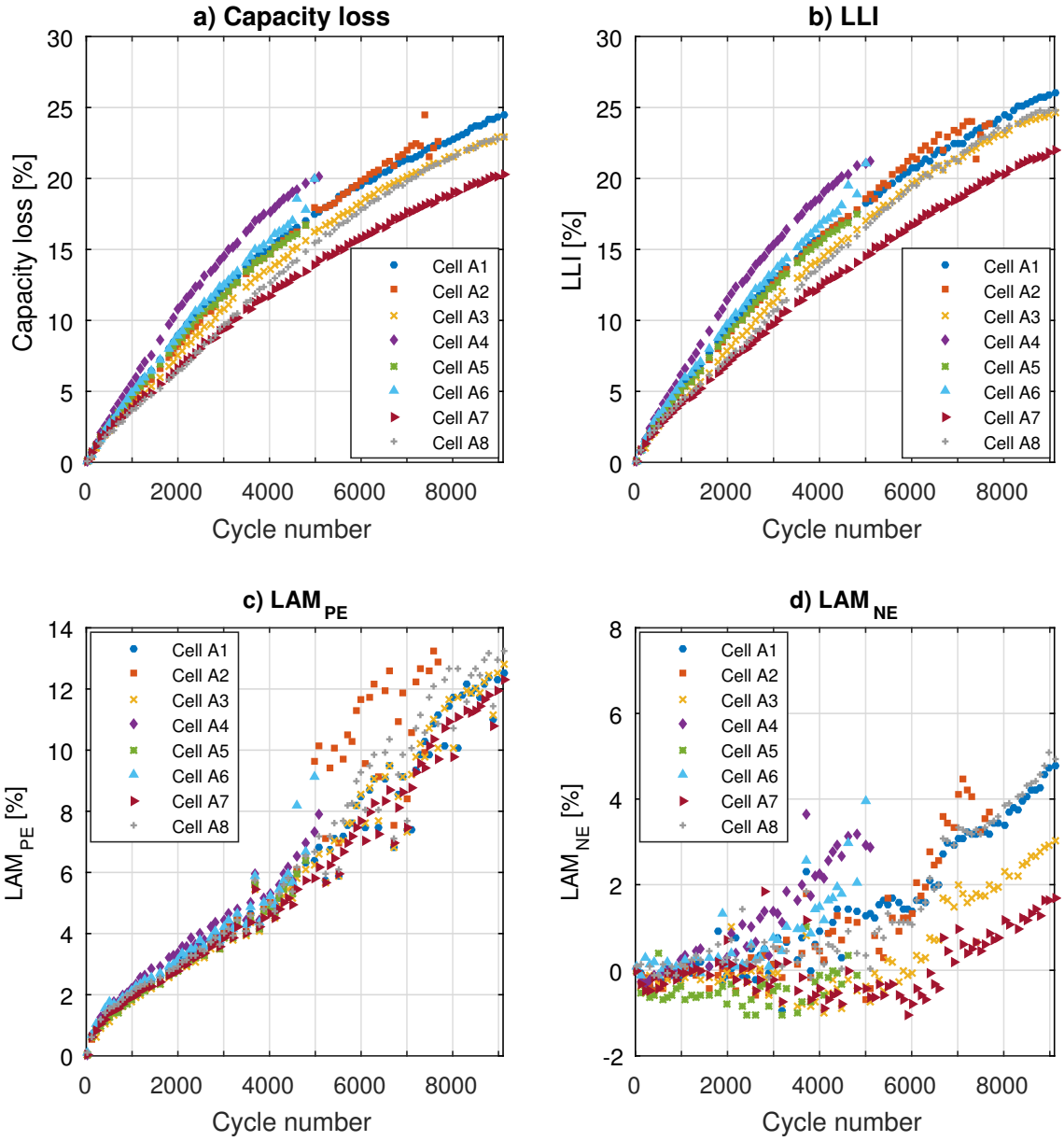

Fig. 5.13 a) Measured capacity loss, b) estimated LLI, c) estimated $\mathrm{LAM_{PE}}$ and d) estimated $\mathrm{LAM_{NE}}$.

cell A2 shortly before its failure at cycle 7700. Cells A3 and A7 exhibited the latest onset of LAM_{NE} at around cycle 6000, and the smallest extent of LAM_{NE} at 3% and 2%, respectively, by cycle 9100.

The estimation of degradation signatures revealed significant differences in degradation between the different cells of the same batch, exposed to the same operating conditions. These differences in degradation are likely to be linked to the wide spread in cycle life observed between the cells. The results suggest that at least three different pathways of degradation were responsible for the failure of cells A2, A4, A5, A6 and A8:

1. **NE-limited:** Cells A6 and A4 failed after roughly 5000 cycles. The cells showed an early onset of LAM_{NE} between cycle 2000 and 3000 and a higher rate of capacity loss than the remaining cells. One possible explanation could be differences in the quality of the graphite negative electrode; *e.g.* inhomogeneities leading to electronic isolation of parts of the negative electrode material, as previously observed for this type of cells and illustrated in Figure 3.1. Another reason could be differences in resistance in the welding joints of the negative electrode current collectors near the cell tabs caused by imperfections in the tab welding. This would lead to lower currents in the affected electrode sheets, leaving the remaining sheets exposed to higher currents and consequently faster rates of negative electrode degradation.

2. **PE-limited:** Cell A2 failed after 7700 cycles with a distinct and rapid increase in LAM_{PE} from cycle 5000, which coincided with an increase in LLI. These findings suggest the occurrence of a sudden destructive event in the positive electrode of cell A2. One possible explanation is electronic contact loss of a significant portion of the active positive electrode material, which could be due to the development of cracks. The noisy capacity measurements and LAM_{PE} estimates after cycle 5000 could indicate that the electronic contact to the

affected portion of the positive electrode was partially re-established—an effect comparable to a loose contact.

3. **Combined failure mode:** Cell A8 failed after 9100 cycles with a late onset of LAM_{NE} (around cycle 5000) but a similar extent of LAM_{NE} to cells A2, A4, and A6. Around cycle 6000, cell A8 showed the second highest rate of LAM_{PE} after cell A2. In the early stages of its cycle life, cell A8 exhibited the lowest rate of capacity loss and LLI, together with cell A7. The LLI of cell A8 notably exceeded that of cell A7 after roughly 3000 cycles, at which point there was no measurable difference in the capacities of cell A7 and A8 (see Figure 5.13, a) and b)). This increase in LLI could indicate higher rates of surface layer formation, which later contributed to the blocking of active surface sites, causing apparent LAM_{NE} and LAM_{PE}. It is not clear what may have caused these higher rates of LLI. At the time of failure, cell A8 had experienced less capacity loss than cell A1 and the same amount of capacity loss as cell A3, both of which are still functioning. The failure of cell A8 appeared to owe to a combination of LAM_{NE}, LAM_{PE} and LLI.

The reasons for the early failure of cell A5 are not immediately obvious from the inspection of the estimated degradation signatures. At the time of writing, cells A1, A3, and A7 were still functioning but the estimated degradation signatures indicate that cell A1 is following a similar trajectory as cell A8, and its end-of-life appears to be imminent. Cell A7 clearly outperforms all other cells and is likely to exhibit the longest cycle life.

Within this batch of eight identical Kokam 740 mAh pouch cells, significant differences in degradation and failure modes were identified. The different modes of failure are likely to be linked to the wide spread in cycle life observed for this cell batch.

One possible reason for the differences in cycle life and estimated degradation signatures are internal variations in material properties originating from the cell manufacturing process. Another reason could be the effects of non-uniform environmental temperatures inside the thermal chamber and the respective position of the cells. Although surface temperatures among the cells were found to vary by less than 1 °C, the effects of small differences in temperature accumulate over long periods of time and could account for different degradation and failure modes.

5.4.5 Towards end-of-life prediction

From inspection of Figure 5.13, a) it appears unlikely that the measured cell capacity or capacity loss provides sufficient information for the prediction of cell failures. No obvious changes in the trajectories of the capacity measurements were observed, which could indicate imminent cell failure. Moreover, the sequence of cell failures could not be predicted using the relative differences in capacity loss between the cells at any given point in time. This can be illustrated as follows. If, for instance, the total amount of capacity loss was used to predict cell failures at cycle number 4700 (immediately before the cell A5 reached its end-of-life), the predicted sequence of failures would be A4, A6, A1, A5, A2, A3, A8, A7, as opposed to the true sequence A5, A6, A4, A2, A8, with cells A1, A3 and A7 still functioning at the time of writing.

The estimated degradation signatures, particularly $\mathrm{LAM_{NE}}$ and $\mathrm{LAM_{PE}}$, provide additional information, which may allow for a more accurate prediction of cell failure. One possible method for end-of-life prediction is presented in this section, consisting of two stages using estimated degradation signatures:

1. Classification of failure modes.

2. End of life prediction based on cross-validation of degradation signatures and remaining cycle life.

Step 1 was conducted, qualitatively, in Section 5.4.3, suggesting at least three distinct modes of failure. In step 2 the recorded cycles to failure and corresponding estimates of degradation signatures of one or more failed cells are used to predict the end-of-life of another cell. The correlation between cycles to failure and estimated degradation signatures is quantified by means of a leave-one-out cross-validation [138, p. 69-71]. The results of the cross-validation indicate whether the degradation signatures contain additional information that can be used to predict end-of-life.

The cycles to failure are calculated by a polynomial regression on the estimated degradation signatures. The data used for the regression are divided into a training data set and a test data set. Both data sets are taken from a group of cells which experienced the same mode of failure. This approach requires data from two or more failed cells. At the time of writing, only the negative electrode-limited failure mode was associated with two or more cells—cells A4 and A6. Although cell A5 could not be unambiguously associated with the same failure mode, it is included in the cross-validation due to the similarity in its cycle life.

Estimated values of $\mathrm{LAM_{NE}}$ and $\mathrm{LAM_{PE}}$ were combined in a polynomial model of structure

$$y = a_0 + a_1 x + a_2 x^2 + ... + a_n x^n + a_{n+1} z + a_{n+2} z^2 + ... + a_{n+m} z^m + \epsilon \qquad (5.42)$$

where y is the number of cycles to failure, x is $\mathrm{LAM_{NE}}$, n is the number of $\mathrm{LAM_{NE}}$ model terms, z is $\mathrm{LAM_{PE}}$, m is the number of $\mathrm{LAM_{PE}}$ model terms, a_0 to a_{n+m} are the estimated model parameters and ϵ is the unobserved random error with zero mean. The polynomial model used for the cross-validation was identified by evaluating Equation 5.42 for $n = \{1, 2, ..., 5\}$ and $m = \{1, 2, ..., 5\}$, and comparing the computed cycles to failure with the actual cycles to failure. The model

$$y = a_0 + a_1 x + a_2 z + a_3 z^2 + a_4 z^3 + a_5 z^4 + \epsilon \qquad (5.43)$$

delivered the best results and was used for the cross-validation. In matrix form, Equation 5.43 can be expressed as

$$\begin{bmatrix} y_1 \\ y_2 \\ \vdots \\ y_n \end{bmatrix} = \begin{bmatrix} 1 & x_1 & z_1 & z_1^2 & z_1^3 & z_1^4 \\ 1 & x_2 & z_2 & z_2^2 & z_2^3 & z_2^4 \\ \vdots & \vdots & \vdots & \vdots & \vdots & \vdots \\ 1 & x_n & z_n & z_n^2 & z_n^3 & z_n^4 \end{bmatrix} \begin{bmatrix} a_0 \\ a_1 \\ \vdots \\ a_5 \end{bmatrix} + \begin{bmatrix} \epsilon_1 \\ \epsilon_2 \\ \vdots \\ \epsilon_n \end{bmatrix} \tag{5.44}$$

for n estimates of x ($\mathrm{LAM_{NE}}$) and z ($\mathrm{LAM_{PE}}$), which form the design matrix $\mathbf{X}$. The parameter vector $\vec{a}$ is estimated by

$$\hat{\vec{a}} = (\mathbf{X}^T\mathbf{X})^{-1}\mathbf{X}^T\vec{y}. \tag{5.45}$$

In order to evaluate the advantage of using $\mathrm{LAM_{NE}}$ and $\mathrm{LAM_{PE}}$ for end-of-life predictions, the prediction results are compared to a base case, where predictions are made using only measured capacity loss in a second degree polynomial model

$$y = a_0 + a_1 x + a_2 x^2 + \epsilon \tag{5.46}$$

where y are the cycles to failure, x is the measured capacity loss, ζ_0 to ζ_2 are the model parameters and ϵ is the unobserved random error with zero mean. Equation 5.46 is solved for the parameter vector $\vec{a}$, using the same data sets of y as above, by applying Equation 5.45. It was found that higher degree polynomials did not improve the prediction results of end-of-life predictions using capacity loss measurements.

Both the base case prediction and advanced prediction using LAM are repeated for all cells in a leave-one-out pattern. This means that the parameter vector $\vec{a}$ is estimated three times for the base and advanced case, using two of the three failed cells A4, A5 and A6 as training data set and the third cell as validation data set so that each of the three cells is used for validation once. The data sets of all cells have

the same size and span 3000 cycles to failure. The results of the cross-validation are displayed in Figure 5.14. Estimated cycles to failure are plotted against true cycles to failure as blue markers. The red line serves as a reference to the true cycles to failure. RMSE values calculated from the residuals of estimated versus true cycles to failure are displayed in the plots. The advanced method using LAM is shown in the left column of Figure 5.14 and the base case in the right column.

Figure 5.14 demonstrates that end-of-life predictions based on estimated LAM yield superior results compared to predictions based on measured capacity loss for all test cases. RMSE values for the advanced prediction are less than one third of those of the base case for the predictions on cell A4 and less than half for cells A5 and A6. Using the estimated LAM, the end-of-life can be predicted with an error of ~ 250 cycles, up to 3000 cycles in advance. By contrast, using measured capacity loss, the prediction error can be greater than 800 cycles.

5.5 Conclusions

The OCV model developed in Chapter 2 and the diagnostic algorithm presented in Chapter 3 were used to estimate the degradation signatures of eight unmodified Kokam 740 mAh pouch cells throughout their cycle lives. Taking a Bayesian approach to parameter estimation made it possible to estimate LLI, $\mathrm{LAM_{PE}}$ and $\mathrm{LAM_{NE}}$ and their corresponding uncertainties, which revealed high levels of certainty in the estimated degradation signatures. It was found that the OCV model identified using the fresh cells remained valid until the end-of-life of the tested cells.

Regarding the aspect of safety, none of the cells indicated the development of safety-critical conditions throughout their cycle lives. Sufficient amounts of excess negative electrode material prevented conditions to favour lithium plating, even after the loss of active negative electrode material.

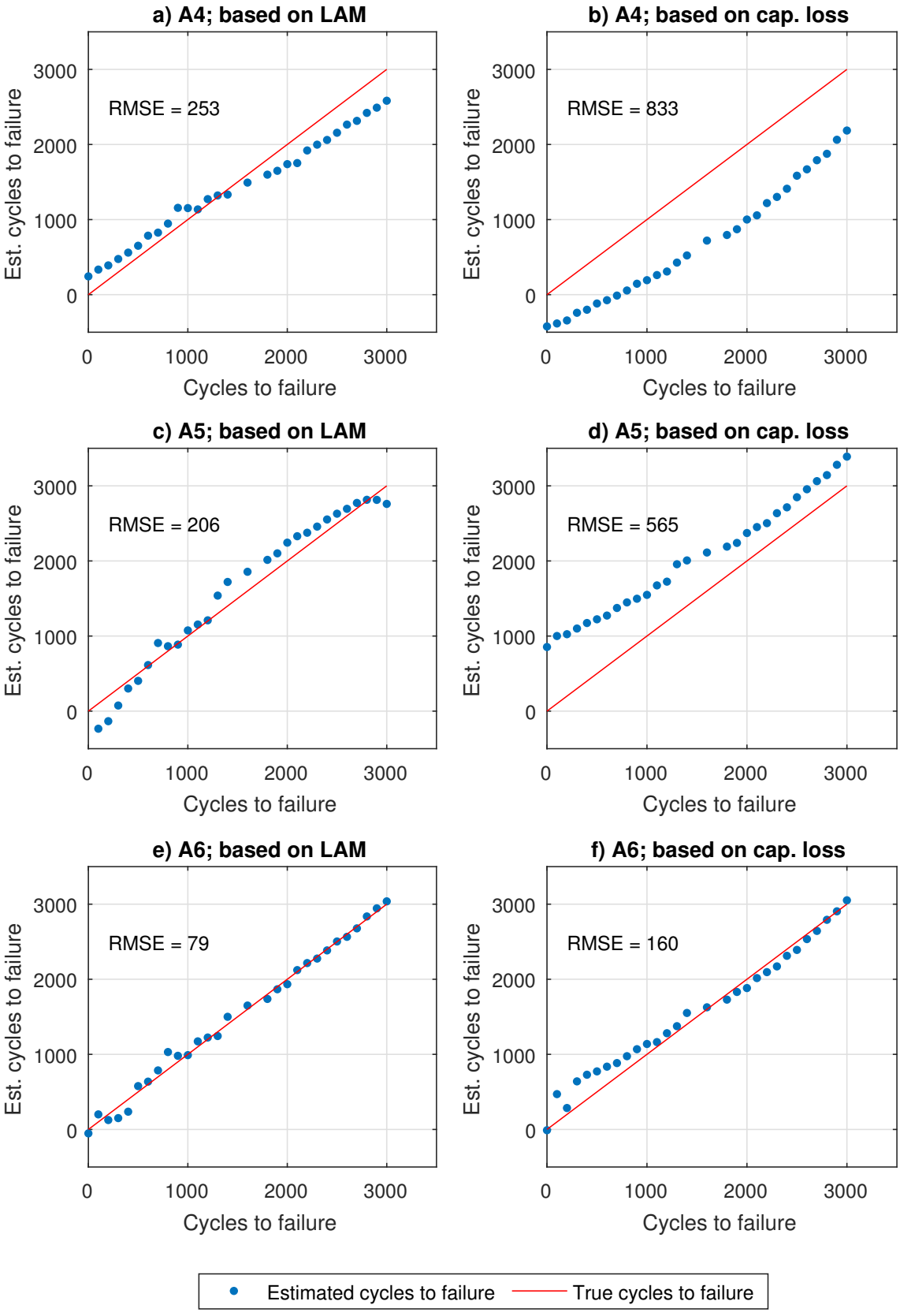

Fig. 5.14 Leave-one-out cross-validation of degradation signatures $\mathrm{LAM_{PE}}$ and $\mathrm{LAM_{NE}}$ as end-of-life predictors. Left column: Cycles to failure estimated using $\mathrm{LAM_{PE}}$ and $\mathrm{LAM_{NE}}$; right column: Cycles to failure estimated using capacity loss measurement.

Out of eight tested cells, five had reached their end-of-life at time of writing. For these five cells, at least three different prevalent degradation signatures were identified:

1. NE-limited
2. PE-limited
3. Combined

These different pathways of degradation are likely to be the reason for the large spread in cycle life, ranging from 4800 cycles to $>$ 9100 cycles. This study shows that identical cells exposed to the same environmental conditions and usage patterns do not necessarily experience the same modes of degradation or failure. This finding highlights the importance of tracking the degradation of individual cells and demonstrates that it is not possible to generalise degradation even among cells of the same batch. It is unlikely that physics-based degradation models, using environmental and operating conditions for inputs and assuming identical cell properties, would be able to predict such differences of degradation and wide spread in cycle life.

The degradation and failure modes identified in this work provide useful insights for the improvement of cell design. From the differences in prevalent degradation signatures and cycle life it can be deduced that the active electrode materials of the tested cells lack uniformity. This could be due to inhomogeneities in the microstructure of the electrode materials, as well as differences in the composition or manufacturing process. Small differences in environmental temperature over long time periods could also have an impact on degradation and failure modes. The exact reasons can only be established with a post-mortem analysis.

The estimated loss of active material of both the positive and negative electrode was used to predict the end-of-life of three failed cells. The results demonstrate that the estimated LAM significantly improves the predictions of cell failures compared

to predictions based on measured capacity loss. Accurate and reliable end-of-life predictions for Li-ion cells are crucial for the improvement of the design and reliability of commercial multi-cell systems. Future work should include the extension of cell failure predictions to all tested cells once the remaining cells have reached their end-of-life.

Chapter 6

Conclusions and future work

This work presents a holistic approach for the diagnosis and prognosis of degradation in Li-ion cells. Thermodynamic information on the individual electrodes, contained in the OCV of Li-ion cells, is harnessed to identify the nature and quantify the extent of degradation in terms of three different degradation signatures: LLI, $\mathrm{LAM_{PE}}$ and $\mathrm{LAM_{NE}}$. The estimated degradation signatures are used to identify the onset of potential safety hazards, to categorise cells in terms of likely modes of failure and to inform end-of-life predictions.

6.1 Contributions

The contributions of this work can be summarised as follows.

1. A novel parametric OCV model for Li-ion cells, which accounts for operating temperature and effects of degradation [116].

2. A diagnostic algorithm capable of identifying and quantifying electrode-specific degradation signatures by fitting of cell OCVs [30].

3. Experimental validation of the effects of LLI, $\mathrm{LAM_{PE}}$ and $\mathrm{LAM_{NE}}$ on the OCV of Li-ion cells [30].

4. Improvement of end-of-life prediction for Li-ion cells using estimated degradation signatures.

6.1.1 A novel parametric OCV model

Key features of the presented OCV model are its

- ability to account for operating temperature,
- ability to return electrode potentials, creating a 'virtual reference electrode',
- ability to account for effects of degradation,
- ease of parameterisation and
- chemistry-agnostic structure.

Not only does this OCV model form the basis of the proposed diagnostic algorithm but it can also improve the efficiency and performance of existing battery models, which typically use OCV/capacity look-up tables or empirical functions. Failure to consider effects of operating temperatures and degradation on the OCV/capacity relationship of a Li-ion cell results in inaccuracies in estimations of SoC and SoH. If effects of operating temperature and/or degradation on cell OCV are to be considered in OCV look-up tables, a multi-dimensional look-up table would have to be created, comprised of many data-sets recorded at different temperatures and states of life, which is not likely to be feasible. Similarly, empirical functions would have to be fitted to OCV data sets recorded at various temperatures and states of life of a Li-ion cell.

An electrode-level OCV model effectively provides a virtual reference electrode, which enables the monitoring of the individual electrode potentials. This can be used to ensure safe operation by identifying excessive PE potentials, which can lead to thermal runaway, or negative NE potentials, which can cause the onset of

lithium plating. Moreover, the ability to track PE and NE potentials can enable the development of improved charge and discharge patterns, which may prolong the cell's lifetime. The cell's cut-off voltages can be dynamically adjusted in accordance with the voltage limits of the electrodes, rather than maintain rigid cell voltage limits.

6.1.2 A diagnostic algorithm to estimate degradation signatures

Crucial innovations in the proposed diagnostic algorithm include its

- ability to identify degradation at the electrode level from the OCV (or pseudo-OCV) measurement of a full cell,
- ability to identify potential safety hazards and
- ease of parameterisation.

The algorithm can identify and quantify the three degradation signatures LLI, $\mathrm{LAM_{PE}}$ and $\mathrm{LAM_{NE}}$ by fitting OCV or pseudo-OCV measurements of a full-cell directly, unlike most existing diagnostic techniques, which rely on differentiation of measurements and/or qualitative, simulation-based interpretation of the results. This makes the algorithm easily applicable to repeated cell characterisations and less sensitive to measurement noise.

Moreover, the diagnostic algorithm was demonstrated to identify potential safety hazards, such as excessive PE potentials and conditions to favour lithium plating on the NE.

Another valuable application of the diagnostic algorithm is to identify cell-to-cell variabilities in quality and performance, which is important for both quality control and end-of-life estimation.

6.1.3 Improvement of end-of-life prediction

The information on electrode-specific degradation signatures obtained from the diagnostic algorithm was utilized for end-of-life prognosis in two ways; (i) for a qualitative classification of likely failure modes and (ii) for a quantitative estimation of the remaining useful life of commercial Li-ion cells.

This work demonstrates the need to classify cells into different failure modes prior to, or in conjunction with, end-of-life prediction. This is due to significant cell-to-cell variations in terms of quality and lifetime, which were revealed by long-term tests on identical cells with very little initial variability in performance, exposed to the same operating conditions. Different failure modes are, in this case, likely due to inherent material inhomogeneities, which are manifested and enhanced over time. Inhomogeneous degradation can be expected to play an even greater role in practical applications, where individual cells of multi-cell systems are subject to non-uniform exposure to stress factors, such as temperature and current.

Following the classification of the cells into different failure modes, the use of $\mathrm{LAM_{PE}}$ and $\mathrm{LAM_{NE}}$ in end-of-life predictions significantly improved the estimation results compared to using only capacity measurements, as is the case for many existing prognostic methods.

6.1.4 Practical relevance

A fundamental motivation for the work in this thesis is the relevance to practical applications. The described methods were designed for and tested with commercially available Li-ion cells. This work was intended to be directly applicable to diagnostic systems in multi-cell Li-ion battery management systems.

A diagnostic system employing the presented methods could function in the following manner. The OCV model is parameterised once, using OCV (or pseudo-OCV) measurements recorded on a pristine single cell as well as on one PE half-cell

and one NE half-cell, made from harvested commercial electrode material. During operation of the multi-cell system, pseudo-OCV measurements are recorded on a regular basis, for example as part of a maintenance or characterisation procedure. The degradation signatures are estimated for each recorded pseudo-OCV data set. Potential safety hazards, such as excessive PE potentials or suspected onset of lithium plating are flagged in order to ensure safe operation. As the cells degrade, their voltage limits are adjusted in accordance with the electrode voltage limits, which are tracked using the OCV model. This prolongs the cells' lifetime and helps to ensure safe operation. The degradation signatures are also used to estimate the end-of-life of individual cells, which are continuously updated with incoming pseudo-OCV measurements. End-of-life predictions for individual cells are used to schedule maintenance or replacement of the multi-cell system and provide an estimate of the depreciation of the battery.

Greater certainty about the reliability, safety, required maintenance and depreciation of Li-ion battery systems can significantly improve the competitiveness of battery electric storage in both automotive and stationary applications. The findings presented in this work are therefore not only of technological but also of commercial interest.

6.2 Future work

6.2.1 Hysteresis in OCV

The OCV model presented in Chapter 2 does not address the issue of hysteresis in the OCV of Li-ion cells [139–141]. Various approaches have been reported in the literature to model hysteresis in Li-ion cells. Baronti *et al.* [142] applied the Preisach model [143] to LFP cells. Roscher *et al.* [144] took an empirical approach by calculating a hysteresis factor through normalised integration of the charge throughput.

For the purpose of estimating degradation through the fitting of OCV or pseudo-OCV measurements, the OCV model presented in Chapter 2 is sufficient so long as the measurements are consistently recorded during charge or discharge. However, for accurate SoC estimation, a hysteresis model should be included, since small inaccuracies in the OCV can lead to substantial errors in SoC estimation [62].

6.2.2 Degradation data

The availability of data on long-term tests of Li-ion cells are a limiting factor for the development and validation of methods and models for the diagnosis and prognosis of degradation in Li-ion cells. This is also true for the approach to end-of-life prediction presented in Chapter 5, which has, so far, been applied to three out of eight cells of the long-term experiments. In order to prove the reproducibility of this approach, more data are required.

The scarcity of long-term degradation in the academic community is a good reason to develop flexible techniques, which do not rely on highly specific measurements, such as the true OCV of individual cells. This was one reason why the presented methods utilize low-rate charge or discharge voltage curves (pseudo-OCV measurements) rather than the true OCV, since those data are more widely available. However, the presented method could be further improved by combining it with a dynamic model in order to compute the cells' OCV from voltage measurements recorded under higher rates. This is not only beneficial for the development of diagnostic and prognostic techniques, but also for practical applications, where voltage data recorded under higher rates are also more easily available.

Moreover, further data are required on different cell chemistries in order to confirm the assumption that the presented approach is chemistry-agnostic. Similarly, further experiments with different operating parameters should be conducted, in order to

investigate the performance of the proposed methods for cells exposed to different conditions, such as temperature, cycle depth, cycle rates, etc.

6.2.3 Multi-cell systems

The presented approach relies heavily on the availability of cell-level voltage data. In real multi-cell systems, individual cells are typically connected in parallel in order to increase the total capacity of the battery. In such a set-up, the measured voltage data are an aggregation of all cell voltages in the parallel module. An experimental investigation is required to demonstrate the performance of the presented methods when applied to voltage measurements obtained on a parallel module-level.

6.2.4 Next steps

The presented methodology will be applied to all cells of the long-term experiments, once they have reached their end-of-life. This will help consolidate the findings of the end-of-life estimation procedure. Post-mortem materials analyses will be conducted on the faded cells in order to validate the degradation and failure modes produced by the diagnostic algorithm. Identifying the exact physical or chemical mechanisms behind the observed degradation can help build a more fundamental understanding of degradation, which can be used to improve end-of-life prediction.

Other methods for end-of-life prediction using the estimated degradation signatures will be investigated, aside from the presented linear regression analysis. Such methods could include model-based non-linear regression, neural networks and Gaussian processes. Findings from the post-mortem analysis will be used to inform model-based methods for end-of-life prediction.

The classification of failure modes will be implemented in a more principled manner, compared to the presented qualitative approach, *e.g.* based on Bayesian decision theory.

Ideally, the long-term experiments will be repeated with a different cell type in order to prove that the approach is truly chemistry-agnostic.

Finally, the methodology will be applied to a portable 1.2 kW, 2 kWh, Li-ion energy storage system, being developed at the Energy and Power Group. This will help validate the proposed approach for degradation diagnostics and end-of-life predictions in a real-world scenario. Moreover, the energy storage system will be used to test the performance of the diagnostic technique for the case of parallel cell connections, where only an aggregated cell voltage is available, as opposed to true individual cell voltages in the case for series connections. Eventually, the ability to track individual electrode voltages in the energy storage system will be used to optimise charge and discharge patterns and cell voltage limits with the aim to prolong the cells' lifetime.

References

[1] M. Armand and J. Tarascon, "Building better batteries," *Nature*, vol. 451, no. 7179, pp. 652–657, 2008.

[2] B. Dunn, H. Kamath, and J. M. Tarascon, "Electrical Energy Storage for the Grid: A Battery of Choices," *Science*, vol. 334, no. 6058, pp. 928–935, 2011.

[3] J. M. Tarascon and M. Armand, "Issues and challenges facing rechargeable lithium batteries," *Nature*, vol. 414, no. 6861, pp. 359–367, 2001.

[4] B. Scrosati and J. Garche, "Lithium batteries: Status, prospects and future," *Journal of Power Sources*, vol. 195, no. 9, pp. 2419–2430, 2010.

[5] C. H. Doh, D. H. Kim, H. S. Kim, H. M. Shin, Y. D. Jeong, S. I. Moon, B. S. Jin, S. W. Eom, H. S. Kim, K. W. Kim, D. H. Oh, and A. Veluchamy, "Thermal and electrochemical behaviour of C/LixCoO2 cell during safety test," *Journal of Power Sources*, vol. 175, no. 2, pp. 881–885, 2008.

[6] Q. Wang, P. Ping, X. Zhao, G. Chu, J. Sun, and C. Chen, "Thermal runaway caused fire and explosion of lithium ion battery," *Journal of Power Sources*, vol. 208, pp. 210–224, 2012.

[7] J. Zhang and J. Lee, "A review on prognostics and health monitoring of Li-ion battery," *Journal of Power Sources*, vol. 196, no. 15, pp. 6007–6014, 2011.

[8] L. Lu, X. Han, J. Li, J. Hua, M. Ouyang, and Y. Zheng, "A review on the key issues for lithium-ion battery management in electric vehicles," *Journal of Power Sources*, vol. 226, pp. 272–288, 2013.

[9] S. S. Choi and H. S. Lim, "Factors that affect cycle-life and possible degradation mechanisms of a Li-ion cell based on LiCoO2," *Journal of Power Sources*, vol. 111, pp. 130–136, 2002.

[10] M. Broussely, P. Biensan, F. Bonhomme, P. Blanchard, S. Herreyre, K. Nechev, and R. Staniewicz, "Main aging mechanisms in Li ion batteries," *Journal of Power Sources*, vol. 146, no. 1-2, pp. 90–96, 2005.

[11] K. Jalkanen, J. Karppinen, L. Skogström, T. Laurila, M. Nisula, and K. Vuorilehto, "Cycle aging of commercial NMC/graphite pouch cells at different temperatures," *Applied Energy*, vol. 154, pp. 160–172, 2015.

[12] I. Bloom, B. W. Cole, J. J. Sohn, S. A. Jones, E. G. Polzin, V. S. Battaglia, G. L. Henriksen, C. Motloch, R. Richardson, T. Unkelhaeuser, D. Ingersoll, and H. L. Case, "An accelerated calendar and cycle life study of Li-ion cells," *Journal of Power Sources*, vol. 101, no. 2, pp. 238–247, 2001.

[13] C. Monroe and J. Newman, "Dendrite Growth in Lithium/Polymer Systems," *Journal of The Electrochemical Society*, vol. 150, no. 10, p. A1377, 2003.

[14] S. Santhanagopalan, P. Ramadass, and J. Z. Zhang, "Analysis of internal short-circuit in a lithium ion cell," *Journal of Power Sources*, vol. 194, no. 1, pp. 550–557, 2009.

[15] R. Bhattacharyya, B. Key, H. Chen, A. S. Best, A. F. Hollenkamp, and C. P. Grey, "In situ NMR observation of the formation of metallic lithium microstructures in lithium batteries.," *Nature materials*, vol. 9, no. 6, pp. 504–510, 2010.

[16] Z. Li, J. Huang, B. Yann Liaw, V. Metzler, and J. Zhang, "A review of lithium deposition in lithium-ion and lithium metal secondary batteries," *Journal of Power Sources*, vol. 254, pp. 168–182, 2014.

[17] T. Ohsaki, T. Kishi, T. Kuboki, N. Takami, N. Shimura, Y. Sato, M. Sekino, and A. Satoh, "Overcharge reaction of lithium-ion batteries," *Journal of Power Sources*, vol. 146, no. 1-2, pp. 97–100, 2005.

[18] G. L. Plett, "Extended Kalman filtering for battery management systems of LiPB-based HEV battery packs. Part 1. Background," *Journal of Power Sources*, vol. 134, no. 2, pp. 252–261, 2004.

[19] V. Pop, H. J. Bergveld, P. P. L. Regtien, J. H. G. Op het Veld, D. Danilov, and P. H. L. Notten, "Battery Aging and Its Influence on the Electromotive Force," *Journal of The Electrochemical Society*, vol. 154, no. 8, p. A744, 2007.

[20] M. Dubarry, V. Svoboda, R. Hwu, and B. Y. Liaw, "Capacity and power fading mechanism identification from a commercial cell evaluation," *Journal of Power Sources*, vol. 165, no. 2, pp. 566–572, 2007.

[21] D. Andrea, *Battery management systems for large lithium-ion battery packs*. London: Artech House, 2010.

[22] P. Balakrishnan, R. Ramesh, and T. Premkumar, "Safety mechanisms in lithium-ion batteries," *Journal of Power Sources*, vol. 155, pp. 401–414, 2006.

[23] M. Petzl and M. A. Danzer, "Nondestructive detection, characterization, and quantification of lithium plating in commercial lithium-ion batteries," *Journal of Power Sources*, vol. 254, pp. 80–87, 2014.

[24] J. Vetter, P. Novák, M. R. Wagner, C. Veit, K. C. Möller, J. O. Besenhard, M. Winter, M. Wohlfahrt-Mehrens, C. Vogler, and A. Hammouche, "Ageing

mechanisms in lithium-ion batteries," *Journal of Power Sources*, vol. 147, no. 1-2, pp. 269–281, 2005.

[25] D. Aurbach, B. Markovsky, I. Weissman, E. Levi, and Y. Ein-Eli, "On the correlation between surface chemistry and performance of graphite negative electrodes for Li ion batteries," *Electrochimica Acta*, vol. 45, no. 1-2, pp. 67–86, 1999.

[26] V. Agubra and J. Fergus, "Lithium ion battery anode aging mechanisms," *Materials*, vol. 6, no. 4, pp. 1310–1325, 2013.

[27] S. K. Jung, H. Gwon, J. Hong, K. Y. Park, D. H. Seo, H. Kim, J. Hyun, W. Yang, and K. Kang, "Understanding the Degradation Mechanisms of LiNi0.5Co0.2Mn0.3O2 Cathode Material in Lithium Ion Batteries," *Advanced Energy Materials*, vol. 4, pp. 1–7, 2014.

[28] P. Novák, F. Joho, M. Lanz, B. Rykart, J. C. Panitz, D. Alliata, R. Kötz, and O. Haas, "The complex electrochemistry of graphite electrodes in lithium-ion batteries," *Journal of Power Sources*, vol. 97-98, pp. 39–46, 2001.

[29] P. Verma, P. Maire, and P. Novák, "A review of the features and analyses of the solid electrolyte interphase in Li-ion batteries," *Electrochimica Acta*, vol. 55, no. 22, pp. 6332–6341, 2010.

[30] C. R. Birkl, M. R. Roberts, E. Mcturk, P. G. Bruce, and D. A. Howey, "Degradation Diagnostics for Lithium Ion Cells," *Journal of Power Sources*, vol. 341, pp. 373–386, 2017.

[31] J. Wang, P. Liu, J. Hicks-Garner, E. Sherman, S. Soukiazian, M. Verbrugge, H. Tataria, J. Musser, and P. Finamore, "Cycle-life model for graphite-LiFePO4 cells," *Journal of Power Sources*, vol. 196, no. 8, pp. 3942–3948, 2011.

[32] Z. Li, L. Lu, M. Ouyang, and Y. Xiao, "Modeling the capacity degradation of LiFePO4/graphite batteries based on stress coupling analysis," *Journal of Power Sources*, vol. 196, pp. 9757–9766, nov 2011.

[33] M. Safari, M. Morcrette, a. Teyssot, and C. Delacourt, "Life-Prediction Methods for Lithium-Ion Batteries Derived from a Fatigue Approach," *Journal of The Electrochemical Society*, vol. 157, no. 6, p. A713, 2010.

[34] M. Safari, M. Morcrette, a. Teyssot, and C. Delacourt, "Life Prediction Methods for Lithium-Ion Batteries Derived from a Fatigue Approach," *Journal of The Electrochemical Society*, vol. 157, no. 7, p. A892, 2010.

[35] W. He, N. Williard, M. Osterman, and M. Pecht, "Prognostics of lithium-ion batteries based on Dempster-Shafer theory and the Bayesian Monte Carlo method," *Journal of Power Sources*, vol. 196, no. 23, pp. 10314–10321, 2011.

[36] C. Chen and M. Pecht, "Prognostics of lithium-ion batteries using model-based and data-driven methods," *Proceedings of the IEEE 2012 Prognostics and System Health Management Conference (PHM-2012 Beijing)*, pp. 1–6, 2012.

[37] V. Klass, M. Behm, and G. Lindbergh, "A support vector machine-based state-of-health estimation method for lithium-ion batteries under electric vehicle operation," *Journal of Power Sources*, vol. 270, pp. 262–272, 2014.

[38] J. Guo, Z. Li, and M. Pecht, "A Bayesian approach for Li-Ion battery capacity fade modeling and cycles to failure prognostics," *Journal of Power Sources*, vol. 281, pp. 173–184, 2015.

[39] D. Liu, W. Xie, H. Liao, and Y. Peng, "An Integrated Probabilistic Approach to Lithium-Ion Battery Remaining Useful Life Estimation," *Ieee Transactions on Instrumentation and Measurement*, vol. 64, no. 3, pp. 660–670, 2015.

[40] L. Liao and F. Kottig, "A hybrid framework combining data-driven and model-based methods for system remaining useful life prediction," *Applied Soft Computing Journal*, vol. 44, pp. 191–199, 2016.

[41] S. Paul, C. Diegelmann, H. Kabza, and W. Tillmetz, "Analysis of ageing inhomogeneities in lithium-ion battery systems," *Journal of Power Sources*, vol. 239, pp. 642–650, 2013.

[42] I. Bloom, A. N. Jansen, D. P. Abraham, J. Knuth, S. A. Jones, V. S. Battaglia, and G. L. Henriksen, "Differential voltage analyses of high-power, lithium-ion cells 1. Technique and application," *Journal of Power Sources*, vol. 139, no. 1-2, pp. 295–303, 2005.

[43] M. Dubarry, V. Svoboda, R. Hwu, and B. Y. Liaw, "Incremental Capacity Analysis and Close-to-Equilibrium OCV Measurements to Quantify Capacity Fade in Commercial Rechargeable Lithium Batteries," *Electrochemical and Solid-State Letters*, vol. 9, no. 10, p. A454, 2006.

[44] M. Dubarry, V. Svoboda, R. Hwu, and B. Y. Liaw, "Capacity loss in rechargeable lithium cells during cycle life testing: The importance of determining state-of-charge," *Journal of Power Sources*, vol. 174, no. 2, pp. 1121–1125, 2007.

[45] M. Dubarry and B. Y. Liaw, "Identify capacity fading mechanism in a commercial LiFePO4 cell," *Journal of Power Sources*, vol. 194, no. 1, pp. 541–549, 2009.

[46] M. Dubarry, C. Truchot, B. Y. Liaw, K. Gering, S. Sazhin, D. Jamison, and C. Michelbacher, "Evaluation of commercial lithium-ion cells based on composite positive electrode for plug-in hybrid electric vehicle applications. Part II. Degradation mechanism under 2C cycle aging," *Journal of Power Sources*, vol. 196, no. 23, pp. 10336–10343, 2011.

[47] M. Dubarry, C. Truchot, M. Cugnet, B. Y. Liaw, K. Gering, S. Sazhin, D. Jamison, and C. Michelbacher, "Evaluation of commercial lithium-ion cells based on composite positive electrode for plug-in hybrid electric vehicle applications. Part I: Initial characterizations," *Journal of Power Sources*, vol. 196, no. 23, pp. 10328–10335, 2011.

[48] M. Dubarry, C. Truchot, B. Y. Liaw, K. Gering, S. Sazhin, D. Jamison, and C. Michelbacher, "Evaluation of Commercial Lithium-Ion Cells Based on Composite Positive Electrode for Plug-In Hybrid Electric Vehicle Applications: III. Effect of Thermal Excursions without Prolonged Thermal Aging," *Journal of the Electrochemical Society*, vol. 160, no. 1, pp. A191–A199, 2012.

[49] M. Dubarry, C. Truchot, and B. Y. Liaw, "Synthesize battery degradation modes via a diagnostic and prognostic model," *Journal of Power Sources*, vol. 219, pp. 204–216, 2012.

[50] A. J. Smith and J. R. Dahn, "Delta Differential Capacity Analysis," *Journal of The Electrochemical Society*, vol. 159, no. 3, p. A290, 2012.

[51] B. Wu, V. Yufit, Y. Merla, R. F. Martinez-Botas, N. P. Brandon, and G. J. Offer, "Differential thermal voltammetry for tracking of degradation in lithium-ion batteries," *Journal of Power Sources*, vol. 273, pp. 495–501, 2015.

[52] Y. Merla, B. Wu, V. Yufit, N. P. Brandon, R. F. Martinez-Botas, and G. J. Offer, "Novel application of differential thermal voltammetry as an in-depth state-of-health diagnosis method for lithium-ion batteries," *Journal of Power Sources*, vol. 307, pp. 308–319, 2016.

[53] Y. F. Reynier, R. Yazami, and B. Fultz, "Thermodynamics of Lithium Intercalation into Graphites and Disordered Carbons," *Journal of The Electrochemical Society*, vol. 151, no. 3, p. A422, 2004.

[54] W. Waag, C. Fleischer, and D. U. Sauer, "Critical review of the methods for monitoring of lithium-ion batteries in electric and hybrid vehicles," *Journal of Power Sources*, vol. 258, pp. 321–339, 2014.

[55] G. L. Plett, "Extended Kalman filtering for battery management systems of LiPB-based HEV battery packs," *Journal of Power Sources*, vol. 134, no. 2, pp. 262–276, 2004.

[56] G. L. Plett, "Extended Kalman filtering for battery management systems of LiPB-based HEV battery packs. Part 3. State and parameter estimation," *Journal of Power Sources*, vol. 134, no. 2, pp. 277–292, 2004.

[57] M. Verbrugge and B. Koch, "Generalized Recursive Algorithm for Adaptive Multiparameter Regression," *Journal of The Electrochemical Society*, vol. 153, no. 1, p. A187, 2006.

[58] I. S. Kim, "A Technique for Estimating the State of Health of Lithium Batteries through a Dual-Sliding-Mode Observer," *IEEE Transactions on Power Electronics*, vol. 25, no. 4, pp. 1013–1022, 2010.

[59] B. Saha and K. Goebel, "Modeling Li-ion Battery Capacity Depletion in a Particle Filtering Framework," in *Annual Conference of the Prognostics and Health Management Society*, pp. 1–10, 2009.

[60] J. Remmlinger, M. Buchholz, M. Meiler, P. Bernreuter, and K. Dietmayer, "State-of-health monitoring of lithium-ion batteries in electric vehicles by on-board internal resistance estimation," *Journal of Power Sources*, vol. 196, no. 12, pp. 5357–5363, 2011.

[61] C. Fleischer, W. Waag, H. M. Heyn, and D. U. Sauer, "On-line adaptive battery impedance parameter and state estimation considering physical principles in reduced order equivalent circuit battery models," *Journal of Power Sources*, vol. 260, pp. 276–291, 2014.

[62] S. Zhao, S. R. Duncan, and D. A. Howey, "Observability Analysis and State Estimation of Lithium-Ion Batteries in the Presence of Sensor Biases," *IEEE Transactions on Control Systems Technology*, vol. 25, no. 1, pp. 326–333, 2017.

[63] S. Atlung, K. West, and T. Jacobsen, "Dynamic Aspects of Solid Solution Cathodes for Electrochemical Power Sources," *Journal of The Electrochemical Society*, pp. 1311–1321, 1979.

[64] G. Ning and B. N. Popov, "Cycle Life Modeling of Lithium-Ion Batteries," *Journal of The Electrochemical Society*, vol. 151, no. 10, p. A1584, 2004.

[65] R. Spotnitz, "Simulation of capacity fade in lithium-ion batteries," *Journal of Power Sources*, vol. 113, no. August 2002, pp. 72–80, 2003.

[66] P. Ramadass, B. Haran, P. M. Gomadam, R. White, and B. N. Popov, "Development of First Principles Capacity Fade Model for Li-Ion Cells," *Journal of The Electrochemical Society*, vol. 151, no. 2, p. A196, 2004.

[67] J. Christensen and J. Newman, "A Mathematical Model for the Lithium-Ion Negative Electrode Solid Electrolyte Interphase," *Journal of The Electrochemical Society*, vol. 151, no. 11, p. A1977, 2004.

[68] M. Safari, M. Morcrette, A. Teyssot, and C. Delacourt, "Multimodal Physics-Based Aging Model for Life Prediction of Li-Ion Batteries," *Journal of The Electrochemical Society*, vol. 156, no. 3, p. A145, 2009.

[69] M. B. Pinson and M. Z. Bazant, "Theory of SEI Formation in Rechargeable Batteries: Capacity Fade, Accelerated Aging and Lifetime Prediction," *Journal of the Electrochemical Society*, vol. 160, no. 2, pp. A243—-A250, 2012.

[70] I. Laresgoiti, S. Kabitz, M. Ecker, and D. U. Sauer, "Modeling mechanical degradation in lithium ion batteries during cycling: Solid electrolyte interphase fracture," *Journal of Power Sources*, vol. 300, pp. 112–122, 2015.

[71] R. Fu, S. Y. Choe, V. Agubra, and J. Fergus, "Development of a physics-based degradation model for lithium ion polymer batteries considering side reactions," *Journal of Power Sources*, vol. 278, pp. 506–521, 2015.

[72] M. Safari and C. Delacourt, "Simulation-Based Analysis of Aging Phenomena in a Commercial Graphite/LiFePO4 Cell," *Journal of The Electrochemical Society*, vol. 158, no. 12, p. A1436, 2011.

[73] Q. Zhang and R. E. White, "Capacity fade analysis of a lithium ion cell," *Journal of Power Sources*, vol. 179, no. 2, pp. 793–798, 2008.

[74] J. Christensen and J. Newman, "A Mathematical Model of Stress Generation and Fracture in Lithium Manganese Oxide," *Journal of The Electrochemical Society*, vol. 153, no. 6, p. A1019, 2006.

[75] E. Prada, D. D. Domenico, Y. Creff, J. Bernard, and F. Huet, "Simplified Electrochemical and Thermal Model of LiFePO4 -Graphite Li-Ion Batteries for Fast Charge Applications," *Journal of the Electrochemical Society*, vol. 159, no. 9, pp. 1508–1519, 2012.

[76] E. Prada, D. Di Domenico, Y. Creff, J. Bernard, V. Sauvant-Moynot, and F. Huet, "A Simplified Electrochemical and Thermal Aging Model of LiFePO4-Graphite Li-ion Batteries: Power and Capacity Fade Simulations," *Journal of the Electrochemical Society*, vol. 160, no. 4, pp. A616–A628, 2013.

[77] G. K. Prasad and C. D. Rahn, "Model based identification of aging parameters in lithium ion batteries," *Journal of Power Sources*, vol. 232, no. null, pp. 79–85, 2013.

[78] S. Santhanagopalan, Q. Guo, and R. E. White, "Parameter Estimation and Model Discrimination for a Lithium-Ion Cell," *Journal of The Electrochemical Society*, vol. 154, no. 3, pp. A198–A206, 2007.

[79] R. Deshpande, M. Verbrugge, Y. T. Cheng, J. Wang, and P. Liu, "Battery Cycle Life Prediction with Coupled Chemical Degradation and Fatigue Mechanics," *Journal of the Electrochemical Society*, vol. 159, no. 10, pp. A1730—-A1738, 2012.

[80] P. C. Paris and F. Erdogan, "A Critical Analysis of Crack Propagation Laws," *Journal of Basic Engineering*, vol. 85, no. 4, pp. 528–533, 1963.

[81] R. Fu, M. Xiao, and S. Y. Choe, "Modeling, validation and analysis of mechanical stress generation and dimension changes of a pouch type high power Li-ion battery," *Journal of Power Sources*, vol. 224, pp. 211–224, 2013.

[82] V. Ramadesigan, K. Chen, N. A. Burns, V. Boovaragavan, R. D. Braatz, and V. R. Subramanian, "Parameter Estimation and Capacity Fade Analysis of Lithium-Ion Batteries Using First-Principles-Based Efficient Reformulated Models," *ECS Transactions*, vol. 158, no. 9, pp. 11–19, 2009.

[83] A. P. Schmidt, M. Bitzer, Á. W. Imre, and L. Guzzella, "Experiment-driven electrochemical modeling and systematic parameterization for a lithium-ion battery cell," *Journal of Power Sources*, vol. 195, no. 15, pp. 5071–5080, 2010.

[84] V. Ramadesigan, K. Chen, N. A. Burns, V. Boovaragavan, R. D. Braatz, and V. R. Subramanian, "Parameter Estimation and Capacity Fade Analysis of Lithium-Ion Batteries Using Reformulated Models," *Journal of The Electrochemical Society*, vol. 158, no. 9, pp. A1048–A1054, 2011.

[85] J. C. Forman, S. J. Moura, J. L. Stein, and H. K. Fathy, "Genetic identification and fisher identifiability analysis of the Doyle-Fuller-Newman model from experimental cycling of a LiFePO 4 cell," *Journal of Power Sources*, vol. 210, pp. 263–275, 2012.

[86] J. Marcicki, M. Canova, A. T. Conlisk, and G. Rizzoni, "Design and parametrization analysis of a reduced-order electrochemical model of graphite/LiFePO4 cells for SOC/SOH estimation," *Journal of Power Sources*, vol. 237, pp. 310–324, 2013.

[87] S. J. Harris and P. Lu, "Effects of Inhomogeneities - Nanoscale to Mesoscale - on the Durability of Li-Ion Batteries," *The Journal of Physical Chemistry C*, vol. 117, pp. 6481–6492, 2013.

[88] T. Bach, S. Schuster, E. Fleder, J. Müller, M. Brand, H. Lorrmann, A. Jossen, and G. Sextl, "Nonlinear aging of cylindrical lithium-ion cells linked to heterogeneous compression," *Journal of Energy Storage*, vol. 5, pp. 212–223, 2016.

[89] M. Fleckenstein, O. Bohlen, M. A. Roscher, and B. Bäker, "Current density and state of charge inhomogeneities in Li-Ion battery cells with LiFePO4 as cathode material due to temperature gradients," *Journal of Power Sources*, vol. 196, no. 10, pp. 4769–4778, 2011.

[90] R. Srinivasan, B. G. Carkhuff, M. H. Butler, and A. C. Baisden, "Instantaneous measurement of the internal temperature in lithium-ion rechargeable cells," *Electrochimica Acta*, vol. 56, no. 17, pp. 6198–6204, 2011.

[91] R. Srinivasan, "Monitoring dynamic thermal behavior of the carbon anode in a lithium-ion cell using a four-probe technique," *Journal of Power Sources*, vol. 198, pp. 351–358, 2012.

[92] X. Lin, H. E. Perez, J. B. Siegel, A. G. Stefanopoulou, Y. Li, R. D. Anderson, Y. Ding, and M. P. Castanier, "Online parameterization of lumped thermal dynamics in cylindrical lithium ion batteries for core temperature estimation

and health monitoring," *IEEE Transactions on Control Systems Technology*, vol. 21, no. 5, pp. 1745–1755, 2013.

[93] M. Fleckenstein, S. Fischer, O. Bohlen, and B. Bäker, "Thermal Impedance Spectroscopy - A method for the thermal characterization of high power battery cells," *Journal of Power Sources*, vol. 223, pp. 259–267, 2013.

[94] P. Wang, X. Zhang, L. Yang, X. Zhang, M. Yang, H. Chen, and D. Fang, "Real-time monitoring of internal temperature evolution of the lithium-ion coin cell battery during the charge and discharge process," *Extreme Mechanics Letters*, vol. 9, pp. 459–466, 2016.

[95] R. R. Richardson, S. Zhao, and D. A. Howey, "On-board monitoring of 2-D spatially-resolved temperatures in cylindrical lithium-ion batteries: Part I. State estimation via impedance-based temperature sensing," *Journal of Power Sources*, vol. 326, pp. 377 – 388, 2016.

[96] R. R. Richardson, S. Zhao, and D. A. Howey, "On-board monitoring of 2-D spatially-resolved temperatures in cylindrical lithium-ion batteries: Part II. State estimation via impedance-based temperature sensing," *Journal of Power Sources*, vol. 327, pp. 726–735, 2016.

[97] G. H. Kim, K. Smith, J. Ireland, and A. Pesaran, "Fail-safe design for large capacity lithium-ion battery systems," *Journal of Power Sources*, vol. 210, pp. 243–253, 2012.

[98] F. Rufus, S. Lee, and A. Thakker, "Health monitoring algorithms for space application batteries," *International Conference on Prognostics and Health Management*, 2008.

[99] E. Thomas, I. Bloom, J. Christophersen, and V. Battaglia, "Statistical methodology for predicting the life of lithium-ion cells via accelerated degradation testing," *Journal of Power Sources*, vol. 184, no. 1, pp. 312–317, 2008.

[100] J. I. Park, S. H. Baek, M. K. Jeong, and S. J. Bae, "Dual Features Functional Support Vector Machines for Fault Detection of Rechargeable Batteries," *IEEE Transactions on Systems, Man, and Cybernetics, Part C (Applications and Reviews)*, vol. 39, no. 4, pp. 480–485, 2009.

[101] W. Chen, W. Chen, M. Saif, M. Li, and H. Wu, "Simultaneous Fault Isolation and Estimation of Lithium-Ion Batteries via Synthesized Design of Luenberger and Learning Observers," *IEEE Transactions on Control Systems Technology*, pp. 1–9, 2013.

[102] A. Singh, A. Izadian, and S. Anwar, "Fault diagnosis of Li-Ion batteries using multiple-model adaptive estimation," *Industrial Electronics Society, IECON 2013 - 39th Annual Conference of the IEEE*, pp. 3524–3529, 2013.

[103] Z. Liu, Q. Ahmed, G. Rizzoni, and H. Hongwen, "Fault Detection and Isolation for Lithium-ion Battery System using Structural Analysis and Sequential Rresidual Generation," in *Proceedings of the ASME 2014 Dynamic Systems and Control Conference*, pp. 1–10, 2014.

[104] A. Sidhu, A. Izadian, and S. Anwar, "Adaptive Nonlinear Model-Based Fault Diagnosis of Li-Ion Batteries," *Industrial Electronics, IEEE Transactions on*, vol. 62, no. 2, pp. 1002–1011, 2015.

[105] Y. Zheng, X. Han, L. Lu, J. Li, and M. Ouyang, "Lithium ion battery pack power fade fault identification based on Shannon entropy in electric vehicles," *Journal of Power Sources*, vol. 223, pp. 136–146, feb 2013.

[106] H. Witzenhausen, S. Kabitz, and D. U. Sauer, "Coupled thermal and impedance based spatially resolved electric model for fault analysis of lithium ion battery modules," *2012 Electrical Systems for Aircraft, Railway and Ship Propulsion*, pp. 1–6, 2012.

[107] W. R. McKinnon and R. R. Haering, "Physical Mechanisms of Intercalation," in *Modern Aspects of Electrochemistry*, pp. 235–304, Springer, 15 ed., 1983.

[108] T. Ohzuku and A. Ueada, "Phenomenological Expression of Solid-State Redox Potentials of LiCoO2 LiCo1/2Ni1/2O2 and LiNiO2 insertion Electrodes," *Journal of the Electrochemical Society*, vol. 144, no. 8, pp. 2780–2785, 1997.

[109] T. Zheng and J. R. Dahn, "Lattice-gas model to understand voltage profiles of LiNi x Mn 2-x O 4/L i electrochemical cells," *Physical Review B*, vol. 56, no. 7, pp. 3800–3805, 1997.

[110] P. A. Derosa and P. B. Balbuena, "A Lattice Gas Model Study of Lithium Intercalation in Graphite," *Journal of The Electrochemical Society*, vol. 146, no. 10, pp. 3630–3638, 1999.

[111] S. Wang, J. Wang, L. Vu, J. Purewal, S. Soukiazian, and J. Graetz, "On Line Battery Capacity Estimation Based on Half-Cell Open Circuit Voltages," *Journal of the Electrochemical Society*, vol. 161, no. 12, pp. A1788–A1793, 2014.

[112] Y. Xing, W. He, M. Pecht, and K. L. Tsui, "State of charge estimation of lithium-ion batteries using the open-circuit voltage at various ambient temperatures," *Applied Energy*, vol. 113, pp. 106–115, 2014.

[113] S. Schwunk, S. Straub, and M. Jung, "Online Parameterization of a Function Describing the Open-Circuit Voltage by a Least Square Method with Adaptive Forgetting Factor," *Journal of the Electrochemical Society*, vol. 160, no. 11, pp. A2155–A2159, 2013.

[114] C. Weng, J. Sun, and H. Peng, "A unified open-circuit-voltage model of lithium-ion batteries for state-of-charge estimation and state-of-health monitoring," *Journal of Power Sources*, vol. 258, pp. 228–237, 2014.

[115] W. Weppner and R. A. Huggins, "Determination of the Kinetic Parameters of Mixed Conducting Electrodes and Application to the System Li3Sb," *Journal of The Electrochemical Society*, vol. 124, no. 10, pp. 1569–1578, 1977.

[116] C. R. Birkl, E. McTurk, M. R. Roberts, P. G. Bruce, and D. A. Howey, "A Parametric Open Circuit Voltage Model for Lithium Ion Batteries," *Journal of The Electrochemical Society*, vol. 162, no. 12, pp. A2271–A2280, 2015.

[117] E. McTurk, C. R. Birkl, M. R. Roberts, D. A. Howey, and P. G. Bruce, "Minimally Invasive Insertion of Reference Electrodes into Commercial Lithium-Ion Pouch Cells," *ECS Electrochemistry Letters*, vol. 4, no. 12, pp. A145–A147, 2015.

[118] K. J. Vetter, *Electrochemical Kinetics - Theoretical Aspects*. New York, London: Academic Press, 1967.

[119] V. V. Kharton, *Solid state electrochemistry I: fundamentals, materials and their applications*. John Wiley & Sons, 2009.

[120] J. Honerkamp, *Statistical Physics*. Berlin, Heidelberg: Springer, 3 ed., 2012.

[121] J. R. Dahn, "Phase diagram of LixC6," *Physical Review B*, vol. 44, no. 17, pp. 9170–9177, 1991.

[122] M. W. Verbrugge and B. J. Koch, "Electrochemical Analysis of Lithiated Graphite Anodes," *Journal of The Electrochemical Society*, vol. 150, no. 3, pp. A374–A384, 2003.

[123] M. Verbrugge, D. Baker, and X. Xiao, "Formulation for the Treatment of Multiple Electrochemical Reactions and Associated Speciation for the Lithium-Silicon Electrode," *Journal of The Electrochemical Society*, vol. 163, no. 2, pp. A262–A271, 2016.

[124] S. J. Harris, A. Timmons, D. R. Baker, and C. Monroe, "Direct in situ measurements of Li transport in Li-ion battery negative electrodes," *Chemical Physics Letters*, vol. 485, no. 4-6, pp. 265–274, 2010.

[125] H. M. Dahn, A. J. Smith, J. C. Burns, D. A. Stevens, and J. R. Dahn, "User-Friendly Differential Voltage Analysis Freeware for the Analysis of Degradation Mechanisms in Li-Ion Batteries," *Journal of the Electrochemical Society*, vol. 159, no. 9, pp. A1405–A1409, 2012.

[126] A. Marongiu, N. Nlandi, Y. Rong, and D. Sauer, "On-board capacity estimation of lithium iron phosphate batteries by means of half-cell curves," *Journal of Power Sources*, vol. 324, pp. 158–169, 2016.

[127] X. Han, M. Ouyang, L. Lu, J. Li, Y. Zheng, and Z. Li, "A comparative study of commercial lithium ion battery cycle life in electrical vehicle: Aging mechanism identification," *Journal of Power Sources*, vol. 251, pp. 38–54, 2014.

[128] F. Orsini, A. Du Pasquier, B. Beaudoin, J. Tarascon, M. Trentin, N. Langenhuizen, E. De Beer, and P. Notten, "In situ Scanning Electron Microscopy (SEM) observation of interfaces within plastic lithium batteries," *Journal of Power Sources*, vol. 76, pp. 19–29, 1998.

[129] S. Santhanagopalan, P. Ramadass, and J. Z. Zhang, "Analysis of internal short-circuit in a lithium ion cell," *Journal of Power Sources*, vol. 194, no. 1, pp. 550–557, 2009.

[130] S. S. Zhang, K. Xu, and T. R. Jow, "Study of the charging process of a LiCoO2-based Li-ion battery," *Journal of Power Sources*, vol. 160, no. 2 SPEC. ISS., pp. 1349–1354, 2006.

[131] S. Tippmann, D. Walper, L. Balboa, B. Spier, and W. G. Bessler, "Low-Temperature Charging of Lithium-ion Cells Part I: Electrochemical Modeling and Experimental Investigation of Degradation Behavior," *Journal of Power Sources*, vol. 252, pp. 305–316, 2013.

[132] S. U. Kim, P. Albertus, D. Cook, C. W. Monroe, and J. Christensen, "Thermoelectrochemical simulations of performance and abuse in 50-Ah automotive cells," *Journal of Power Sources*, vol. 268, pp. 625–633, 2014.

[133] Y. Wang, S. Nakamura, M. Ue, and P. B. Balbuena, "Studies To Understand Surface Chemistry on Carbon Anodes for Lithium-Ion Batteries:Theoretical Reduction Mechanisms of Ethylene Carbonate," *Journal of the American Chemical Society*, vol. 123, no. 47, pp. 11708–11718, 2001.

[134] K. Edström, T. Gustafsson, and J. Thomas, "The cathode–electrolyte interface in the Li-ion battery," *Electrochimica Acta*, vol. 50, no. 2-3, pp. 397–403, 2004.

[135] L. Somerville, J. Bareno, P. Jennings, A. McGordon, C. Lyness, and I. Bloom, "The Effect of Pre-Analysis Washing on the Surface Film of Graphite Electrodes," *Electrochimica Acta*, vol. 206, pp. 70–76, 2016.

[136] M. Andre, "The ARTEMIS European driving cycles for measuring car pollutant emissions," *Science of The Total Environment*, vol. 334-335, pp. 73–84, 2004.

[137] C. M. Bishop, *Pattern Recognition And Machine Learning*. New York: Springer, 2013.

[138] B. D. Ripley, *Pattern recognition and neural networks*. Cambridge: Cambridge University Press, 2007.

[139] T. Zheng and J. Dahn, "Hysteresis observed in quasi open-circuit voltage measurements of lithium insertion in hydrogen-containing carbons," *Journal of Power Sources*, vol. 68, no. 2, pp. 201–203, 1997.

[140] W. Dreyer, J. Jamnik, C. Guhlke, R. Huth, J. Moskon, and M. Gaberscek, "The thermodynamic origin of hysteresis in insertion batteries.," *Nature materials*, vol. 9, no. 5, pp. 448–453, 2010.

[141] F. Baronti, W. Zamboni, N. Femia, R. Roncella, and R. Saletti, "Experimental analysis of open-circuit voltage hysteresis in lithium-iron-phosphate batteries," *IECON Proceedings (Industrial Electronics Conference)*, pp. 6728–6733, 2013.

[142] F. Baronti, N. Femia, R. Saletti, C. Visone, and W. Zamboni, "Hysteresis Modeling in Li-Ion Batteries," *IEEE Transactions on Magnetics*, vol. 50, no. 11, pp. 1–4, 2014.

[143] I. D. Mayergoyz, *Mathematical models of hysteresis and their applications*. New York: Elsevier, 2 ed., 2003.

[144] M. A. Roscher and D. U. Sauer, "Dynamic electric behavior and open-circuit-voltage modeling of LiFePO4-based lithium ion secondary batteries," *Journal of Power Sources*, vol. 196, no. 1, pp. 331–336, 2011.

Appendix A

A.1 EDX images, cell 1 and cell I

EDX colour maps of NE and PE samples extracted from the unmodified cell 1 are illustrated in Figures A.1 and A.3, respectively. EDX colour maps of NE and PE samples extracted from the 3-electrode cell I are shown in Figures A.2 and A.4, respectively. Both cells were exposed to 120 cycles at $-10\,^{\circ}\mathrm{C}$ with repeated low-rate characterisation at $25\,^{\circ}\mathrm{C}$ (see Table 4.1).

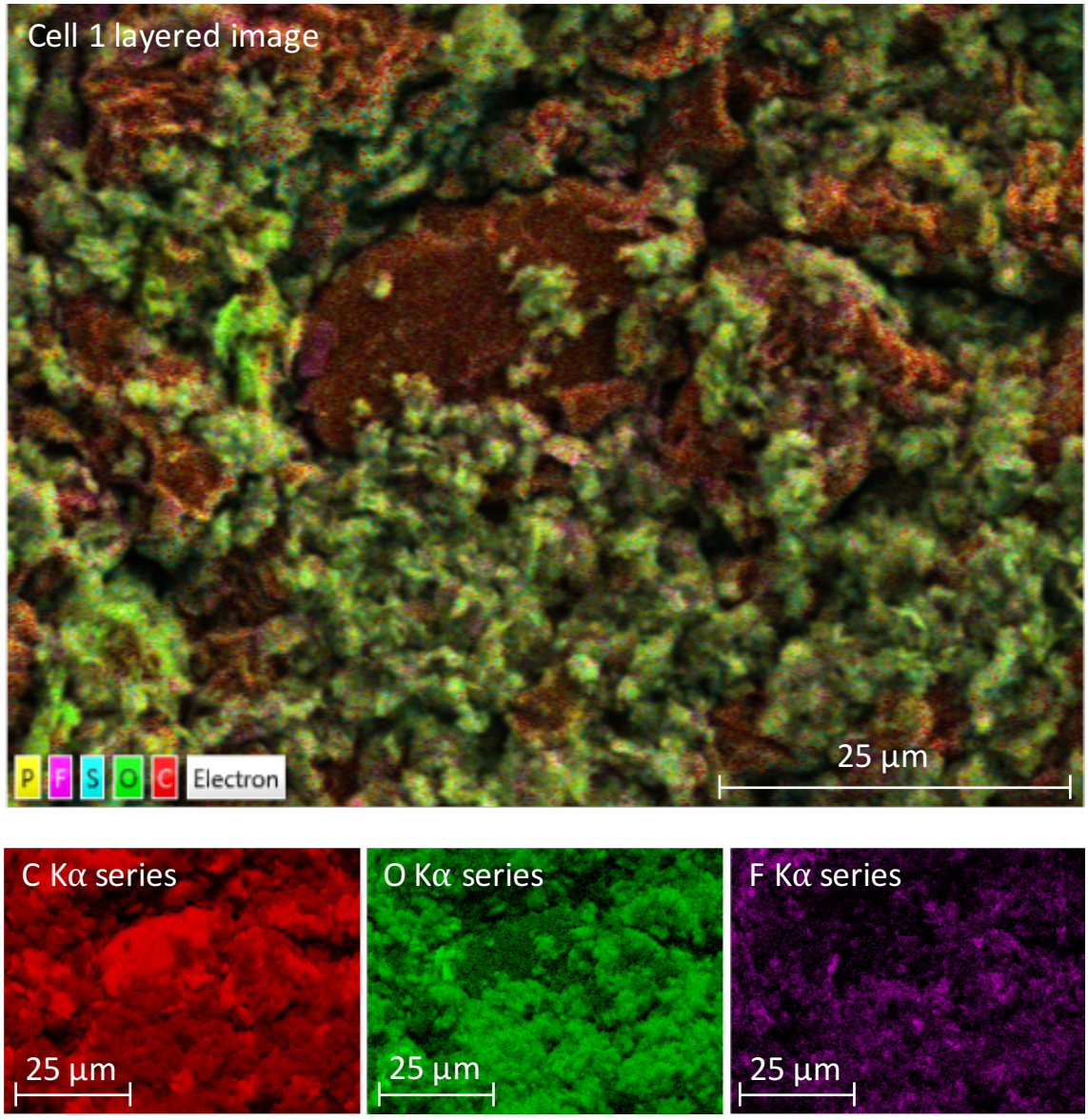

Fig. A.1 EDX, cell 1 anode; layered image (top) and Kα series of C, O and F (bottom).

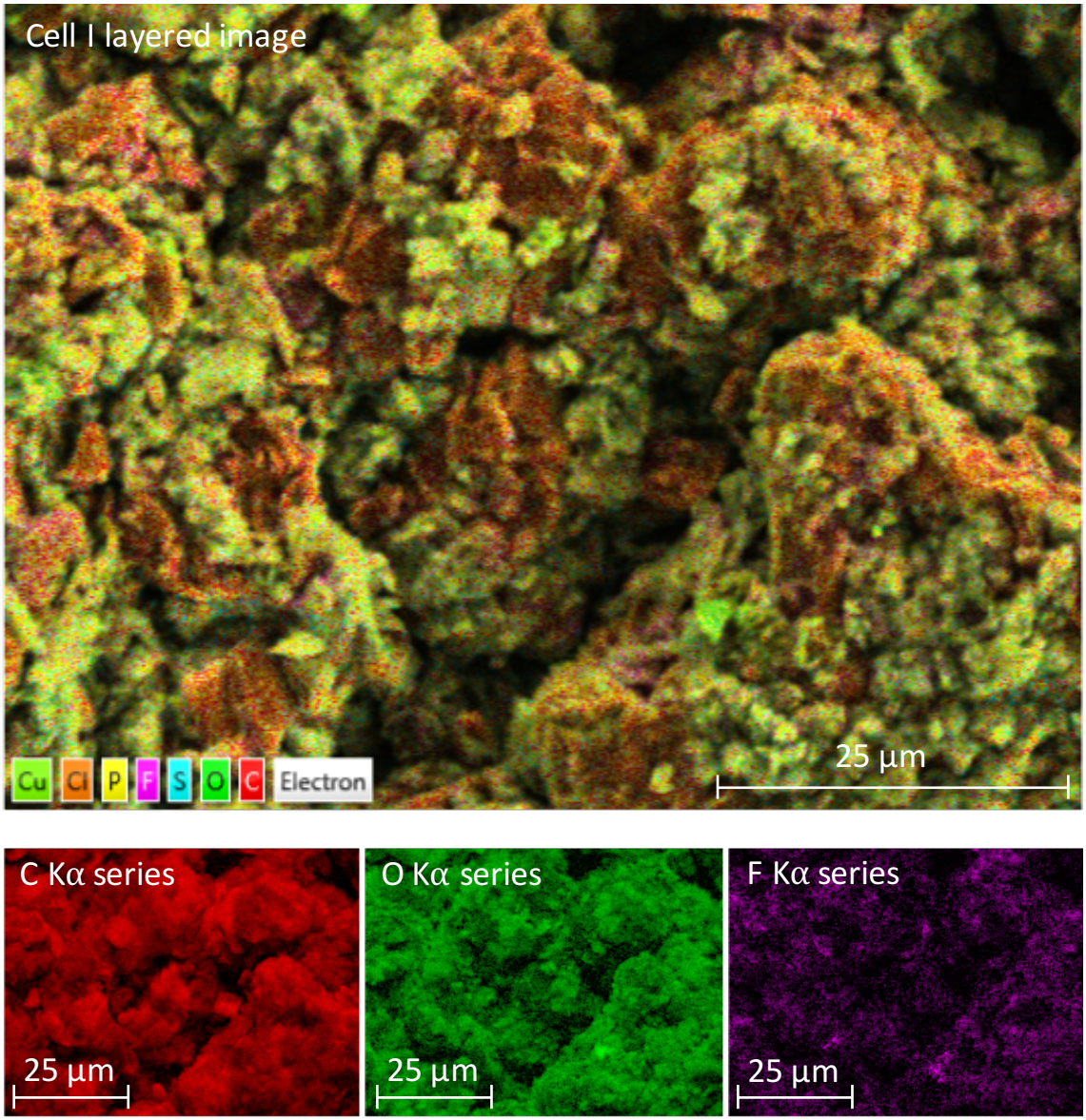

Fig. A.2 EDX, cell I anode; layered image (top) and Kα series of C, O and F (bottom).

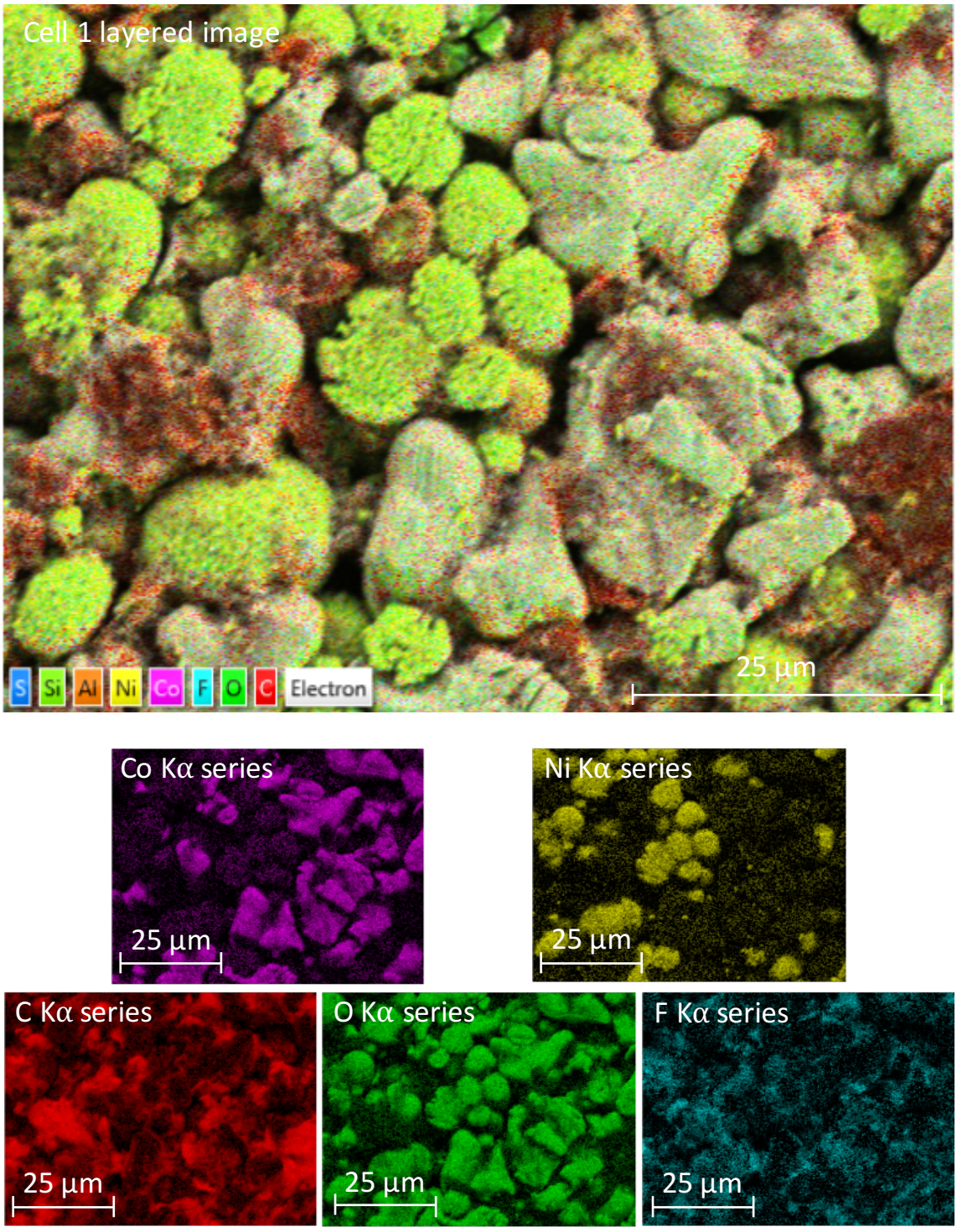

Fig. A.3 EDX, cell 1 cathode; layered image (top) and Kα series of Co, Ni, C, O and F (bottom).

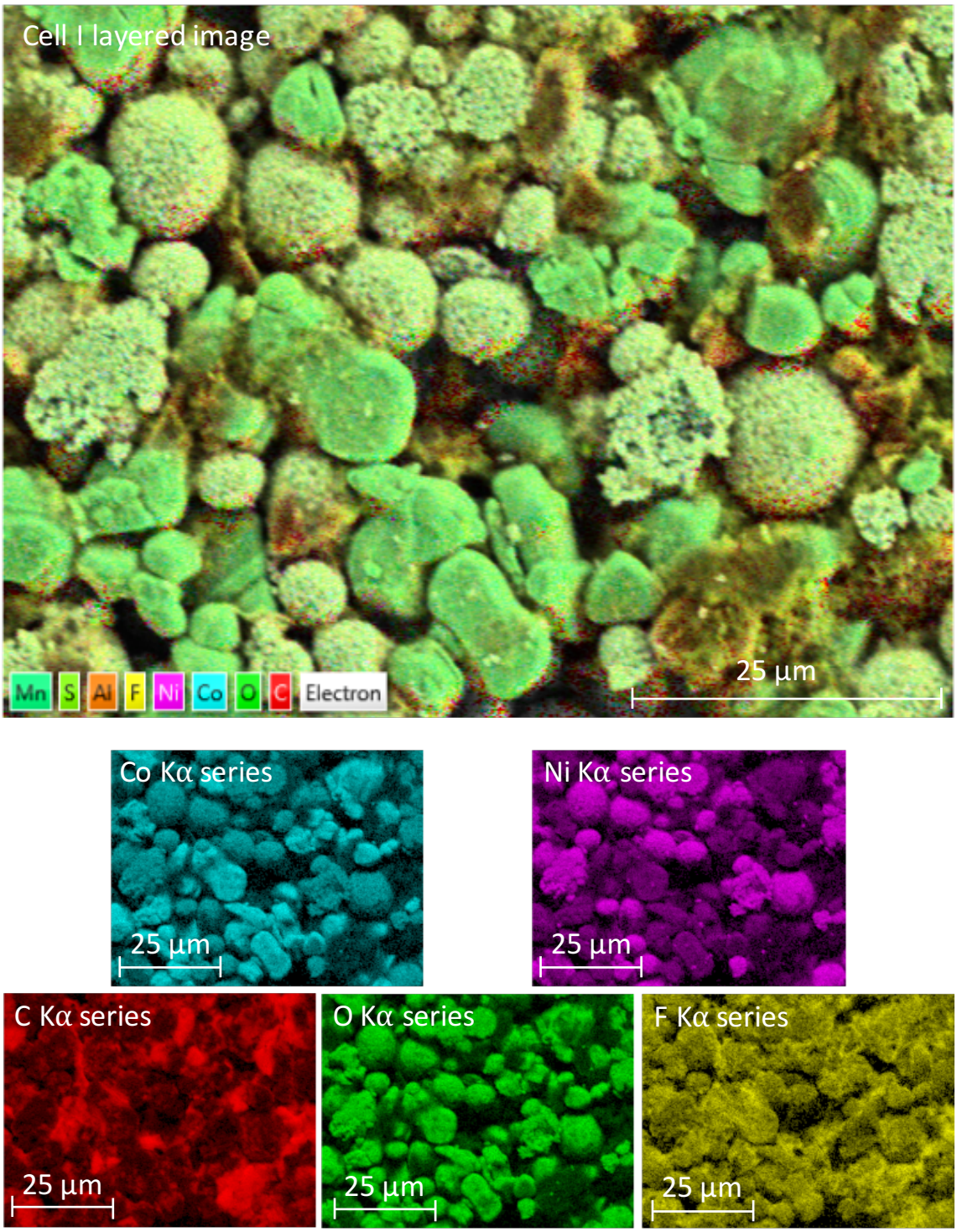

Fig. A.4 EDX, cell I cathode; layered image (top) and Kα series of Co, Ni, C, O and F (bottom).

Appendix B

B.1 Artemis urban drive cycle

The Artemis urban drive cycle [136] is given as a time series of speed, which must be converted to current values for the cycling tests described in Chapter 5. This was done using a basic model for vehicle dynamics, considering only the main loss components of drag and rolling resistance, according to Equation B.1. The assumed parameter values used in Equation B.1 are listed in Table B.1.

$$F = m\dot{v} + \frac{1}{2}\rho C_d A v^2 + C_r m g \tag{B.1}$$

where F is the force of propulsion, m the vehicle mass, v the velocity, ρ the density of air, A the frontal surface area of the vehicle, C_d the coefficient for drag, C_r the coefficient for rolling resistance and g the gravitational acceleration.

Table B.1 Vehicle model parameters.

Parameter	**Value**
m	$1000\,\mathrm{kg}$
A	$2\,\mathrm{m}^2$
C_d	0.3
ρ	$1.2\,\mathrm{kg/m}^3$
C_r	0.023

For simplification, it is assumed that the battery provides a constant voltage and current is proportional to the motor torque demand and, thus, proportional to the required force of propulsion, as calculated in Equation B.1. Inefficiencies in the drive-train, power electronics etc. mainly influence absolute power requirements and are neglected, since only the profile dynamics are of interest for this experiment. In order to obtain a current profile scaled to the maximum discharge current, the required propulsion force is calculated according to Equation B.1, normalised by the maximal force and multiplied by a maximum discharge current rate of 6.75 C (5 A). The maximum discharge rate was chosen as the maximal current capability of the battery tester. Charging currents occurring during regenerative braking events are scaled by a factor of 60%, which is the assumed efficiency of energy recovery. It should be pointed out that the drive cycle dynamics were considered to be the most important aspect of a real-world usage scenario for this work. The dynamics of the drive cycle are reflected by the speed profile, as adopted from the Artemis drive cycle. Absolute power requirements and vehicle-specific losses were not considered to be of importance for this study.

The generated current profile was imported as a time series of current (one current value per second) into Bio-Logic's EC-Lab battery test software. At the time of the start of the experiments, the ability of EC-Lab software to import time series was limited to roughly 1000 entries. To overcome this issue, the drive cycle was cut after roughly 800 s and the section was repeated four times to emulate the duration of one drive cycle. The reduced section of the drive cycle is illustrated in Figure B.1 a) and the complete drive cycle used for the cell tests in Figure B.1 b).

The complete drive cycle lasts 52 min. The average discharge current of the drive cycle is 1.36 A, which corresponds to a rate of 1.84 C. At the end of one completed drive cycle, the cells were discharged to 44% SoC. A relatively high SoC at the end of the drive cycle was chosen to prevent triggering the lower voltage limit of the cells once the cells are degraded and exhibit a high internal resistance.

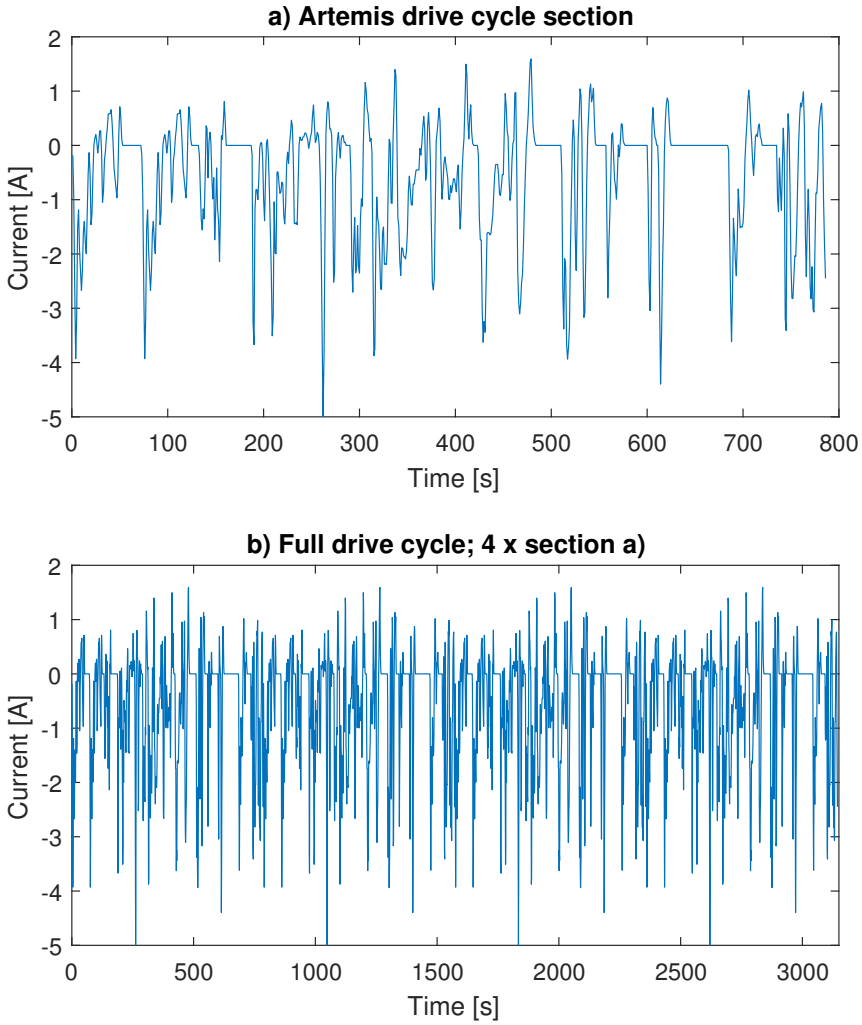

Fig. B.1 a) Reduced section of Artemis drive cycle; b) Full drive cycle used for cell tests composed of four repetitions of the section in a).

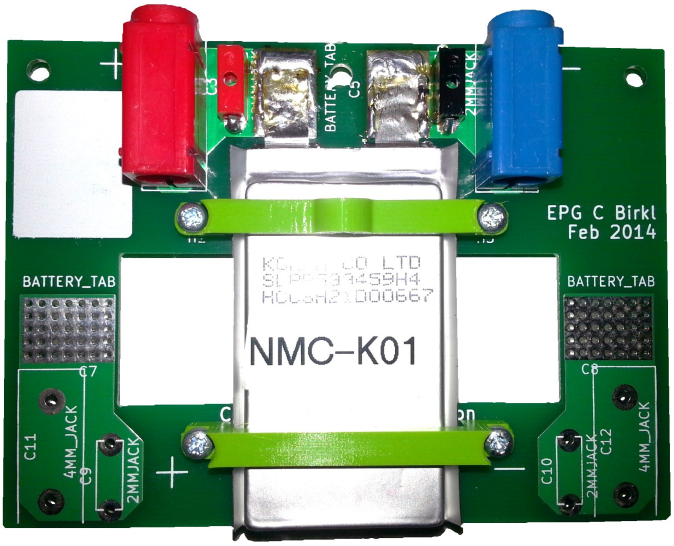

Fig. B.2 Custom cell holder for pouch cells.

B.2 Cell holder design

In order to create reliable and durable contacts between the cells and the battery tester for the long-term experiments described in Chapter 5, cell holders were designed and built, to which the cell tabs were soldered (see Figure B.2). The battery tester was connected to the cell holder through four banana plugs and sockets; two for the current leads and two for the voltage measurements. The resistance of the cell holder between the plugs and the contact pads for the cell tabs was determined by calculating the difference between the real component of the impedance measured on a 1 Ω resistor and the real component of the impedance measured on the cell holder with the same resistor soldered onto the pads of the cell holder (current and sensing connections connected to the respective plugs on the cell holder). The impedance was measured using a Bio-Logic MPG250 with a current amplitude of 300 mA at a frequency of 20 kHz. The resistance of the cell holder was determined to be less than 1 mΩ.

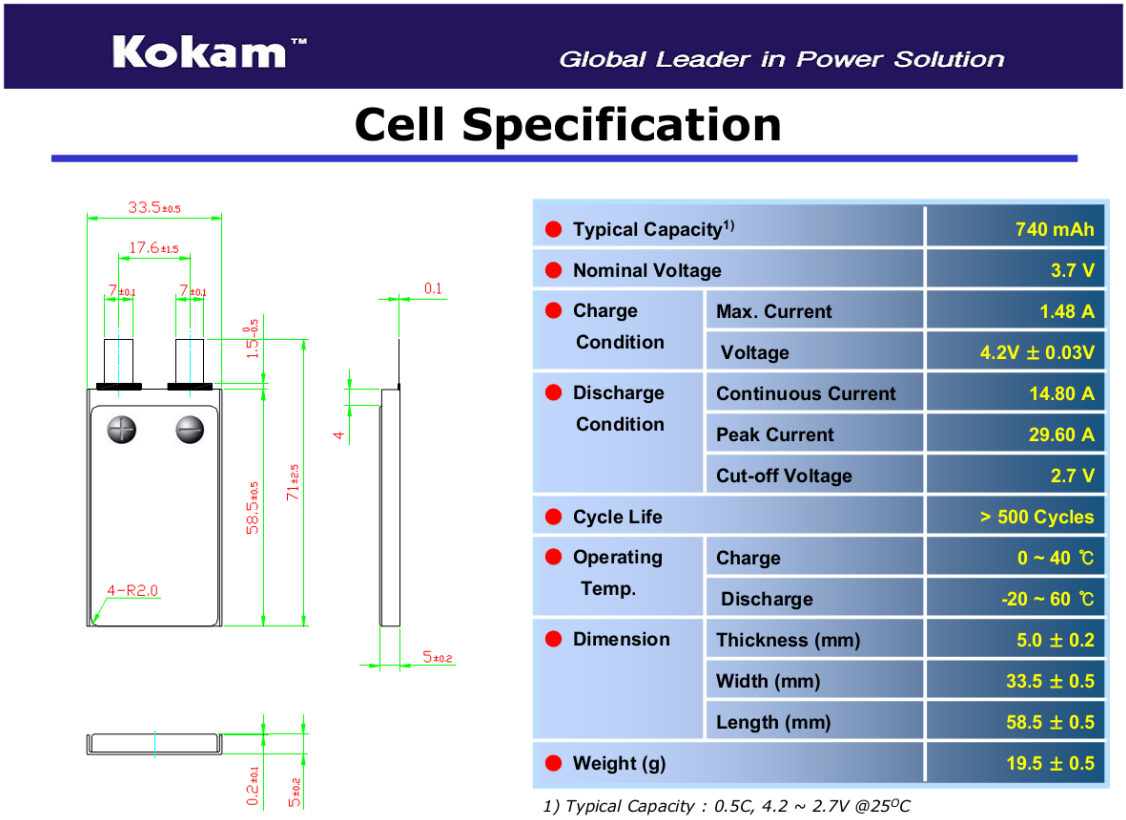

Fig. B.3 Cell specifications provided by the manufacturer.

B.3 Cell specifications

Figure B.3 provides the manufacturer's cell specifications for the Kokam pouch cells used for all experiments in this work.